The Silesian University of Technology

Faculty of Automatic Control, Electronics and Computer Science

Computer Science

Phd thesis

Multispectral Endoscopic Imaging in Photodynamic Diagnosis by Monte Carlo Simulation of Light Propagation in Human Tissue

Andrzej Zacher

Supervisor: prof. hab. dr inż. Konrad Wojciechowski

Gliwice, 2011

Contents

List of papers

1. A. Zacher: Numerical Simulation of Endoscopic Images in Photodynamic Diagnosis. Lecture Notes In Computer Science, 5337:333-344, 2008.

   Abstract: This paper introduces a photon subsurface scattering method to simulate light transport in human colon tissue. First the theoretical model and parameters of human tissue including autofluorescence phenomenon was presented. Then it was described the Monte-Carlo model of steady-state light transport in multi-layered colon. The goal of this investigation is to simulate the light propagation in tissue and to collect the data containing the effect of fluorescence. This information will be used to generate images. Pictures taken for different adjustment of light parameters should define a configuration for which cancerous structures are visible quickly and precisely. Real medical devices can adjust their parameters to the simulated ones and help with efficient diagnosis and recognition of diseased structures.

2. A. Zacher: Initial angle of light rays and their influence on the total distribution, scattering and absorption in human tissue. Studia Informatica, 4(87):37-52, 2009.

   Abstract: This paper describes the method of light transport in human colon tissue. The structure is treated as a turbid medium, so that subsurface scattering model can be applied. Extended photon mapping algorithm is utilized to add a contribution of fluorescence phenomenon and finally generate images. The quantitative dependencies between photon's angle of incidence and their distribution in the tissue are going to be shown. This investigation can be later used to find the best position of endoscope during cancer seeking and recognition.

3. A. Zacher: Mathematical model of human tissue in photodynamic cancer recognition, Studia Informatica, 4(87):53-66, 2009.

   Abstract: This paper presents the method of light propagation in human tissue. Subsurface scattering model together with photon mapping is applied to generate images. Surface and volumetric photon maps were used to fully describe the fluorescence phenomenon. The qualitative comparison between images will be presented to find the best camera angle of incidence. Moreover, multi-spectral images rendered during simulations are verified with real, scientific images.

4. A. Zacher: Utilization of Multi-spectral Images in Photodynamic Diagnosis. Lecture Notes in Computer Science, 6375:367-375, 2010.

Abstract: This paper introduces multi-spectral images for healthy and cancerous parts of human skin. It compares light spectrum calculated from those images with spectrum obtained from simulation. First the mathematical model of tissue and Monte Carlo algorithm of light propagation in turbid media is presented. This theory was then extended to imitate the fluorescence phenomenon, necessary for cancer recognition. Then the processing method of non-normalized multi-spectral images was described. Finally both results were compared to confirm that the assumed model is correct. Having all those information it will be possible to simulate such environment, which applied into reality, would make the cancer diagnosis much faster.

5. A. Zacher: The spectral analysis of human skin tissue using multi-spectral image. Lecture Notes in Computer Science, 6375:376-384, 2010.

Abstract: This paper analyses the properties of human skin, when the light source from different angles and positions was applied. It answers the question how the tissue appearance varies and how the changes of radiance distribution can be observed on multi-spectral images. As long as they contain raw data, that wasn't changed by any postprocessing algorithm, they directly represent light spectrum and its intensity. All images were taken at wavelengths ranging from 400nm to 720nm with step 16nm long. As the next experiment the reflectance spectrum of healthy and diseased tissue was compared. Due to fluorophore concentration and utilizing multi-spectra images, it was possible to unambiguously determine cancerous part of human skin tissue.

6. A. Zacher, A. Świtoński, R. Bieda, S. Kwiatek, W. Latos, G. Cieślar, A. Sieroń, K. Wojciechowski: Symulacyjne badania wybranych aspektów procesu endoskopowego obrazowania wielospektralnego. Przeglad Elektrotechniczny (Electrical Review), ISSN 0033-2097, R. 86 NR 12/2010.

Abstract: This paper analyses the properties of human skin, when the light source from different angles and positions was applied. It answers the question how the tissue appearance varies and how the changes of radiance distribution can be observed on multi-spectral images. As long as they contain raw data, that wasn't changed by any postprocessing algorithm, they directly represent light spectrum and its intensity. All images were taken at wavelengths ranging from 400nm to 720nm with step 16nm long. As the next experiment the reflectance spectrum of healthy and diseased tissue was compared. Due to fluorophore concentration and utilizing multi-spectra images, it was possible to unambiguously determine cancerous part of human skin tissue.

1   Introduction

Photodynamic diagnosis and tumor therapy was invented at the beginning of 80'. Investigations of fluorescence from endogenous and exogenous molecules in cells and tissues are very common, especially in vivo and ex vivo studies [1]. This is a harmless method of cancer diagnosis and removal of infected structures. Specific substances with fluorescent characteristic injected into bloodstream are collected by the cancerous cells. They can be recognized by increased red color intensity, if the light of specified wavelength is applied. Photofrin is the only one fluorophore that was allowed to be used by the Food and Drug Administration. Fortunately, there are also natural fluorophores in human tissues that fluoresces when the laser light is applied. The contrast between neoplastic and non-neoplastic tissues is characterized by changes related to several endogenous fluorophores. Their distribution in the tissue is depth-dependent. The main fluorophores in the epithelial layer are tryptophan, reduced nicotinamide adenine dinucleotide (NADH) and flavin adenine dinucleotide (FAD), while collagen is the primary fluorophore in the stroma. Recent high resolution fluorescence imaging studies showed that the intensity of fluorescence and distribution of fluorophores changes with carcinogenesis. For example, the fluorescence of collagen decreases within the stroma of neoplastic tissues relatively to that of normal tissues. Within the epithelium, the NADH fluorescence of dysplastic regions is increased relatively to that of normal epithelial cells, while the opposite result is observed for FAD [2]. Changes in their fluorescent properties can be helpful to locate and recognize cancerous cells much faster e.g. by image processing methods [3]. That is why more and more attention is attracted to understand the microscopic source and mechanism of light-induced autofluorescence (LIF) in diseased and normal human tissues. The growing interest in characterization of UV and VIS wavelength excitation (250-520 nm) and fluorescence emission spectra (260-750 nm) of known and suspected endogenous biological fluorophores and exogenous photosensitizer agents contribute to increase the number of new methods simulating the behavior of light in contact with fluorophores [4].

Recently, another method of cancer recognition was presented. After local, oral or intravenous administration of 3-aminolaevulinic acid (ALA), as the result of haem metabolic cycle, a very active protoporphyrin IX (PpIX) is accumulated in cells. This leads to morphological changes of the cells and increased sensitivity to light illumination. It turned out that malignant tumor produces more of that fluorophore (PpIX) than healthy or non-malignant tissues. Type of enzymes regulating haem cycle and their amount influence the concentration of protoporphyrin IX [5]. This ability is very widely used during cancer monitoring and detection.

Photodynamic diagnosis is of great interest for medicine [6].

According to [7] there is no quick, accurate and reliable method to diagnose early states of cancerogenesis. However, fluorescence spectroscopy has a big potential to play that role. It analyzes quantitatively the measure of various optical features during fluorescence phenomenon. It describes a fluorescence quantum yield and lifetime of biological molecules, when light of different wavelength is applied like UV, VIS, near-infrared (NIR) or infrared (IR). It presumes that fluorescence intensity of a molecule depends on its concentration, its absorbing power for the initial wavelength and its quantum yield of the registered light [7]. Fluorescent spectroscopy analyzes the surface of the suspicious area, without the necessity of cutting out the tissue sample. Additionally it can be utilized by endoscopes to diagnose internal parts of human body. If successfully applied it would reduce the health care cost and minimize complications, since it is completely noninvasive. Fluorescence spectroscopy has the potential to improve the number of patients with positive outcome.

In order to understand better what is happening with light inside the tissue during fluorescent phenomenon, a various methods for light propagation were investigated. The laser, which produces non-ionising and monochromatic light was available for medicine already in 1960's. Its properties were quickly valued, since it can be customized in such a way that the light is absorbed only by specific molecules and the others remain unaffected. Laser light can form spots of different shapes and sizes, and thus making the resulting energy more or less intensive. This radiation can be further transformed in either thermal, mechanical or chemical energy causing prompt or delayed cell death. This selectivity property is the main advantage of this technique [8].

However, photodynamic therapy (PDT) still suffers from several drawbacks. Different doses of light and photosensitisers should be applied during medical treatment for different patients. There is no standardized way to calculate those values. Another problem concerns accumulation of fluorophores also in healthy cells, which introduce a danger to injure healthy and sensitive tissue regions [9]. The efficacy of this method strongly depends on selective excitation of the cancerous area. Analyzing the fluorescence lifetimes of photosensitizers collected inside living cells may contribute to better understanding of in vivo PDT dosage measurements using imaging and time-domain spectroscopy. Since only photofrin and delta-aminolevulinic acid (ALA) induced protoporphyrin IX (PpIX) have been approved for clinical use, their characteristics was investigated. Described in literature time-domain methods may be good candidates for in vivo PDT dosage monitoring [10]. Despite of that, it is still important to recognize the internal structure of cancer, its development and progress. Gene mutations distort the cellular phenotype and gene expression profile, causing changes in cell morphology and metabolism. The relation between genetic changes and resulting biological

activity is very important from the point of understanding biology of the cancer [11].

Those physical deformation influences the way light is reflected from the tissue. The optics of human skin was widely described in [12]. During experiment the tissue was divided into layers with different inherent optical properties, caused by various concentration of blood, melanin and keratin. All of those substances have different optical properties. Melanins and keratins in the epidermis, and elastin and collagen fibers in the dermis were identified as the primary scatterers in skin. Moreover, scattering efficiency does not change rapidly with wavelength. To the group of main absorbers was included blood, melanosomes and keratin.

The effect of light polarization and fluorescence at the same time was simulated and presented in [13]. Light rays and polarization phenomenon can be modeled as an electromagnetic wave of a given frequency. It propagates through the scene as a discrete ray oscillating in a perpendicular plane to the ray direction. Fluorescence phenomenon, on the other hand, is caused by the pigment molecules, which re-emit the incident light at different, lower wavelengths. In order to uniquely encode the energy transfer between different wavelengths, a knowledge of a special material property is needed, which is called re-radiation matrix (EEM). In this way it is possible to obtain an emission spectra for any excitation wavelength.

Monte Carlo method is a technique that uses stochastic model to simulate different physical processes. In order to simulate light propagation in skin tissue, every light source emits small packets of energy called photons throughout the scene and records their position changes. Thy are considered as neutral and their wave nature is neglected. Once photon is launched it can be moved and reflected or refracted from the tissue surface. When penetrating the internal part of the tissue a packet can be absorbed, scattered or its wavelength can change if fluorescent phenomenon occurred [14]. Since every simulation is basing on actions that happen randomly, the results of similar experiments do not give the same results. Photons are traced in the scene until they escape the tissue or are terminated. The simulation is finished when desired number of particles was emitted. It enables then to calculate statistically such physical quantities as the absorption distribution, time-of-flight or exiting position. In order to obtain appropriate precision a large number of packets needs to be traced [15]. The results and details of such simulation were presented in [16]. A seven layer tissue model was presented, including absorption and scattering coefficient for different wavelengths. Autofluorescence properties of a skin and distribution of excitation laser light inside the tissue were analyzed. Finally, very detailed simulations were performed describing autofluorescence escape function, fluorescence efficiency and fractorial contributions of different skin layers.

The final positions of photons on the tissue surface can be stored in a special

structure called photon map. If the photon was reflected from the tissue, then its new direction is computed using the BRDF of the surface. Reliable and accurate images can be only rendered if the reflectance of surfaces is accurately simulated. Physical reflectance measurements giving the bidirectional reflectance distribution function (BRDF) of an opaque surface, ensure the correctness of obtained results [17]. In order to generate the final image of a simulated tissue it is necessary to perform rendering by applying Monte Carlo ray tracing. Every pixel radiance is calculated by emitting a ray from the camera through the pixel into the scene. At the first surface intersection the algorithm finds nearest neighbor sample estimates in the photon map and calculate their average [18].

As already said optical spectroscopy has the potential to reduce delays in treatment and the number of unnecessary biopsies. However, this technique can be additionally enhanced by utilizing the idea of multi-spectral imaging. It further increase sensitivity of diagnosis and is able to identify early cancer symptoms not visible with traditional white light sources [11].

Surface-spectral reflectance is a property of the object's surface and provides the spectral reflectance curve, which can uniquely describe materials it is made of. It defines an object's color, which can be however differently perceived by human observers or camera devices. Surface reflectances are spectrally high dimensional and cannot be properly detected by normal camera with only three color channels (RGB). Since light of different wavelength enters the skin to different level, it is necessary to investigate each wavelength separately. Images taken for different wavelengths are called multi-spectral. They can also capture light from frequencies not naturally visible by human e.g. infrared. Multi-spectral imaging technology has a big potential. It enables to reproduce the original color very accurately and recognize materials the object is made of independently from illumination [19].

In many cases multi-spectral images contain distortions and noise coming from imaging conditions or just measurement physics. However, they still enables to detect a data corresponding to known or unknown material signatures. Especially in fluorescence microscopy, multi-spectral imaging helps to identify unwanted background emission, spatial regions of autofluorescence and other tissue components [20]. A list of applications is much longer and includes geological research, plant and mineral identification, environmental and wetlands mappings, bathymetry and many others. Processing of multi-spectral images requires reducing the spectral dimensionality without loosing important information and finally classify every image pixel to a material of known spectral parameters. Such properties has a technique proposed by [21], which detects signatures of interests and neglect unwanted components without loosing critical spectral data. The orthogonal subspace projection (OSP) projects every pixel vector to the orthogonal subspace of undesired signatures and in such a way removes interfering

components from the signal. By projecting the residual back to signature of interest, the algorithm maximizes signal-to-noise ratio. As the result initial pixel vector is represented by one-dimensional value representing classified material. This approach can be extended to more than one signature of interest.

2   Motivation and Thesis

The primary goal of this dissertation is the application of fluorescence phenomenon of human skin tissues in the process of harmless and non-invasive cancer detection and enhancing that procedure by usage of multi-spectral images. Since many factors contribute to the outcome of the image acquisition, it is very difficult to compare multi-spectral images for different cancer types and different patients. Additionally, the cost and availably of optical devices limit the scope of experiments and analysis of obtained results. Taking into account mentioned difficulties it is necessary to improve and simplify the photodynamic diagnosis. For this reason the following thesis were formulated:

- **It is possible to create mathematical model of subsurface light transport of chosen human tissue, defined by absorption, scattering and fluorescence phenomenon.** This model should be characterized by parameters, which are different for various tissue types. Those parameters are commonly available and quite good described in literature. Tissue defined in such a way, should be easy to enhance by additional physical phenomenon (i.e. polarization) or components (i.e. blood vessels, mitochondria etc.). The model should enable the analysis of light propagation in any desired moment of time and the effect of fluorescence in details.

- **It is possible create such a model, which basing on the Monte Carlo method is able to generate multi-spectral images qualitatively compliant with real multi-spectral images taken during photodynamic diagnosis.** The validity of such a model is a fundamental goal of this dissertation. The possibility of generation multi-spectral images of similar properties like real images would enable a more detailed analysis of data acquisition process from the point of view of simplification and optimization. For this reason the next thesis can be formulated.

- **The created model enables to optimize the chosen parameters of image acquisition process like light incident angle, the light source spectrum or the distance to the investigated tissue surface and enables to unambiguously distinguish between cancerous and healthy tissue sample.** The optical device used during photodynamic diagnosis is embedded into endoscope. Its position, distance, initial angle or light source spectrum have a big importance on final result and data analysis. Finding the optimal parameters of the endoscope should speed up and simplify the diagnosis and at the same time provide more accurate diagnosis.

In order to prove that all thesis described above are true, it is necessary to decompose them into smaller tasks, which are easier to analyze and draw conclusions from. For this reason the following problems were defined:

1. Define parameters and optical model of human skin tissue,
2. Define types and concentration of natural fluorophores in human skin tissue,
3. Simulate the propagation of light rays in human skin tissue utilizing photon maps,
4. Propose the most efficient light source parameters during photodynamic diagnosis,
5. Propose the best angle of endoscopic device with respect to tissue surface during photodynamic diagnosis,
6. Analyze quantitatively the process of light transport in human skin tissue using photon map algorithm,
7. Investigate autofluorescence phenomenon and fluorescence of cancerous human skin tissue with photosensitisers,
8. Generate images representing human skin tissue with similar appearance and properties like real tissue sample,
9. Analyze multi-spectral images and their properties,
10. Propose the most optimal methods of using multi-spectral images in photodynamic diagnosis,
11. Compare multi-spectral images of human skin tissue with multispectral images generated during photon mapping simulation.

All of this issues are going to be addressed in the next chapters and summarized in conclusions.

3 Previous work

In literature the idea of non-invasive tumor diagnosis is very popular. For this reason different method of light propagation are investigated like Monte Carlo or diffuse model to better understand the tissue properties. Finding scattering and absorption parameters and the concentration of each fluorophore for healthy and diseased tissue is one of the main goals. Different ideas were analyzed. For example in [22] a model for subsurface light transport in translucent materials was introduced. It is the extension of bidirectional reflectance distribution function (BRDF) that assumes that light entering a material leaves the it at the same position. This approximation is valid for metals, but fails for translucent materials which exhibit significant transport below the surface. That is why bidirectional surface scattering distribution function (BSSRDF) was proposed to describe the light propagation between two rays that hit the surface. However, adding to this model a fluorescent behavior is not straightforward and cannot be used easily to simulate such properties of tissues.

In [23] the optical effects of translucency and coloration due to the composition of minerals near the surface was demonstrated for granite, marble and sandstone models of statues. The simulation of the scattering of light inside the stone was performed using a general subsurface Monte Carlo ray tracer.

Volume photon mapping that includes fluorescence phenomenon was presented in [24]. The Full Radiative Transfer Equation (FRTE) was solved. As the next step Fermat's law was applied to simulate a global illumination solution which supports non-linear light paths. Physically-correct simulation of volume fluorescence in participating media, caused by inelastic scattering and efficient computation of caustics was introduced.

In [25] a new algorithm for rendering translucent materials that combines photon tracing with diffusion was presented. Instead of sampling lighting at the surface, photons are traced into the material and stored volumetrically at their first interaction with the material. The proposed approach is as efficient as previous Monte Carlo sampling approaches based on the dipole or multipole diffusion approximations and demonstrates that it is more accurate and captures several illumination effects that was previously ignored.

The shading model that is able to efficiently and accurately render thin and multi-layered translucent materials were described in [26]. The original multi-dipole algorithm was extended to account rough surfaces and mismatched indices of refraction. Diffusion profiles from translucent slabs were combined utilizing Kubelka-Munk theory. Obtained multi-layered model of light diffusion was successfully applied to leaf, paint, paper, human skin and other similar materials.

The diffusion theory to describe steady-state light transport for point, line and plane sources was applied in [27] and compared with Monte Carlo results. They were able to accurately describe the shape of the fluence rate distributions due to light sources, but the absolute values were difficult to calculate. The adaptation of the method to fluorescence measurements and photodynamic therapy were presented as well.

In order to better understand tissue properties, skin samples were frozen and cut into pieces of about 10μm thick. Using microscope to excite the emission of autofluorescence and Monte Carlo simulation, it was possible to reconstruct in vivo skin autofluorescence spectrum. Seven-layer model with different optical parameters - like refractive index, scattering, absorption and regeneration of fluorescence photons - for each layer and each wavelength was proposed. The highest fluorescence detection efficiency in the skin was observed for dermis. Besides the blood absorption bands, comparison of the measured spectra with the reconstructed in vivo spectrum showed good agreement [28].

Fiber optic probe geometries to selectively measure fluorescence spectra from different sublayers within human epithelial tissues was investigated in [2]. They goal was to improve the endogenous fluorescence contrast between neoplastic and nonneoplastic tissues. They proposed two basic fiber optic probe geometries, which are called the variable aperture (VA) and multidistance (MD) approaches and compared with fluorescence measurements from human cervical epithelial tissues. They presented a simple tissue model and showed some numerical results without rendering them graphically. The importance of fibre configuration was also presented in [29], where the median sampling depth and photon pathlength were calculated. For single fibre probe simulated with one-layered skin model, the shallowest median sampling depth was found. It was suggested that the choice of a probe with a small fibre separation is better when sampling depth is not so important.

The Monte Carlo model was extended and verified in [30]. Now, the basic idea was improved to account for the fluorescent behavior in tissues. The model was validated with real experiments as well. An efficient method of Monte Carlo simulation was also developed in [31]. They investigated how the converging laser beam propagates in a turbid medium and noticed that steady-state distribution of the photon density can be calculated depending on depth in the object.

Tissue properties and parameters like absorption, scattering and fluorescence were measured and described in many in vivo investigations like [32] or [33]. Fluorescent properties of a tissue and contribution of different substances to final spectrum intensity was described in [34].

Very precise optical model of port wine stain was presented in [35]. The data was extracted from 6μm thick histology sections, which then were photographed and digitized with 2μm per pixel resolution. The epidermis, dermis and blood were

manually identified to create a three-dimensional matrix with values representing tissue type. Having described internal structure of a skin deformation, it was possible to perform Monte Carlo simulation and collect the energy deposition in different parts of a tissue grid. The simulation executed for wavelengths 532nm and 585nm showed that the greatest energy was accumulated in superficial blood vessels. Moreover, more energy was deposited in dermis and blood for 532nm rather than for 585nm. It was noted that big complexity of the model make it difficult to interpret the results.

Morphological and biochemical changes discovered in cancerous tissue disturb its absorption, scattering and fluorescence properties. In vivo optical spectroscopy can examine changes associated with pre-cancer phase. Im [11] there was described a recent study in two key areas: characterizing nuclear morphology using light scattering spectroscopy and investigating changes between epithelial cells and stroma at early stages of carcinogenesis. It is needed to utilize both approaches as long as fluorescence and reflectance spectra contain complementary information.

The identification of normal and cancerous colorectal tissues was performed in [36] by applying autofluorescence spectroscopy. The reflectance spectra for excitations in range from 280 to 400 nm with 10 nm steps was used. For each sample the - so called - "two-peak ratio" value was computed to differentiate between normal and cancerous tissues at different excitation wavelengths. By employing the Student's t-test and furthermore Receiver Operating Characteristic (ROC) curves, the 330 nm excitation wavelength appeared to be the most optimal.

Laserinduced autofluorescence (LIAF) spectroscopy for colon tumours was performed in [37]. The observation was taken for the healthy and adenocarcinoma of human tissues. In range from 520-620nm, the spectral shapes of tumour and normal tissue were very similar and the intensities of healthy tissues were three times higher than those with cancer. The opposite difference in intensities was measured for wavelengths in range from of 625-720nm. The investigation proved that for excitation 457,9nm the intensity ratio of the emission at 580 nm to the emission at 630nm or 680 can be used to distinguish cancerous tissue from the normal one.

The comparison of the optical properties of normal and adenomatous human colon tissue was performed in [38]. For each tissue sample, three main optical tissue parameters were estimated i.e. absorption and scattering coefficients and anisotropy factor. Obtained differences indicated morphological changes in healthy and adenomatous structures.

A technique for the study of diffuse reflectance spectra from normal and diseased tissue by retrieving their optical properties was presented in [39]. A data gathered from both types of tissues was fitted into model. The quantitative information about the tissue content, scattering and absorption properties of a

medium was provided. Described technique could be applied to rapidly analyze the condition of human skin in vivo in a noninvasive way.

Time-resolved fluorescence was investigated in experimental and theoretical ways in [40]. A normal muscle tissue and a sarcoma tumor with porphyrin photosensitizer in the middle was used. The fluorescence emission was studied by comparing fluorescence decay of photosensitizer in different stages of cancer growth. It was noticed in the in vivo experiment that the fluorescence from the normal tissue decayed more quickly than from the tumor structure. Decay is also dependent on the tumor thickness - the thicker cancer, the more delayed decay. On the other side, in [41] fluorescence decays were compared between males and females and among people in age ranging from 10 to 70 years. Investigations were performed on different locations i.e. the arm, the palm and the cheek. Obtained results perfectly fit to three-exponential fluorescence decay model. This paper is of particular interest with the possibility to monitor diseases and skin conditions such as skin cancer and ulcers. Those information can be useful for tumor diagnosis.

Problem of energy transport in scattering medium was solved in [42] using Feynman approach. It utilizes path integrals method to obtain the most probable way the light propagate in medium and provides results without making diffusion approximation. Scattering events determined mainly by phase function make it possible to calculate probability distribution function for a photon to follow a given path between two point within given time. Data generated by Monte Carlo simulation and compared to this analytical solution gives perfect agreement. Path integral approach could be probably used to solve the inverse problem, where having optical measurements of a tissue internal structure could be recognized.

Some ways of rendering fluorescent phenomenon in computer graphics were described in [43]. It was noticed that the reflected light from the fluorescent material depends on the angle of the incident light. The greater the angle, the more visible the effect of frequency and color shifting. The phenomenon occurs only if a photon interacts with colorant molecules. This implies a penetration of the diffuse substrate resulting in radiant energy and spectrum changes. Finally, a BRDF model based on the idea of a layered microfacet technique was provided. Also a combination of Phong lobes and Lambert model were compared with layered varnish model, which gave the best results.

Multi-spectral images were used in [44] to analyze whether gene amplification in cells is morphologically or genetically related to prior tumor invasion. Very useful for that purpose were Beltrami flow-based reaction-diffusion and directional diffusion filters. In [45] extended the Hidden Markov Chain (HMC) model to perform a segmentation of multi-sepctral images. In order to keep mutual dependence between the layers, the Independent Component Analysis (ICA) was adopted. The outcome of unsupervised classification on a four bands SPOT-IV

signal was presented. Also in [46] a method was proposed to design an automatic classifiers for discrimination between cancerous and healthy tissue. It was suggested that spectra is not sufficient to recognize fully between those two tissue classes, however some high degree of discrimination is possible. In order to do that spectral features should be selected carefully using either some kind of heuristic or proposed Haar wavelet packet method.

The topic of cancer detection and recognition is very popular in the recent years. This is why in the next chapters a model of human skin tissue will be analyzed to find the best camera and light parameters to catch cancerous changes quicker and earlier. Also a method basing on multi-spectral images will be presented as the most promising.

4   The optical model of human tissue

Translucent objects are very popular in our daily lives. All materials such as skin, marble, wood, wax etc. exhibit this property. They are perceived as soft and gentle due to the fact that light enters the object and is absorbed and scattered inside. This process is known as subsurface scattering. The scattered light gets diffused and blurs the effect of small geometric details on the surface, softening the overall look. Moreover, scattered light can pass through translucent structures. This effect is especially noticeable when the structure is lit from behind [47]. It differs from the other models, where the light after interaction with the object is scattered back according to BSDF. Here, the light leaves the object at different position than it was initially captured. That is why the unique appearance of translucent materials cannot be achieved with simple surface reflection models [48].

Human tissue is a good example of material where the effect of translucence is noticeable and dominant. The most popular morphological model assumes that a human skin consists of seven layers [49]:

1. Stratum corneum
2. Epidermis
3. Papillary dermis
4. Superficial vascular plexus
5. Reticular dermis
6. Deep vascular plexus
7. Dermis

Over 15% of a total body mass is occupied by skin. It is considered as the one of the largest human organ. Three main structures can be distinguished: outer epidermis, the dermis and the subcutaneous tissue. It consists of blood vessels, hair follicles, nerves and glands. The skin protects the body from the external environment and radiation, prevents the water loss, regulates the temperature and has good absorbing properties. It is also responsible for sensory perception and is a tight immunological barrier.

The epidermis has no lymphatic or blood vessels. It is build mainly from the multilayered and continously renewing epithelium. The stratum corneum or horny layer is composed of dead cells. It can be characterized by high chemical or mechanical resistance. It contains no water inside. The epidermal cells are created by keratinocytes of the stratum malpighii. They are tranformed from melanosomes produced by melanocytes residing in the basal layer. Melanin con-
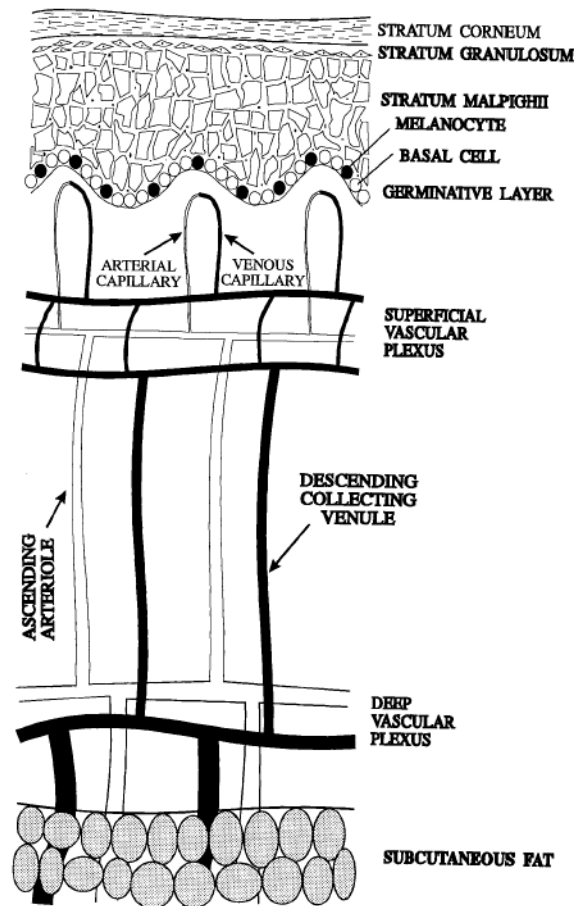
Figure 4.1: The 7-layer model of human skin tisue [16]

tained in the melanosomes is the complex protein of high UV radiation absorbing properties. It attenuates the light before it reaches viable skin cells.

The dermis which lies below the epidermis contains collagen and elastic fibers located in a viscous gel of water and mucopolysacharides. They protects both layers from separation due to streching forces. The number of cells in the dermis is smaller in comparison to epidermis. The papillary dermis as the uppermost dermal layer consists nerves, capillaries and lymphatics. Underlying reticular dermis has fewer cells, but contains more fibres and vessels. Two kind of plexuses are observable in terms of the blood vessels distribution in a skin. One in papillary dermis with branches toward the epidermis, the other near the bottom of the dermis. It plays the role of heat regulator and cell feeder. The dermis does not contain melanin. Collagen and elastin fibers show scattering properties, since their diameters are larger than the UV light wavelengths. The collagen of type III is contained in papillary dermis, where it is represented by small-diameter fibers. Collagen of type I builds the recticular dermis. Finally, the dermis is supported by subcutaneous fatty tissue, which is an insulator, a source of energy and force

absorber [16].

The human tissue can be defined as infinitely long and wide multi-layered structure with thickness long enough to absorb all the light. The key parameters of each medium are the following:

- n - refractive index - a ratio of the speed of light in vacuum to that in the given medium
- u_a - absorption coefficient - a probability of photon being absorbed per unit infinitesimal pathlength,
- u_s - scattering coefficient - a probability of photon being scattered per unit infinitesimal pathlength,
- g - anisotropy factor - an average of cosine value of deflection angle

It is assumed that the top ambient medium is air with refractive index equal to 1. This model was widely described in [50] and proved by laboratory investigations.

Optical properties of different tissues and the problem of light transport were widely described in [51]. Multiple and strongly scattering tissues like brain and skin tissues or vessel walls, and weakly scattering highly translucent structures such as eye tissues were discussed. Main scatterers in biotissues are mostly cellular organelles like mitochondria. Absorption mainly depends on the water content in biotissues. To find optical parameters of biotissues the algorithms for solving the inverse problem was described.

4.1 Absorption and scattering

The absorption of a light by tissue is strongly wavelength dependent. Various absorbing molecules affects different regions of spectra. The energy absorbed by chromophores is mainly converted to heat. However, it can be also converted to fluorescent light wave or used for a photochemical reaction.

Water concentration in skeletal muscle is approximately 75% and in fatty tissue it is on average 30%. Water absorbs in the ultraviolet up to about 200nm wavelength. Then the absorption is low and equals to even $0.0001mm^{-1}$. Above 600nm it start rising by reaching its peak by 950nm when its absorption dominates over other chromophores in tissue.

Haemoglobin as the oxygen-carrier in the red blood cells absorbs the light in visible wavelength region. It is the strongest chromophore in human tissue. The concentration of haemoglobin is usually only of a few percent of volume. The highest absorption peak of oxy-haemoglobin is localized at about 411nm. Two others are visible at 542nm and 577nm. Deoxy-haemoglobin has its maximum absorption at 433nm and another peak at 556nm. These spectral differences between haemoglobin molecules binding oxygen can be used to determine changes in haemoglobin saturation.

The 18% and 29% in the normal male and female body respectively is the average percentage of adipose (fatty) tissue. It contains of approximately 70% of lipids, which fat droplets consume most of the volume of the adipose cells. Its absorption spectrum has its highest peak at about 930nm and lower at 760nm. In visible wavelength region lipids report low absorbing properties.

Melanin is a dark pigment which gives the color to for example hair and skin. Its absorbtion spectrum decreases exponentially with the wavelength and does not show any local peaks. The measuremnt of melanin optical properies is difficult, becasue it cannot be dissolved or extracted from skin without changing its physical parameters.

For breast tissue it is assumed that only some chromophores influences the absorbing spectrum. In such a case the total absorbtion coefficient was calculated using oxy- and deoxy-haemoglobin concentrations of 20 μM and 10 μM respectively, a fat concentration of 30% and water 70%. It turned out that the absorption is quite low between 600nm and 1300nm. For shorter wavelengths the influence of haemoglibin is critical. On the other hand for higher wavelengths the water decreases light penetration. The optical window described above can be used during medial diagnosis and treatment, since it enables reaching structures deep below the tissue surface.

The scattering properies of tissue are not so wavelength dependent as it was in case of absorbtion. The scattering coefficient decreases exponentially and reports no sharp features. The scattering is strongly forward directed, non isotrapic and typical value of anisotropy g for mammalian tissues is ranging between 0.7-0.95. Since the medical diagnosis is using mainly the optical window, it is assumed that the anisotropy factor is equal to 0.9 and the scattering coefficient to $1mm^{-1}$.

From the microscopic point of view the absorption is described by biomolecules in the tissue, while scattering by larger microscopic structures with different refractive index. The average refractive index of most tissues ranges between 1.38-1.41 at 633nm wavelength, with 1% change per 100nm in the visible light band. To the main scatterers belong the mitochondria, the cell membrane, the cell nucleus, lysosomes and Golgi apparatus. It was proven that most of the scattering takes place inside the cell rather than at the cell membrane. Mitochondria are responsible for isotropic scattering. The influence of nucleus on large angle scattreing and cell membrane on small angle scattering was determined in [32].

4.2   The fluorescence phenomenon

The physical phenomenon that changes light initial wavelength and happens in many substances including biological tissues is called fluorescence. The molecules that absorb the light and release the excess of energy by emitting light of different wavelength are called fluorophores. Two kind of energy levels can be recognized:

- singlet state (S) - if electron spins are paired
- triplet state (T) - if electron spins are unpaired

Singlet state is the ground state of most molecules - see figure 4.2. The incoming photon can be absorbed if its energy corresponds to the energy difference between an excited and the ground state of the molecule. Since the absorption bands are very broad and overlap each other due to the strong interactions between molecules, the photon energy can be used for excitation to the higher energy level of a molecule. During absorption of a photon, the molecule is excited from the ground state S_0 to vibrational level of S_1. Then it is quickly relaxed to zero vibrational state from which it can further return to initial state by generating heat (internal conversion) or emitting photon (fluorescence). As long as the relaxation ends in any vibrational level in S_0, the emitted spectra will be not a sharp peak at a distinct wavelength, but will be broadly distributed. Moreover, because some energy was lost during that process, the fluorescence will have lower energy and longer wavelength than initial photon. It is also possible that through intersystem crossing the molecule will be converted to the triplet state T_1. Finally, it can be moved to the ground state again by the internal conversion or a photon emission (phosphorescence). Also other processes like permanent structure change or chemical reaction of the excited molecule with the neighborhood can occur [16].
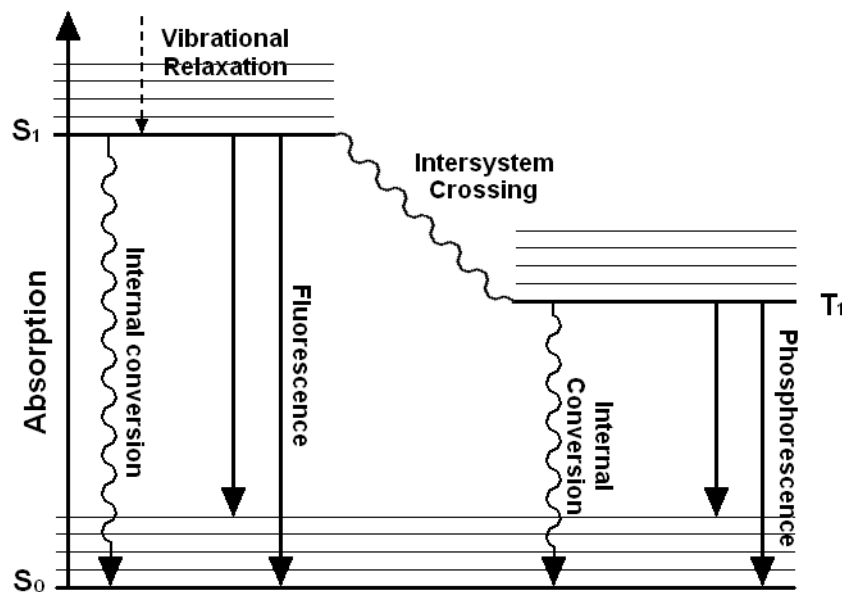

Figure 4.2: Schematic diagram of processes occurring during fluorescence

Human skin also contains natural fluorophores such as NADH, tryptophan (aromatic amino acid), collagen and elastin (structural proteins). This kind of fluorescence, which does not involve adding external fluorophores, is called autofluorescence.

Differences in tissue structure between healthy and malignant tissue create a basis for the diagnostic of possible demarcation in neoplastic tissue. This optical behavior makes the fluorescence spectroscopy a valuable tool to study the condition of biological tissues [41]. Generally, tissue internal fluorophores undergo fluorescent phenomenon for the visible wavelength band and emits light in the UV and near-UV region. Comparing tumor tissue with its healthy surrounding resulted in higher intensity of autofluorescence for normal tissue [15]. The endogenous tissue fluorophores can be divided into following groups involving:

- cellular energy metabolism
- structural proteins

Collagen and elastin contribute significantly to the fluorescence signal excited by 337nm wavelength light. They are fibrous proteins present mainly in connective tissue. There are several different types of collagen. Each of them has slightly different optical properties and fluorescence maxima. Collagen I - composing 90% of collagen in the body - is available in skin and internal organs. For excitation 340nm it has its maximum fluorescence peak at 395nm. Collagn of type IV occurs in the basement of epithelial tissues membrane. On the other side elastin excited with 337nm wavelength light fluoresces at 410nm.

NADH contributes significantly to the metabolism of a cell. About 80% of NADH is located in the cells mitochondria, while the rest is situated in cyto-sol. For the wavelength 350nm it has its maximum peak at 460nm. The oxidized form of NADH does not show fluorescent properties when excited above 300nm.

In aqueous solution and excitation light equals 250nm, tryptophan emits photons of maximum intensity at 350nm. Its contribution to tissue fluorescence is small when excited with light above 300nm. The amount of this amino acid can be greater in premalignant states of a tissue than in normal tissue.

Flavins, lipofuscin and endogenous porphyrins are the other endogenous fluorophores in human tissue. [32]

The contrast between normal and malignant tissue can be further enhanced by applying tumor selective drug. The diagnosis shouldn't base only on the changes in autofluorescence spectra, which result in overall intensity decrease in tissue with cancer. The demarcation criterion can be improved utilizing a combination of fluorescence from endogenous fluorophores and porphyrins accumulated in the malignant cells [8]. Those substances have the property that their fluorescence emission spectra is localized in red and near infrared wavelength region and because of that can easily distinguished from the normal blue-green autofluorescence emission. To main tumor markers belong: hematoporphyrin derivatives (HpD), meso-tetra-(hydroxyphenyl)-chlorin (MTHPC), pheophorbide-a, pthalocyanine, benzoporphyrin derivative (BPD), hypercin and tin etiopurpurin (SnET2). In the blue light wavelength region they show strong absorption characteristic. Generally

they are administered orally, intravenously or topically and their accumulation in the tumor is correlated with the vascularity of a tissue.

Another photosensitizing agent is the lutetium texaphyrin which is selectively phototoxic to tumors and show absorption and fluorescence property in the near infrared spectral region.

The other photosensitizers working as contrast agents has to fulfill safety and toxicity criteria. This group of exogenous fluorophores contains Nile blue and its derivatives, caretenoporphyrins, fluorescin angiography and indocyanine green and are in routine clinical use. The latter two substances have fluorescence and absorption characteristic in VIS and NIR spectral bands, respectively [7].

Protoporphyrin IX (PpIX) is a fluorescent tumor marker that naturally exist in the body. As the intermediate product of haem-cycle, an elevated PpIX concentration can be obtained by administration of 5-aminolevulinic acid (ALA) [15].
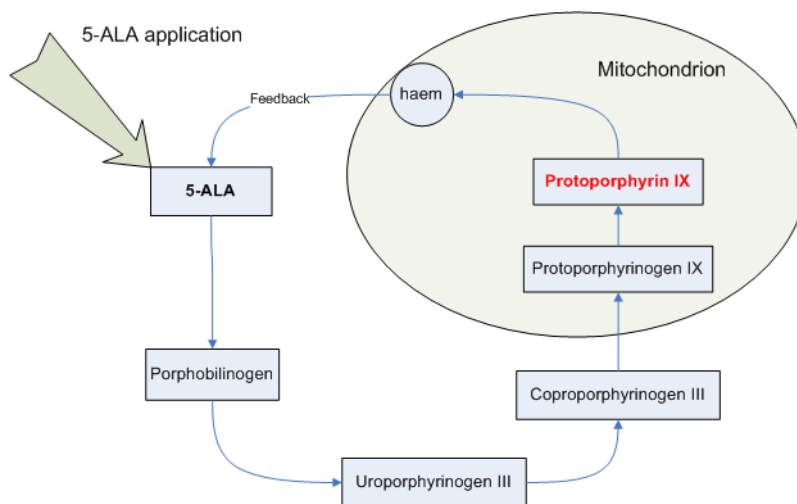

Figure 4.3: Mechanism of 5-ALA induced protoporphyrin IX fluorescence [52].

As the result, tumor cells are able to synthesise more PpIX than non-malignant tissue, since they contain different amount of enzymes regulating the haem cycle [5]. PpIX is widely used in PDT and excited at 405nm, it emits a fluorescence spectra in red light region with peaks at 635nm and 705nm. For diagnostic purpose much lower doses are necessary than during therapeutic procedures .

It needs to be stressed that the fluorescence spectra is strongly affected by tissue optical properties and especially by those absorbers which influence excitation or fluorescence light. They will decrease the overall intensity, but the shape of the spectra will stay rather unchanged since the absorption coefficient is lower in the visible region and higher for the light in violet and near-UV region [15].

The investigation performed for human colon tissue showed which fluorophore dominates in fluorescent spectrum. They were preseted for three different phases

of cancerogenesis.

	Normal	**Hyperplasia**	**Adenoma**
Epithelial cells	no fluorescence	no fluorescence	fluorescence (probably NADH)
Lamina propria	collagen signal	increased collagen signal	decreased collagen signal
Submucosa	collagen signal	decreased collagen signal	decreased collagen signal and increased haemoglobin absorption

Table 4.1: Reasons for different fluorescence spectra [32]

That observation can be utilized in the process of early cancer detection. It was noticed that normal and pathologic structure of the tissue has different fluorescence properties. In the colon tissue the mucosa is the top layer consisting of tubular crypts which are surrounded by a connective tissue structure mostly composed of collagen. Under the mucosa, approximately 450 μm below the tissue surface there is the submucosa, a layer of connective tissue also mainly composed of collagen. However in dysplastic tissue, the crypts are irregular in shape and size and become disorganized. Dysplastic colon tissue proves similar morphology to that of normal colon (flat dysplasia), or it can be characterized by additional gross morphological changes (adenomatous polyp) [53].

Since each fluorescent molecule has different optical properties, its reaction to the excitation light can vary. When light of specific wavelength is applied, the fluorophore does not emit light at another frequency, but the resulting spectra is widely distributed over the large region. Moreover, the emitted light cannot have lower frequency than the initial impulse beam. If the excitation light contains peaks at different wavelengths then the contribution from each wavelength needs to be calculated. For more complicated spectral shapes the superposition principle can be useful for calculating the final emission spectra. From the macroscopic point of view it is necessary to find such a transformation that easily produces the fluorescence spectrum for any given light interacting with molecule. For this reason excitation-emission matrix (EEM) can be very helpful.

A fluorescence EEM is a two-dimensional contour plot, where each contour identifies points of equal fluorescence intensity. It represents the fluorescence intensities as a function of excitation and emission wavelengths [7]. Excitation-emission matrix uniquely identifies how each fluorophore interacts with photon and as the outcome what light will be produced. It describes how the emission spectra changes for different light excitation spectrum.
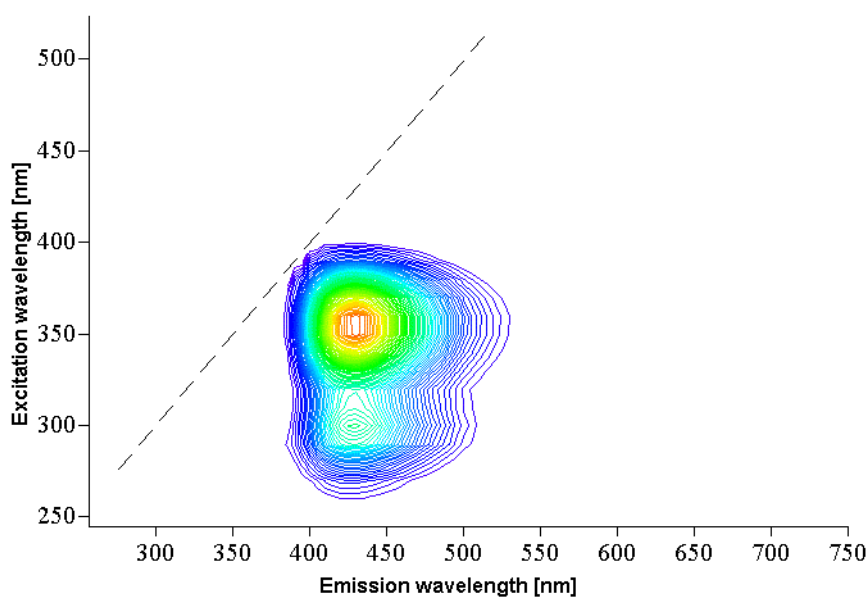
Figure 4.4: Example of EEM of a molecule. The highest values of intensity are drawn in red color, the lowest in violet [4]

On the other hand the investigation and generation of EEM can be important to indicate the differences between normal and tissue with cancer. Ranging excitation wavelengths from 260 to 540 nm it was possible to obtain autofluorescence and emission spectra of investigated areas for both cases. It resulted in a three-dimensional matrices describing optical properties and concentration of endogenous fluorophores. In [54], emission spectra of healthy and adenomatous tissues at given excitation wavelengths were compared. The appearance of fluorescence peaks in both normal and cancerous tissues was explained by the existence of various fluorophores that generates signal. It proves that laserinduced autofluorescence is able to distinguish between normal and cancerous colonic tissues. Low concentration of NAD(P)H and FAD and big influence of amino acids and protoporphyrin IX define the malignant colonic tissues. It turned out that 340, 380, 460 and 540 nm are the best excitation wavelengths for diagnosis of colonic cancer.

The emission-excitation values of mammalian cells outside the range of intrinsic protein fluorescence were measured and investigated in [55]. The obtained effect of fluorescence was most noticeable in discrete cytoplasmic vesicles. The fluorescence was low in freshly prepared cultures, growing to its maximum at increased cell numbers. The spectra of whole cells was compared with spectra of known cellular metabolites. It turned out that the fluorescence probably originates from NADH, riboflavin, flavin coenzymes and flavoproteins bound in the mitochondria. In [56] Monte Carlo simulation and diffusion theory allowed to compute spatially resolved fluorescence and excitation and emission reflectance.

Using a point source model of fluorescence, the fluorophore concentration at the given excitation wavelength was recovered with a accuracy of 11.4%. Obtained results were consistent with published values.

4.3   Simplified model

The seven layer skin optical model was presented in [49]. All optical parameters were registered for excitation light equal 520nm. For the simplicity of simulation, the model will be not differentiated between various wavelengths. It was assumed that all parameters are constant and independent from the light spectrum. The composition of human skin and especially the epidermis was introduced also in [57]. The information about biological dosimetry of the skin in vivo i.e. UVR dose for a given solar wavelength at different tissue layer, is very valuable for skin cancer risk assessment.

Layer	Thickness d $[\mu m]$	Refractive index n	$u_a[\text{cm}^{-1}]$	$u_s[\text{cm}^{-1}]$	g
Stratum corneum	10	1.45	no data	no data	no data
Epidermis	80	1.4	40	570	0.77
Papillary dermis	100	1.4	5	500	0.77
Superficial vascular plexus	80	1.39	24.5	500	0.79
Reticular dermis	1500	1.4	5	500	0.77
Deep vascular plexus	70	1.34	181	500	0.96
Dermis	160	1.4	5	500	0.77

Table 4.2: Tissue parameters for seven layer skin for 520nm

Similar model of human skin tissue was presented in [58]. Absorption coefficients of oxy- and deoxy-hemoglobin, water and other parts of tissue were calculated. All those factors contributed to compute total diffuse reflectance for different wavelengths. The simulation outcome was compared with in vivo experimental results and showed they are in good agreement with each other. Moreover, it was noted that basing on reflectance spectra, the model fitting analysis using multi-linear regression, could give quantitative amount of chromophores in human skin.

Because of the fact that the fluorescence phenomenon plays important role in tissue reflectance spectra, the light is not only absorbed and scattered under the surface of the object, but also its spectrum changes relatively to material the tissue consists of. In order to implement this behavior in the system an additional parameter was introduced:

- d - the probability of interaction a photon sample with a fluorophore

When that interaction occurs, a photon changes its optical properties according to special matrix transformations. The excitation-emission matrix of main natural fluorophores in human skin and exogenous fluorophores that enhance the demarcation between tumor and healthy skin was presented in figure 4.5.

The simplest possible model of human tissue is proposed. It consists of infinitely long and wide single-layered structure characterized by the following parameters, that was calculated as the average of tissue parameters for 520nm:

n_{air}	n_{layer}	$u_a[cm^{-1}]$	$u_s[cm^{-1}]$	g	d_{col}	d_{por}
1	1.4	43	511	0.8	0.2	0.1

Table 4.3: Simplified tissue model and parameters

It means that the optical parameters of tissue like absorbing and scattering coefficient or anisotropy factor are constant throughout the whole tissue profile.

The collagen is the main fluorophore that builds reticular dermis. Additionally to simulate skin cancer and increase the contrast between healthy and neoplastic skin, it was assumed that in the middle of the tissue is localized a small tumor where protoporphyrin IX is concentrated.

All parameters describing probability of photon interaction (d_{col}, d_{por}) were only a good guess, they are not proven by any laboratory investigations. However, those assumption were good enough to simulate light propagation in human skin tissue.

Extracting the intrinsic fluorescence properties of tissue is the main goal of [59]. Monte-Carlo-based model was developed to obtain fluorescence spectra from combined fluorescence and diffuse reflectance spectra i.e. independently from absorption and scattering properties of investigated medium. The proposed model was verified using 11 phantom configurations containing blood as an absorber, polystyrene as a scatterer and furan-2 as a fluorophore. The intrinsic fluorescence spectra and intrinsic fluorophore intensity with an error not greater than 10% were retrieved. By applying Monte Carlo simulations in [60], a liquid phantom quantitative, measurements of fluorochrome concentrations were also possible to calculate. A single optical fiber that transports excitation light and records fluorescence seemed to be sufficient for most applications. It is additionally insensitive to different concentrations of absorbers and scatterers within a tissue. Also using Monte Carlo model it was possible in [61] to extract the influence of NADH and collagen fluorescence, and scattering and absorption properties in cervical tissue. The simulation showed the correlation with clinical data and indicated that normal and dysplastic tissue differs mainly by increased NADH and decreased collagen fluorescence.

In this publication [62], an eight-layer model of human skin was used. Optical properties of tissue were considered as a function of wavelength (absorption and

(a) EEM of Collagen I

(b) EEM of Elastin

(c) EEM of NADH

(d) EEM of tryptophan

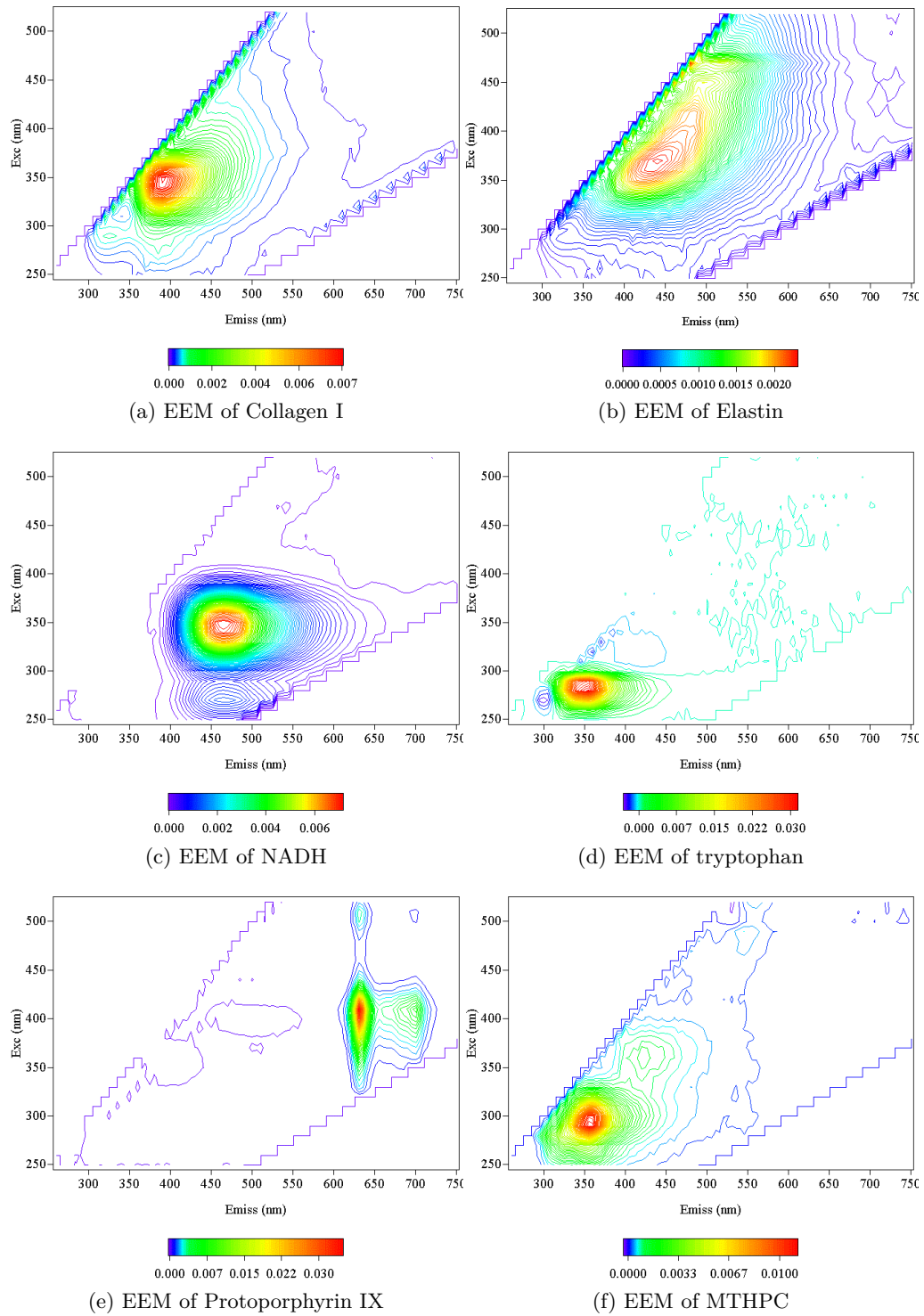(e) EEM of Protoporphyrin IX

(f) EEM of MTHPC

Figure 4.5: Excitation-emission matrices of common fluorophores [4]

scattering). Additionally microsphere fluorescent materials were implanted under the tissue surface. Their excitation and emission spectrum were represented by six discrete data points. The simulations were performed to predict the distribution of excitation and fluorescent photons. Photons escaping the tissue were scored in a positional matrix together with their respective wavelengths and weights. It turned out that about 7% of input light is diffusely reflected. Moreover, about 20% of the input light that escaped the tissue surface was converted to fluorescence. Simulations indicated that the quantitative analysis of emitted photons is possible. In [63] emission of fluorescence was presented as a function of the depth of fluorescence generation and radial escape position. It turned out that deeper layers also affect fluorescence, because only 35–40% of the remitted fluorescence was caused by the photons initially directed downward. Obtained results were compared with a heuristic model. Another investigation simulated signal from a fluorophore submerged inside a tissue and tried to calculate fluorescence intensity [64]. For fluorophore located in the tissue at various depths the relative difference of signal was found to be at most 30%.

5   Light propagation in turbid media

There are two different theories describing the wave propagation in random media. The multiple scattering or analytical theory utilizes e.g. Maxwell equations to obtain result for single particle tracking. It considers interactions between many particles and calculate the statistical average. Differential equations can also include such fundamental effects like diffraction, interference or multiple scattering. Unfortunately, since skin is not uniform in shape, it consists many layers, has hair follicles and shows anisotropic properties, it cannot be used to obtain reasonable solutions.

The radiative or transport theory, however, concentrates on the propagation of intensities. It starts with the heuristic observations that results in differential equation similar to formulas describing kinetic theory of gases (Boltzmann equation) or neutron transport theory. The methods needs only several parameters: average absorption μ_a and scattering μ_s coefficients and phase function. All of these values can be determined experimentally. This method was found very useful for light propagation in tissue.

A short description of the radiative transport equation as a basis to all light propagation models was introduced in [65]. Different approaches (direct, indirect and iterative) for determination of optical properties were presented. The Kubelka-Munk coefficients and the transport coefficients as the example of non iterative ways to calculate tissue parameters were compared. It was suggested that iterative procedures like diffusion theory, adding-doubling models and Monte Carlo are too complicated to solve the transport equations.

The basic quantity in the transport equation is the radiance $L(r, s)$ also called the intensity. It is the average power flux density at position r from a specific direction s per unit solid angle. It has the unit $W \cdot cm^{-2} \cdot sr^{-1}$. The radiation is isotropic, if it is independent of direction s. In such a case the power radiated from the surface can be calculated from the Lambert's cosine law. Since the tissue exhibit anisotropic properties the phase function which describes the amount of light scattered from direction s into the direction s' will depend on anisotropy factor g. [16]

The transport equation can be defined as:

$$(s \cdot \nabla) = -\mu_t L(r, s) + \mu_s \int_{4\pi} p(s, s') L(r, s) d\omega', \qquad (5.1)$$

where:
$d\omega'$ - differential solid angle in the direction s',
μ_t - is the sum of absorption and scattering coefficients $(\mu_a + \mu_s)$,
$p(s, s')$ - phase function.

31

The equation describes the rate of change of the intensity at point r in the direction s. It directly result from the energy conservation principle and can be decomposed into the intensity lost due to absorption and scattering and the intensity gained due to scattering from all directions into the direction s. Moreover, the light emission from the whole volume due to fluorescence phenomenon can additionally increase the radiance $L(r, s)$.

The transport equation only holds true if the following assumptions are satisfied [14]:

- the medium is homogeneous,
- each particle is independent of all others,
- scattering by all particles can be described by single function (phase function),
- the light is incident for longer than a few nanoseconds (steady state distribution),
- there are no light sources in the medium.

5.1   Monte Carlo simulation

For the first time a Monte Carlo technique was referred by N. Metropolis and S. Ulam in 1949. It builds a stochastic model to determine a value of physical quantity using an expected value of random variable. This value is calculated by averaging the number of independent samples representing the random variable. In order to do that random numbers must follow the distribution of the estimated variable [50].

In Monte Carlo simulation light is treated as a photon bundle, which does not influence other molecules in the medium. Once entered the tissue, the photon is moved a given distance where it may be absorbed, scattered, reflected internally or out of the tissue. To generate new scattering angles inside the object, phase function may be utilized. The photon is repetitively moved until it either is completely absorbed or escapes from the tissue. If the photon is absorbed, the position of that incident is recorded. If the photon escapes from the tissue, the transmission or reflection of the photon is stored. This procedure is repeated until the desired number of photons have been traced and recorded. As the number of photons propagated approaches infinity, the overall reflection, transmission, and absorption profiles approach real values. This data can be later compared with medical investigations for the tissue with similar optical properties [66].

Its propagation is divided into small movements calculated in the iterative way. At each step the history of absorbing and scattering processes are recored. The method describes local rules of light propagation expressed as probability distribution functions. Thousands of different trajectories are necessary to compute in order to obtain the desired accuracy of the solution. It is required to

trace ($\sim 10^6 - 10^9$) photons to get the relative error less than a percent. Since the accuracy is proportional to $\frac{1}{\sqrt{N}}$ where N is the number of propagated photons, the simulation needs large amount of computational time [14].

Monte Carlo simulation does not treat a photon as wave phenomenon. Such properties as phase and polarization are simply ignored. Since light is scattered and absorbed many times by tissue, features mentioned above get quickly randomized. The simulation concentrates on radiant energy transport in turbid medium and is based on macroscopic optical properties that are equally distributed over small unit of volume [50].

5.1.1 Launching a photon

Each photon can be characterized by three quantities. The current position in Cartesian coordinate system is specified by x, y and z. The direction of photon propagation is described by normalized vector r or by directional cosines:

$$
\begin{aligned}
\mu_x &= r \cdot x' \\
\mu_y &= r \cdot y' \\
\mu_z &= r \cdot z'
\end{aligned}
\tag{5.2}
$$

where x', y' and z' are the unit vectors along each axis. Each photon is additionally initialized with weight equal unity, which represents the energy possessed by packet.

This technique enables tracking many trajectories at the same time. Every photon starts the simulation from the light source localized above the tissue. If it is a laser beam, each packet will be assigned with the same initial direction r. For point light sources the photon initial direction will be equally distributed over the whole hemisphere around the light origin.

When the photon hits the surface it can be reflected or transmitted inside the tissue. The Snell's law indicates the relationship between the angle of incidence α_i and the angle of transmission α_i.

$$
\frac{sin(\alpha_i)}{sin(\alpha_t)} = \frac{n_t}{n_i},
\tag{5.3}
$$

where n_i and n_t are the refractive indices of the medium from which the photon incidents and to which it is transmitted, respectively. α_i can be calculated as $cos^{-1}\mu_z$.

The probability that a photon will be reflected can be defined by the Fresnel formula:

$$
R(\alpha_i) = \frac{1}{2}\left[\frac{sin^2(\alpha_i - \alpha_t)}{sin^2(\alpha_i + \alpha_t)} + \frac{tg^2(\alpha_i - \alpha_t)}{tg^2(\alpha_i + \alpha_t)}\right],
\tag{5.4}
$$

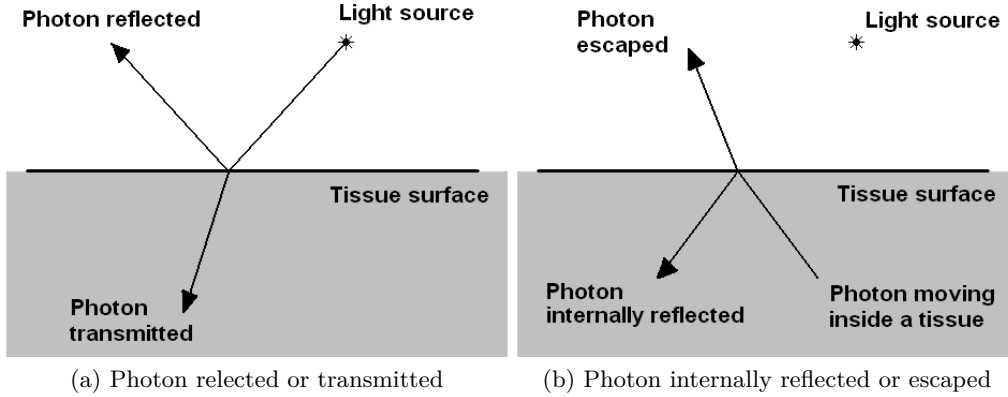(a) Photon relected or transmitted   (b) Photon internally reflected or escaped

Figure 5.1: Light interaction at tissue boundary

In order to determine whether the packet is reflected back or enters the tissue it is necessary to generate a random number ζ_1 and compare it with incident reflectance $R(\alpha_i)$:

- For $R(\alpha_i) \geq \zeta_1$ - the photon is internally reflected and its direction must be updated by simple reflection $\mu'_z = -\mu_z$,
- For $R(\alpha_i) < \zeta_1$ - the photon escapes the tissue. In this case all photon parameters are internally stored, but since it moves away, it is not propagated any more and is terminated.

Since the photon undergoes the interaction with a tissue, its weight needs to be changed:

$$W' = W - WR(\alpha_i), \tag{5.5}$$

The same situation can also occur inside a tissue at the boundary between layers with different optical properties or at tissue/air interface when a photon will be either internally reflected or will escape the tissue. In such a case its parameters are stored in the simulation memory.

5.1.2 Moving a photon

In every iteration a photon located under a tissue surface is moved. Monte Carlo simulation outlines two different methods for calculating the new photon position: variable and fixed stepsize method. The latter approach is slow since the photon must be propagated many times before it is either absorbed or scattered. The total distance before absorption occurs is rather long, what is not acceptable for highly scattering media.

Variable stepsize method does not have such disadvantages. Monte Carlo algorithm varies the distance Δs the photon is moved at every iteration. It is defined in such a way that after a movement either absorption or scattering event must occur. Basing on a sampling of the probability distribution function for photon's free path $s \in [0, \infty)$, the stepsize Δs can be calculated.

By definition, the interaction coefficient μ_t is the probability of interaction per unit pathlength in the interval $(s', s' + ds')$:

$$\mu_t = \frac{-dP\{s \geq s'\}}{P\{s \geq s'\}ds'}, \tag{5.6}$$

After integrating:

$$d(ln(P\{s \geq s'\})) = -\mu_t ds', \tag{5.7}$$

Finally integrating over s' in the range $(0, \Delta s)$ results in:

$$ln(P\{s \geq \Delta s\}) - ln(P\{s \geq 0\}) = -\mu_t \cdot \Delta s + \mu_t \cdot 0, \tag{5.8}$$

Since it is assumed that $P\{s \geq 0\} = 1$, the following equation is obtained:

$$P\{s \geq \Delta s\} = e^{-\mu_t \Delta s}, \tag{5.9}$$

Or rearranging:

$$P\{s < \Delta s\} = 1 - e^{-\mu_t \Delta s}, \tag{5.10}$$

Now, a uniformly distributed random number ζ_2 can be assigned to cumulative distribution function:

$$\Delta s = \frac{-ln(1 - \zeta_2)}{\mu_t}, \tag{5.11}$$

After substituting $\zeta_3 = 1 - \zeta_2$ and $\mu_t = \mu_a + \mu_s$:

$$\Delta s = \frac{-ln(\zeta_3)}{\mu_a + \mu_s}, \tag{5.12}$$

Since the stepsize was calculated the photon can be moved in a desired direction:

$$\begin{aligned} x' &= x + \mu_x \Delta s \\ y' &= y + \mu_y \Delta s \\ z' &= z + \mu_z \Delta s \end{aligned} \tag{5.13}$$

Skin tissue consist of many layers with different optical properties. It can happen that a photon experiences a movement from one to another layer before

the interaction occurs. In such a case the sampling equation can be obtained from
5.12:

$$\sum_i \mu_{ti}\Delta s_i = -ln(\zeta_1),\tag{5.14}$$

where:
i - the index of the layer the photon propagates,
μ_{ti} - the interaction coefficient of the i-th layer,
Δs_i - the step size in the specific layer [16].

5.1.3   Photon absorption or scattering

After a movement a photon is either absorbed or scattered. The probability it
is absorbed can be defined as a ratio of absorption and interaction coefficients.
In order to determine which of the event occurred another random number is
necessary:

$$\zeta_4 < \frac{\mu_a}{\mu_a + \mu_s},\tag{5.15}$$

where ζ_4 is uniformly distributed between zero and one.

The photon is absorbed if the inequality 5.15 holds true, otherwise the photon
is scattered. The change in the photon weight due to attenuation is calculated in
the following way:

$$W' = W - W\frac{\mu_a}{\mu_a + \mu_s},\tag{5.16}$$

If the scattering event occurred two different angles need to be sampled sta-
tistically. The deflection angle is defined by the angle θ in the interval $[0, \pi)$.
Basing on probability density function proposed by the Henyey and Greenstein
the following equation holds, that helps to calculate the deflection angle:

$$p(cos(\theta)) = \frac{1 - g^2}{2(1 + g^2 - 2gcos\theta)^{3/2}}\tag{5.17}$$

where the anisotropy g is defined in the interval $[-1, 1]$.

A value of zero specifies isotropic scattering and the value near one a very for-
ward directed scattering. It was confirmed experimentally that Henyey-Greenstein
phase function can be applied for tissues very well in terms of scattering. The
value of anisotropy in the visible spectrum is often equal to ~ 0.9.

The angular dependence of scattering in human dermis was investigated in
[67]. A goniometric apparatus and HeNe laser beam was used together with tissue
samples of various thicknesses. They presented the reflected and transmitted light
as a function of angles and specified the scattering phase function basing on
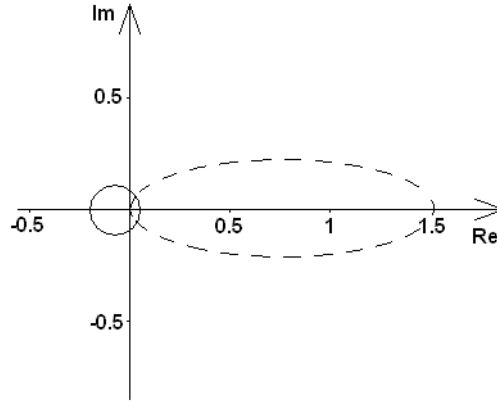
Figure 5.2: Plots of Hanyey-Greenstein phase fuction for *g* equal to -0.35 and 0.67. Negative anisotrophy value (solid line) describe phase function that primarily scatter light back in the incident direction, and positive anisotrphy value (dashed line) defines phase function that mainly scatter light forward [68]

Henyey-Greenstein approach. The computed average deflection angle was equal to 35° for a scattering event and a total attenuation constant to 190^{-1}.

The choice of $cos(\theta)$ can be expressed as a function of random number:

$$cos(\theta) = \begin{cases} \frac{1}{2g}\left[1 + g^2 - \left(\frac{1-g^2}{1-g+2g\zeta_5}\right)^2\right] & \text{for g} \neq 0 \\ 2\zeta_5 - 1 & \text{for g} = 0 \end{cases} \tag{5.18}$$

The second angle describing the scattering event is the azimuthal angle which is defined in the interval $[0, 2\pi)$. This time the probability distribution function is constant, so the angle is calculated by simple multiplication:

$$\psi = 2\pi\zeta_6, \tag{5.19}$$

Having both scattering angles (θ, ψ) calculated, the new direction of a photon can be calculated by:

$$\mu'_x = \frac{sin\theta}{\sqrt{1-\mu_z^2}}(\mu_x\mu_z cos\psi - \mu_y sin\psi) + \mu_x cos\theta$$

$$\mu'_y = \frac{sin\theta}{\sqrt{1-\mu_z^2}}(\mu_y\mu_z cos\psi - \mu_x sin\psi) + \mu_y cos\theta \tag{5.20}$$

$$\mu'_z = -sin\theta cos\psi\sqrt{1-\mu_z^2} + \mu_z cos\theta$$

If the angle is very close to the $90°(|\mu_z| > 0.99999)$, another formula should be utilized:

$$\mu'_x = sin\theta cos\psi$$

$$\mu'_y = sin\theta sin\psi \tag{5.21}$$

$$\mu'_z = SIGN(\mu_z)cos\theta$$

where $SIGN(\mu_z)$ returns 1 when μ_z is positive and -1 when negative.

In this way new direction of propagation was calculated and the photon can be moved again by another Δs. This process goes on until the photon is terminated.
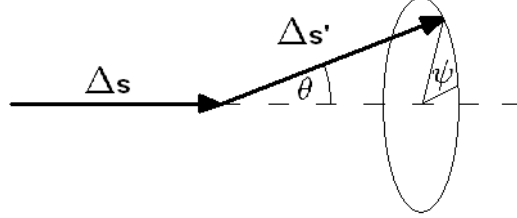

Figure 5.3: Photon scattering - deflection and azimuthal angles

It is necessary to note that a photon undergoes interaction (absorption or scattering) only at the end of the step.

5.1.4   Photon storing or termination

Photon originally launched from the light source can be terminated by reflection or transmission out of a tissue. On the other side, the weight of the photon propagating inside a medium is decremented during many iterations. If after another photon attenuation the resulting weight is smaller than a given threshold (like $W_{th} = 0.0001$) then there is no need to continue the photon movement, since it does not contain any useful information. However, the photon cannot be easily terminated, because still the energy conservation principle must be preserved. A technique called Russian roulette provides the solution. It gives one chance in m (e.g. $m = 10$) for a photon to survive with weight $m \cdot W$. Otherwise its energy is set to zero and photon is terminated.

$$W = \begin{cases} mW & \text{if } \zeta_7 \leq 1/m \\ 0 & \text{if } \zeta_7 > 1/m \end{cases} \tag{5.22}$$

where ζ_7 is uniformly distributed random number.

If photon survived and after many interactions reaches the air/tissue interface and escaped then its weight, exit angle and position are stored in the memory. This process continues by launching another light packet until desired number of photons is collected on the tissue surface. In order to obtain total diffuse reflection with acceptable precision for different light source shape, at least 100000 photons need to be stored. For computer graphic application minimum one million photons is necessary.

5.2   Photon mapping algorithm

A Monte Carlo model of light transport was chosen to simulate the photon distribution and interaction with turbid media. It is very well tailored for quantitative

analysis of light propagation. However, the default implementation of this technique describes the fluorescence phenomenon in very limited way. In order to include the photon spectral properties to the Monte Carlo model and illustrate graphically obtained results a particle-tracking algorithm called Photon Mapping was applied.

The Photon Map algorithm was developed in 1993-1994. First papers about this method were published in 1995. This is a comprehensive, a two-pass algorithm that is able to simulate most of global illuminations effects like diffuse inter-reflections, caustic and participating media in complex scenes. It has the same flexibility as normal Monte Carlo ray tracing method, but computational time is reduced. It assumes constructing paths from the light source and store at each vertex the amount of incident energy represented by the photon. If required number of samples were tracked and collected, this data is used at rendering time to estimate final intensity and color of the queried position. The algorithm tries to separate the representation of a scene from its geometry and collects illumination information in an specially adjusted data structure [69].

Compared to other method of global illumination Photon Maps have many advantages. Photon tracing step is independent from the computing measurement part, recorded samples can be reused to generate images from different points of view. It is relatively fast even for complex scenes and handles non-diffuse surfaces and caustic effects. Low frequency noise, efficiency, quality of final images and reasonable memory usage for storing the photons, make this algorithm one of the most important in computer graphics. Normal Monte Carlo ray tracing methods such as path tracing, bidirectional path tracing and Metropolis are out of date [70].

The photon map algorithm has some desirable properties that makes it useful in global illumination computations. It is relatively fast and simple to parallelize. It can handle a mixture of specular, glossy, and diffuse reflection and transmission including caustics effect. It can handle very complex scenes, since the photon map is independent of surface representation [71].

5.2.1 Pass I - Photon emission

The point of photon tracing is to calculate indirect illumination on diffuse surfaces. This goal is reached by emitting particles of energy called photons from the light sources, tracing them through the scene, and storing them at diffuse surfaces. Each photon packet has assigned a spectrum with energy proportional to the spectrum of the light source. That radiance of a photon, described by its color spectrum, expresses its weight W. It is something that was not covered by Monte Carlo method. Instead of assigning only a single value representing energy of a photon, additionally its whole spectrum described by 21 discrete values specifying wavelengths from 400nm to 720nm with stepsize 16nm was initialized.

The distribution of the photons should correspond to distribution of the emissive power of the light source. In order to shoot the photons one has to know what type of light source is involved:

- point light source - photons are emitted in uniformly distributed random directions from the point,
- directional light source - all photons are emitted in the same direction, but from origin outside the scene,
- area light source - photons are emitted from random positions on the surface, with directions limited to hemisphere. The emission directions are taken from cosine distribution. Moreover, they can be restricted to the maximal angle they cannot exceed.

The artifacts related to the variation of the indirect illumination through the image can be visible and arise to the serious problem. To reduce that variation during rendering, it is desirable to emit the photons as evenly as possible, with the uniform allocation. In this way also the effect of flickering is eliminated. This is especially visible when few images are generated one after another of the same scene, but photons are distributed from the light source in the random way. Depending on complexity of the scene, the same parts of the objects will be illuminated in slightly different way. To get rid of those effects stratification of quasi random sampling can be applied. In such a case, photons are evenly distributed and ordered in repeatable manner. Radical inverse is one of the most simple stratification methods. It bases on the idea that a positive integer value n can be described in a base b with a sequence of digits $d_m...d_2d_1$ uniquely determined by:

$$n = \sum_{i=1}^{\infty} d_i b^{i-1}, \qquad (5.23)$$

The radical inverse function Φ_b in base b converts a nonnegative integer n by reflecting these digits about the decimal point. As the result the floating-point value in $[0, 1)$ is obtained:

$$\Phi_b(n) = 0.d_1 d_2...d_m, \qquad (5.24)$$

As the example van der Corput sequence is presented (base 2):

n	$d_m...d_2d_1$	$\Phi_2(2)$
1	1	0.1=1/2
2	10	0.01=1/4
3	11	0.11=3/4
4	100	0.001=1/8
5	101	0.101=5/8
...	...	...

Table 5.1: Calculation of van der Corput sequence

In general case as the base of radical inverse function, one of the prime numbers is taken. It works perfectly also in a multidimensional case and ensures high discrepancy [68]. In the scene with multiple light sources, photons should be emitted from each light source separately. All photons have the same power, so the only thing that distinguishes bright and dark light sources is the number of photons emitted. Also the number of photons in the scene should be the same for the scene containing single light source and for the scene with many light sources (because each light take parts less in the overall illumination and fewer photons need to be sent out) [70].

5.2.2 Pass I - Photon tracing

After the emission, the photon is traced through the scene using photon tracing. Each photon has assigned its position, direction and color, which is generally described by RGB values or spectrum (as it will be described later). It is an iterative procedure of finding an intersection point of particle path with first object in that direction. During a contact with a surface a packet deposits some energy, before it is scattered in new direction. That information is stored in photon map, which in the next pass will be used in rendering process. The main advantage when computing an estimate of a given measurement is that, only once samples are generated and traced through the scene. They can be reused to compute the outcome for different scene conditions and camera positions.

There are three different outcomes as the result of hitting the object by the photon. It can be reflected, absorbed or transmitted. The choice depends on the Russian roulette technique, where random variable decides what interaction occurred. The direction of the outgoing photons is described by the material of the object the photon has hit - bidirectional scattering distribution function (BSDF). It is a mathematical description of light scattering properties of a surface [72]. Reflection follows the model of four different distributions: diffuse, glossy specular, perfect specular and retro-reflective. Most real objects scatters light in the way that is a mixture of those types. Diffuse surfaces reflect light equally in all direction. There is no physical example of such a material, but very similar properties exhibit matte paint and chalkboard. Glossy specular objects scatter light in a set of reflected directions, what is perceived as blurry reflection of other objects. Plastic or high-gloss paint can be treated as glossy specular surfaces. Perfect specular surfaces like mirror or glass scatter light in only one outgoing direction. Finally, retro-reflective objects reflects light mostly back to the incident direction. As an example velvet and Earth's moon can be mentioned.

A photon that arrived at the object carries the history of its interactions. Depending on their types it participates in several types of object illuminations:

- direct illumination - ray of the light that hit the object directly without being scattered previously,

(a) Diffuse

(b) Glossy specular

(c) Perfect specular
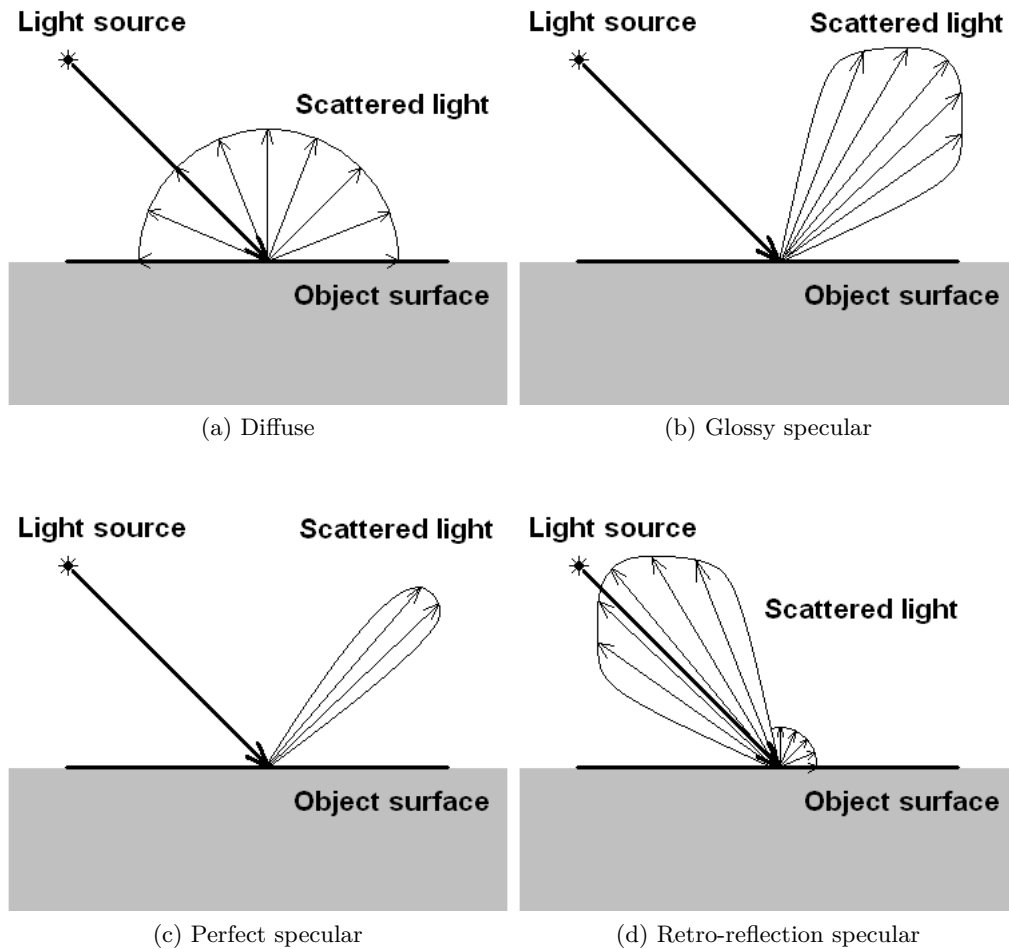
(d) Retro-reflection specular

Figure 5.4: Different types of light reflection

- caustic illumination - ray of the light that intersected a nonspecular surface after being reflected or transmitted by specular surfaces,
- indirect illumination - ray of the light that undergoes all other kind of interactions.

On figure 5.5 some examples of typical photon paths were presented. Two first paths generates caustic illumination, the last one indirect illumination:

- a - specular reflection, 2 diffuse reflections and absorption
- b - 2 specular transmissions followed by absorption
- c - 2 diffuse reflections and final absorption

Each intersection point contains the information about incident illumination and weight, so that it is well know from which direction a packet arrived. Addi-
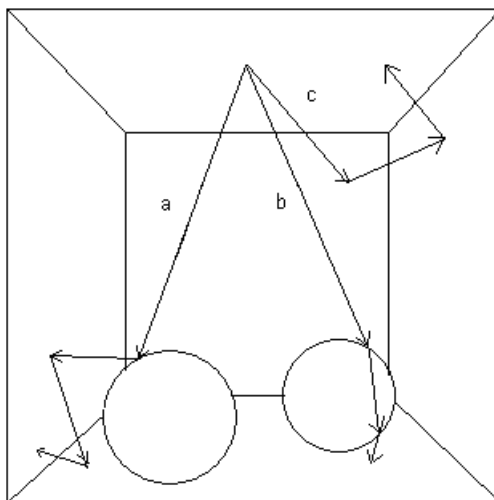
Figure 5.5: Photon rays in the scene. Two balls are situated in the box, right one is made of glass, another one is made of metal.

tionally photons are stored only at nonspecular objects, since particles collected on specular surfaces would not give any useful information during rendering [68].

5.2.3   Pass I - Photon storing

Photons are only stored when they hit diffuse surface. It does not make any sense to store photons for specular surfaces, because the probability of finding a photon that matches the specular direction is equal to zero, so in this way it is not possible to visualize e.g. mirror effects. For this situation standard ray tracing is helpful [70].

Structure that contains all photons is called Photon Map. Each photon can be stored more than once depending on number of interactions along the photon path. A photon map is a data structure, usually a balanced kd-tree, created to store information about photon hits. Each node of the kd-tree contains the data about the coordinates of the hit point (x, y, z), color spectrum, incident direction of the photon, and other important information. Interactions can happen not only at object surfaces, volumes also take part in the light transport. This is often the case when in the scene participating media occurs, like candle smoke or a fog. The photons that hit participating media are stored in another structure called volumetric photon map.

Depending on the place where the photon undergoes the interaction in the scene, surface and volumetric photon map are created. Surface photon map for photons located only on the surface of the object, volumetric photon map for photons inside an object or located in participating media [69].

It is efficient to create even three photon maps. Each of them will be responsible for another illumination effect. Each of the photon maps is created separately

in another photon tracing step:

- caustic photon map - contains photons that hit at least one specular surface before being absorbed,
- global photon map - used for illumination of all diffuse surfaces,
- volumetric photon map - handles participating media (inside and outside objects).

In literature volumetric photon mapping was used to simulate light propagation in smoke [73] and multi-scattering in human hairs [74]. Some optimization methods were presented in [75].

It is profitable to store caustic photons in another structure, because in order to obtain high quality of the image with this phenomenon, generally more photons have to be traced than for example global illumination.

If the photon enters a medium like a fog, smoke or human tissue then it is not stored in the photon map directly at the boundary. The packet travels through the medium until it interacts with surrounding and changes its current direction. Every time the scattering event occurs the photon is stored in volumetric photon map and continues the propagation through the scene. The procedure is repeated until it leaves the medium or hit the diffuse object and is stored in surface (global) photon map.

Photons are only created during the first pass, in the second pass called rendering they are used to calculate estimates of the incoming flux and the reflected radiance at many different points in the whole scene. In order to make those computations correctly it is necessary to find the nearest photon in the Photon Map. This operation is done very often so it is important to invent a good way for representing Photon Map, so that locating the nearest photons can be done in the fastest possible way. The data structure has to be compact so that the usage of memory is small and fast access to each record is ensured. It should also allow fast searching of photons and handle non-uniform distributions. A natural choice of data structure that fulfills all the requirements is a kd-tree. Since the tree is created only once for a given scene and used many times during rendering it is natural to consider balancing of the tree. The time needed to find a photon in balanced kd-tree has the worst time performance of $O(logN)$, where N is the number of records allocated in the tree. Another advantage of this structure is the property that a balanced kd-tree can be represented using heap-like model, where element 1 is the root of the tree, and the element i has element $2i$ as left child and element $2i+1$ as right child. When the large number of photons is used, this leads to significant savings in memory.

In order to balance a kd-tree, the splitting dimension has to be taken into account. This is the only one difference between balancing kd-tree and normal, binary tree. The algorithm starts with choosing a splitting dimension of a set. After that the median of the points in that dimension has to be found. In other

(a) Step 1   (b) Step 2

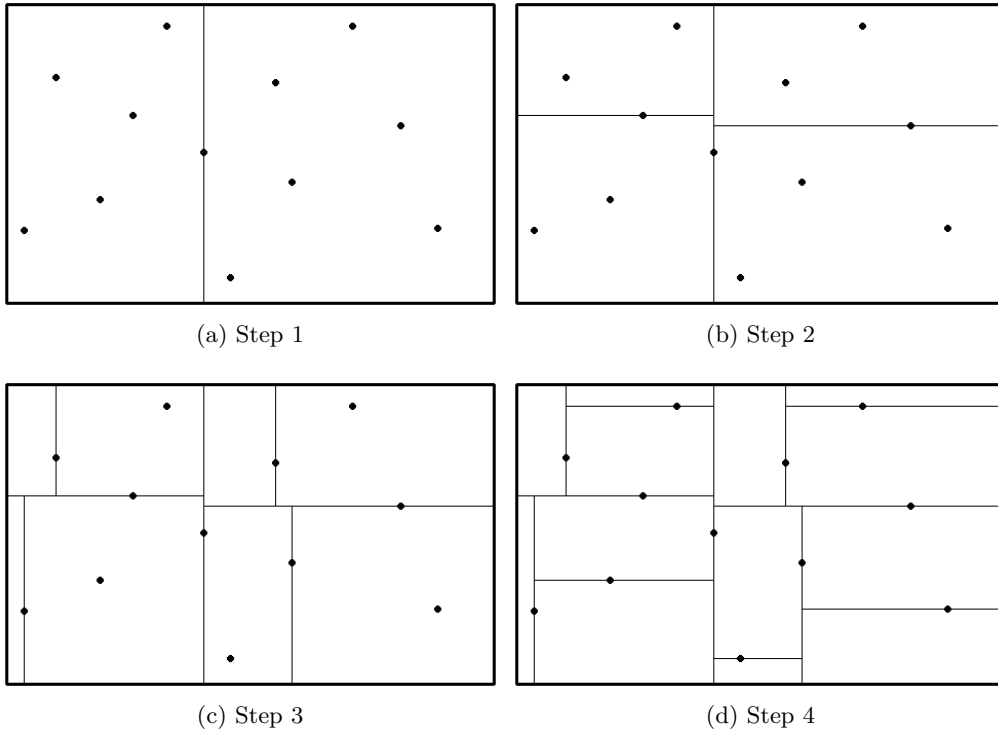(c) Step 3   (d) Step 4

Figure 5.6: The process of generating balanced kd-tree

words the set is represented by the root node of the tree but the left and right subtrees are created from the two sets divided by the median point. The distribution of points within the set decides how to select the splitting dimension. The most popular criterion is the variance or the maximum distance between the points. It is efficient to choose the largest maximum distance between the points as the splitting dimension. The time complexity of the balancing algorithm is $O(NlogN)$.

The most important feature of the photon map method is the capability to calculate the radiance estimates at any non-specular (diffuse) surface point in any given direction. Photon map can be treated as a description of the incoming flux. This information has to be integrated to compute the radiance:

$$L_r(x,\omega) = \int_{\Omega_x} f_r(x,\omega,\omega_i)L_i(x,\omega)cos\theta_i d\omega_i, \tag{5.25}$$

where:

L_r - the reflected radiance at x in direction,

f_r - the BRDF (bidirectional reflectance distribution function) at x,

Ω_x - the (hemi)sphere of incoming directions,

L_i - the incoming radiance.

Because the photon map provides information about the incoming flux the formula above can be rewritten to:

$$L_r(x, \omega) = \int_{\Omega_x} f_r(x, \omega, \omega_i) \frac{d^2 \Phi_i(x, \omega_i)}{dA_i}, \tag{5.26}$$

Using the photon map and locating the n photons that have the shortest distance to x, the incoming flux Φ_i can be approximated.

Finally, by estimation of the integral, the following formula was obtained:

$$L_r(x, \omega) \approx \sum_{i=1}^{n} \frac{f_r(x, \omega, \omega_i) \Delta \Phi_i}{\pi r^2}, \tag{5.27}$$

The accuracy depends on the number of photons stored in the photon map and used in the formula. To find the nearest photons a disc is used. It can happen that wrong photons will be taken into account for radiance computation. This effect will be visible on sharp edges of the objects and in the corners. To get rid of that effect additional filtering is needed. The main idea of filtering is to find photons that are close to the point of interests x and increase their weight. Since the photons are stored at surfaces that are two-dimensional, a 2d-filter which is normalized over the region defined by the photons should be considered. The most popular are 2 filters:

- the cone filter - basing on the distance d_p between x and the photon p a weight ω_{pc} is assigned to each photon according to the formula:

$$\omega_{pc} = 1 - \frac{d_p}{kr}, \tag{5.28}$$

  where:
  $k \geq 1$ - a filter constant,
  r - the maximum distance.

- the Gaussian filter - uses the assumption about locally flat surfaces. It is simple, image based Gaussian filter.

$$\omega_{pg} = \alpha \left[1 - \frac{1 - e^{-\beta \frac{d_p^2}{2r^2}}}{1 - e^{-\beta}} \right], \tag{5.29}$$

  where:
  d_p -the distance between photon p and x,
  α and β - specific filter constants.

To obtain a good performance of the photon map algorithm it is critical to efficiently find the nearest photons. Normally, for a given scene, the number of

photon map queries can be very large. The search algorithm is a simple extension of typical search functions for binary trees. It is connected to range searching where kd-trees are commonly used because of good performance and their optimal storage. The procedure that finds the nearest neighbors of the query point begins at the root of the kd-tree. It goes down the tree and adds photons to a list if they are not further away than a certain distance. In order to find n nearest neighbors the list is sorted. The photon that is outside the given distance can be removed if the list is full and a new, closer photon was found. If it is the case, in order to adjust the range of the query, the distance d to the root element can be used. Thus parts of kd-tree that are further away than d can be omitted. Instead of normal distances a computation of squared distances can be used. Real distances are not necessary, but calculations of square root are time consuming [70].

5.2.4 Pass II - Rendering

Having the photon map and being able to compute the radiance estimate from it, rendering pass can be started. Photon map has very important feature - it is view independent. It means that a single map has to be constructed for an environment and the scene can be rendered from any desired view, by tracing paths from the camera to the scene [76]. Photon map can be easily visualized by computing the radiosity values at the vertices of the mesh.

The full global illumination approach can only be reached using distribution ray tracing algorithm. The pixel radiance is calculated by averaging a number of sample estimates. The sample is generated by tracing a ray from the camera eye through each pixel of the image plane into the scene. In such a way a final image is created.

The outgoing radiance L_o is the sum of the emitted L_e and reflected radiance L_r:

$$L_o(x, \omega) = L_e(x, \omega) + L_r(x, \omega), \tag{5.30}$$

One of the ways for calculating L_r is Monte Carlo integration technique. However, this method is very costly in terms of rendering time. As already described in previous chapter, more efficient algorithm can be found by using the knowledge of the BRDF and the incoming radiance in combination with the photon map. The BRDF can be divided into a sum of two components: a specular $f_{r,s}$, and a diffuse $f_{r,d}$:

$$f_r(x, \omega, \omega_i) = f_{r,d}(x, \omega, \omega_i) + f_{r,d}(x, \omega, \omega_i), \tag{5.31}$$

Additionally the incoming radiance can be determined using three components:

$$L_i(x, \omega) = L_{i,l}(x, \omega) + L_{i,c}(x, \omega) + L_{i,d}(x, \omega), \tag{5.32}$$

where:

- $L_{i,l}(x, \omega)$ - direct illumination - direct lighting coming from different light sources
- $L_{i,c}(x, \omega)$ - caustic - indirect illumination where the phenomenon of specular reflection or transmission occurs.
- $L_{i,d}(x, \omega)$ - indirect illumination - the situation where the photon has been reflected diffusely at least once.

Finally we obtain the formula for reflected radiance:

$$L_r(x, \omega) =$$

$$\int_{\Omega_x} f_r(x, \omega, \omega_i) L_i(x, \omega) cos\theta_i d\omega_i + \qquad \text{Direct Illumination}$$

$$\int_{\Omega_x} f_{r,s}(x, \omega, \omega_i) [L_{i,c}(x, \omega) + L_{i,d}(x, \omega)] cos\theta_i d\omega_i + \qquad \text{Specular and glossy reflection}$$

$$\int_{\Omega_x} f_{r,d}(x, \omega, \omega_i) L_{i,c}(x, \omega) cos\theta_i d\omega_i + \qquad \text{Caustic}$$

$$\int_{\Omega_x} f_{r,d}(x, \omega, \omega_i) L_{i,d}(x, \omega) cos\theta_i d\omega_i + \qquad \text{Multiple diffuse reflections}$$

$$(5.33)$$

Direct illumination is often the most significant term of the expression and has to be computed precisely. It describes the contribution to the reflected radiance by the direct illumination. Direct illumination is responsible for light effects, to which the human eye is highly sensitive such as shadow edges. It is quite simple to calculate the contribution from different light sources in ray tracing based algorithms. At the query point shadow rays are sent towards the light sources to check for possible intersection with objects. If shadow ray does not hit any object, then the contribution from the light source is taken into account in the integral computation, otherwise it is ignored.

Specular and glossy reflection is not calculated using photon map. The integral is dominated by $f_{r,s}$ component, which has a narrow peak around the mirror direction. In order to properly classify different directions within the narrow peak, a huge number of photons would be necessary. Typical Monte Carlo ray tracing based on $f_{r,s}$ with importance sampling can be used instead of this strategy. It is pretty efficient and relatively small number of sample rays has to be traced for correct computations.

Caustic term is computed by using a radiance estimate from the caustic photon map. Because the number of photons in caustic photon map is big, the final effect will be of high quality. Caustic effects are never calculated using Monte Carlo ray tracing. It would be very inefficient and result in the bad quality of the final image. Approximate solution can be done using radiance estimate from global photon map.

Multiple diffuse reflections result in a very "soft" illumination. It represents incoming light that was reflected diffusely at least once after it left the light source. As in the previous case the approximate solution can be evaluated from the global photon map. The accurate result needs to be calculated using Monte Carlo ray tracing that bases on BRDF with the estimate of the flux. The information from the photon map is exploited to concentrate the samples into the important directions only, instead of testing multiple bounces of indirect illumination [70].

5.2.5 Pass II - Ray marching

Global illumination in scenes with participating media was introduced in [77]. The algorithm is focused on bidirectional Monte Carlo ray tracing and uses photon maps to reduce noise and increase efficiency. For this purpose a volume photon map containing photons in participating media was used. It was also needed to derive a new radiance estimate for photons in the volume photon map. This method could effectively simulate effects such as multiple volume scattering, color bleeding between volumes and surfaces, and volume caustics.

For the scenes with participating media, the radiance seen directly by the observer L_o is the sum of the emitted L_e and reflected radiance L'_r through participating media:

$$L_o(x, \omega) = L_e(x, \omega) + L'_r(x, \omega), \tag{5.34}$$

When a ray hits a given point on a surface, radiative transfer equation (RTE) describes the process of light transport. It defines the radiance from direction ω that reaches a camera located at position x. It is a sum of the incident illumination of the intersected surface and the sum of in-scattered radiances along the ray inside participating medium, which can be expressed as:

$$L'_r(x, \omega) \approx T_r(x \leftrightarrow x_s) L_r(x_s, \omega) + \int_0^s T_r(x \leftrightarrow x_s) \mu_s(x_t) L_i(x, \omega) dt, \tag{5.35}$$

where:

S - number of steps,

$\mu_t(x_t)$ - extinction coefficient equal to $\mu_a + \mu_s$ (assumed constant),

$\tau(x \leftrightarrow x_s)$ - optical thickness defined as $\int_{x_s}^x \mu_t(x) dx = \int_{x_s}^x \mu_t dx = \mu_t(x_s - x)$,

$T_r(x \leftrightarrow x_s)$ - transmittance defined as $e^{-\tau(x \leftrightarrow x_s)}$,

$L_r(x_s, \omega)$ - illumination computed from ray tracing,

$L_i(x_t, \omega)$ - in-scattered radiance computed using photon maps.

The in-scattered radiance depends on radiance at x_t from all directions ω_t can be described as:
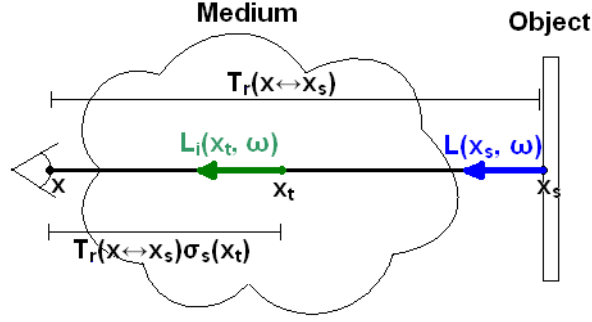
Figure 5.7: The total radiance is the sum of the radiance from the surface and subsequent in-scattered radiance along the ray.

$$
\begin{aligned}
L_i(x_t,\omega) &= \int_{\Omega_{4\pi}} p(x_t,\omega,\omega_t)L(x_t,\omega_t)d\omega_t \\
&= \int_{\Omega_{4\pi}} p(x_t,\omega,\omega_t)\frac{d^2\Phi_i(x_t,\omega_t)}{\mu_s(x_t)dV} \\
&\approx \frac{1}{\mu_s(x_t)}\sum_{p=1}^{n} p(x_t,\omega_p,\omega_t)\frac{\Delta\Phi_p(x_t,\omega_{t,p})}{\frac{4}{3}\pi r^3},
\end{aligned} \tag{5.36}
$$

where:

$\Delta\Phi_p$ - power of photon p,

$p(x_t,\omega_p,\omega_t)$ - normalized phase function,

dV - the volume of the sphere containing the photons. It is worth to mention that for surface photon map not sphere but disk area dA was used.

r - maximum radius where neighbor photons were found,

n - number of neighbor photons.

The presented idea is called Ray Marching, when at each step the contribution of photons is calculated and summed up. However, during rendering numerical integration is necessary:

$$
\begin{aligned}
L'_r(x,\omega) &\approx T_r(x \leftrightarrow x_s)L_r(x_s,\omega) + \sum_{t=0}^{s} T_r(x \leftrightarrow x_s)\mu_s(x_t)L_i(x_t,\omega)\Delta x \\
&\approx T_r(x \leftrightarrow x_s)L_r(x_s,\omega) + \sum_{t=0}^{s} T_r(x \leftrightarrow x_s)\Delta x \sum_{p=1}^{n} p(x_t,\omega_p,\omega_t)\frac{\Delta\Phi_p(x_t,\omega_p)}{\frac{4}{3}\pi r^3},
\end{aligned}
$$
$$\tag{5.37}$$

where:

Δx - length of each segment (constant for every t).

Aggregation of density estimation along the ray requires searching for photons within volumetric photon map. This double-iterative approach is quite expensive,

but still more efficient than simple path tracing technique. The ray marching algorithm can be even more optimal if photons were not gathered twice as it is in case of overlapping neighbor spheres or if the step size is small enough so that no photon is omitted. Since such problems may occur quite often when performing simulation, appropriate calibration is needed [75].

5.2.6   Tone mapping

The final part of rendering regards mapping of previously calculated radiosity values to produce realistic images of captured scenes. It is not an easy task, since the limitations presented by prints on photographic papers or display devices enforce some knowledge about the object and environment. In order to properly reflect the contrast in the scene, not only artistic but also technical experience is needed. It is very difficult to create satisfactory images. The challenges found in conventional photography are mainly the same as those faced during rendering or capturing digital images. From the tone reproduction perspective the digital images are "perfect" negatives, because the luminance data wasn't lost due to the film process restrictions [78].

Display devices, due to their internal structure, have limited dynamic range in terms of producing realistic images. The problem of rendering artificial or natural scenes is still observable in cinematography, photography, visualization and printing. The best results are obtained when each situation is considered separately and the image is tuned manually on the target display. The most challenging task would be to replace the manual approach with a computational algorithm. Many ideas are basing on the fact that the image reproduction procedure can be described as an optimization problem. It tries to find the best fitting contrast parameters in all ranges of a tone-scale.

A tone mapping algorithm should perform such a conversion so that the obtained pixel values are in the range 0-255. The resulting tones displayed on particular devices of well defined capabilities are perceived as realistic and looks convincing for the human. This problem is particularly important from the point of recent research in display technologies (OLED, LCD etc.) and applications like electronic books, home entertainment or mobile displays. Such crucial parameters as contrast, peak brightness and black level, which additionally change due to different light conditions (office light or sunlight). It means that the same image displayed on different devices will not produce the expected appearance. In [79] there was proposed a tone-mapping operator, which basing on the display device characteristic is able to render the best images with the least possible visible contrast distortions.

In the real world, it is very common for scenes to have radiance values in range from 0.1 to 1000. It is five order of magnitude to display the brightest and the darkest part of the environment. However, the human eye is more sensitive to

changes in local contrast than to total brightness. It is very critical to find such methods that compress those extra orders of magnitude. To the most popular tone reproduction operators belong:

- maximum to white operator - it is one of the simplest possible tone mapping operation. It iterates over all pixels in the image to find the one with the highest value. This pixel is mapped to the maximum luminance value of the display device. The rest of the pixels are proportionally scaled over the whole range. One of its disadvantages concerns not basing on human visual system at all. For example, exactly the same images are obtained for initial and 100 times brighter light in the scene. Additionally, the another drawback is more critical when rendering images using photon maps. Even one pixel with very high luminance value can make the whole image looks dark. However, it works good for scenes with low dynamic range in the image.

- contrast-based scale factor - this operator concentrates on keeping the same contrast in the generated image. It is basing on the idea that measures the smallest change in luminance noticeable by human visual system, called adaptation luminance or just noticeable difference (JND). The larger JND, the larger change is needed in luminance to be perceived correctly by human. The algorithm implements a constant scale factor and tries to analyze a given region of the initial image to find an area that is noticeably different from the rest to the observer. Display pixel values are scaled appropriately, so that different regions are noticeably different and the dynamic range is not wasted. The formula for scale factor is described by the following equation:

$$s = \left(\frac{1,219 + (Y_d^a)^{0.4}}{1,219 + (Y_w^a)^{0,4}} \right), \tag{5.38}$$

where:
Y_d^a - adaptation luminance of a display,
Y_w^a - adaptation luminance of a world.

The only unknown parameter here is the world adaptation luminance Y_w^a, which should be computed basing on the part of the scene the observer is looking at. Since this information cannot be available, the contrast-based scale operator computes a logarithmic average of the whole luminance in the original image. This kind of average does not allow small bright areas to dominate over the rest of the image [68].

5.3 Final algorithm as a consolidation of previous ideas

Human skin tissue was modeled as purely diffuse surface. It is an example of object, which does not only reflect the light, but also transmit it inside. It means that light penetrates the structure of skin just below the surface. Since the tissue can be treated as a turbid medium, it is possible to apply a Monte Carlo technique together with photon mapping to trace and store the packets of energy. Additionally ray marching can be utilized to render the effect of subsurface scattering.

The most important effect that needed careful handling was fluorescence phenomenon - figure 5.8. To accomplish this idea a couple of assumptions were necessary:

- photon mapping algorithm was extended with Monte Carlo model of light propagation in turbid media to describe the way volumetric photons are gathered,
- since fluorescence phenomenon is dominant optical process in the human tissue, only fluorescent photons are stored in photon maps. It means that only photons that underwent interaction with fluorescent molecule in the past are collected and used later during rendering.
- the implementation concentrated only on indirect illumination, which results in presenting light that was scattered under the tissue surface and had a chance to contact fluorescent structures of a skin. Direct photon map is neglected since it does not give any useful information about fluorescence, because photons do not penetrate the object and are reflected back,
- in order to correctly visualize the tissue reflectance spectrum two photons map were used: surface and volumetric photon map.

After specifying the foundation of the whole experiment, it is possible to combine Monte Carlo model and photon mapping together, so that they perform appropriate function in the desired way and order. Now it is possible to define all steps performed in the first pass of algorithm.

1. Photon is generated, initialized with the spectrum of the light source and launched
2. If it didn't intersect any object then start from the beginning with new photon
3. Check if photon was reflected utilizing equation 5.4 and start from the beginning with new photon if this is true,
4. Update weight according to equation 5.5
5. Calculate new direction according to equation 5.3
6. Repeat the following steps until photon escaped the tissue:
    - Move photon by a stepsize defined by equation 5.12
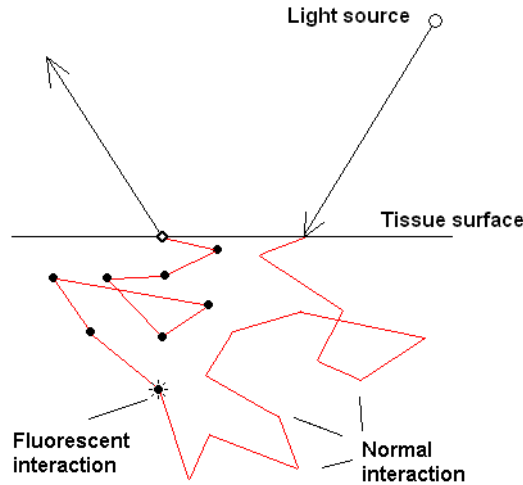
Figure 5.8: Photons interact many times with molecules changing their direction. Only some fraction of them escapes the tissue and is stored into surface photon map (open dot). Others are completely absorbed. If the fluorescence phenomenon occurs, what happens very rarely, the photon is stored into volumetric photon map every time it interacts with tissue (closed dots)

- Make sure it didn't escaped the object,

- Generate a random variable and check, what molecule the packet interacted with (d coefficient),

- If the fluorescence occurs update the photon spectrum using excitation-emission matrix. Mark the packet with "fluorescent" state flag.

- Generate another random variable to decide whether the photon is absorbed or reflected. In case of absorption the energy of the photon is reduced by the equation 5.16. If the photon is only scattered, then its direction is updated by equation 5.18 and 5.19.

- If the photon is "fluorescent" then store it in the volumetric photon map,

7. If the photon is "fluorescent" then store it in the surface photon map. The photon is terminated.

8. Start the whole procedure from the beginning. Repeat the algorithm until the desired number of photons is collected in surface and volumetric photon map.

The presented flow of events can be described by the block diagram 5.9. Every rectangle expresses a procedure that needs to be performed at a given moment. Lines and arrows show the relationship between particular blocks and location of the next step. Condition blocks represented by diamonds help to coordinate the decision making.
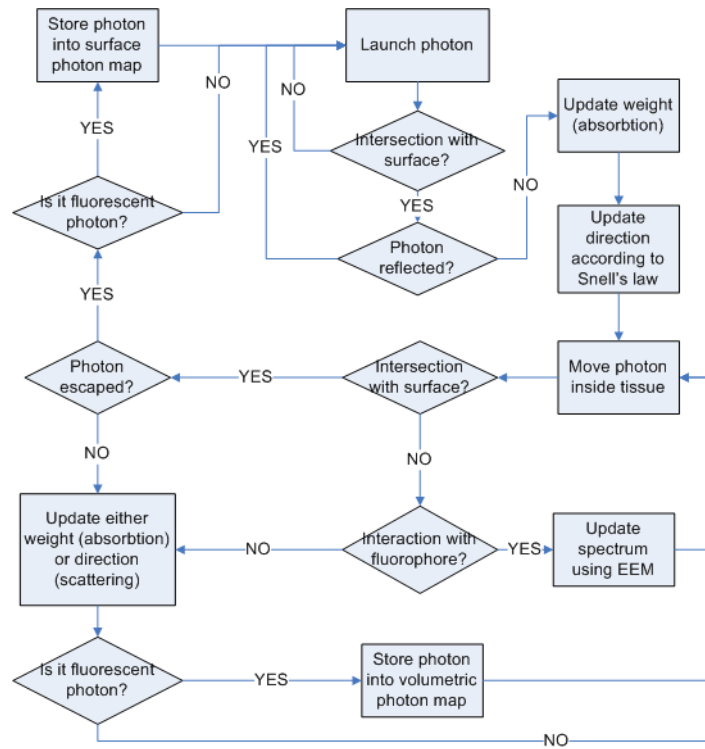
Figure 5.9: Flow diagram of proposed Monte Carlo model

In the second phase of simulation the rendering is performed. The first important observation from equation 5.35 is that component $L_r(x_s, \omega)$ is equal to zero. It was assumed that there is no illumination from behind the tissue object. In other words the medium is so thick that light is not able to travel through the whole skin to the camera.

The second assumption that was made is utilizing surface and volumetric photon maps at the same time. To compute in-scattered radiance, first of all the radiance at the medium surface is calculated using surface photon map and then iteratively moving by a given stepsize radiance is accumulated along the ray. Every time a volumetric photon map is used for partial computation. Taking all those considerations into account the equation 5.37 was rewritten to:

$$L'_r(x,\omega) \approx T_r(x \leftrightarrow x_s) L_r(x_s,\omega) + \sum_{t=0}^{s} T_r(x \leftrightarrow x_s)\mu_s(x_t)L_i(x_t,\omega)\Delta x$$

$$\approx \sum_{t=0}^{s} T_r(x \leftrightarrow x_s)\mu_s(x_t)L_i(x_t,\omega)\Delta x$$

$$\approx L_i(x_0,\omega) + \sum_{t=1}^{s} T_r(x \leftrightarrow x_s)\mu_s(x_t)L_i(x_t,\omega)\Delta x$$

$$\approx \sum_{p=1}^{n} p(x_0,\omega_p,\omega_0)\frac{\Delta\Phi_p(x_0,\omega_p)}{\pi r^2} + \sum_{t=1}^{s} T_r(x \leftrightarrow x_s)\Delta x \sum_{p=1}^{n} p(x_t,\omega_p,\omega_t)\frac{\Delta\Phi_p(x_t,\omega_p)}{\frac{4}{3}\pi r^3},$$

$$(5.39)$$
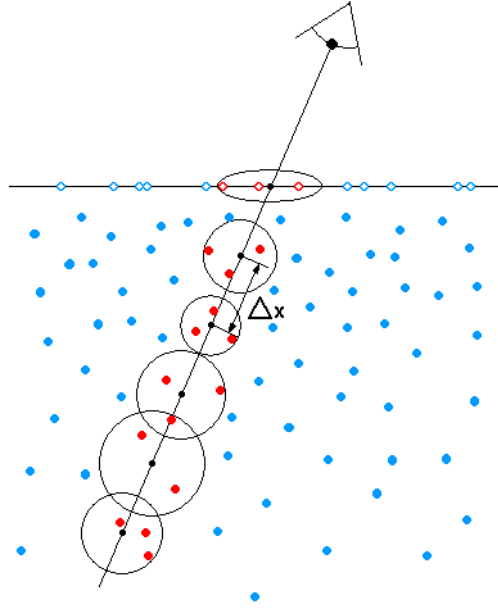
Figure 5.10: Ray marching and photon gathering with constant step size. Open dots represent photons in surface photon map, closed dot symbolize photons in volumetric photon map

Figure 5.10 describes the ray marching idea with two photon maps. On the tissue surface the predefined number of photons is gathered from surface photon map. The circle shows the distance to the farthest localized photon from the query point. Along the ray, at each sampling point, an in-scattered radiance is computed by collecting specific number of photons that are located in the minimal sphere around it. It can be observed that the size of a circle or sphere changes with query point or with the position inside tissue.

5.3.1   Calculating emission spectrum using EEM

The database containing the fluorescence EEMs of 35 possible endogenous fluorophores, was used. All data was measured using standard fluorescence spectrophotometer. For each excitation wavelength, EEM gives the emission spectrum that needs to be normalized and then multiplied by the carried initial energy. Moreover, the quantities in electronic database are discrete values; for example the step size for excitation wavelengths is 10nm and the step size for the emission wavelengths is 5nm [4]. Such a situation causes problems when the given excitation wavelength cannot be mapped to the appropriate emission spectrum. This inconsistency in sample rate was solved by duplicating the same spectrum to the wavelengths located between sample points. It means that wavelengths 520nm and 515nm (510nm and 505nm etc.) would have the same emission spectrum. In this way the small error was introduced to the computations, but the sample rate for excitation and emission wavelengths is the same now.
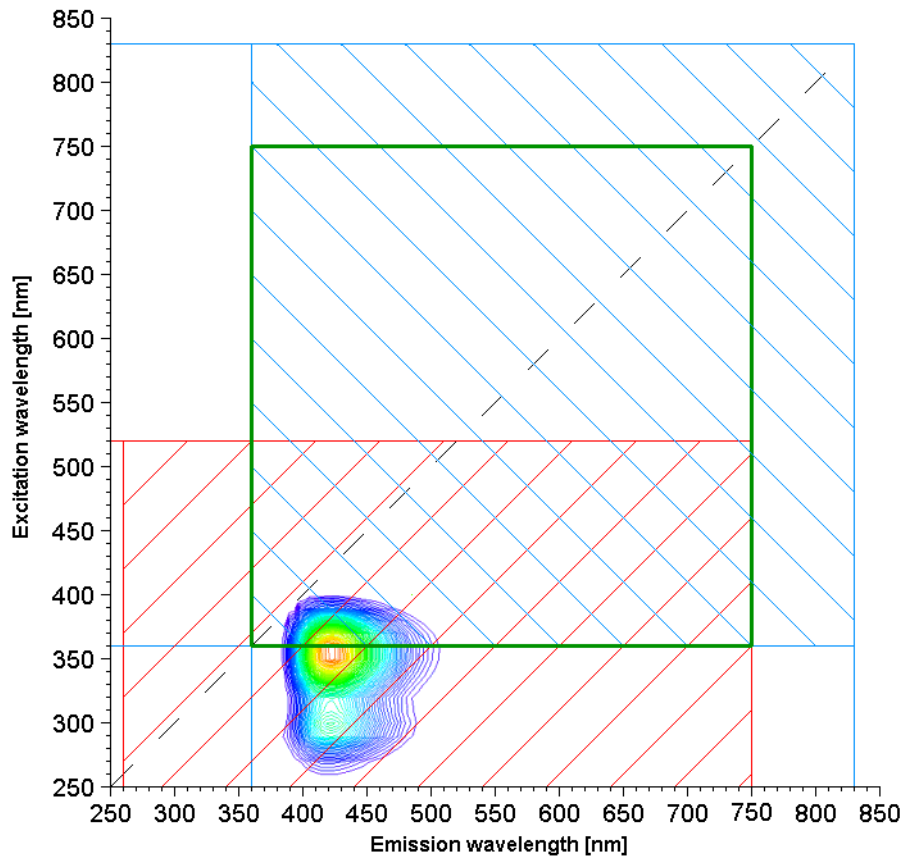
Figure 5.11: Specifying spectrum dimension

Figure 5.11 shows the part of EEM that was used during computation. Red area expresses original EEM. Blue area defines visible light. Visible color spectrum starts at 360nm so there is no need to compute spectrum lower than that

value. Data from EEM ends at 750nm so this value will be assumed as maximal. Since emission dimension is defined in range 360-750m also dimension of excitation spectrum should be in that range. For excitation wavelengths grater than 520nm the emission spectrum was set to zero, what is a good assumption for most fluorophores. Green square indicates the matrix of transformations from excitation to emission spectrum, that was utilized. Other wavelengths were omitted.

To calculate the emission spectrum, the superposition principle will be used. It means that the partial emission spectrum for each excitation wavelength will be computed and summed up. Partial emission spectrum for the given wavelength is defined as the multiplication of excitation spectrum and appropriate emission spectrum from EEM. It guarantees that total weight of emission spectrum is not grater than the initial excitation weight.

Afterwards it is necessary to normalize all quantities. In order to do that all values from EEM were summed up to obtain total energy and the result was inverted. Finally, each value from emission spectrum was multiplied by the obtained number and in such a way final spectrum was calculated.

5.3.2   Source code

The configuration file for PBRT simulation engine is very easy to read. The input parameters changed frequently between separate experiments, but the general overview is presented below. It contains photon mapping algorithm, camera, sampler and image properties, including scene parameters like light sources and tissue surface.

```
1   #Definition of photon mapping process
2   SurfaceIntegrator "photonmap"
3           "integer nused" [10]               #Number of neighbor photons looked for
4           "integer causticphotons" [0]       #Number of required caustic photons
5           "integer directphotons" [0]        #Number of required direct illumination photons
6           "integer indirectphotons" [400000] #Number of required indirect illumination photons
7           "integer volumetricphotons" [0]    #Number of required volumetric photons
8           "bool directwithphotons" ["true"]  #Is direct illumination computed using photons?
9           "bool finalgather" ["false"]       #Is final gathering needed?
10          "float maxdist" [0.1]              #Maximum distance from query point
11
12  #Camera position and direction
13  LookAt 0 0 0   0 0 -1 0 -1 0
14  Translate 0 -0.2 0
15  Rotate 0 1 0 0
16  Translate 0.5 -2.5 -0
17
18  #Camera parameters
19  Camera "perspective"
20          "float fov" [90 ]                 #Field of view
21          "float hither" [0.001 ]           #Distance to hither plane
22          "float yon" [1e+30 ]              #Distance to yon plane
23          "float screenwindow" [-1 1 -1 1 ] #Screen coordinates
24
25  #Film parameters
26  Film "pngfilm"
27          "integer xresolution" [400 ]      #Image width
28          "integer yresolution" [400 ]      #Image height
29          "string tonemapper" "maxwhite"    #Tone mapping method used
```

```
30
31   #Sampling parameters
32   Sampler "stratified"
33           "integer xsamples" [2]          #Filter width
34           "integer ysamples" [2]          #Filter height
35            "bool jitter" ["false"]        #No anti-aliasing by jittering
36
37   WorldBegin
38
39   #Area light source 1 parameters
40   AttributeBegin
41   AreaLightSource "area"
42           "float coneangle" [45]          #Angle alpha
43           "integer nsamples" [2]          #Number of samples
44           "float L" [50]                  #Initial photon energy
45
46   #Light position
47   Translate 0 2.5 0
48   Rotate -0 1 0 0
49   Rotate 180 1 0 0
50   Translate -0.65 0 -0
51
52   #Light shape and size
53   Shape "disk" "float radius" [0.1]
54   AttributeEnd
55
56   #Area light source 2 parameters
57   AttributeBegin
58   AreaLightSource "area"
59           "float coneangle" [45]          #Angle alpha
60           "integer nsamples" [2]          #Number of samples
61           "float L" [50]                  #Initial photon energy
62
63   #Light position
64   Translate 0 2.5 0
65   Rotate -0 1 0 0
66   Rotate 180 1 0 0
67   Translate -0.35 0 -0
68
69   #Light shape and size
70   Shape "disk" "float radius" [0.1]
71   AttributeEnd
72
73   #Material type (diffuse) and spectrum definition of human skin tissue
74   Material "matte" "color Kd" [
75   ...
76   #Here goes spectrum values
77   ...
78   ]
79
80   #Tissue layer parameters
81   LayerBegin
82           "float n" 1.4                   #Tissue refractive index
83           "float ua" 43                   #Tissue absorption coefficient
84           "float us" 511                  #Tissue scattering coefficient
85           "float g" 0.8                   #Tissue anisotropy factor
86           "float height" 1                #Tissue height
87
88   #Shape of the layer surface
89   Include "../../../scenes/geometry/tissue.pbrt"
90
91   #Definition of fluorophores, their density and location
92   #Component "Blood"        "float density" 10
93   Component "CollagenVII"   "float density" 20
94   #Component "NADH"         "float density" 15
95   #Component "FAD"          "float density" 5
96   Component "Protoporphyrin" "float density" 10 "point e" [-0.5 2.5 -1] "float radius" 0.25
97   LayerEnd
98
99   WorldEnd
```

Listing 5.1: Configuration file for PBRT

Th listing below describes the method for calculating emission spectra after photon interacts with fluorescent molecule. More details are available in 5.3.1. Please note that the number of samples in excitation spectrum (step size 5nm) is greater than in the EEM matrix (step size 10nm). For this reason values from excitation values were duplicated so that they are equal.

```cpp
bool PhotonIntegrator::UpdateFluorescence(Layer *l, Spectrum *a, Point iSect) {
    bool is_fluorescent = false;
    int i,j,k;
    const int colSamples = Spectrum::GetColorSamples();
    double len;

    // Check if photon is inside one of the sphere containing fluorophore
    for (k=0; k<l->components.size(); k++) {
        len = ((Vector)l->components[k]->pnt-(Vector)iSect).Length();
        if ((l->components[k]->radius != 0) &&
            (len<l->components[k]->radius)) {
            break;
        }
    }

    float comp = RandomFloat()*100;
    float part = 0;
    for (i=0; i<l->components.size(); i++) {
        // If photon is outside cancer region, then neglect fluorophore
        if ((k==l->components.size()) && (l->components[i]->radius != 0)) {
            continue;
        }
        // Check if fluorescent interaction occurred
        part += l->components[i]->density;
        if (part >= comp) {
            break;
        }
    }
    if (i >= l->components.size()) {
        return false;
    }

    // Fluorescent interaction occurred - update spectrum
    Spectrum out;
    Component *cp = l->components[i];

    // EEM array is written from back to beginning
    // Calculate number of samples
    int ex_num = (cp->ex_start-cp->ex_end)/cp->ex_step+1;
    int em_num = (cp->em_end-cp->em_start)/cp->em_step+1;

    // Since PBRT spectrum sarts from 360nm and EMM spectrum starts from 250nm
    // Calculate excitation offset that is 360nm = 250nm + 10nm*11
    int ex_offset = ex_num - 11;
    // Calculate emission offset that is 360nm = 260nm + 20*5nm
    int em_offset = 20;

    // Set fluorescent flag
    is_fluorescent = true;

    // Calculate emission spectrum
    // The second emission spectum is duplicated to cover the whole excitation range
    for (i = 0; i < colSamples; ++i) {
        for (j = 0; j < ex_offset; ++j) {

            out.c[i] += a->c[j*2]  * cp->eem[ex_offset-1-j][i+em_offset];
            out.c[i] += a->c[j*2+1]* cp->eem[ex_offset-1-j][i+em_offset];
        }
```

```
59        }
60
61        // Normalize spectrum by the energy of the whole EEM and custom parameter (8)
62        for (i = 0; i < colSamples; ++i) {
63            out.c[i] = out.c[i] / cp->all / 8;
64        }
65
66        // Substitute result to photon spectrum
67        for (j = 0; j < colSamples; ++j) {
68            a->c[j] = out.c[j];
69        }
70
71        return is_fluorescent;
72   }
```

Listing 5.2: PBRT source code of emission spectrum calculation using EEM

The photon mapping algorithm was presented below. Only the most interesting part of this method was presented e.i. photon tracing and storing phase. Rendering procedure remains unchanged, so it was not described here. For simplicity irrelevant parts of the source was removed. The listing starts from launching a photon, finding intersection, moving, absorbing, scattering, calculating fluorescence and storing either to surface or volumetric photon map. The flow diagram of this method is presented in 5.9.

```
1    void PhotonIntegrator::Preprocess(const Scene *scene) {
2        if (scene->lights.size() == 0) return;
3        // Initialize photon maps
4        ProgressReporter progress(nCausticPhotons+nDirectPhotons+
5            nIndirectPhotons+nVolumetricPhotons, "Shooting photons");
6        vector<Photon> indirectPhotons;
7        indirectPhotons.reserve(nIndirectPhotons);
8        vector<Photon> volumetricPhotons;
9        volumetricPhotons.reserve(nVolumetricPhotons);
10       vector<Photon> directPhotons;
11       directPhotons.reserve(nDirectPhotons);
12
13       // Initialize photon shooting statistics
14       static StatsCounter nshot("Photon Map",
15           "Number of photons shot from lights");
16       bool indirectDone = (nIndirectPhotons == 0);
17       bool volumetricDone = (nVolumetricPhotons == 0);
18       bool directDone = (nDirectPhotons == 0);
19
20       Intersection photonIsect;
21       Layer *currLayer;
22       Layer *nextLayer;
23       float ei, et;
24       Point newIsect;
25       Shape *a;
26       float step;
27       Vector wo, wi;
28
29       // Shoot photons until one of the maps is full
30       while ((!indirectDone) || (!volumetricDone) || (!directDone)) {
31           ++nshot;
32           bool fluorescent = false;
33           // Give up if we're not storing enough photons after 500000 tracings
34           if (nshot > 500000 &&
35               unsuccessful(nIndirectPhotons,
36                           indirectPhotons.size(),
37                           nshot)) {
38             Error("Unable to store enough photons.  Giving up.\n");
39             return;
```

```
40              }
41          // Trace a photon path and store contribution
42          // Choose 4D sample values for photon
43          float u[4];
44          u[0] = (float)RadicalInverse((int)nshot+1, 2);
45          u[1] = (float)RadicalInverse((int)nshot+1, 3);
46          u[2] = (float)RadicalInverse((int)nshot+1, 5);
47          u[3] = (float)RadicalInverse((int)nshot+1, 7);
48          // Choose light to shoot photon from
49          int nLights = int(scene->lights.size());
50          int lightNum =
51              min(Floor2Int(nLights * (float)RadicalInverse((int)nshot+1, 11)),
52              nLights-1);
53          Light *light = scene->lights[lightNum];
54          float lightPdf = 1.f / nLights;
55          // Generate photonRay from light source and initialize its spectrum (alpha)
56          RayDifferential photonRay;
57          float pdf;
58          Spectrum alpha =
59              light->Sample_L(scene, u[0], u[1], u[2], u[3],
60                  &photonRay, &pdf);
61          if (pdf == 0.f || alpha.Black()) continue;
62          alpha /= pdf * lightPdf;
63
64          if (!alpha.Black()) {
65              // Follow photon path through scene and record intersections
66              currLayer = NULL;
67              nextLayer = NULL;
68
69              while (Roulette(&alpha)) {       // Russian roulette for photon termination
70                  float phi = RandomFloat();
71                  // Calculate step
72                  if (currLayer != NULL) {
73                      step = -log(phi)/(currLayer->ua+currLayer->us);
74                  }
75                  else {
76                      step = INFINITY;
77                      ei = 1;
78                  }
79                  // Calculate intersection of ray with photon
80                  newIsect = photonRay.o + photonRay.d*step;
81                  scene->Intersect(photonRay, &photonIsect);
82                  if ((currLayer == NULL) && (photonRay.maxt >= INFINITY))
83                      break;
84
85                  // Check if photon intersects a tissue surface
86                  if (step > photonRay.maxt) {
87
88                      // If first photon/surface intersection then it is direct illumination
89                      if (step == INFINITY) {
90                          alpha *= scene->Transmittance(photonRay);
91                          Photon photon(photonIsect.dg.p, alpha, -photonRay.d);
92                          if (!directDone) {
93                              directPhotons.push_back(photon);
94
95                              // Store photon in direct photon map
96                              if (directPhotons.size() == nDirectPhotons) {
97                                  directDone = true;
98                                  nDirectPaths = (int)nshot;
99                                  directMap =
100                                     new KdTree<Photon,
101                                             PhotonProcess>(directPhotons);
102                             }
103                             progress.Update();
104                         }
105                     }
106
107                     BSDF *photonBSDF = photonIsect.GetBSDF(photonRay);
108                     // Get photon direction
109                     wo = photonRay.d;
```

```
110                         Vector lwo=photonBSDF->WorldToLocal(wo);
111                         float cosi = CosTheta(lwo);
112                         // Check if photon entered new tissue layer
113                         bool entering = photonIsect.dg.nn.z < 0.;
114
115                         // Initialize next layer
116                         try {
117                             a = ((GeometricPrimitive*)(photonIsect.primitive))->GetShape();
118                             if (!entering) {
119                                 nextLayer = ((Triangle*)(a))->GetMesh()->layerDefUp;
120                             }
121                             else {
122                                 nextLayer = ((Triangle*)(a))->GetMesh()->layerDefDown;
123                             }
124                         }
125                         catch (...) {
126                             Error("It shouldn't happen at all");
127                         }
128
129                         // Get refractive indices
130                         if (currLayer == NULL) {
131                             ei = 1;
132                         }
133                         else {
134                             ei = currLayer->n;
135                         }
136
137                         if (nextLayer == NULL) {
138                             et = 1;
139                         }
140                         else {
141                             et = nextLayer->n;
142                         }
143
144                         // Compute transmitted ray direction - Snell's law
145                         float sini2 = SinTheta2(lwo);
146                         float eta = ei / et;
147                         float sint2 = eta * eta * sini2;
148                         // Handle total internal reflection for transmission
149                         if ((sint2 > 1.) && (entering)) {
150                             break;
151                         }
152                         float cost = sqrtf(max(0.f, 1.f - sint2));
153                         if (entering) cost = -cost;
154                         float sintOverSini = eta;
155                         Vector lwi = Vector(sintOverSini * -lwo.x,
156                                 sintOverSini * -lwo.y,
157                                 cost);
158                         wi = -photonBSDF->LocalToWorld(lwi);
159                         photonRay = RayDifferential(photonIsect.dg.p, wi);
160                         float ai;
161                         float at;
162                         // Get incident and transmitted angle
163                         if (entering) {
164                             ai = acos(cosi);
165                             at = acos(-cost);
166                         }
167                         else {
168                             ai = acos(-cosi);
169                             at = acos(cost);
170                         }
171                         // Calculate Fresnel formula
172                         float R = 0.5f*((sin(ai-at)*sin(ai-at))/(sin(ai+at)*sin(ai+at)) +
173                             (sin(ai-at)*sin(ai-at))*(cos(ai+at)*cos(ai+at))/
174                             (sin(ai+at)*sin(ai+at))/(cos(ai-at)*cos(ai-at)));
175                         float rand = RandomFloat();
176                         // Check if photon enters a new layer
177                         if ((rand>R) && (nextLayer != NULL)) {
178                             currLayer = nextLayer;
179                             // Udapte weight
```

```
180                                  alpha=alpha-alpha*R;
181                                  continue;
182                              }
183                          else {
184                              if (currLayer == NULL) {
185                                  wo.z = -wo.z;                    // Calculate direction when reflected
186                              }
187                              Photon photon(photonIsect.dg.p, alpha, wo);
188
189                              // Store only fluorescent photons
190                              if ((!indirectDone) && (fluorescent)){
191                                  indirectPhotons.push_back(photon);
192
193                                  // Store photon in indirect photon map
194                                  if (indirectPhotons.size() == nIndirectPhotons) {
195                                      indirectDone = true;
196                                      nIndirectPaths = (int)nshot;
197                                      indirectMap =
198                                          new KdTree<Photon,
199                                              PhotonProcess>(indirectPhotons);
200                                  }
201                                  progress.Update();
202                              }
203                              break; // Trace next photon
204                          }
205                      }
206                  else {
207                      // Propagate a photon inside a tissue
208                      // Update fluorescence
209                      if (!fluorescent)
210                          fluorescent |= UpdateFluorescence(currLayer, &alpha, newIsect);
211
212                      phi = RandomFloat();
213                      float probAbsScat = currLayer->ua/(currLayer->ua+currLayer->us);
214
215                      if (phi<probAbsScat) {
216                      // Udapte weight
217                          alpha=alpha-alpha*probAbsScat;
218                      }
219                      else {
220                           // Or scatter
221                          phi = RandomFloat();
222                          float cosTheta;
223                          // Calculate deflection angle
224                          if (currLayer->g > 0) {
225                              cosTheta = 1/(4*M_PI*currLayer->g)*(1+currLayer->g*currLayer->g-
226                                  (1-currLayer->g*currLayer->g)*(1-currLayer->g*currLayer->g)/
227                                  (1-currLayer->g+2*currLayer->g*phi)/
228                                  (1-currLayer->g+2*currLayer->g*phi));
229                          }
230                          else {
231                              cosTheta = 2*phi-1;
232                          }
233                          float sinTheta = sqrt(1-cosTheta*cosTheta);
234
235                          phi = RandomFloat();
236                          // Calculate azimuthal angle
237                          float cosAzi = cos(2*M_PI*phi);
238                          float sinAzi = sin(2*M_PI*phi);
239                          // Calculate new photon direction
240                          if (abs(photonRay.d.z)>0.99999) {
241                              wi.x = sinTheta*cosAzi;
242                              wi.y = sinTheta*sinAzi;
243                              wi.z = photonRay.d.z/abs(photonRay.d.z)*cosTheta;
244                          }
245                          else {
246                              wi.x = sinTheta/sqrt(1-photonRay.d.z*photonRay.d.z)*
247                                  (photonRay.d.x*photonRay.d.z*cosAzi-photonRay.d.y*sinAzi)+
248                                  photonRay.d.x*cosTheta;
249                              wi.y = sinTheta/sqrt(1-photonRay.d.z*photonRay.d.z)*
```

```
250                            (photonRay.d.y*photonRay.d.z*cosAzi+photonRay.d.x*sinAzi)+
251                            photonRay.d.y*cosTheta;
252                        wi.z = -sinTheta*cosAzi*sqrt(1-photonRay.d.z*photonRay.d.z)+
253                            photonRay.d.z*cosTheta;
254                    }
255                }
256
257                wi = Normalize(wi);
258                photonRay = RayDifferential(newIsect, wi);
259                Photon photon(photonRay.o, alpha, wi);
260
261                // Store only fluorescent photons
262                if ((!volumetricDone) && (fluorescent)) {
263                    volumetricPhotons.push_back(photon);
264
265                    // Store photon in volumetric photon map
266                    if (volumetricPhotons.size() == nVolumetricPhotons) {
267                        volumetricDone = true;
268                        nVolumetricPaths = (int)nshot;
269                        volumetricMap =
270                            new KdTree<Photon,
271                                PhotonProcess>(volumetricPhotons);
272                    }
273                    progress.Update();
274                }
275            }
276        }
277    }
278    BSDF::FreeAll();
279    }
280
281    progress.Done();
282 }
```

Listing 5.3: PBRT source code of photon mapping algorthm

For more details about source code please look into source code or PBRT Guide here [68].

6 The application of Monte Carlo simulation

Endoscopy is a medical procedure used to investigate the internal surfaces of an organ by inserting a special device into the body. The endoscope consists of a thin tube with fiber optics to transmit light. Illuminated structures are then viewed through an eyepiece or video camera fixed to the tube [80]. The example of the tip of the endoscope is presented below. Generally two light sources are available and small camera.
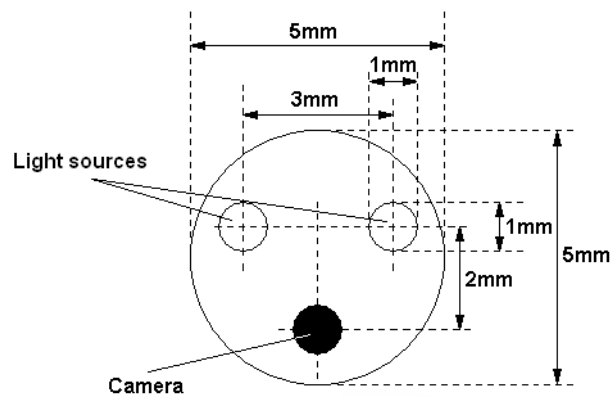
Figure 6.1: Schema presenting the head of endoscope - bottom-view. Parameters are similar to the real device and were used during simulations

The light sources can be treated as area lights with cone angle $\alpha = 45°$. Moreover the head of endoscope may be rotated. Angle β specifies the deviation from the completely perpendicular position with respect to tissue surface. In our case $\beta = 15°$.

The tool that was used in this work for generating images according to photon mapping algorithm was PBRT engine. This is not commercial computer program written in C++. PBRT is available with the source code and the book [68] that gives highly detailed description of most of the functions. Efficiency was not the goal of this software. It takes often minutes or even hours to render highly detailed and complex images. All tissue images in this paper were rendered about 40 minutes on AMD Sempron^{TM} 2.00 GHz with 512 MB RAM and AtiRadeon 9600 graphics card. Unfortunately PBRT does not support subsurface scattering model, but because of its simple plug-in architecture, the functionality could be extended. Photon mapping algorithm was changed and revised to implement full Monte Carlo model of Light Transport in turbid media.
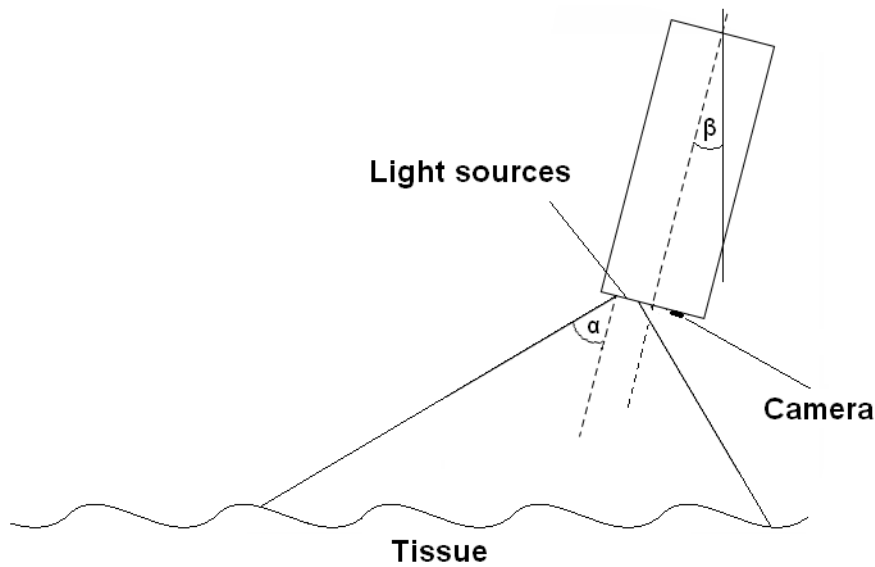
Figure 6.2: The head of endoscope during operation - side-view. Only first light source is visible, the second one is behind.

6.1   The comparison of surface and volumetric photon map

The first simulation was performed for completely flat tissue surface without any distortions. The tip of the endoscope was located 1cm above and perpendicular to the object $\beta = 0°$. For such configuration three kind of experiments were performed with the following setup parameters:

- number of photons collected in surface photon map - 50000 photons,
- number of photons collected in volumetric photon map - 50000 photons,
- only photons, which spectrum changed during interaction with fluorescent molecules were stored,
- number of lookup photons - 20 photons,
- maximal distance during photon lookup - 0.1cm,
- the number of steps during volumetric rendering - 5
- step size during volumetric rendering is not constant. It is a distance from intersection point to point 0.05cm below the tissue surface calculated along the ray and divided by step size.
- tissue parameters described in table 4.3.

Every time two different tone reproduction operators were investigated: maximum to white and contrast-based scale operators. The results are presented in Table 6.1.

For maximum to white operator surface photon maps works very well. The number of rendered photons is big enough to cover the whole illuminated region. If
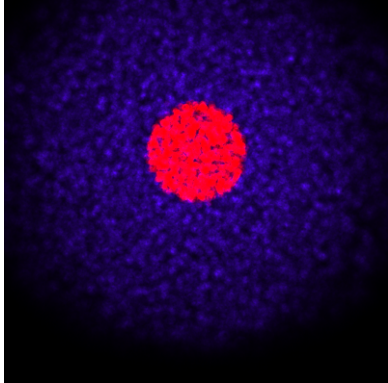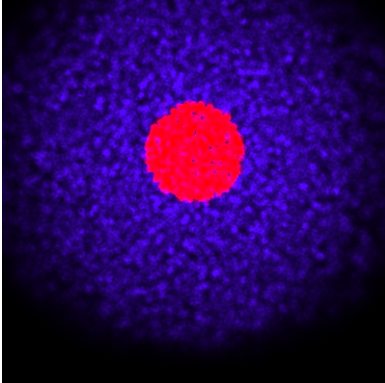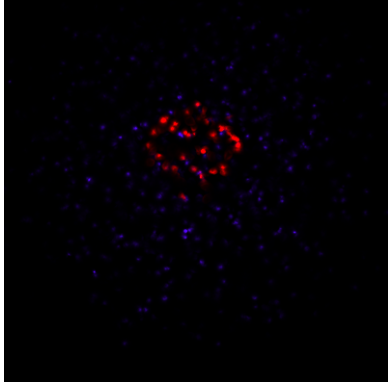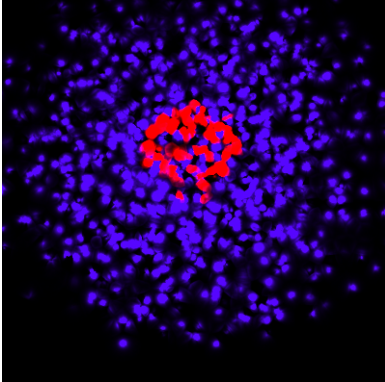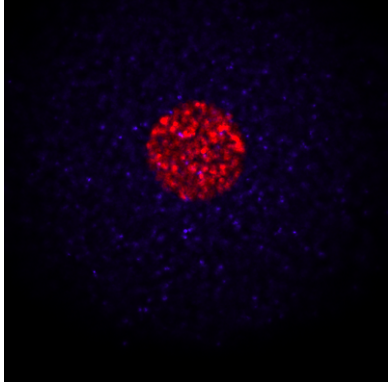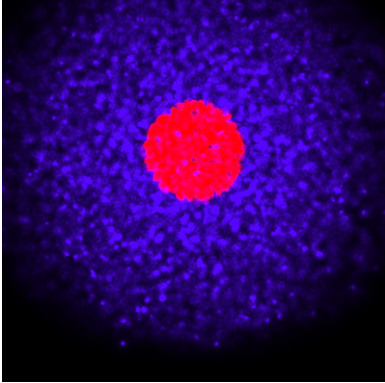
	Maximum to white operator	Contrast-based scale factor
Surface photon map	Time of rendering: 220s	Time of rendering: 222s
Volumetric photon map	Time of rendering: 314s	Time of rendering: 311s
Surface and volumetric photon map	Time of rendering: 460s	Time of rendering: 435s

Table 6.1: The comparison of surface and volumetric photon maps usage for different tone mappers

only volumetric photon map was utilized, the number of visible photons decreased drastically. This is because a couple of very bright photons make the rest of the pixels proportionally scaled, which results in dark image. This is the main disadvantage of using maximum to white operator for tone mapping procedure. Additionally, when both surface and volumetric photons map are rendered at the same time the similar behavior as in the previous case is noticeable. The image looks dark, since it is overwhelmed by very bright pixels in different places.

For contrast-based scale operator the situation is completely different. Using only surface photon map the image looks brighter and the contrast between collagen and protoporhyrin region is greater. Even when only volumetric photon map was used, the number of visible photons exceeds significantly the number of photons when maximum to white operator was used. Additionally all photons seems to have similar intensity. It is an expected result, since their weight only depends on the internal interactions in the tissue. When both photon maps are utilized at the same time, the increased number of photons are visible on the image. That was not a case for maximum to white operator. The image is still much brighter than in opposite situation. This consideration can imply that better images can be obtained when this operator is used.

Extending the usage of a surface photon map with volumetric map makes the time needed for rendering even two times greater. However the results obtained due to this effort are not impressing much. Both images looks very similar. This is why it was decided to use only surface photon map for further investigation. Volumetric photon map does not give any additional and useful information for the further investigation.

6.2   The analysis of the influence of light source spectrum

The next simulation was performed for the different light source spectrum. This time the quality of generated images is much better, since the number of photons was increased noticeably. Here are the parameters of the experiment:

- number of photons collected in surface photon map - 400000 photons,
- no photons collected in volumetric photon map,
- only photons, which spectrum changed during interaction with fluorescent molecules were stored,
- number of lookup photons - 350 photons,
- maximal distance during photon lookup - 0.1cm.
- tissue parameters described in table 4.3.

Very interesting effect was observed for the series of images 6.3a - 6.3e generated by laser beam. The peak spectrum of UV color light was moved from left to right. It is visible quite good that the collagen photons are the brightest at

the beginning, then constantly fade and their intensity is going down. The reason comes from the shape of collagen EEM - figure 4.5a. For lower excitation wavelengths the emission spectrum is higher, for higher excitation the emission energy is going down and it is almost zero in the figure 6.3e. Similar effect is noticeable for protoporphyrin photons, which intensity is low at the beginning and then increases with higher excitation spectrum range, but not so fast. This is also because of EEM of protoporphyrin - Figure 4.5e. The initial wave spectrum after contact with fluorescent molecule still possesses some amount of energy, even for higher wavelengths. When the collagen photons are almost invisible the protoporphyrin intensity is still big enough. It means that it is worth to find such a light source spectrum that reduces the impact of collagen fluorescence and increases the intensity of protoporphyrin. That is why the laser beam of wavelength equal to 400nm - figure 6.3e - shows visually the advantage of UV light source, since it concentrates only on one spectral wavelength and produces desired results.

Results presented in figure 6.3b and figure 6.3f can be also analyzed, although energy carried by the ideal, white light source is much greater than for the ultraviolet laser beam. Basing on figure 5.11, most of the white light energy is lost, since the EEM is defined only to maximal wavelength equal to 520nm. All other excitation wavelength are neglected. Even if those excitations were taken into account then for excitation wavelengths in range 600nm-750nm the emission spectrum is still nearly zero, so it does not influence the final intensity. The most interesting excitation range is in the beginning of the spectrum range. This part influence the final color to the greater extent. Collagen fluoresces mostly for UV color spectrum, it means that probably the best would be to apply light beam with wavelengths in range 360nm-420nm.

Looking again at figure 6.3b and figure 6.3f it is noticeable that the color of healthy part of tissue is different at these two pictures. In both situations it is bluish. One can say that for the case where the white light source was used the color of photons that contacted with collagen and protoporphyrin are to some degree similar - protoporphyrin photons are red and collagen photons are violet. This is because the white light source gives some energy to the whole spectral range and the laser beam only to some part of the spectrum. If a contrast perspective is considered, for ultraviolet laser beam the contrast between protoporphyrin and collagen is noticeable and the cancerous part of a tissue is better visible, despite of the low brightness of the whole image. However from the intensity point of view white light is more than better. Cancerous region of a tissue has the greatest intensity and dominates over weak collagen photons.

Interesting result was noticed for the mercury lamp - figure 6.5. Protporphyrin fluoresces in red color as it was expected, but the same color is visible also for collagen. This is because the spectrum of mercury lamp has very small values for ultraviolet wavelengths. It means that influence of the expected blue color
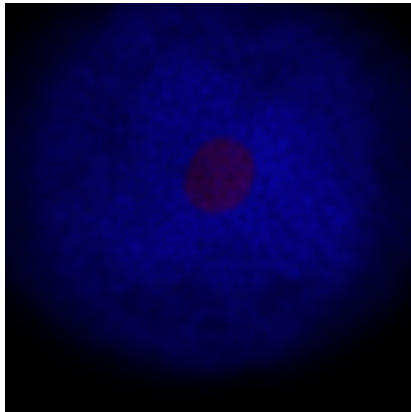
(a) The output for laser beam of 360nm. Initial photon energy equals to 50000 a.u.
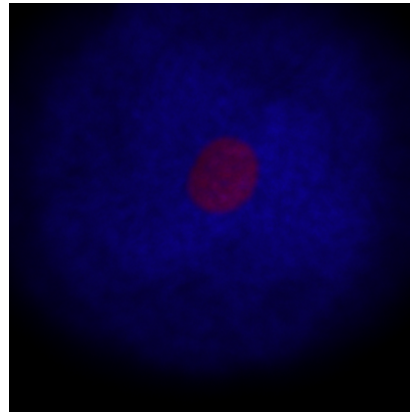
(b) The output for laser beam of 370nm. Initial photon energy equals to 50000 a.u.
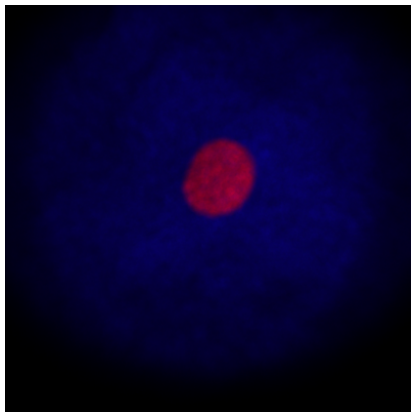
(c) The output for laser beam of 380nm. Initial photon energy equals to 50000 a.u.
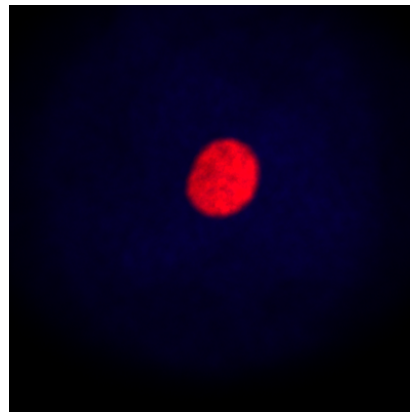
(d) The output for laser beam of 390nm. Initial photon energy equals to 50000 a.u.

(e) The output for laser beam of 400nm. Initial photon energy equals to 50000 a.u.
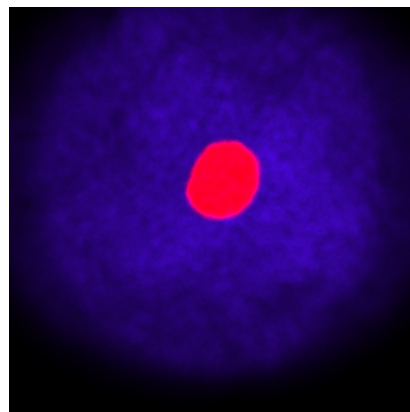
(f) The output for ideal light described in range 360-750nm. Initial photon energy equals to 50000 a.u. for every wavelength

Figure 6.3: Simulated human tissue for given excitation light.
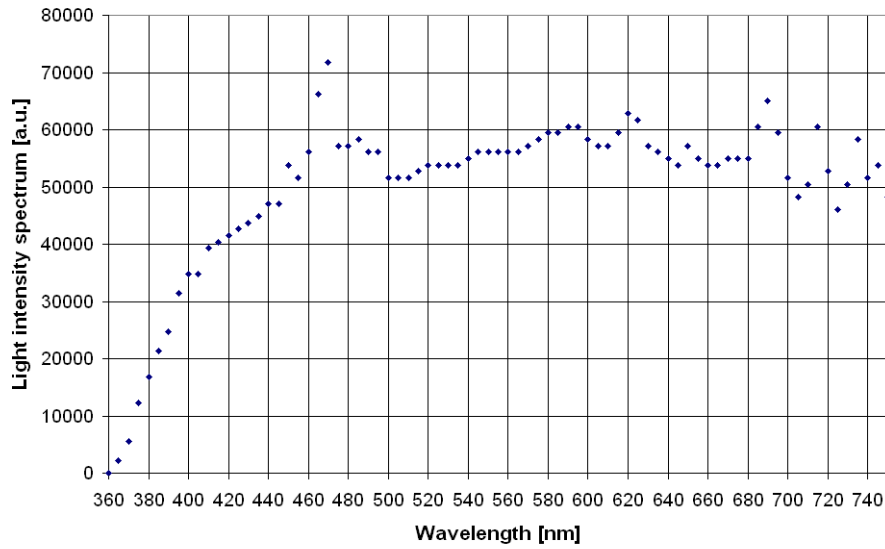
Figure 6.4: The spectrum of xenon lamp [81].

is reduced at the cost of very high red color peak in mercury light spectrum. That energy multiplied by emission values retrieved from EEM gives red color as a dominant part of the resulting spectrum. It implies that mercury lamp is not good enough to use during photodynamic diagnosis. The color similarity between protoporphyrin and collagen part of a tissue make it not recommended for medical usage.
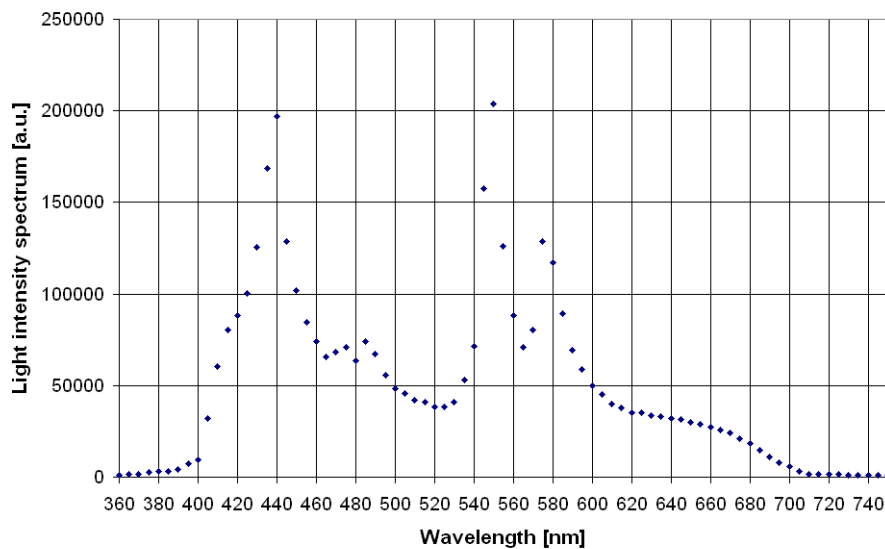
Figure 6.5: The spectrum of mercury lamp [82].

Finally for xenon light collagen photons seem to be pink instead of blue color. The reason of that effect is related with the shape of the spectrum. For UV wavelengths the function is going up, after that it stays at almost the same level

(a) The output image for mercury lamp

(b) The output image for xenon lamp
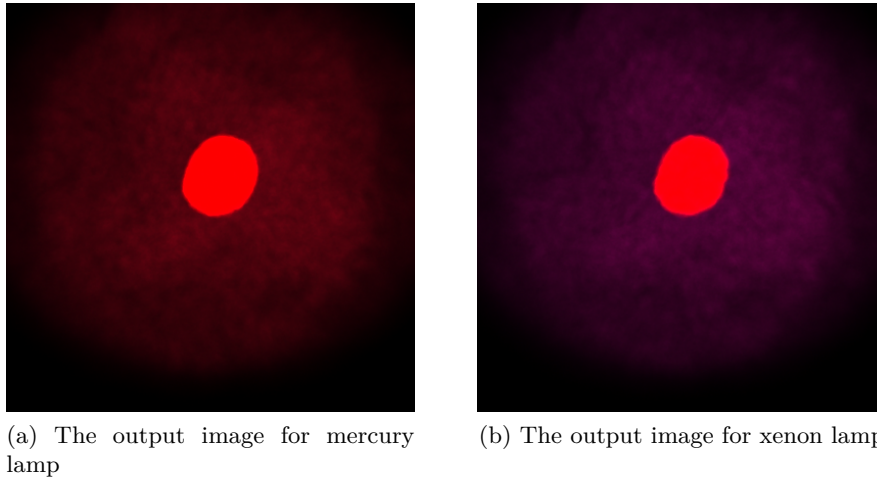
Figure 6.6: Simulated human tissue for mercury and xenon excitation light.

to the end of the range. The contribution of those constant values is very small due to the specific structure of collagen EEM. The most important is ultraviolet part, which despite of low values has significant role in the final appearance. This kind of light sources are widely used in endoscopes today.

6.3   The qualitative analysis of the influence of light source incidence angle

The simulation was performed for different light position. Cancerous regions, where protoporphyrin was concentrated (red color), give the most interesting information for medicine. It is necessary to identify such situations as quick as possible. The rest of structure contains collagen only (blue color). Applied light source was a laser beam with 380nm wavelength.

For this tissue model six images were rendered for different angle of view β every time. In order to obtain good looking results, the simulation was performed for the following configuration:

- number of photons collected in surface photon map - 400000 photons,
- no photons collected in volumetric photon map,
- only photons, which spectrum changed during interaction with fluorescent molecules were stored,
- number of lookup photons - 350 photons,
- maximal distance during photon lookup - 0.1cm.
- tissue parameters described in table 4.3.
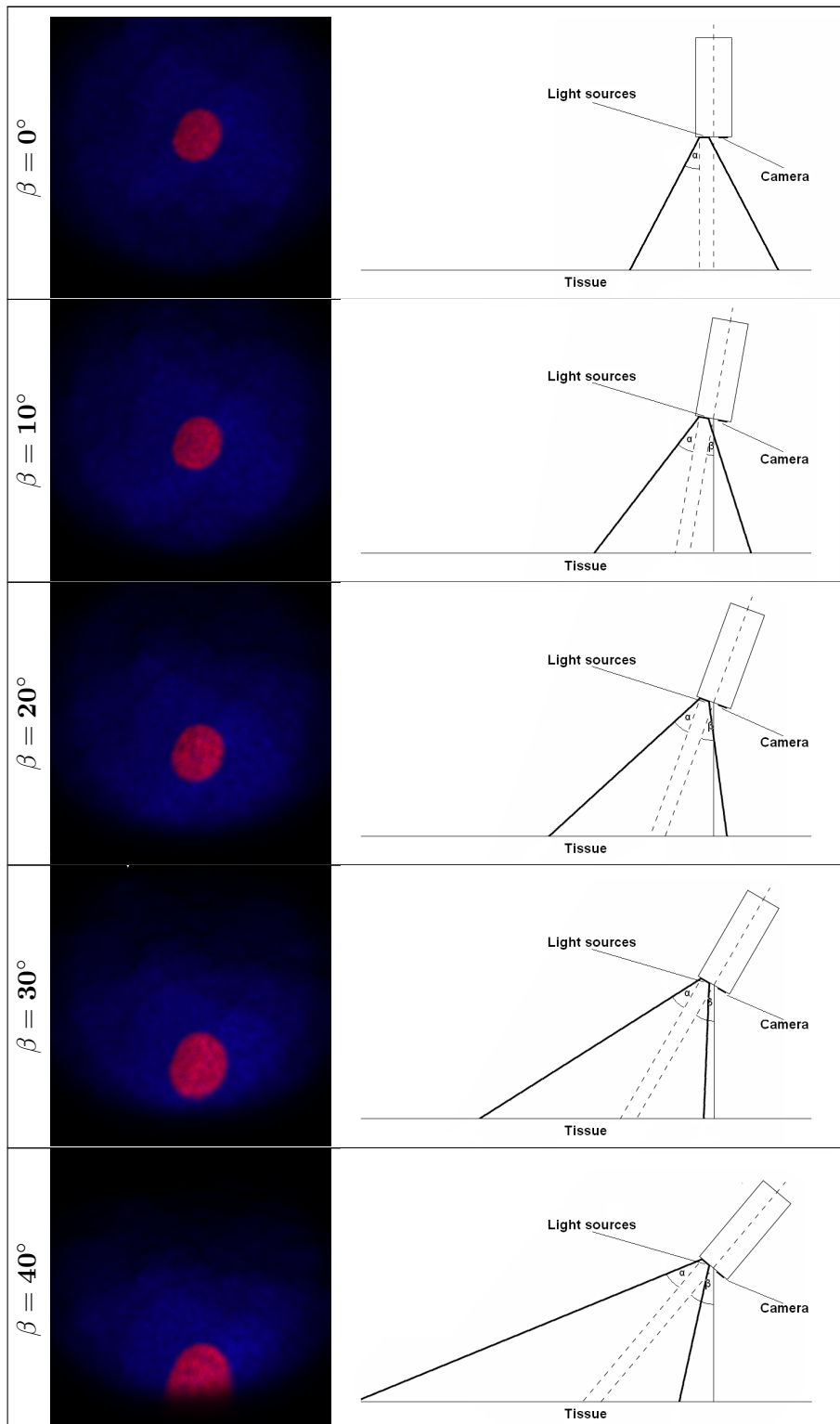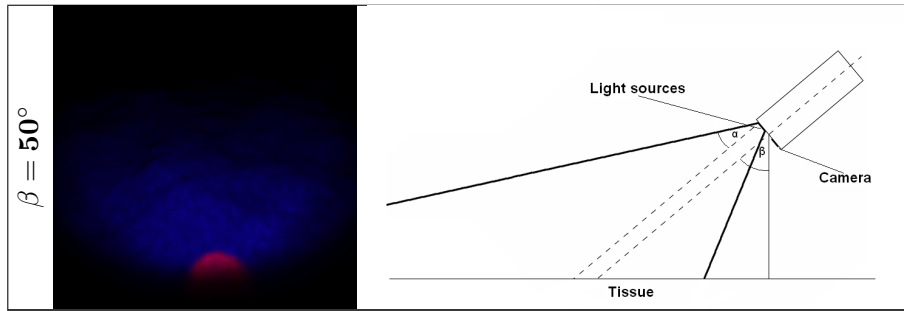
Table 6.2: Tissue surface for different camera angle of view β

Best quality images were obtained for β between $0°$ and $30°$. For larger angles images get darker and darker, what is especially visible on light borders. It means that the number of photon traced in the scene should be changed for different views of camera. That value cannot remain constant, otherwise the image is not clear and smooth any more. Looking at red part of all pictures, where cancerous structure was added and protoporhyrin concentrated, better results were obtained for angles $20°$ and $30°$. Its appearance is rather uniform and that structure is stronger illuminated. Quantitative analysis would give more accurate results, but even now it seems that the best angle of view is not $0°$. Simulations point out that for the best angle β, one should look somewhere else, probably around $20° - 30°$ interval. This is going to be the goal of other experiments.

In this publication [83], there was described how various angles of incidence influence surface and subsurface components of the reflection model. They presented a model for subsurface scattering in layered surfaces in terms of one-dimensional linear transport theory. The external appearance of a face and a cluster of leaves from experimental data describing their layer properties, were simulated. It also showed how volume or surface functions (BRDF and BTDF) change for different values of anisotropy and thickness of the layer.

6.4 The quantitative analysis of the influence of light source incidence angle

Although the light propagation in human tissue is rather good known topic described in literature, the quantitative analysis of its properties and influence of incident angle on absorption and scattering of photons need to be still investigated. Simulations in this paper are going to propose the best initial angle of light source, for witch energy reflected from the tissue to camera is the highest. It is necessary to stress that the parameters of simulation strongly influence the final result. For example for human colon tissue the outcome would be different.

In the scene containing - as previously - cancerous and healthy part 12 simulations were performed, each for different angle β. The influence of changing this angle is going to be investigated. In each case 400000 photons were stored in surface photon map. Both light sources are assumed to be UV area lights with cone angle $\alpha = 15°$ and white light source. The experiment started for $\beta = 0°$ and was changed by $5°$ every time. It was assumed that the tissue surface is completely flat, all distortions were neglected.

6.4.1 The influence of light source incidence angle on the number of emitted photons

In order to store 400000 photons in surface photon map, it was necessary to trace about 440000 photons in the scene. It does not matter whether photon is fluorescent or not, it is always put into photon map. It means that about 9% of them was absorbed by the tissue and after entering the structure, they never escaped. Figure 6.7 describes how many photons were needed to store exactly 0.4 million of photons on the surface for different incident angle β.
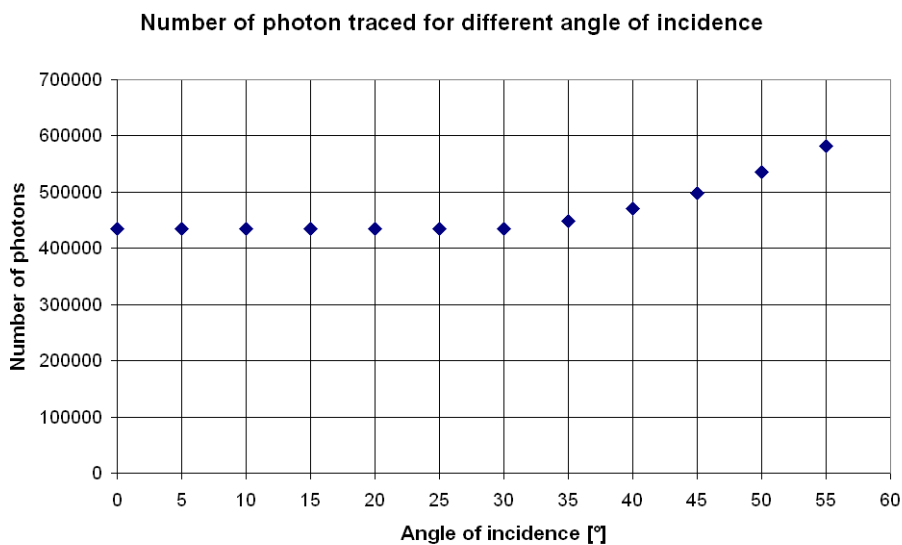
Figure 6.7: Number of photons vs. angle of incidence.

For angles between $\beta = 0°$ and $\beta = 30°$, the number of photons taking part in the simulation is more or less constant. When the angle exceeds $30°$, almost perfectly linear behavior is observed. The graph is going up, which means that greater number of photons is needed when the angle of view gets increased. For small angles the tissue absorbs energy of the light rays to the lower extent than for angels around $\beta = 50°$. For maximal angle of incidence photons are more often reflected without entering the tissue. The difference of number of photons needed in boundary cases, tends to even 37%.

6.4.2   The influence of light source incidence angle on the total energy of emitted photons

Next, energy of photons were investigated. Each photon traced from the light source has the same, constant energy. That energy changes during contact with tissue - the photon can be absorbed, scattered or its spectrum (energy) may be altered. In the end of simulation, the energy of each photon stored in the surface photon map was summed up, giving the total power. The following graph represents the overall energy of photons for different angle of camera in arbitrary units. There is no direct relation between power of photon used in the simulation and real physical quantities.

Total energy of photons for different angle of incidence
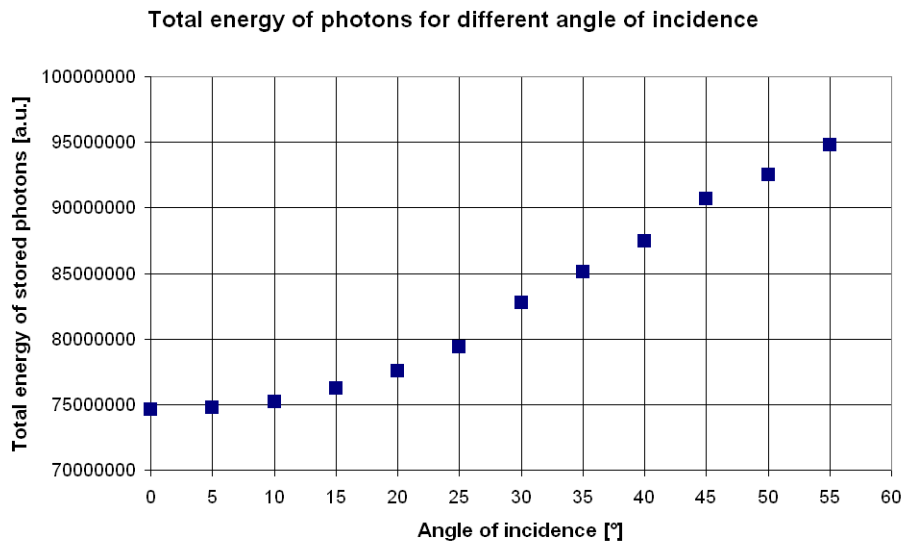
Figure 6.8: Total energy of photons vs. angle of incidence.

The investigation shows that the lowest energy was observed for angle $\beta = 0°$. It means that in such a situation packets of energy get involved into different interactions inside tissue more often than for other angles. They lose their power many times before they finally gets back to the tissue surface and escapes. It proves again that for small angles the absorption is a dominant factor. The situation changes when the angle of incidence is increased. The amount of energy is linearly rising, which means that tissue penetration is lower and the photons do not interact with other molecules so many times. It turned out that total energy for initial endoscope placement is about 21% smaller than for the final position.

If the total energy of photons stored in photons map is divided by the initial energy of all photons traced in the scene, a very interesting graph is produced - Fig. 6.9.

The investigation shows that for small angles the energy is rising and reaches its maximum value somewhere around $\beta = 30°$. The goal is to find the angle for which the total energy of all photons is the greatest and the absorption is the
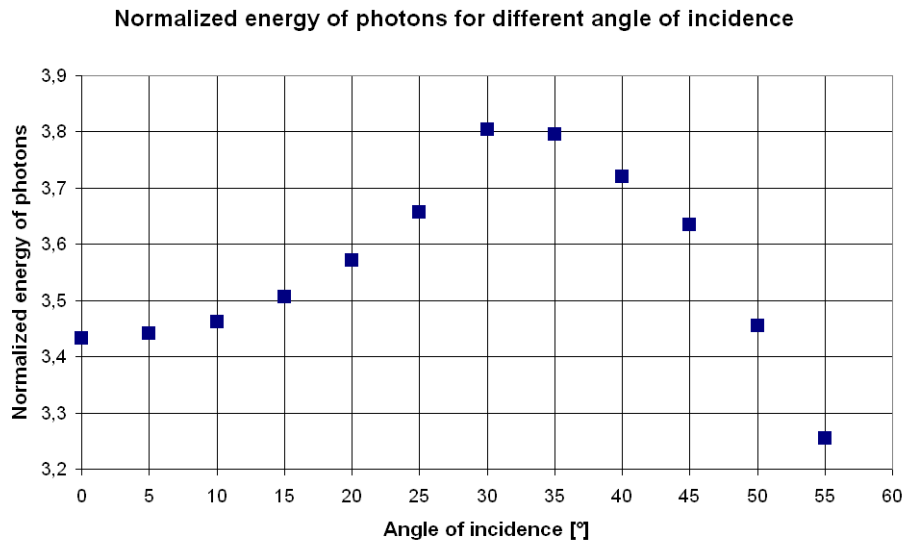
Figure 6.9: Normalized energy of photons vs. angle of incidence.

smallest. Probably angles around this value should be investigated more deeply during other experiments, but again, it will change if different tissue parameters would be applied. At this moment, it gives medicine the first hint about the most accurate angle of the head of endoscope in relation to tissue surface, for which pathological changes inside the structure are the best visible.

6.4.3   The investigation of the specular reflection effect

Another experiment was concentrated on the directions of all photons stored on the surface photon map. For each packet it was checked if it is visible on the camera screen. If it is true, then the angle between photon exitant vector and vector pointing from the packet to camera position was calculated. If that angle was not greater than 15°, that photon was assumed to play essential role in the image rendering process and marked as important. Their influence should be more noticeable, than contribution of photons pointing in other directions. The more packets that are "important" were stored in photon map, the better quality of the final image is going to be. Figure 6.10 shows how the number of photons, we are interested in, changed for different angles the endoscope is working.

The plot above can be treated as linear again. It is interesting that in the best case not even 6% of all the photons stored in the map, fulfill our criterion. For angle $\beta = 55°$ it is only about 3%. The function is decreasing, so the best looking images should be obtained for endoscope perpendicular position. But it is not necessarily true, because the investigation didn't take into account the energy of the photons. Probably some of them have proper exitant direction, but its energy is so small that they can be neglected. This simulation needs additional power related criterion in order to draw more accurate conclusions.
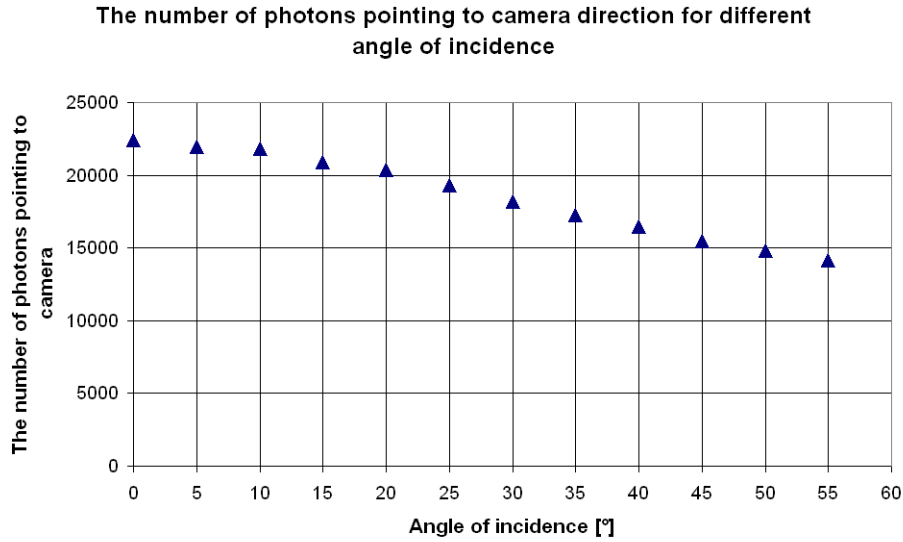
Figure 6.10: The number of photons pointing to camera vs. angle of incidence.

6.4.4   The estimation of the quantum yield

The quantum yield (ϕ)is a measure of the energetic efficiency of radiative process. In all light-dependent phenomenon it can be defined as the rate at which a desired event occurs to the number of photons that was absorbed during the process. In other words, a quantum yield is a measure of the efficiency describing the relation between absorbed light and production of a particular effect [84]. In our case this formula can be rewritten as:

$$\phi = \frac{number\ of\ fluorescent\ photons}{number\ of\ emitted\ photons}, \tag{6.1}$$

If all traced photons contacted the fluorescent molecule and were stored in the surface photon map, then this efficiency would be equal to 100%. However, this in not a case and 6.11 presents the results for different incident angle.

The obtained plot is constant in the beginning and then goes down quite linearly and have greatest efficiency value for $\beta = 0°$ equal to 77%. For $\beta = 55°$ the quantum yield reaches the value of 55%. These two boundary values suggest, that the greater the angle of incidence is the more photons get absorbed or reflected from the tissue and the fluorescence phenomenon occurrence frequency is smaller.

6.4.5   The estimation of the maximal penetration depth

In the next simulation for every photon the maximal penetration depth was registered. It didn't matter whether such particle escaped the tissue and was stored in photon map or not. Only their deepest possible position was important. In order to do that the tissue object was divided vertically into 0.001cm clusters
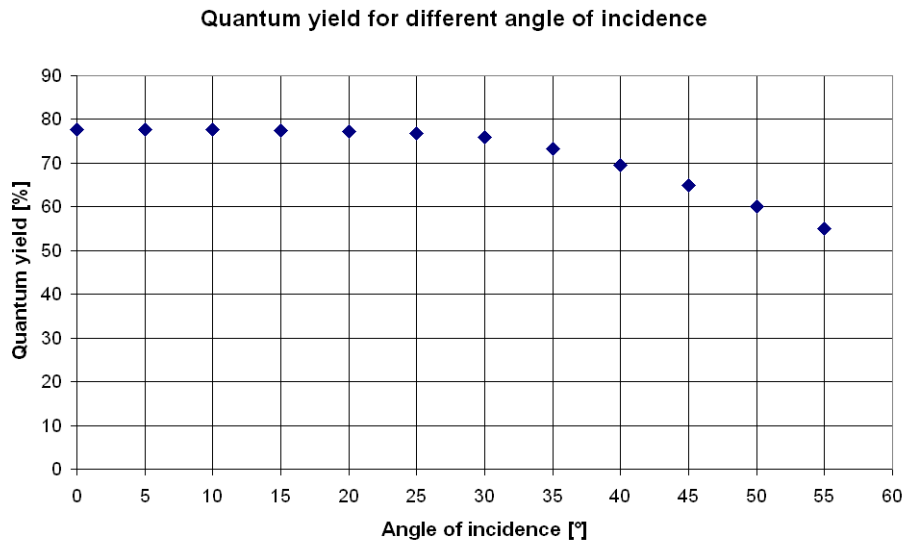
Figure 6.11: The quantum yield vs. angle of incidence.

initiated with zero as default. If the maximal penetration depth of a photon was found, then it was mapped to the appropriate interval and finally to cluster. Associated values got incremented and the whole array was presented in the form of graph 6.12.
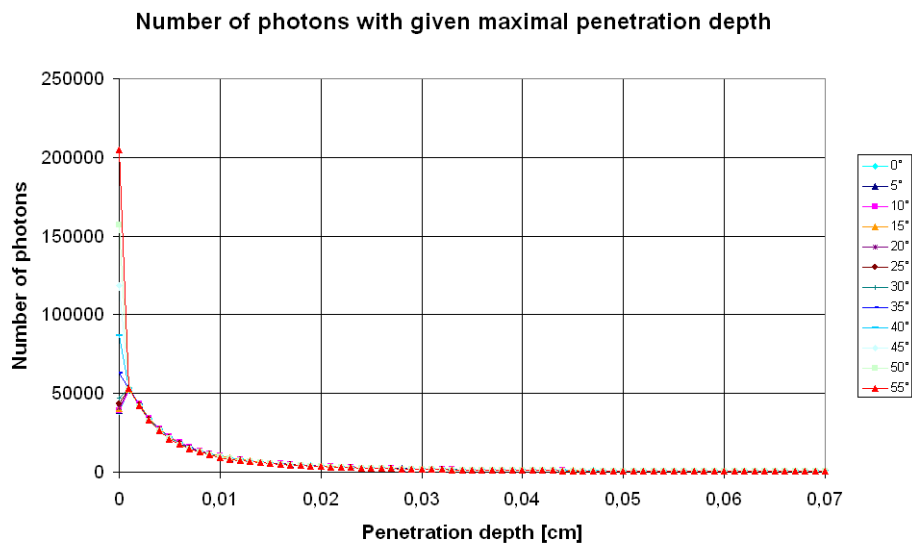
Figure 6.12: The overall number of photons with given maximal penetration depth vs. angle of incidence.

It is easy to notice that for low incident angle the plot is going up in the beginning and then falls down to reach negligible values for 0.07cm. It is important to stress it, that all plots for different incident angle are almost similar for depths greater than 0.002cm. The most interesting part happens just below the tissue

surface. It seems that for angles between $0° - 30°$ the number of photons that penetrated the tissue shallowly is smaller than for the neighboring clusters. They probably more often go down and are not reflected out the medium. This is why their maximal penetration depth is so low. It also means that more photons are going deeper and interacts with molecules inside more often. But because they get absorbed, their energy is also falling, so that they were not able to penetrates deeper.

For angles in interval $30° - 55°$ the inclination of the plot is so big that photons do not penetrate the tissue so often. They go inside, get scattered once or twice and finally get released out of the structure. This effect is dominant. The influence of photons that got deeper in the tissue is not so noticeable. Described phenomenon can be observed on the plots, where the number of photons is going down all the time and no extremum value is marked.
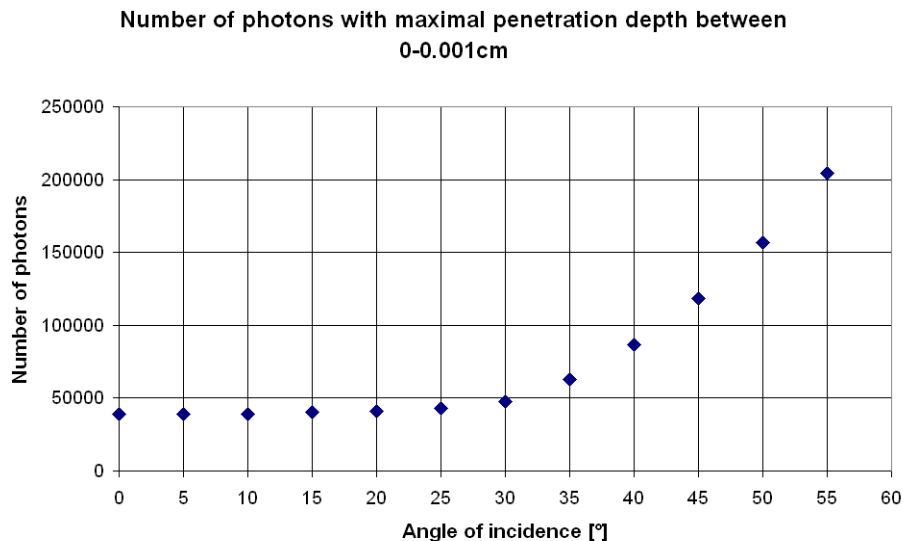
Figure 6.13: The overall number of photons with maximal penetration depth between 0-0.001mm vs. angle of incidence.

In order to prove the last concept the number of photons in the first cluster were compared for different angle of incidence - Figure 6.13. It can be noticed that the number of photons is going up quite linearly. Moreover, the value for $0°$ is five times smaller than for $55°$. It suggests that changing the angle of incidence, photons spend a shorter time below a tissue surface and more often are escaping the object. Some of them had probably no chance to interact with fluorescent molecule, which means that the desired fluoresce phenomenon can occur more rarely than for initial angles. This can be also confirmed by the quantum yield graph - Figure 6.11.

In the one but last simulation some work has been done to investigate what was the overall maximum depth the photon is able to go through. For each photon
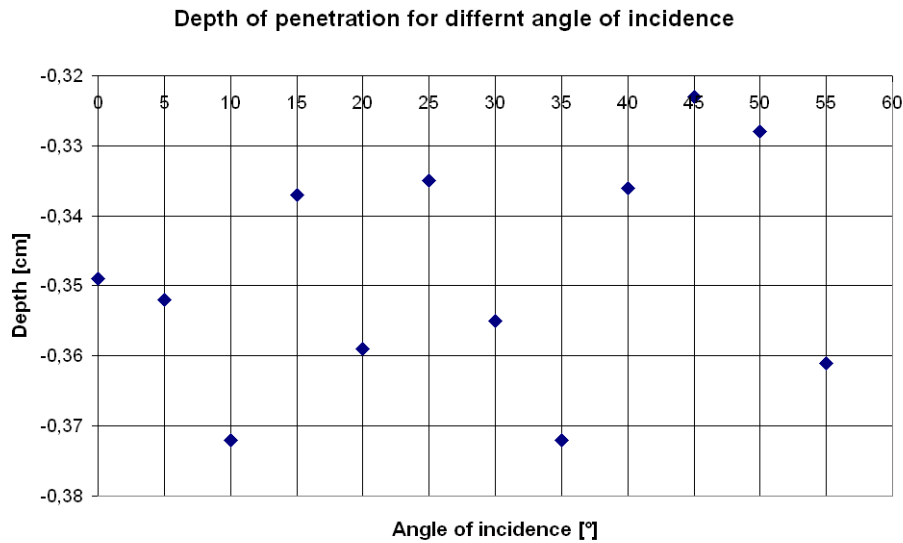
Figure 6.14: The overall maximal penetration depth vs. angle of incidence.

the deepest value was taken, but only the highest from all of them was drawn on the plot. Figure 6.14 describes how the maximal depth of penetration changes for different angle of view. Basically it does not change when increasing angle of incidence and remains at the constant level of about -0.35cm. In particular cases the values are greater or smaller from the mean depth, but no correlation could be observed with the initial angle. This is a simulation error, which would be smaller if the greater number of photons were traced. In such a case packets would be distributed in the tissue more evenly and not only one - as it is now - but many photons, would indicate the maximal depth the photon is able to enter.

6.4.6 The excitant angle investigation of photons stored in photon map

During last experiment for each photon stored in the photon map it's excitant vector was placed in the center of hemisphere. The hemisphere was divided into 3D bins: vertically into 10 bins - each equal to 9°, horizontally into 36 bins - each equal to 10°.

Each photon was then placed into one and only one bin in the hemisphere, appropriate for the exitant direction. The number of packets in every bin was counted and drawn in the polar coordinate system. First column represents vertical angles in range between $0° - 45°$, the second is for range between $45° - 90°$. Table 6.3 shows the distribution of exitant directions of photons in the tissue for different angle of incidence β. For $\beta = 0°$ each polar plot representing one vertical direction looks like a circle, what means that for light perpendicular direction, exitant vectors of all the photons are equally distributed. It proves that light propagation algorithm is not biased in any way.
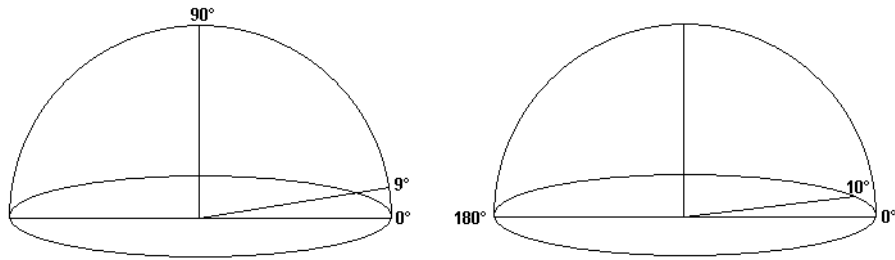
Figure 6.15: Division of the hemisphere into bins 9° wide vertically and 10° wide horizontally. Together 360 bins.

When the angle of incidence grows, small changes in the shape of each circle are observed. They gets ellipsoidal in shape and shifted along vector pointing 180°. It means that exitant photons are not directed towards the endoscope, but in completely opposite direction. However, those changes start for small vertical angles and after that other levels are affected. It means that distribution of angles above 45° remains almost unchanged for different light views. Their shape on the polar plot is only little ellipsoidal and the amplitude gets smaller. For the angle of incidence equal to 50° there are 2 bins containing more than 2000 photons pointing along horizontal 180° direction. These are photons with vertical angle around 20° and 30°. Then other ellipsoidal plots are visible with gradually smaller distortions in shape. It is needed to stress out, that the effect described above is observable for small view angles of light α only. The narrower the light beam is, the more noticeable this effect appears. Here the cone angle of light was defined as $\alpha = 45°$.
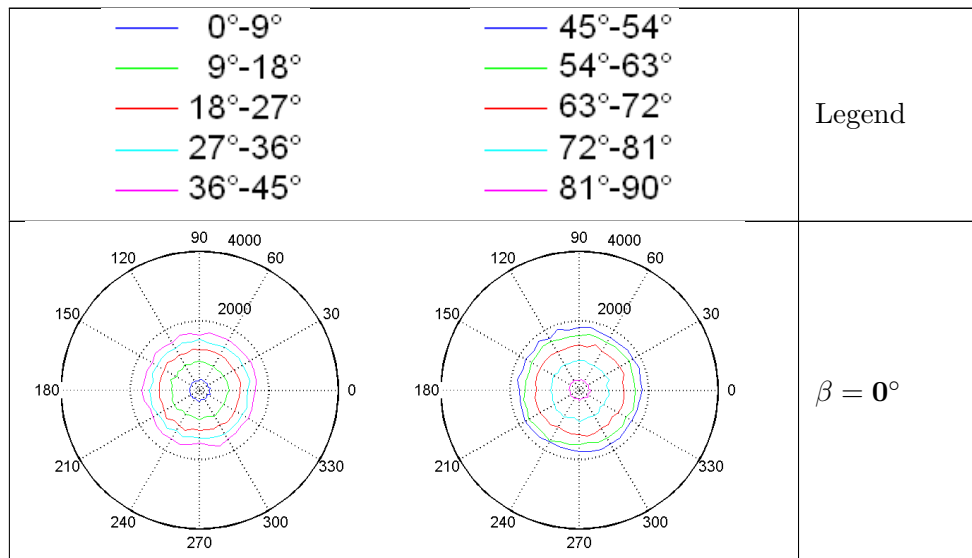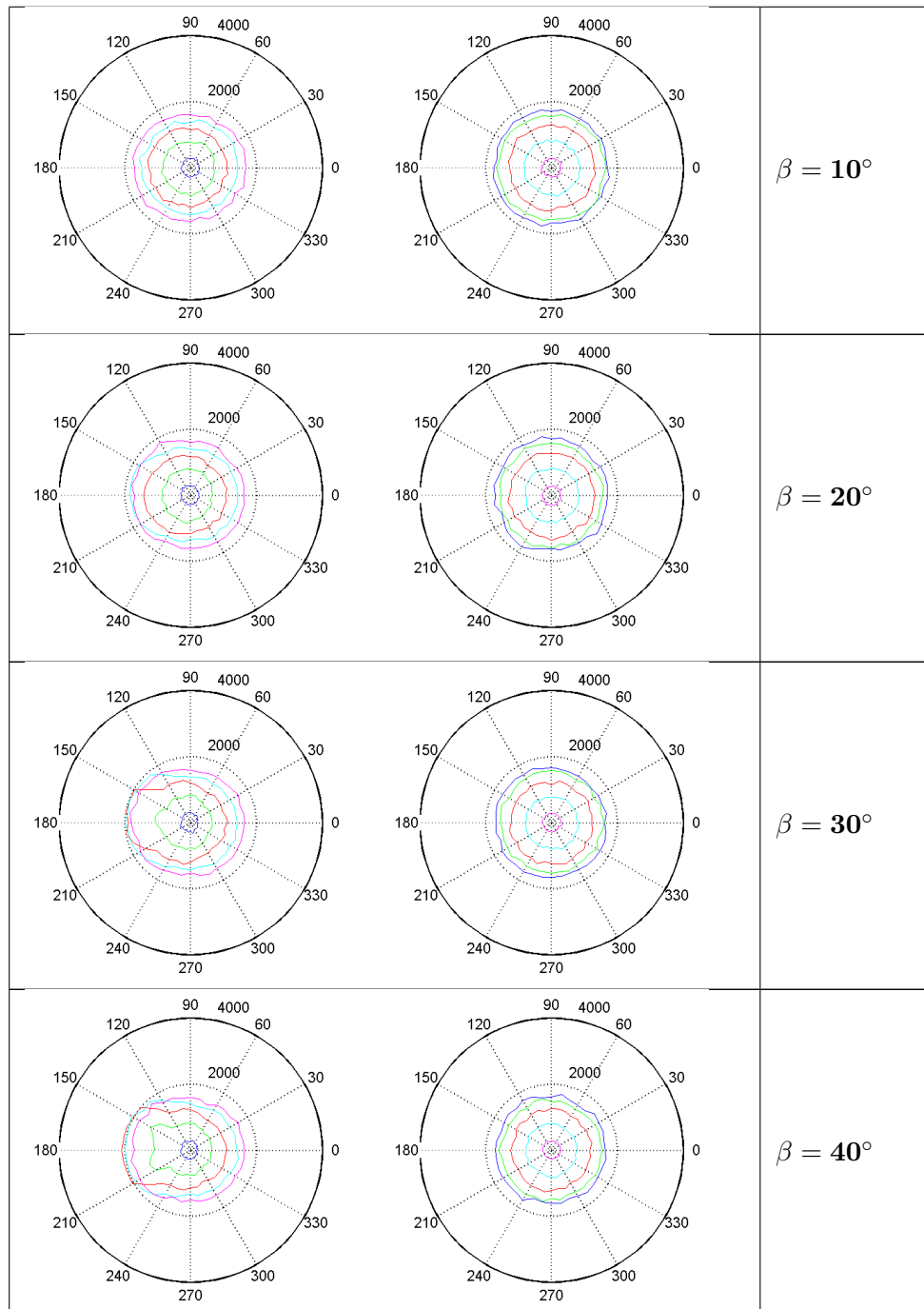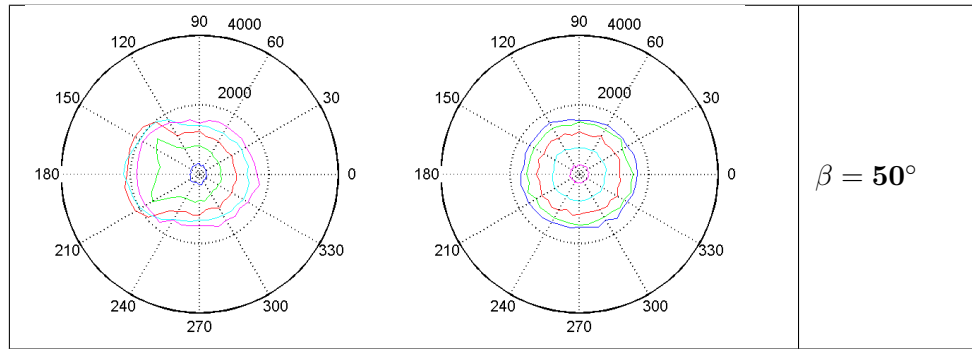
Table 6.3: The distribution of photon exitant directions

Monte Carlo simulations of light transport are widely described in literature. In [85] predictions and diffusion models for homogeneous media were compared in with properties characteristic of highly light-scattering tissues. Some graphs and sketches were described showing radiance in different directions (relative to the incident infinite beam) versus depth, depending on optical properties, influence of albedo and relative index of refraction. Additionally polar plots of radiance at different depths for a scattering medium were introduced.

6.4.7   Summary and conclusions

All of these experiments prove, that the tissue model and chosen algorithm of light transport in turbid media are mathematically correct and give expected results. Increasing the initial angle of incidence, more photons get absorbed and more of them are reflected from the tissue. The shape of graph representing total energy of photons vs. angle β, shows that this relation is also linear after $\beta = 30°$. However, the total illumination to the initial energy plot suggests that the maximal value of this ratio occurs for $\beta = 30°$. The tissue is better illuminated when the endoscope is not perpendicular to the surface, but is rotated by some angle. By isolating photons, that after exiting the tissue was directed to the camera location, it was noticed that their number also changes in linear way. It is also correct, once camera and light sources are in the same place, escaping photons should not point back in the direction they entered the object. Quantum yield, on the other hand, suggest that the fluorescence phenomenon occurs more often when the angle β is small. Analyzing the maximal depth the packets penetrated the tissue for different cases, it seems that it is constant as it was expected. However, further investigations that concentrated on the vertical profile i.e. the distribution of the deepest photons in the structure showed again, that for small angles photons penetrates the tissue deeper before they escape. For larger angles the probability of leaving the object is much higher.

All of those observations, give some idea about what is going on inside the tissue of a human skin. Consideration of the exitant vector distribution also gives interesting result. It proved that the number of photons having vertical angle greater than 45° does not change and is constant for different initial angle β. On the other hand, number of packets directed along 180° horizontally increased significantly. This quantitative analysis describes what is happening with photons contacting with human tissue. It also proposes the range of angles β for which the influence of photons on final image should be the highest. This conclusions should be now compared with generated images and probably verified with real images. But, even now a conclusion arises that the angle of incidence should be greater than 0°, since lots of photons get absorbed before escaping tissue for such a small angle. It also shouldn't be too big, because the effect of fluorescence happens more and more rarely.

Monte Carlo simulations for different geometry or optical parameters can provide very helpful qualitative as well as quantitative result for photodynamic therapy. The dependence between the emission angle of photons from the linear diffuser and mean radiance was described in [86] by simulating a cylinder hollow organ. Also fluence rate versus depth was recorded from tissue-simulating phantom. Obtained results were validated with real tissue phantom.

6.5 The analysis of multispectral images
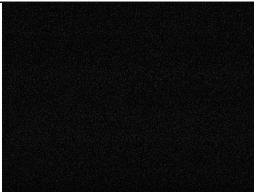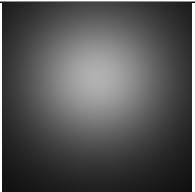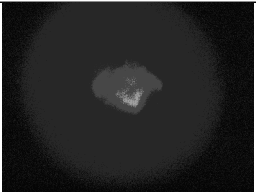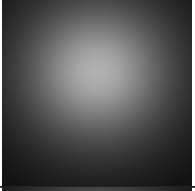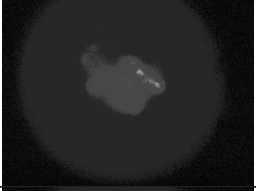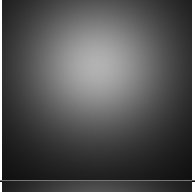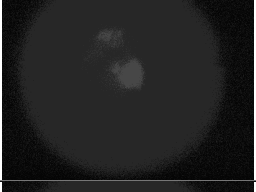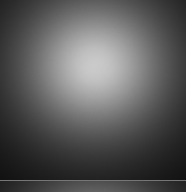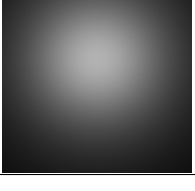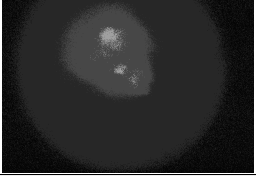
Images taken across the electromagnetic spectrum at different wavelengths are called multi-spectral. Special filters or instruments sensitive to the required wavelength, including ultra-violet or infrared light, are able to register only those data, that are necessary for the desired image component. They are represented by using gray-scale images. Multi-spectral images help to detect additional surface features and to capture information that are almost invisible for human eye. By combining the contribution of each image, it is possible to obtain the discrete color spectrum of each pixel.

This technique can be applied to identify cancerogeneus changes in the human skin. The physical deformation influences the structure of the tissue, so that it reflects light in different way. The optics of human skin was widely described in [12]. Different concentration and localization of absorbers and scatterers in human tissue results in various spectral reflectance. Skin without those substances appears diffusely white, because many skin components have dimensions larger than the wavelengths of visible light. The color depends also on the skin illumination i.e. the position and incident angle of the light rays. Changes in tissue structure caused by tumor activities, can be recognized thanks to fluorescent properties of substances the human skin is made of. Multi-spectral images help to understand how the investigated area looks like in different wavelength, which one is the best

to study deeper and which one gives the information that could be useful in case of photodynamic diagnosis. Each image contains data, that wouldn't be visible with normal camera.

6.5.1   Multispectral images of skin tissue with cancer

Thanks to cooperation with Medical University of Silesia and the Center of Diagnostics and Laser Therapy of Tumors in Bytom, patients suffering from different skin cancers could be investigated. As the result of medical treatment a widely used photosensitizer in photodynamic diagnosis - endo-protoporphyrin IX - was collected in diseased cells. A multi-spectral camera took images for wavelengths in range 400-720nm and constant step size 16nm when white light source was applied. For this reason the Onco-LIFE OLCC from Xillix Technologies was used. To this tissue sample there was assigned a signature 15674/1. Those images were further compared with simulated multi-spectral images of simplified tissue model. It assumes, that tissue consist of only one fluorophore - Protoporphyrin IX. The simulated skin color was an average spectrum of analyzed human skin. The results of comparison are presented in table 6.4.
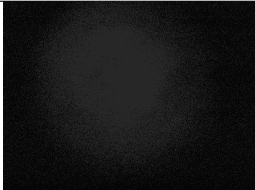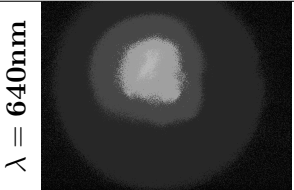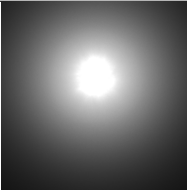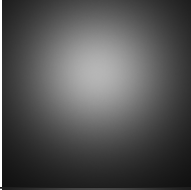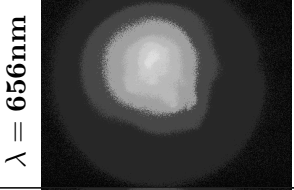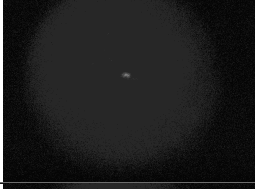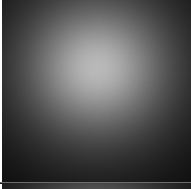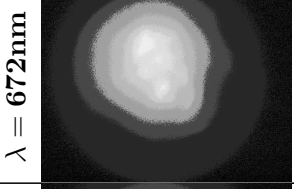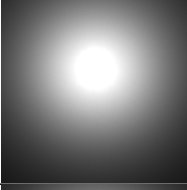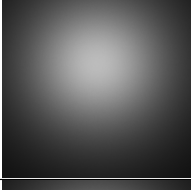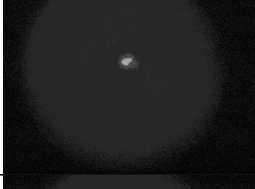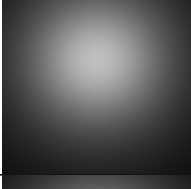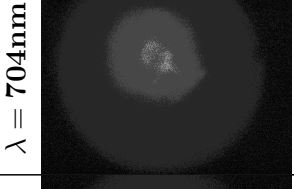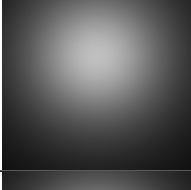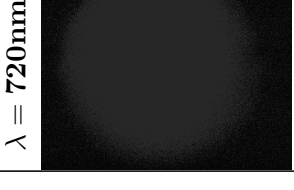
Table 6.4: The comparison of multi-spectral images of skin tissue (15674/1) and simulated protoporphyrin IX for different wavelength λ

It is quite good visible that changes in real multi-spectral images are followed by the simulation. Despite of the fact that slight errors are visible, generally the

presented model behaves well and changes in the intensity are followed by the simulated image. For 624nm the cancerous changes started to be visible and then two peaks are observable - first for 624nm and second for 672nm. Both maxima follow the characteristic of Protoporphyrin IX reflectance spectrum - see figure 6.18. The multi-spectral images don't show a good contrast between cancerous and healthy parts of a tissue. This is because the difference in intensities is too small in comparison to simulated fluorophore. One can say that consecutive intensity changes in multi-spectral images for real and simulated tissue are perceived as similar.

It was also tried to create a color image from a set of multi-spectral images. There is a couple of problems that occurred during processing:

1. All multi-spectral images were acquired manually. It means that an endoscope was held in somebody's hand while taking all 21 photographs. It results in images shifted with respect to other images, so that they do not overlap each other. It can happen that pixel position in first image does not correspond to the same position in another image. Although these inconsistencies are well visible, it was decided to neglect them, since the color information will not change noticeably.

2. Multi-spectral images of some tissue samples were already normalized. This is a problem since the information regarding intensity for each wavelength was compressed. Generally, most of the images used in other experiments were non-normalized and the information was not lost.

3. In order to make those images any better and to be able to compare them in a reasonable way with simulated images, a contrast tone mapper was applied. In such a way all multi-spectral images have some kind of a baseline.

4. Additionally a mapping was necessary to properly transform gray-scale images into color picture. The three-receptor model of color perception that maps any input spectra to tristimulus values (RGB) can be calculated in the following way:

$$R = \int_\lambda S(\lambda)X(\lambda)d\lambda \approx \sum_{i=1}^{n} X_i S_i,$$
$$G = \int_\lambda S(\lambda)Y(\lambda)d\lambda \approx \sum_{i=1}^{n} Y_i S_i, \qquad (6.2)$$
$$B = \int_\lambda S(\lambda)Z(\lambda)d\lambda \approx \sum_{i=1}^{n} Z_i S_i,$$

where:
n - number of samples,
$S(\lambda)$ - input spectrum,
$X(\lambda), Y(\lambda), Z(\lambda)$ - spectral matching curves, which determined by the Com-
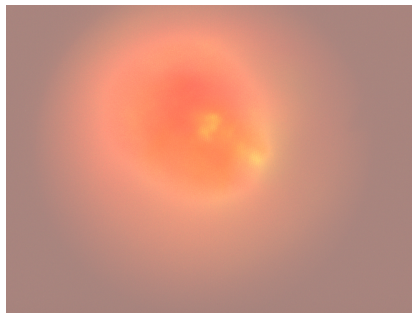
(a) Color image generated from multispectral images
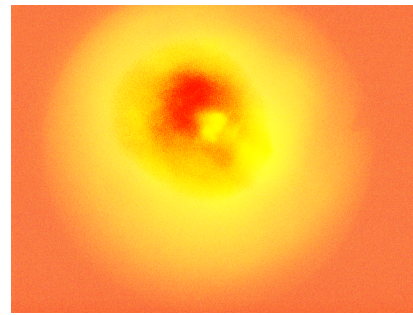
(b) Color image generated from multispectral images with enhanced contrast

(c) Monte Carlo simulated image
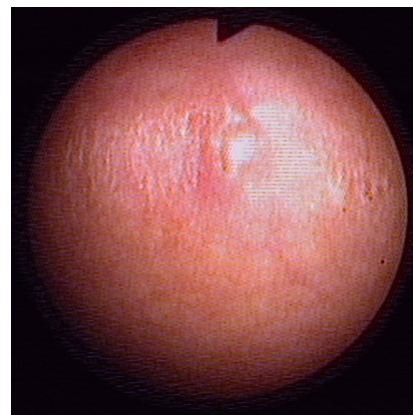
(d) Original image

Figure 6.16: Color images of real and simulated human skin tissue. Red color indicates Protoporphyrin IX.

mission Internationale l'Eclairage (CIE), describe the color sensitivity of human optics.

The input spectra is defined in the wavelength between 400nm-720nm with step 16nm. However, the simulation system is working on spectras defined in range 360nm-750nm and 5nm stepsize. Such discrepancy is the source of additional errors, since it is necessary to perform a mapping from input to system spectra in the beginning. Fortunately, this kind of inaccuracy does not have a big influence on final colored image.

Generated images are presented in figure 6.16. The image obtained from multispectral images does not look like the real image. Some important data is missing when taking images of given wavelength and stepsize. The original picture cannot be reconstructed any more. The red area in the middle was recognized by experts as cancer. It is not well visible, so in order to see it better an another image

(a) Spectrum from the multi-spectral
images

(b) Spectrum from the spectrometer
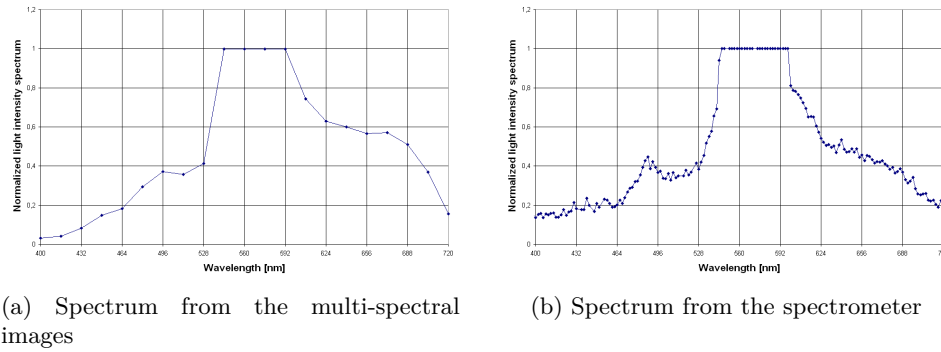
Figure 6.17: Comparison of two method for obtaining light spectrum

was created with increased the image contrast. Now, it can be compared with
simulated image, generated using Monte Carlo technique. In terms of color simi-
larity, the diseased regions show good agreement. Only the intensity is probably
different, but it is not a problem at all, since color is the most interesting part
of the experiment and the brightness of a light source could be adjusted in the
simulation environment.

6.5.2   The comparison of methods for obtaining the reflectance spec-
trum

By obtaining multi-spectral images for 21 different wavelengths, ranging from
400nm to 720nm with 16nm step it is possible to draw a plot representing spec-
trum of a given pixel. Images were not normalized, it means that the intensity of a
color directly represents a spectral radiance at a particular point. The choice of a
pixel is important as long as the tissue surface is not smooth. In the center of the
picture the grey value of 10x10 points were summed up and averaged giving the
intensity of a described region. In such a way the whole reflectance spectrum at
the investigated area was obtained. This method was verified with data obtained
from the spectrometer. As the spectrum normalization method "maximal value
normalization" was chosen - see 7.3.

It can be clearly seen on figure 6.17 that both graphs show rather good cor-
relation with each other. Data from spectrometer were sampled with greater
frequency. This is why some information is missing in multi-spectral images ap-
proach. The smaller peak at 488nm wavelength is well visible at the graph from
spectrometer, while on the other one, where the resolution is much lower, only
slight slope changes were observed. However, the region of saturation is almost
perfectly covered. It starts in both cases at 544nm and ends at 592nm for spec-
trum 6.17a and 596nm for spectrum 6.17b. Finally, plots are going down and
the value of spectral irradiance at 720nm wavelength was equal to 0,15. Such a
good agreement between graphs made it possible to use multi-spectral images in

further analysis.

6.5.3 The comparison of human tissue with BCC

Basal Cell Cancer (BCC) is one of the most popular skin cancer. The sick rate seems to show the relationship with the level of pigmentation. This is why Ultra Violet Radiation (UVR) is the most common reason for BCC in all people races. Also scars, ulcers, immunosuppression and genetic disorders are possible risk factors for BCC occurrence. Most patients are elderly with similar clinical symptoms. Single, translucent nodules with ulceration in the center are in many cases difficult to diagnose, especially when BCC occurs in color of the skin. Investigations showed that 89% of all cases were aligned on the head and neck regions. Mean survival rate for metastatic BCC is between 8 months and 3.6 years [87]

As the next task the multi-spectral images from patients with skin cancer were gathered and compared (see table 6.5). Images for the other patients look very similar.

	BCC	Healthy		BCC	Healthy
$\lambda = 400\text{nm}$			$\lambda = 576\text{nm}$		
$\lambda = 416\text{nm}$			$\lambda = 592\text{nm}$		
$\lambda = 432\text{nm}$			$\lambda = 608\text{nm}$		
$\lambda = 448\text{nm}$			$\lambda = 624\text{nm}$		
$\lambda = 464\text{nm}$			$\lambda = 640\text{nm}$		
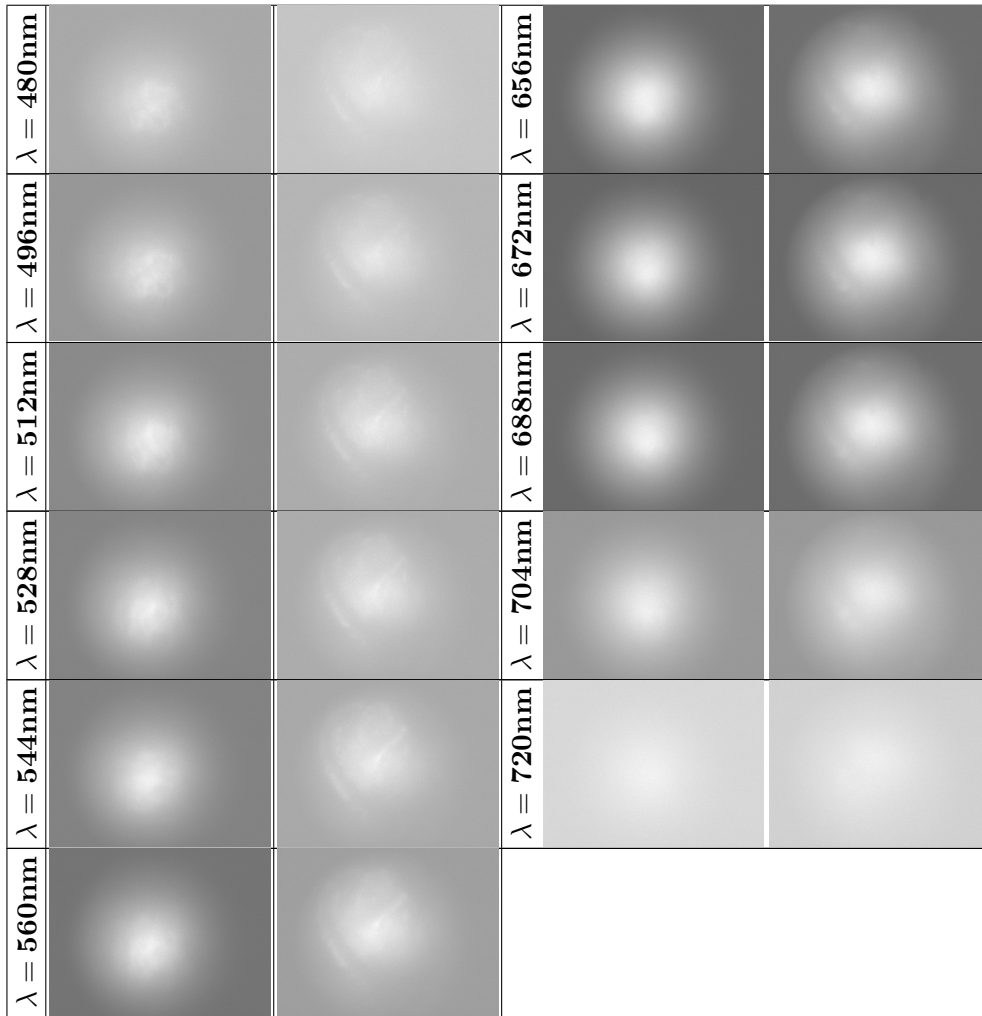
Table 6.5: Multi-spectral images of cheek skin for a white light

In each case 21 grey scale photos were taken for wavelengths between 400nm and 720nm with step equal to 16nm. The luminance value can be treated as an intensity. All images were non-normalized, which means that they were provided as they are and without any changes. It guarantees that any important information wasn't lost during some preprocessing operations. In order to print them on the paper, the contrast of separate images was enhanced. Otherwise they would look totally black. Raw data is useful to analyze the content of pictures, but because of lack of normalization, they cannot be viewed in popular image viewers. When comparing columns from table 6.5, they look very similar. It is difficult to distinguish healthy and cancerous changes by human. This is why more complicated apparatus is needed that will help in diagnosis.

The reflectance spectrum can be created by choosing a point on multi-spectral images and calculating its intensity. As the spectrum normalization method "normalization by maximum possible value" was chosen - see 7.3.

	Patient 1	Patient 2
Tissue with Bcc		
Healthy tissue		
Spectrum difference		
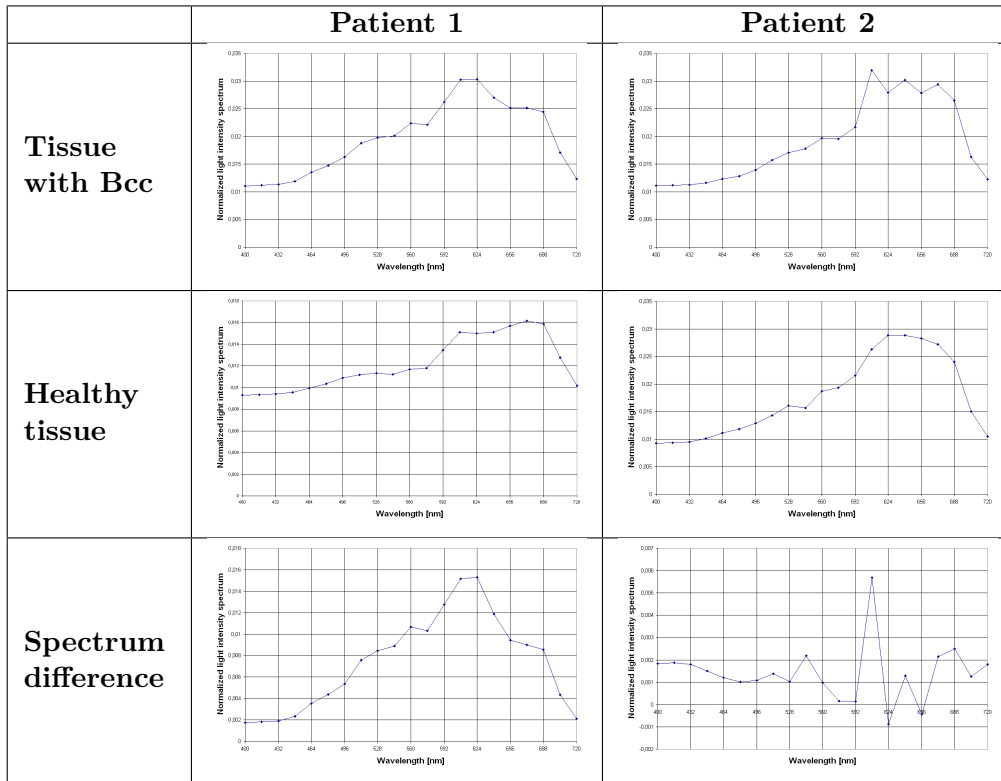
Table 6.6: Light spectrum obtained from multi-spectral images

The comparison of obtained graphs for two different patients with Basal Cell Cancer is presented in table 6.6. It is remarkable for both patients that for BCC spectrum a high peak at 624nm is visible. This way diseased and healthy tissue can be distinguished. After subtracting both spectras from each other the graph showing only differences occurs. It worth to mention that for patient 1 changes are closely related to morphological cancer deformations in tissue and with spectrum of protoporphyrin IX. Data obtained after spectrum subtraction for patient 2 are not of good quality. However they again show that thanks to fluorescent properties of tissue, cancer can be recognized by excessive intensity around 624nm.

This method is not very accurate. For carefully selected samples and pixels in the image, this kind of comparison can be done. Most of the time it is not that easy ad does not bring any reasonable conclusions.

6.5.4 The visualization of human tissue with BCC

Monte Carlo simulation utilizing photons penetrating human skin combined with healthy tissue spectrum is going to display the predicted appearance of analyzed

area. The process of rendering was performed basing on reflectance spectrum of normal skin - signature 13952/2 and 13952/10. Tissue surface was modeled using photon mapping as a flat semi-infinite plane with random distortions making it more realistic. In the middle of the tissue surface a small structure containing highly fluorescent substance - protoporphyrin IX - was injected to simulate the reflectance spectrum of a cancer. Obtained results are presented on table 6.7. The spectrum of cancer was calculated for one of the chosen red pixels. As the spectrum normalization method "maximal value normalization" was chosen - see 7.3.
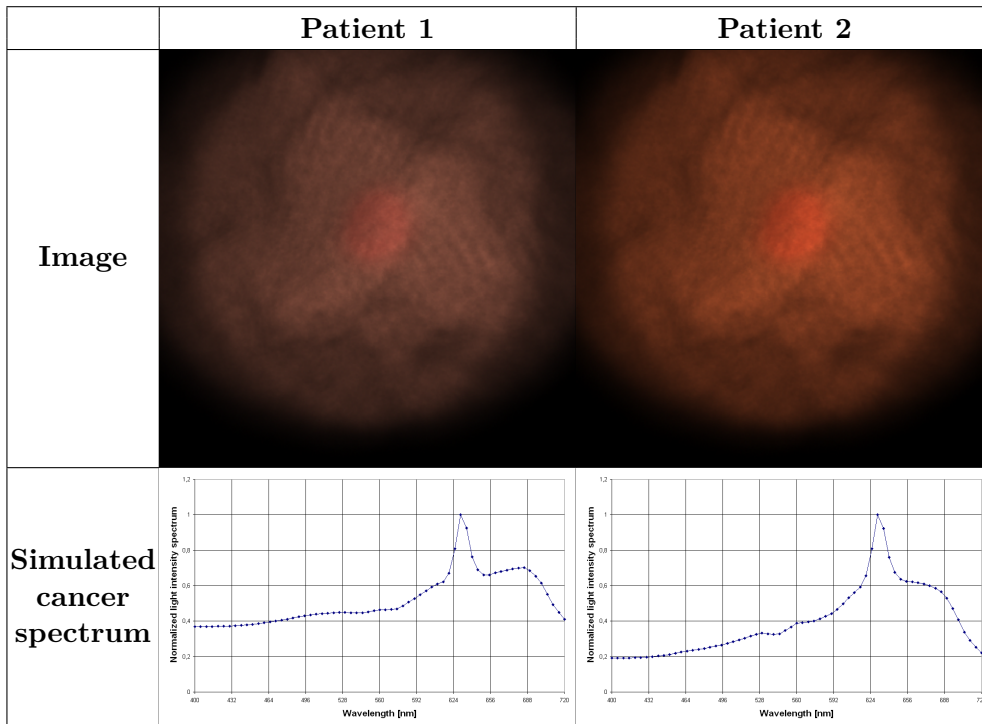
Table 6.7: Image rendering of tissue with BCC for 2 patients - 13952/2 and 13952/10

Depending on how much light is reflected from the tissue, the area of highest light intensity has different size. This effect causes that the details of a surface are missing and only illumination is visible. The color of the skin for both patients differs as well. As long as spectrum is calculated from multi-spectral images it is not ideal. For patient 1 the color of a tissue is similar to that of a skin, but for the second one it is closer to orange color. Actually it is not a problem, because the peak effect in the reflectance spectrum is still observable.

The results of simulation can be compared with multi-spectral images obtained for real tissues (see table 6.6). They are in good agreement with each other and the influence of fluorophores are meaningful for final image appearance. In both cases the spectral highest value can be observed somewhere around

wavelength equal to 624nm. Other differences between original and rendered images are coming from the morphological changes caused by a tumor and cannot be simply considered in the tissue model.

6.5.5 The fluorophore spectrum analysis

Additionally the spectrum of the only fluorophore was extracted from the image after illuminating with white light source (see Figure 6.18). It has an important property that the spectrum value for wavelengths less than about 590nm is equal to zero. Then it goes to its maximum and after that it remains at almost constant level around red color. Its influence is clearly observable on the simulated cancer spectrum in Table 6.7. Having this shape well defined it is important now to find other absorbers that influence the human skin reflectance spectrum. The complete model would improve the analysis, but even now it is very useful and shows the potential of multi-spectral images.
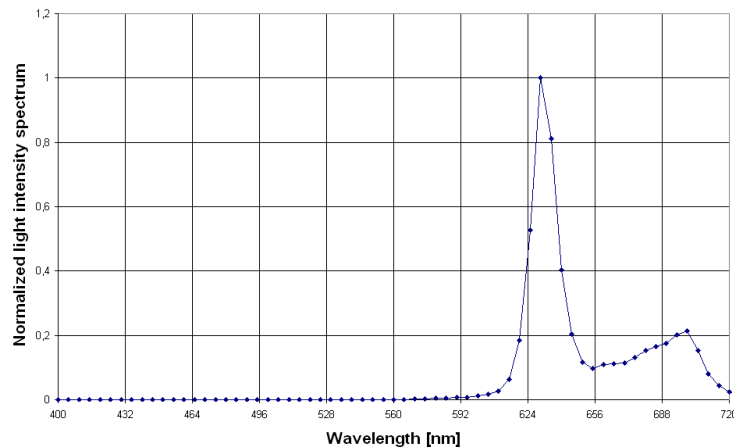
Figure 6.18: The spectrum of protoporphyrin IX obtained for white light.

6.5.6 The influence of endoscope position on the reflectance spectrum

Having a tool for obtaining reflectance spectrum of a given area, a set of multi-spectral images was taken for human healthy wrist tissue. Experiment was performed for three different situations. The camera is mounted, as usual, just below the light source and they always point in the same direction. First, both devices were placed perpendicularly to the surface and 1mm away from the skin. Then the position of endoscope was moved 5mm away from the object without changing its direction. Finally, the incident angle was set to 45°, but this time the position remained unchanged. In each situation multi-spectral images were taken and the comparison of resulting averaged spectra for the whole image, were presented on
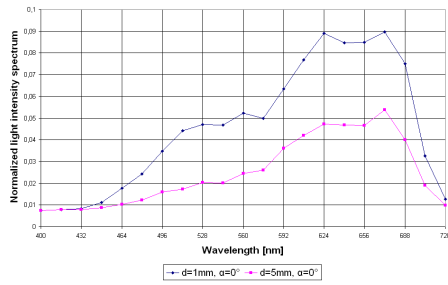
(a) Reflectance   spectrum   for   various distance *d*
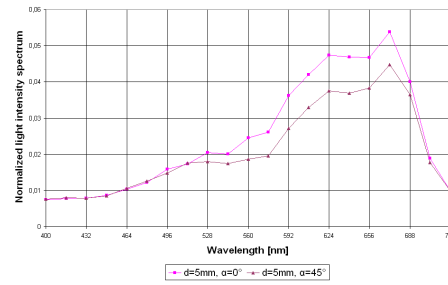
(b) Reflectance   spectrum   for   various incident angle α

Figure 6.19: Reflectance spectrum of human skin tissue for various light source settings
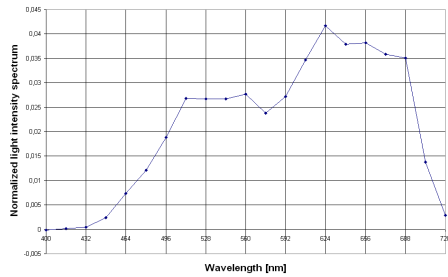
(a) Spectral difference of spectra obtained for various distance *d*
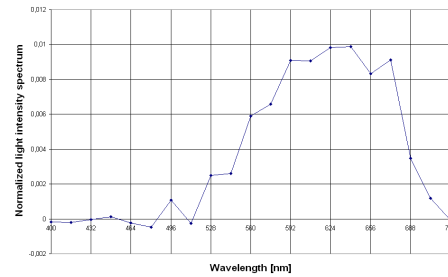
(b) Spectral difference of spectra obtained for various incident angle α

Figure 6.20: Spectral difference of spectra obtained for human skin tissue and various light source settings

figure 6.19 and figure 6.20. As the spectrum normalization method "normalization by maximum possible value" was chosen - see 7.3.

The first graph shows human skin reflectance spectrum for light source 1mm and 5mm away from the surface. It can be observed that for wavelengths between 500nm and 600nm plots differ by constant value. The same was noticed for range 600nm and 700nm, but this time the difference was grater. It means, that moving away the light source from the investigated tissue surface, the changes in the reflectance spectrum do not occur linearly, but are strongly wavelength dependent. It pays attention to the fact that probably there are 2 dominant absorbers in the human skin, which attenuate the light intensity in a different way.

Another observation was made for reflectance spectrum, when the incident angle of light source was changed from the direction completely perpendicular i.e. 0° to 45°. It is worth to stress out that also in this case there are remarkable changes in skin spectrum. As it can be seen the intensity for wavelengths between 400nm and 550nm remains almost the same. The changes are only noticeable for range 550nm to 675nm. It is probably due to the fact that scattering properties of human skin tissue also depends on the wavelength. Moreover, light entering the

tissue at greater angle penetrates the medium only shallowly before it escapes. This results in the smaller photon absorption than for the case where the angle was equal to 0° and the mean free path of photon was much longer.

7 The application of multispectral images

Multi-spectral images can be also used in the other way. Since they provide a detailed description of an image for a given wavelength, they can be combined to deliver feature-rich picture for a desired property. In other words, it is needed to specify what we are looking for and then display pixel by pixel the quantity describing how strong this parameter influences this part of image. As the result grayscale representation is obtained which can be further processed.

Multi-spectral images have a couple of disadvantages. Each of them needs to be removed in a reasonable manner.

1. Every spectral image contains some noise. It is a high frequency noise, which sums up and highly influence the final data. As the result picture does not look smooth and pixel intensities are distorted.

2. Multi-spectral images enable to compute directly the whole spectrum for every needed pixel. However, if sampling interval is too big, a significant number of information can be lost. Currently 21 images representing range from 400nm to 720nm was available with 16nm long step. It means that whenever a spectrum property shorter than sampling interval is looked for, it can be simply missed and not registered by multi-spectral camera.

3. Every spectral image is biased by the light illuminating the analyzed area. Since multi-spectral images for human skin tissue are taken from distance 1mm - 5mm, one can observe that pixels in the middle are higher illuminated than the rest ones. Such influence hides the original image features and adds low frequency distortion.

4. Spectra obtained for pixels from images acquired for different tissue samples are difficult to compare. There is no reference between them, since every situation was illuminated in a bit different way. Also skin of every human being varies. It causes the problem that very similar spectra looks different, because one of them is more flattened, they may have completely different maximal value or they can contain additional unimportant feature. It is very difficult to remove those influences. If comparison of spectra from different patients would be possible, it would be easy to detect cancerogenous changes in the skin.

5. When creating a combined picture from many multi-spectral images it is worth to consider, which tone mapping should be used. One of the most popular operator is max-to-white, where pixels with higher intensities be-

come white. This approach however can be problematic when images are basing on spectra from subsequent pixels. Unimportant noise peaks in constant color image will be magnified to white color, making them the most visible. Such behavior is very undesired, since only important feature should be recognizable.

All of those problems will be addressed in the next chapters. Also a final algorithm for cancer recognition will be presented. But first two well known methods will be described used for multi-spectral image processing and feature recognition.

7.1   Orthogonal Subspace Projection classification

A classification method widely used for multi- and hyper-spectral images is Orthogonal Subspace Projection (OSP). It bases on idea of linear unmixing of mixed pixel vectors, containing a linear combination of endmembers. Individual components can be quantified giving the number describing the amount of a given property in pixel vector. In order for the OSP algorithm to be applicable, the number of samples should be equal or greater than that for classified endmember. This assumption guarantees that there are enough dimensions to perform orthogonal projections coming from separate signatures. In our case this constraint is totally fulfilled by multi-spectral images, since only two signatures was analyzed i.e. isolated cancer spectrum and healthy skin [88].

The main idea of this classifier is to remove all undesired and unwanted signatures in a pixel. Generally those components can be treated as a background. In the end a matched filter is utilized to derive the expected spectral endmember existing in that pixel.

Let's formulate the problem and express a column vector r_i as a mixed pixel vector described by the linear model:

$$r_i = M\alpha_i + n_i, \tag{7.1}$$

where:
r - column vector $l \times 1$,
l - number of samples,
i - pixel number in multi-spectral image,
M - matrix $l \times p$ containing columns of all endmembers,
p - number of distinct signatures,
α_i - column vector $p \times 1$ representing the fraction of the given endmember in r,
n - column vector $l \times 1$ describing additive, white gaussian noise,

In order to separate desired from undesired spectral components, it is needed to reformulate $M\alpha_i$. For situation when only fraction on one endmember needs

to be computed:

$$M\alpha_i = d\alpha_p + U\gamma, \tag{7.2}$$

where:

d - column vector $l \times 1$ containing signature of interest,

α_p - faction of desired component,

U - matrix $l \times (p-1)$ composed of the remaining column from M or background,

γ - column vector $(p-1) \times 1$ containing the remaining fractions of α.

The goal of OSP classification is to find such P that eliminates the influence of matrix of unwanted components U. This operator projects r onto a subspace that is orthogonal to the columns of U by using a least squares optimal interference rejection operator:

$$P = (I - UU^\dagger), \tag{7.3}$$

where:

I - identity matrix,

U - pseudo inverse of U denoted by $U^\dagger = (U^T U)^{-1} U^T$.

The task of operator P is to map d into a space orthogonal to the space spanned by the undesired endmembers in U. Applying it to equation 7.1 and gives:

$$Pr_i = Pd\alpha_d + PU\gamma + n_i, \tag{7.4}$$

Since operator P acting on $U^\dagger$ reduces the whole component to zero, therefore the above formula can be rewritten to:

$$Pr_i = Pd\alpha_d + n_i, \tag{7.5}$$

Now it is necessary to find matched filter x^T for a desired endmember, such that maximizes the signal-to-noise ratio (SNR).

$$\lambda = \frac{x^T P d\alpha_p^2 d^T P^T x}{x^T P E n n^T P^T x}, \tag{7.6}$$

After solving generalized eigenvector problem (not showed here), it turned out that x^T maximizing SNR is:

$$x^T = kd^T, \tag{7.7}$$

where:

k - arbitrary scalar.

Finally, an overall classification operator for a signature of interest in the presence of background signature and white noise can be defined as:

$$q^T = d^T P, \tag{7.8}$$

By applying this operator to all of the pixels in a multi-spectral image, each spectral vector is transformed to a scalar representing a measure of the presence of the endmember of interest. Pixels with the highest intensity denote the existence of the desired signature in the image [89].

7.2   Mean Shift segmentation

There is a number of different nonparametric clustering methods available in the literature. All of them can be divided into two classes: hierarchical clustering and density estimation. First technique generally accumulates, combines or divides the data taking as a criterion some kind of internal measure. Those methods are considered to be time consuming and inefficient. They also suffer from a difficulty to define a good stop criterion during data processing. On the other hand the density estimation clustering technique employs a feature space, which is treated as the empirical probability density function of the chosen parameter. Local maxima of p.d.f. are directly related to the dense regions in the feature space. Basing on their locations, proximity and structure in feature space, associated clusters can be defined.

One of the most popular density estimation method is kernel density estimation. Having a data points in d-dimensional space, the kernel density estimator can be defined as:

$$\hat{f}(x) = \frac{1}{nh^d} \sum_{i=1}^{n} K(\frac{x - x_i}{h}), \tag{7.9}$$

where $K(x)$ must by radially symetric and satisfy:

$$K(x) = ck(\|x\|^2)), \tag{7.10}$$

A good example of such a kernel is multivariate normal kernel:

$$K(x) = (2\pi)^{d/2} exp(-\frac{1}{2} \parallel x \parallel^2), \tag{7.11}$$

From equation (7.9) a density gradient estimation can be obtained, which is proportional to the mean shift vector described as:

$$m_h(y_j) = y_{j+1} - y_j = \frac{\sum_{i=1}^{n} x_i exp(\|\frac{x - x_i}{h}\|^2)}{\sum_{i=1}^{n} exp(\|\frac{x - x_i}{h}\|^2)}, \tag{7.12}$$

Stating that simply, estimate of the density gradient at point x is proportional to the offset of the mean vector in the window from the center of the window:

$$\widehat{\nabla f(x)} \sim \left(\operatorname*{ave}_{x_i \in S_{h,x}} [x_i] - x \right), \tag{7.13}$$

where:

$S_{h,x}$ - is the window centered in x and with radius h.

Recursively moving the window $S_{h,x}$ by the mean shift vector, until it becomes less than a very small threshold i.e. $\nabla f(x) \approx 0$, allows to determine local maxima of density. This approach is guaranteed to converge.

However, when dealing with two-dimensional images an additional factor has to be taken into account. The position of each pixel is defined in a spatial domain, while its gray level or color is expressed in range domain. The different nature of both domains needs to be handled by correct normalization. For this purpose a multivariate kernel was defined as a product of two radially symmetric kernels:

$$K_{h_s,h_r}(x) = \frac{C}{h_s^2 h_r^p} k\left(\left\|\frac{x^s}{h_s}\right\|^2\right) k\left(\left\|\frac{x^r}{h_r}\right\|^2\right),\tag{7.14}$$

where:

x^s and x^r - spatial and range part of feature vector,

h_s and h_r - kernel bandwidths.

Both bandwidth parameters control the size of each kernel and in such a way also define the resolution of local maxima detection. The whole algorithm can be described as:

1. For every pixel x_i in the image:

   - Initialize $y_{i,1} = x_i$,
   - Compute recursively mean shift vector, until it is equal to small threshold according to equation (7.12),
   - Assign to z_i the point of convergence $y_{i,c}$.

2. Group together all z_i which are closer than the h_s in spatial and closer than h_r in region domain. Grouped points represents clusters.

3. Assign to x_i a cluster number it belongs to.

4. Optionally remove all regions in spatial domain that contains less than M pixels.

The only parameters that are needed to define a priori are h_s, h_r and M [90]. The process of segmentation can be additionally optimized by using edge detection mechanism - synergistic segmentation. However, using only gradient magnitude for segmentation is insufficient. In order to create a gradient map two values needs to be defined:

- ρ is the gradient magnitude value. It can be understood as a thickness of the edge. The greater ρ, the more visible the edge is.

- η is the confidence in the presence of an edge in the assumed model, defined in range from 0 to 1. It means that accurate step-edges would have very large η.

This approach guarantees that regions with sharp but weak boundaries will be detected and their boundaries adequately supported by the gradient. Now, for every pixel in the image a weight w_{ij} can be calculated as:

$$w_{ij} = a_{ij} * \rho_{ij} + (1 - a_{ij}) * \eta_{ij}, \tag{7.15}$$

These calculated values can be easily integrated into mean shift segmentation algorithm described earlier. During filtering phase a weighted average is used in equation (7.13), with weights defined as 1 - w_{ij}. To further merge similar regions, for every edge a "boundary strength" measure (e) is computed by averaging all w_{ij} on the boundary between similar clusters. Finally, by defining t, whenever $e < t$ between neighbor regions, the transitive closure operation is performed.

Both image processing methods described above i.e. mean shift segmentation and edge detection were integrated into *Edge Detection and Image Segmentation* (EDISON) system. The application is implemented in C++ and the source code is available on the web [91]. It can be run in Windows or command line mode. The user needs to only specify h_s, h_r, M, ρ, η and threshold t and, as the result, filtered, segmented or even gradient image will be generated.

7.3   Spectrum comparison problem

It is very important to remark the problem of spectra normalization. The question arises how to compare two vectors representing color, but with different energy. The goal is to have such a normalization method for which the difference of two similar spectra is equal to zero vector. However, this task is quite tough. Three normalization methods are described below:

1. Simple vector normalization - every vector element is divided by the length of the whole vector.

$$\hat{x} \equiv \frac{x}{\sqrt{\sum_{i=1}^{n} x_i^2}}, \tag{7.16}$$

   where:
   n - dimension of vector space.

2. Normalization by maximum possible value - every vector element is divided by the maximal value of the spectrum. For multi-spectral images every pixel is defined in range from 0 to 65536. If the light and tissue conditions are similar (for example the same patient) this method of normalization can be reasonable.

3. Maximal value normalization - every vector element is divided by the highest vector value. This operation will bring maximal peaks of two similar spectra to the same level. But when the second spectra was completely different, then anyway its maximal value will be set to one. If the energy carried by the spectrum is important, this kind of function is not appropriate, since it favors every peak value (even from the white noise).

$$\hat{x} \equiv \frac{x}{max(x)}, \tag{7.17}$$

4. Energy preserving normalization - every vector element is divided by the whole energy carried by the signal. However, if there are two signals with the same spectrum, but one of them has bigger peak value, then after normalization the base level of both spectra will not be the same any more. They will be shifted with respect to each other and again cannot be compared easily.

$$\hat{x} \equiv \frac{x}{\sum_{i=1}^{n} x_i s}, \tag{7.18}$$

where:

n - dimension of vector space,

s - the distance between two samples (in our case 16nm).

None of the operations listed above is good enough to use it for spectra comparison. In the succeeding computations, the first method was chosen, since it is the easiest to implement. However both, simple vector normalization and energy preserving normalization, exhibit the same disadvantages.

7.4 Algorithm

It is time to present the whole algorithm in action. As the input it takes 21 multispectral images and as the result displays all processing steps, which finally show the location of the places, where the cancer occurs. It is important to note that when capturing a sequence of images, they should contain not only the suspected, cancerous regions, but mainly healthy parts of tissue. If a cancer covers more than 50% of the recorded area, it would be not recognized as disease.

In the beginning of algorithm two fluorescence spectra were defined. It is a fluorescence response of Protoporphyrin IX when illuminating with white or blue light. Both diagrams were obtained from multi-spectral images of white fabric illuminated with appropriate light. Since every pixel in the image is a vector, in order to find an average image color, all vectors were summed up and divided by the number of pixels. As the spectrum normalization method "simple vector normalization" was chosen - see 7.3.

Having defined a spectrum of white light in form of 21 samples from 400nm to 720nm, it is necessary to convert this spectrum to 79 samples from 360nm to 750nm. Only this kind of spectrum can be read by the application presented in chapters 5-6. In order to resample original spectrum, a simple interpolation was performed.
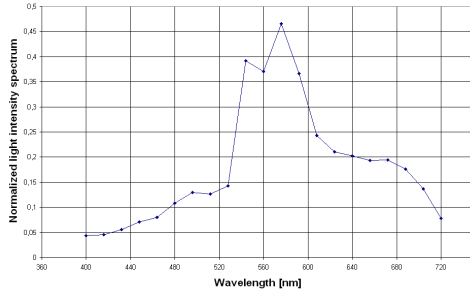
Spectrum from white light (21 samples)
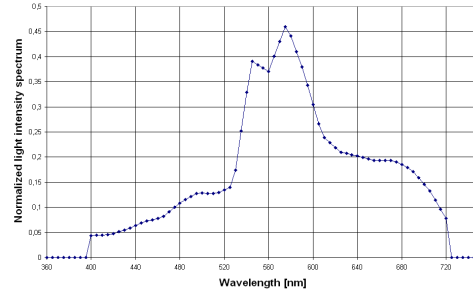
Spectrum from white light (79 samples)
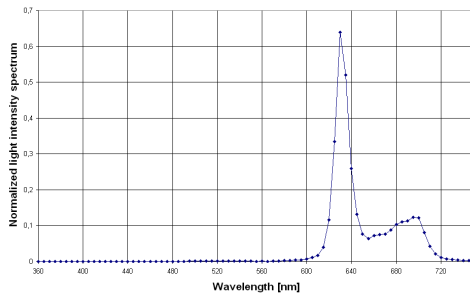
Spectral response on white light of Protoporphyrin IX (79 samples)
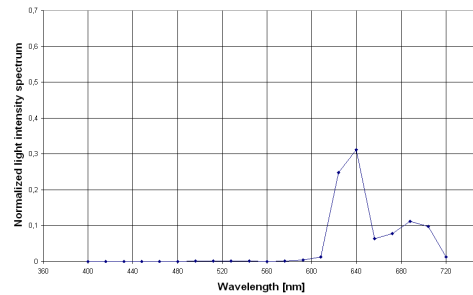
Spectral response on white light of Protoporphyrin IX (21 samples)

Table 7.1: White light spectrum and the response of Protoporphyrin IX

In PBRT a model of human skin tissue was prepared, where the only fluorophore available in the system was Protoporphyrin IX. For simplicity the color of the skin was neglected. The application started tracing photons in the scene, perform subsurface scattering, the fluorescence phenomenon occurred and finally only photons that escaped the tissue was stored in photon map and rendered. The spectrum of the Protoporphyrin IX was registered as a vector of 79 samples. The shape of the spectrum and position of its maxima is exactly the same as in [92]. It means the simulation gave correct results.

The image processing procedure, that is going to be described here, works directly on 21 multi-spectral images. It means that a fluorophore response spectrum cannot be sampled 79 times in range 360nm to 750nm, but it needs to be downsampled. Again, a linear interpolation was applied, but this time the result has some artifacts. For the wave components of higher frequency than the new sample rate the signal is missing. It is very good visible for the main peak value around

630nm, which after transformation was cut off drastically. However, the obtained 21 samples spectra is still good enough to use it in the further processing.

Exactly the same approach was followed for blue light. The most surprising observation is the fluorophore response spectrum, since it looks very similar to the white light response. The root-cause of such appearance can be explained by looking at the structure of protoporphyrin Excitation Emission Matrix (EEM) 4.5e. This particular fluorophore has the biggest emission peak for excitation wavelengths in interval 350nm-450nm. In this range white and blue light excitation spectrum looks quite similar, however blue light shows higher values, because of its blue peak around 464nm. For this reason also emission spectrum is higher, but the shape is almost the same as for the white light.

Spectrum from blue light (21 samples)	Spectrum from blue light (79 samples)
Spectral response on blue light of Protoporphyrin IX (79 samples)	Spectral response on blue light of Protoporphyrin IX (21 samples)

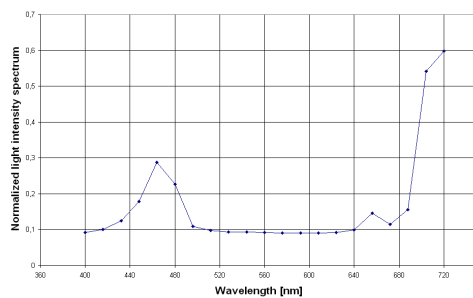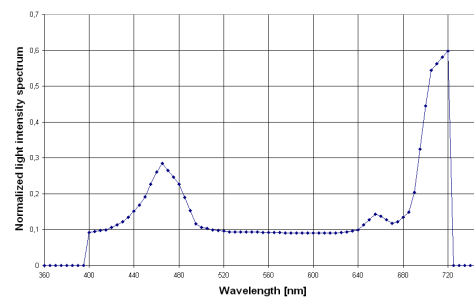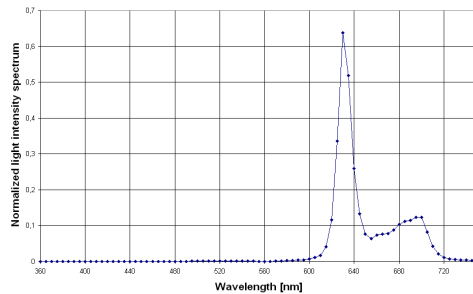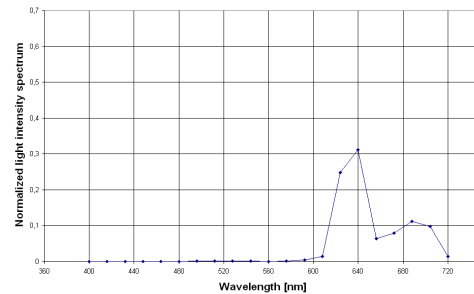Table 7.2: Blue light spectrum and the response of Protoporphyrin IX

7.4.1 Idea 1 - Image filtering

After both light responses were defined a Matlab script reads a sequence of multispectral images into a 3-dimensional matrix. All files should be located in the current working directory and their name should follow the convention presented here: 1_400.png, 2_416.png etc. where first number is the image number in range

from 1 to 21, while the second number is the wavelength for which the photo was captured. This is the original naming style of the camera device.

As the next step the Orthogonal Subspace Projection (OSP) transformation will be utilized for every pixel in the image. As the result 2-dimensional matrix is generated, where the value of every entry represents a measure of the presence of the Protoporphyrin IX in the spectrum. In order to that every spectral vector needs to be multiplied by the classification operator defined in equation 7.8. However first rejection operator needs to be calculated, which needs the spectrum of the healthy tissue as a background - see formula 7.3. Since in the beginning the assumption was made that most of the analyzed region should be covered by healthy skin, the spectrum of undesired spectral components can be calculated as the average of all pixel vectors in the image. It turned out later that such an approach gives acceptable results.

All values obtained after OSP transformation have to be transformed to intensities, which can be displayed on the computer screen. For this reason max-to-white operator was applied. It maps the lowest values to black color (0), the highest to white color (1) and the rest are uniformly interpolated between those two boundary values. Matrix after this operation could be finally stored on the hard drive. Please refer to an image after applying OSP transformation here 7.1a.

Obtained image has a very noticeable, high frequency noise, which was eliminated by applying median filter on the image of size 9x9 pixels 7.1b. Now everything looks smoother and can be further analyzed.

Orthogonal Subspace Projection applied per pixel converts 23-dimensional multi-spectral image (2-dimensions represents position, 21-dimensions describes spectrum of each pixel) into 3-dimensional space. It can be imagined as terrain landscape, where the higher the point is, the greatest is the level of fluorophore concentration (see table 7.3). Because of this fact, only distinct pixels should be isolated, which have a greater intensity than some threshold. A nonlinear transformation was applied for each pixel that amplifies biggest value and suppress the lowest ones. Every intensity defined in range from 0 to 1 was raised to the power of four. This exponent gave the best value and was found by experiments - figure 7.1c.

Looking at table 7.3 it is important to notice, that no matter whether investigated area contains fluorescent substance or not, the OSP image exhibits similar curvature to 2-dimensional Gaussian function. This bias comes from the center of the skin illuminated by the light source. In the middle of the image the light intensity is the highest, but decreases slowly with the distance to the midpoint. This influence interfere the OSP calculation making low values much higher than they really are. Despite of the fact that all vectors used by Orthogonal Subspace Projection were normalized, the impact of higher energy spectrum is still significant. Different spectra cannot be easily compared (see discussion in section

(a) Image after OSP.

(b) Image after median filtering.

(c) Image after nonlinear mapping.

(d) High frequency image.

(e) Image after mean shift filtering.

(f) Gradient image.

(g) Segmented image.

(h) Image with merged regions.
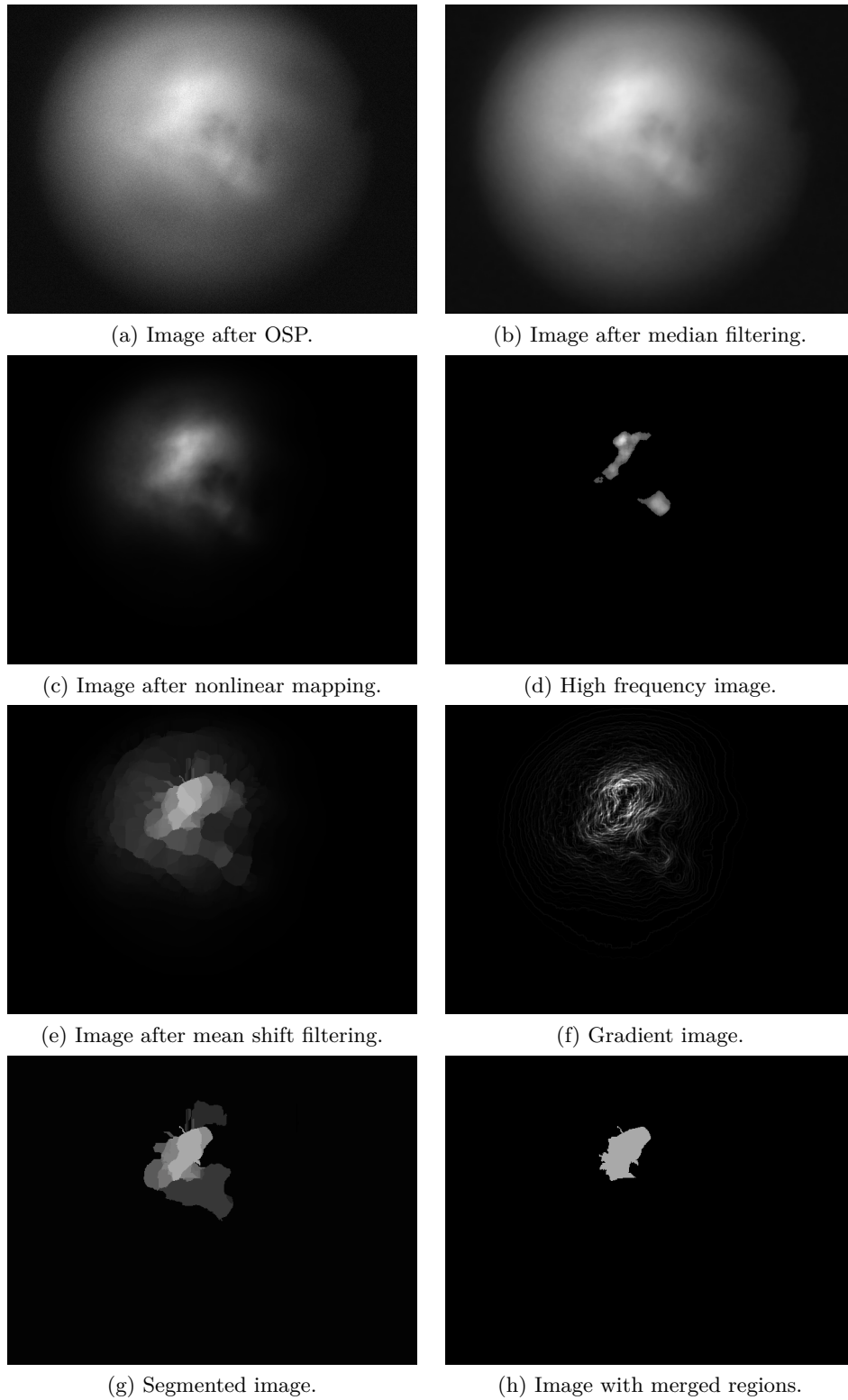
Figure 7.1: Cancer recognition for tissue sample signature - 15674/1 (cancer).
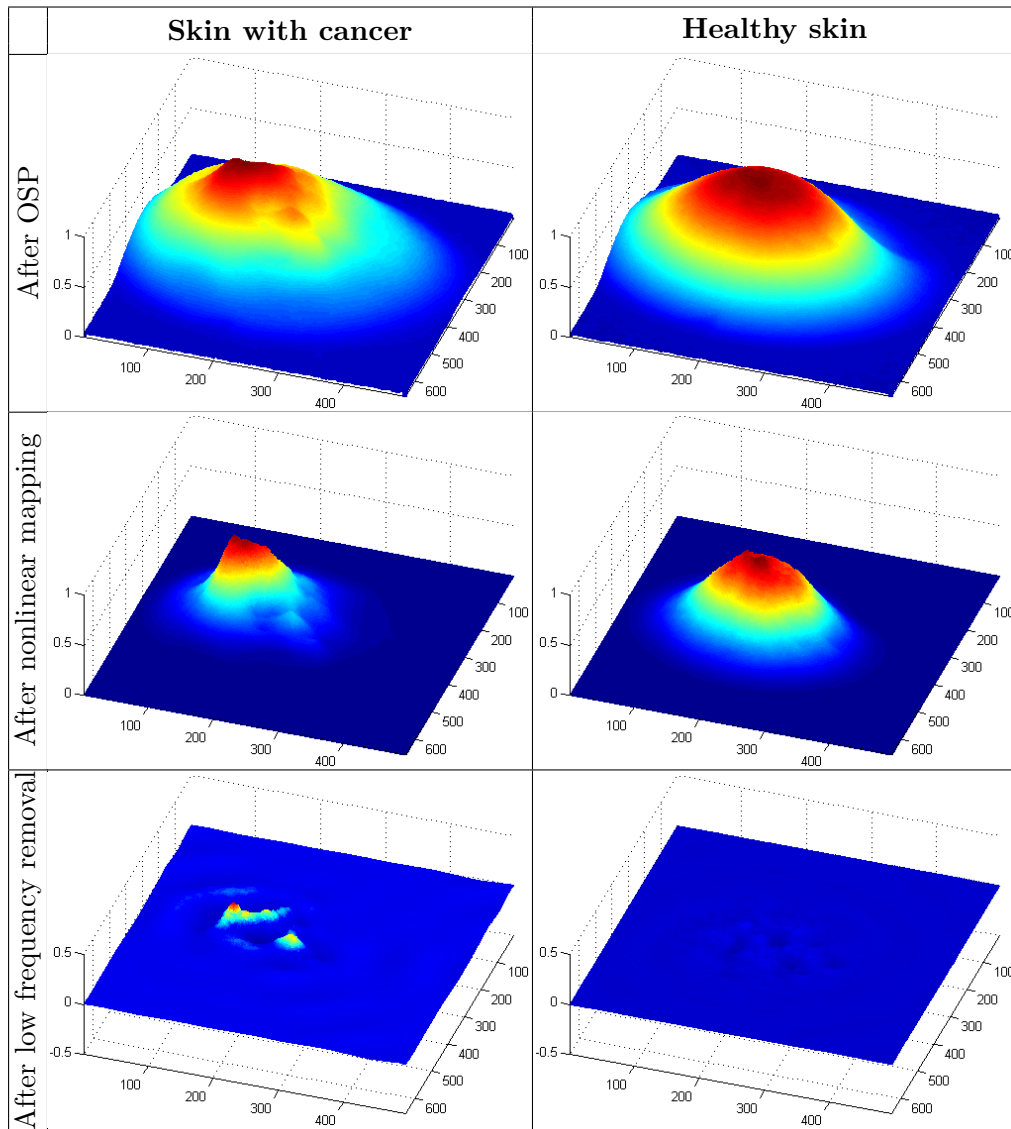
Table 7.3: Comparison the process of filtering for healthy and cancerous skin tissue

7.3).

In order to avoid the effect of central region illumination, a frequency filter was designed according to [93]. The cut off value *K0* was chosen carefully, so that only signal of low frequencies remained, but other signal components were removed. Finally, the 2-dimensional Fourier transform was calculated, then multiplied by filter and eventually 2-dimensional inverse Fourier transform computed. Obtained in this way image was subtracted from the original one leaving only signal of high frequency. As it can be seen in the last row of table 7.3, the bias was removed and the remaining part is of big interest. In the end all pixel values below a given threshold (t=0.05) were removed. Also a closing operator was applied to the image to eliminate not smooth cancer edges. For the result please look at figure 7.1d.

7.4.2 Idea 2 - **Image segmentation**

Instead of applying high pass filter to the OSP image also another approach was investigated. Mean shift filtering with synergistic segmentation based on edge detection mechanism was applied using EDISON application. As the input the following configuration file was prepared:

```
1   //Specify mean shift parameters
2   SpatialBandwidth = 10;
3   RangeBandwidth = 8;
4   MinimumRegionArea = 50;
5   Speedup = MEDIUM;
6   GradientWindowRadius = 1;
7   MixtureParameter = 0.4;
8   EdgeStrengthThreshold = 0.6;
9
10  //Use synergistic segmentation
11  Synergistic ON;
12
13  //Load an image to be segmented
14  Load('out3.pgm', IMAGE);
15
16  //Segment the image
17  Segment;
18
19  //Save the result:
20
21  //The segmented image...
22  Save('segmimage.pgm', PGM, SEGM_IMAGE);
23
24  //The filtered image...
25  Save('filtimage.pgm', PGM, FILT_IMAGE);
26
27  //The gradient map...
28  Save('gradmap.pgm', PGM, GRADIENT_MAP);
29
30  //done.
```

Listing 7.1: Configuration file for EDISON - my.eds

All those parameters were found during many experiments and give the best results for OSP images. For the reference please look at section 7.2, where the

whole algorithm including input and output files was described in details. However, the relation between mathematical symbols and parameters was presented in table 7.4.

Mathematical sybols	EDISON parameters
h_s	SpatialBandwidth
h_r	RangeBandwidth
M	MinimumRegionArea
ρ	GradientWindowRadius
η	MixtureParameter
t	EdgeStrengthThreshold

Table 7.4: Relation between mathematical sybols and EDISON configuration parameters

It was decided to use Mean Shift Synergistic Segmentation, because it relies on gradient vectors between separate pixels. If the gradient is too small, then most probably adjacent points belong to the same cluster. This is the desired behavior, since only rapid changes are of high importance and indicate the appearance of fluorophore in investigated area. This algorithm has also another advantage. It enables to configure parameters of image filtering and segmentation in a handy manner. It is not known how many clusters there is going to be, so popular k-means clustering technique couldn't be used. Additionally basing on the images generated by EDISON, even if the results are not satisfactory, one can draw a proper conclusion about fluorophore concentration. Finally, mean shift segmentation is fast and the outcome of image processing was successful.

It was decided to create filtered 7.1e, gradient 7.1f and segmented image 7.1g as the output files of application. Filtered image shows clustered image before segmentation. It can be analyzed if segmentation phase was too greedy or generous. Gradient image can be also very helpful, since bright and thick lines indicate big changes in pixel intensities and can be analyzed as the potential region of cancer. The only drawback of this approach is the direction of the pixel value changes. From the point of view of feature recognition, only pixels with higher values than background are interesting. However, gradient and also segmented image will indicate not only "hills", but also "valleys" in OSP image. Fortunately it didn't have big influence on final results.

As the last step after image segmentation, additional merging of obtained regions is performed. The idea behind that was to show only black and white image, where white color corresponds to cancerous and black to healthy area. In the beginning of merging operation a background color is found as the biggest

region in the image. It will be located somewhere around black color. Again, if the cancer covers the whole image, this area wouldn't be that dark any more and the merging would fail. Next, the second biggest region is determined and checked if it covers more than 10% of the whole image. If it is true, then make this and all darker colors black as well. Then, it was also necessary to check if regions of brighter pixels have minimal area equals to at least 200 pixels and grayscale value (defined in range from 0-255) grater than 100. If the condition is not fulfilled, the area is merged to background. All those values were found during investigation as they gave the best results.

Finally the number of merged regions is defined. It cannot be greater than the size of color vector or constant parameter equal to four. As the maximum only this number of closest regions to the brightest region are merged together. The rest are treated as background. The resulting image is presented in figure 7.1h.

The procedure of connecting similar, brightest region could be seen as very complicated. However, it was designed and adjusted especially for segmented images of human skin tissue. The main problem that occurred during implementation was with finding background color, since bias from light illumination can cause incorrect classification of healthy skin as cancer. This is why it is checked how big that area is and if too large, then it is considered as background. The presented logic has a disadvantage that minimal area or threshold values can be invalid for some new images. In such a case still all previously generated pictures will be able to identify cancerous changes.

7.4.3 Full Matlab source code

The full source code written in Matlab is available below:

```matlab
%%%%%%%%%%%%%%%%
% Validate image %
%%%%%%%%%%%%%%%%
function main()

cancer_white = [0 0 0.0001 0.0003 0.0006 0.0009 0.002 0.0029 0.0023 0.0019 0.0018 0.0042 ...
0.0101 0.0337 0.6201 0.7799 0.1596 0.1963 0.2802 0.2446 0.0334]'; % Cancer spectrum

cancer_blue = [0 0 0.0002 0.0007 0.0019 0.003 0.0064 0.008 0.0056 0.0047 0.0041 0.0102 ...
0.0257 0.0853 1.5667 1.9685 0.406 0.5031 0.7108 0.6203 0.0853]'; % Cancer spectrum

cancer=cancer_white;                            % choose cancer response either for
% white or blue light
cancer = cancer/norm(cancer);                   % normalized cancer spectrum

tic;                                            % start measuring time

B = load_images(path);                          % load multispectral images
res = osp(B, cancer);                           % calculate OSP
map_image(res);                                 % map intensities
filter_image;                                   % filter image
segment_image;                                  % segment image
merge_image;                                    % merge image

fprintf('Done \n');
```

```matlab
26
27   scrsz = get(0,'ScreenSize');                      % get screen size
28   h = figure;                                        % create window
29   axes('position', [0 0 1 1])
30
31   X1 = imread('out.png');                            % read OSP image
32   X2 = imread('out2.png');                           % read image after median filtering
33   X3 = imread('out3.png');                           % read image after nonlinear mapping
34   X4 = imread('out4.png');                           % read high frequency image
35   X5 = imread('out5.png');                           % read mean shift filtered image
36   X6 = imread('out6.png');                           % read gradient image
37   X7 = imread('out7.png');                           % read segmented image
38   X8 = imread('out8.png');                           % read image with merged regions
39
40   final = [X1 X2 X3 X4; X5 X6 X7 X8];                % concatenate final image
41   imshow(final);                                     % display all images
42
43   pos = get(h,'Position');                           % get its current position and size
44   set(h,'Position',[(scrsz(3)-1000)/2 scrsz(4)/2 1000 380]);    % set new position and size
45
46   toc;                                               % display time of operation
47
48   %%%%%%%%%%%%%%%%%%%%%%%%%%%%%%%%%%%%%%%%%%%%%%%%%%%%%%%%%%%%%%%%%%%
49   % Load multispectral images. They have the following format 1_400.png, %
50   % 2_416 etc. for every wavelength from 400-720 (1-21)                   %
51   %%%%%%%%%%%%%%%%%%%%%%%%%%%%%%%%%%%%%%%%%%%%%%%%%%%%%%%%%%%%%%%%%%%
52   function B = load_images(path)
53   fprintf('\nLoad images\n');
54   num=1;
55   for img=400:16:720
56       file = strcat(int2str(img),'.png');            % concatenate wavelength with format
57                                                      % (e.g 400.png 416.png etc.)
58       prefix = strcat(int2str(num), '_');            % concatenate wavelength number with
59                                                      % "_" (e.g 1_ 2_ etc.)
60       name = strcat(prefix, file);                   % create the filename as concatenation
61                                                      % of previous strings (e.g. 1_400.png
62                                                      % 2_416.png etc.)
63       A=imread(name);                                % read multispectral image
64       B(:, :, num) = A;                              % store the image in 3D matrix
65       num=num+1;                                     % increase the counter
66   end
67
68   %%%%%%%%%%%%%%%%%%%%%%%%%%%%%%%%%%%%%%%%%%
69   % Caclulate OSP for every valid pixel %
70   %%%%%%%%%%%%%%%%%%%%%%%%%%%%%%%%%%%%%%%%%%
71   function res = osp(B, cancer)
72   fprintf('Calculate OSP \n');
73
74   [Y,X,Z]=size(B);                                   % get image height and width
75
76   V = double(reshape(B(:,:,:),Y*X,21)');            % create matrix of vectors
77   z = sqrt(sum(V.*V));                               % caclulate length of every vector
78   V = V ./ z(ones(size(V,1), 1), :);                 % normalize matrix of vectors
79
80   base = sum(V,2)';                                  % calculate the sum of all vectors
81   base = base/norm(base);                            % normalize it
82
83   P = eye(21) - base'*pinv(base);                    % caclulate P matrix (look at OSP)
84   res = cancer'*P*V;                                 % calculate intensities (look at OSP)
85   res = reshape(res, Y, X);                          % reshape to size of the image
86
87   %%%%%%%%%%%%%%%%%%%%%%%%%%%%%%%%%%%%%
88   % Map intensities to image colors %
89   %%%%%%%%%%%%%%%%%%%%%%%%%%%%%%%%%%%%%
90   function map_image(res)
91   fprintf('Write intensity images \n');
92
93   maximum = max(max(res));                           % find maximum for further mapping
94   minimum = min(min(res));                           % find minimum for further mapping
95
```

```matlab
 96    color = (res - minimum) / (maximum - minimum);      % perform mapping, so that minimal
 97                                                         % value has intensity 0 and maximal
 98                                                         % value has intesity 1
 99    imwrite(color, 'out.png');                           % write intensity image
100
101    oMap = medfilt2(color, [9 9]);                       % apply median filter of size 9x9
102    imwrite(oMap, 'out2.png');                           % write intensity image
103
104    oMap = oMap.^4;                                      % add non-linear mapping (x^4) to
105                                                         % supress small values and intensify
106                                                         % big values
107    imwrite(oMap, 'out3.png');                           % write intensity image
108    imwrite(oMap, 'out3.pgm');                           % write image in PGM format
109                                                         % recognizable by EDISON
110
111    %%%%%%%%%%%%%%%%%%%%%%%%%%%%%%%%%%%%%%%%%%%%%%
112    % Remove low frequency signal from the image %
113    %%%%%%%%%%%%%%%%%%%%%%%%%%%%%%%%%%%%%%%%%%%%%%
114    function filter_image()
115    fprintf('Apply filter \n');
116    oFil = double(imread('out3.png'));                   % read input file
117
118    img = oFil./255;                                     % normalize image
119
120    [Y,X]=size(img);                                     % get image height and width
121
122    dx = 1;                                              % sampling interval
123    dy = 1;                                              % sampling interval
124
125    KX0 = (mod(1/2 + (0:(X-1))/X , 1) - 1/2);            % caclulate discrete grid step in X
126    KX1 = KX0 * (2*pi/dx);
127    KY0 = (mod(1/2 + (0:(Y-1))/Y , 1) - 1/2);            % caclulate discrete grid step in Y
128    KY1 = KY0 * (2*pi/dx);
129    [KX,KY] = meshgrid(KX1,KY1);                         % convert wavenumbers into standard
130                                                         % matrix format
131    K0 = 0.06;                                           % cut off value
132    T = (KX.*KX + KY.*KY $<$ K0^2);                      % filter formulation
133
134    g = ifft2(T.*fft2(img));                             % calculate 2D Fourier transform, apply
135                                                         % filter and then calculate 2D inverse
136                                                         % Fourier transform
137    oFil = real(img - g);                                % remove low freq signal from the image
138
139    oFil(oFil$<$0.05) = 0;                               % cut off all values below 0.05
140
141    maximum = max(max(oFil));                            % find maximum for further mapping
142    if (maximum~=0)
143        oFil = oFil/maximum;                             % normalize image
144    end
145
146    se = strel('disk',2);                                % create a mask for edge smoothing
147    oFil = imerode(oFil,se);                             % erode the image
148    oFil = imdilate(oFil,se);                            % dilate the image
149
150    imwrite(oFil, 'out4.png');                           % write filtered image
151
152    %%%%%%%%%%%%%%%%%%%%%%%%%%%%%%%%%%%%%
153    % Perform mean shift segmentation %
154    %%%%%%%%%%%%%%%%%%%%%%%%%%%%%%%%%%%%%
155    function segment_image()
156    fprintf('Perform segmentation \n');
157    system('edi.exe my.eds');                            % run EDISON
158
159    imwrite(imread('filtimage.pgm'), 'out5.png');        % convert the filtered image file to
160                                                         % standard PNG file
161    imwrite(imread('gradmap.pgm'), 'out6.png');          % convert the gradient map file to
162                                                         % standard PNG file
163    imwrite(imread('segmimage.pgm'), 'out7.png');        % convert the output image file to
164                                                         % standard PNG file
165
```

```matlab
166    %%%%%%%%%%%%%%%%%%%%%%%%%
167    % Merge similar regions %
168    %%%%%%%%%%%%%%%%%%%%%%%%%
169    function merge_image()
170    fprintf('Perform merging \n');
171
172    oMer = imread('out7.png');                        % read input file
173    [Y,X]=size(oMer);                                 % get image height and width
174    oMer = reshape(oMer(:,:,1),Y*X,1);                % create greyscale image as a vector
175    u = unique(oMer);                                 % find unique colors
176    h = histc(double(oMer),u);                        % find histogram
177
178    threshold = 100;                                  % the maximal pixel value
179    min_area = 200;                                   % the minimal region
180
181    % find background
182    oMer(oMer$<$=u(find(h==max(h)))) = 0;             % treat biggest (darkest)
183                                                      % area as background
184    u = unique(oMer);                                 % find unique colors
185    h = histc(double(oMer),u);                        % find histogram
186
187    m = max(h(2:size(u,1)));                           % get the peak of histogram,
188                                                      % but neglect first value (background)
189    if (m/Y/X$>$0.1)                                   % if the peak covers more than 10%
190                                                      % of whole image then
191        pos = find(h==m);                             % find color of that peak
192        for i=2:pos
193            oMer(oMer==u(i)) = 0;                     % treat those and darker pixels
194                                                      % as background too
195        end
196
197        for i=(pos+1):size(h,1)                        % for the rest of the colors
198            if ((h(i)$<$min_area) || (u(i) $<$ threshold))    % check if they are big
199                                                              % and bright enough
200                oMer(oMer==u(i)) = 0;                 % if not, then remove them
201            end
202        end
203
204        u = unique(oMer);                             % find again unique colors
205        h = histc(double(oMer),u);                    % find again histogram
206    end
207
208    %merge regions
209    merge = min(size(u,1)-2, 4);                       % caclulate the number
210                                                      % of merged regions
211    for i=1:merge
212        oMer(oMer==u(size(u,1)-i)) = u(size(u,1));    % replace all merged regions near the
213    end                                               % brighest one with the brightest color
214    oMer(oMer~=u(size(u,1))) = 0;                     % substitute the black color
215                                                      % to the rest of the pixels
216    oMer = reshape(oMer, Y, X);                        % create greyscale image as matrix
217    imwrite(oMer,'out8.png');                          % write merged image
218
219    % Delete temporary files
220    delete('out3.pgm');                               % delete unneeded files
221    delete('segmimage.pgm');                          % delete unneeded files
222    delete('filtimage.pgm');                          % delete unneeded files
223    delete('gradmap.pgm');                            % delete unneeded files
```

Listing 7.2: Matlab source code of the whole algorithm

7.5   Results

The algorithm described in previous chapters was successfully applied for different tissue signatures and different light sources. The results are presented in the next

sub-chapters.

7.5.1 White light source

When white light source was applied the results of cancer recognition process looks in the following way.

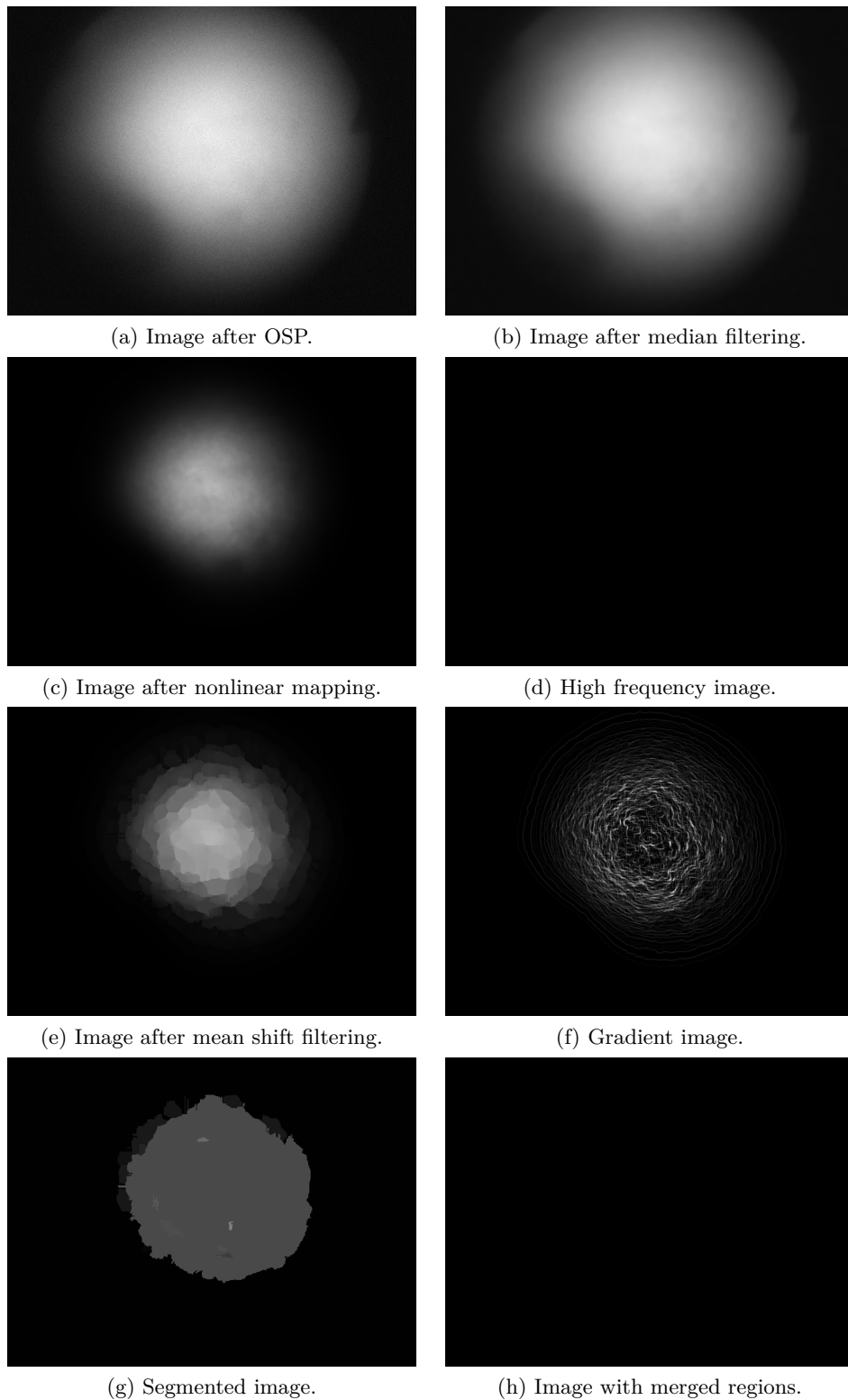(a) Image after OSP.

(b) Image after median filtering.

(c) Image after nonlinear mapping.

(d) High frequency image.

(e) Image after mean shift filtering.

(f) Gradient image.

(g) Segmented image.

(h) Image with merged regions.

Figure 7.2: Cancer recognition for tissue sample signature - 15674/5 (healthy).

(a) Image after OSP.

(b) Image after median filtering.

(c) Image after nonlinear mapping.

(d) High frequency image.

(e) Image after mean shift filtering.

(f) Gradient image.

(g) Segmented image.

(h) Image with merged regions.
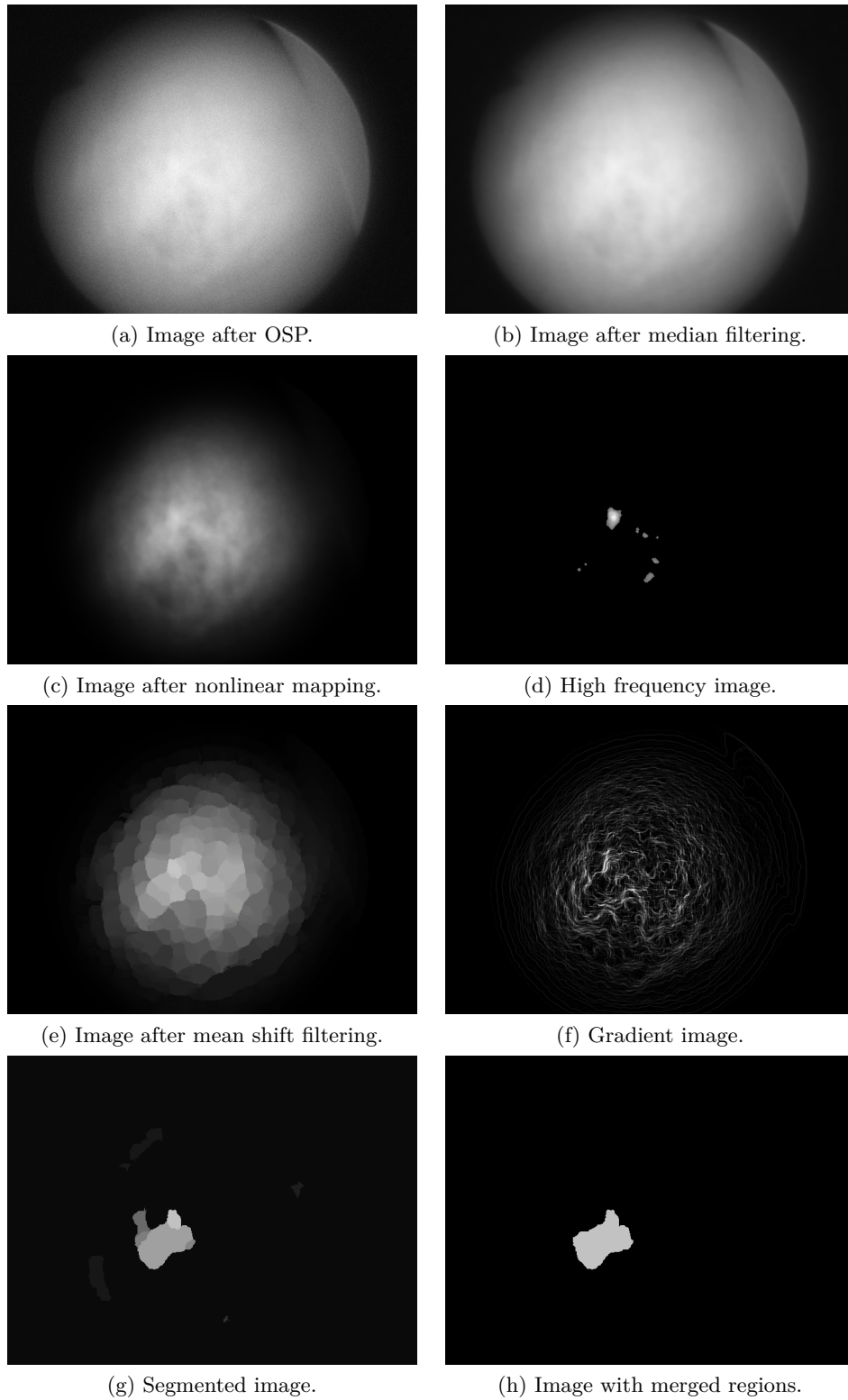
Figure 7.3: Cancer recognition for tissue sample signature - 15674/7 (cancer).

(a) Image after OSP.

(b) Image after median filtering.

(c) Image after nonlinear mapping.

(d) High frequency image.

(e) Image after mean shift filtering.

(f) Gradient image.

(g) Segmented image.

(h) Image with merged regions.
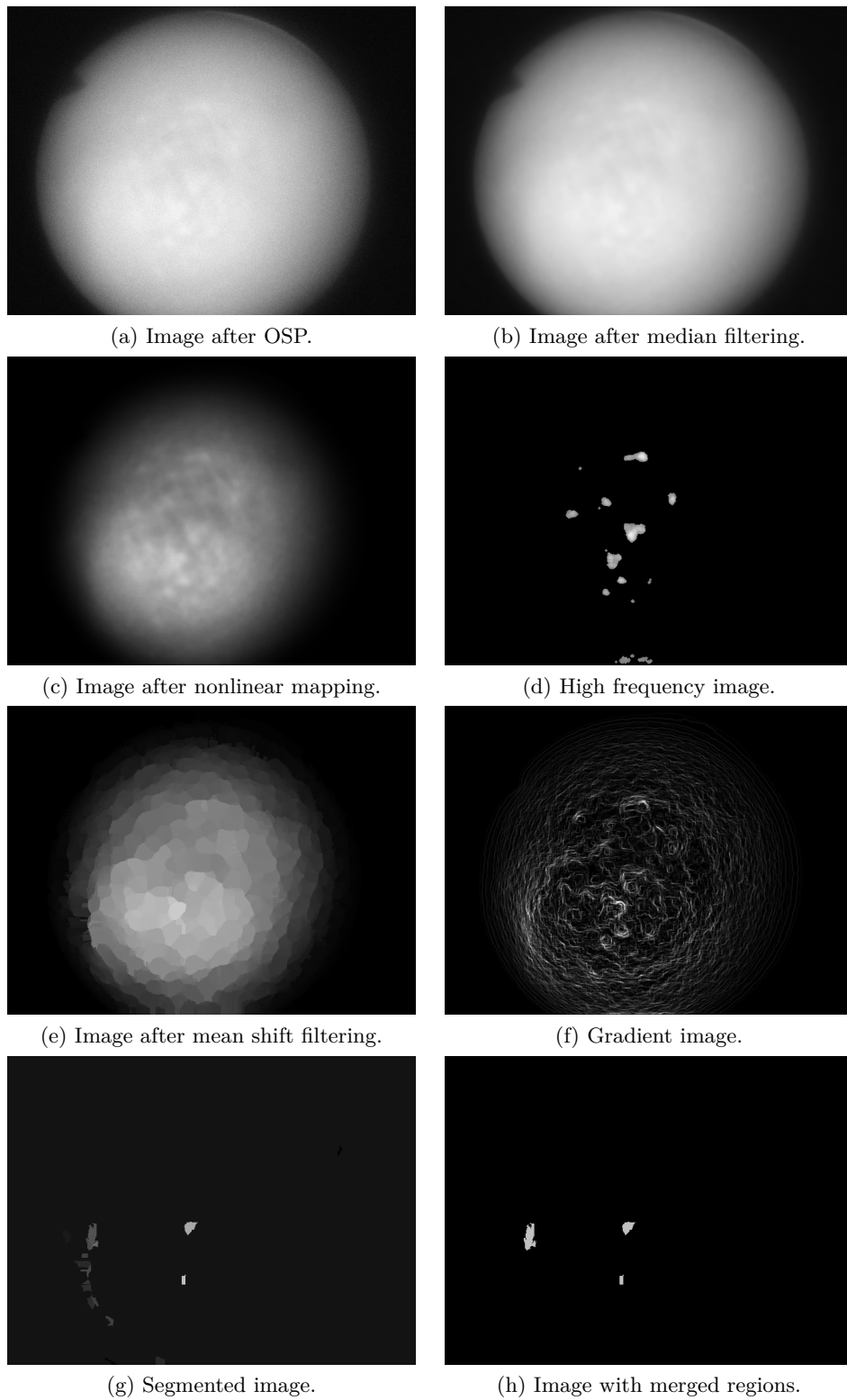
Figure 7.4: Cancer recognition for tissue sample signature - 15674/9 (cancer).

(a) Image after OSP.

(b) Image after median filtering.

(c) Image after nonlinear mapping.

(d) High frequency image.

(e) Image after mean shift filtering.

(f) Gradient image.

(g) Segmented image.

(h) Image with merged regions.
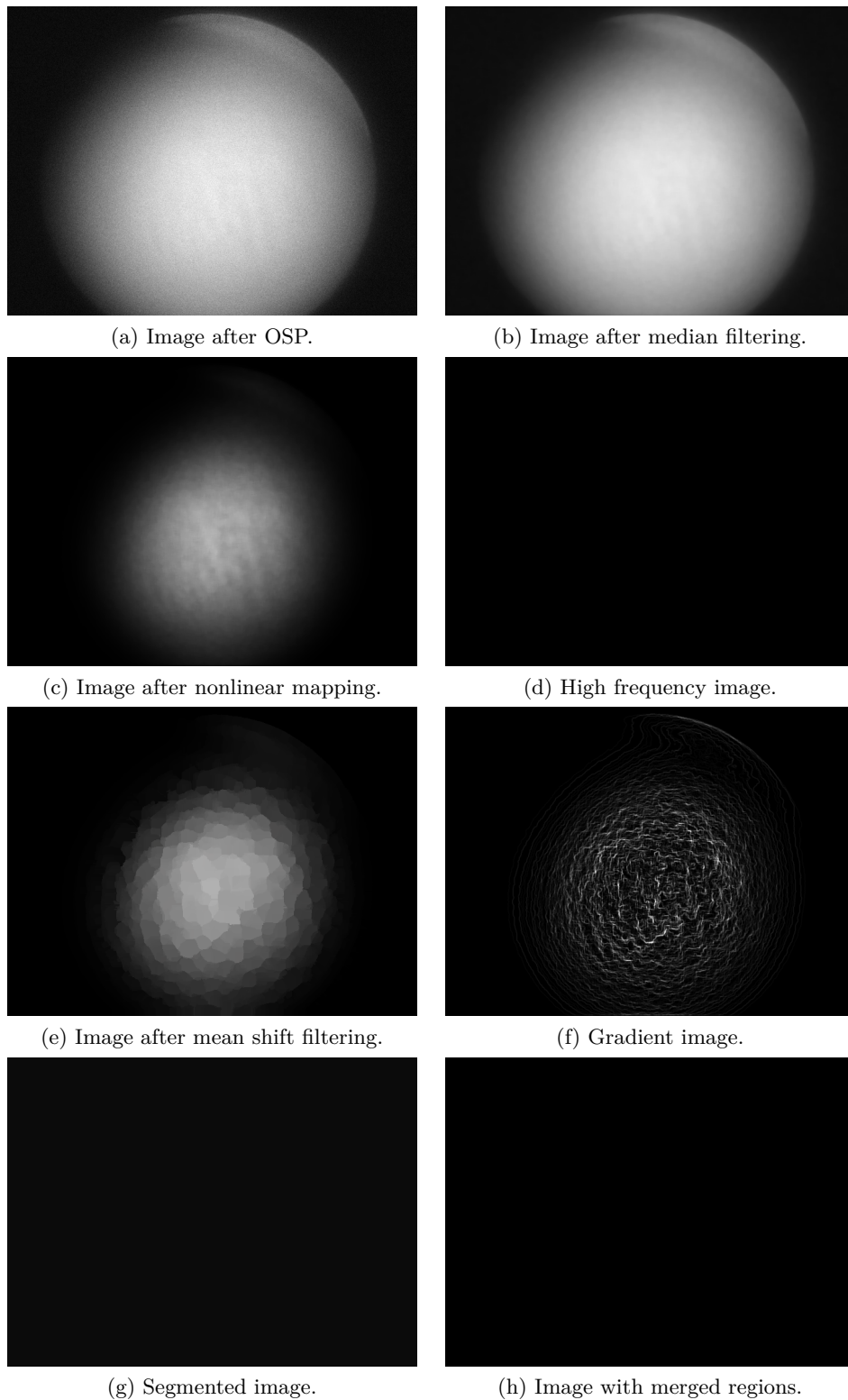
Figure 7.5: Cancer recognition for tissue sample signature - 15674/11 (healthy).

(a) Image after OSP.

(b) Image after median filtering.

(c) Image after nonlinear mapping.

(d) High frequency image.

(e) Image after mean shift filtering.

(f) Gradient image.

(g) Segmented image.

(h) Image with merged regions.
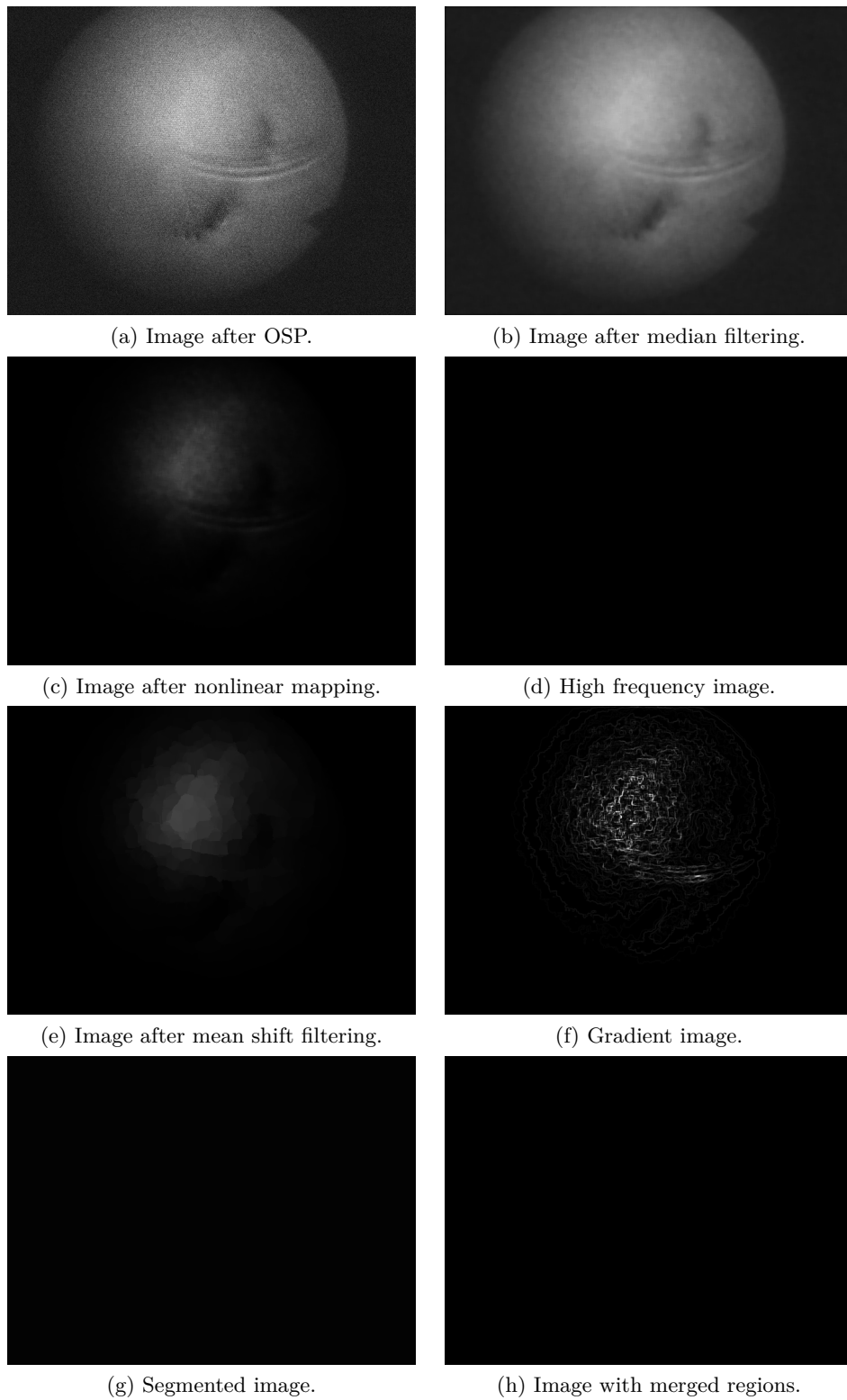
Figure 7.6: Cancer recognition for tissue sample signature - 13602/5 (healthy).

(a) Image after OSP.

(b) Image after median filtering.

(c) Image after nonlinear mapping.

(d) High frequency image.

(e) Image after mean shift filtering.

(f) Gradient image.

(g) Segmented image.

(h) Image with merged regions.
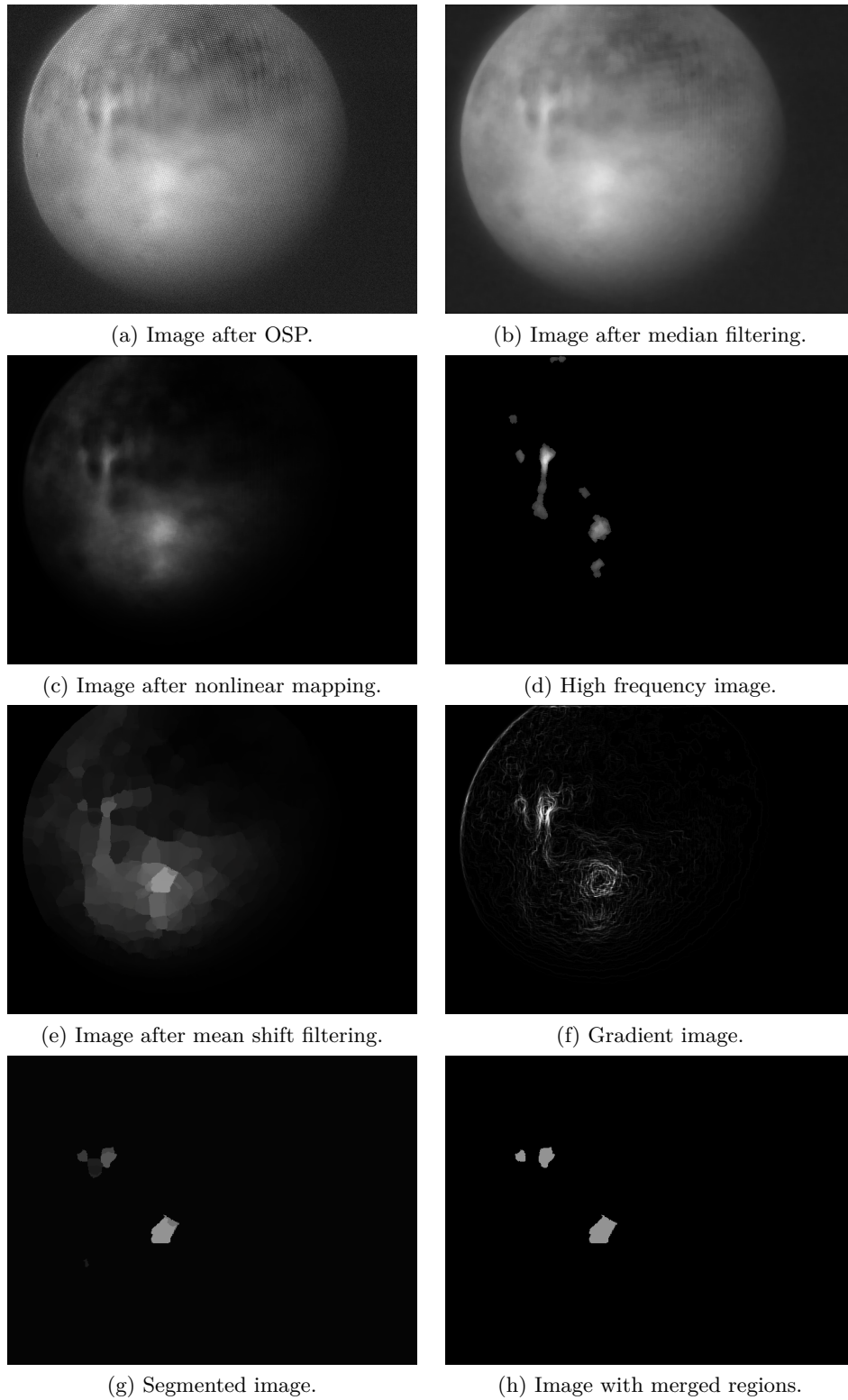
Figure 7.7: Cancer recognition for tissue sample signature - 13602/7 (cancer).

(a) Image after OSP.

(b) Image after median filtering.

(c) Image after nonlinear mapping.

(d) High frequency image.

(e) Image after mean shift filtering.

(f) Gradient image.

(g) Segmented image.

(h) Image with merged regions.
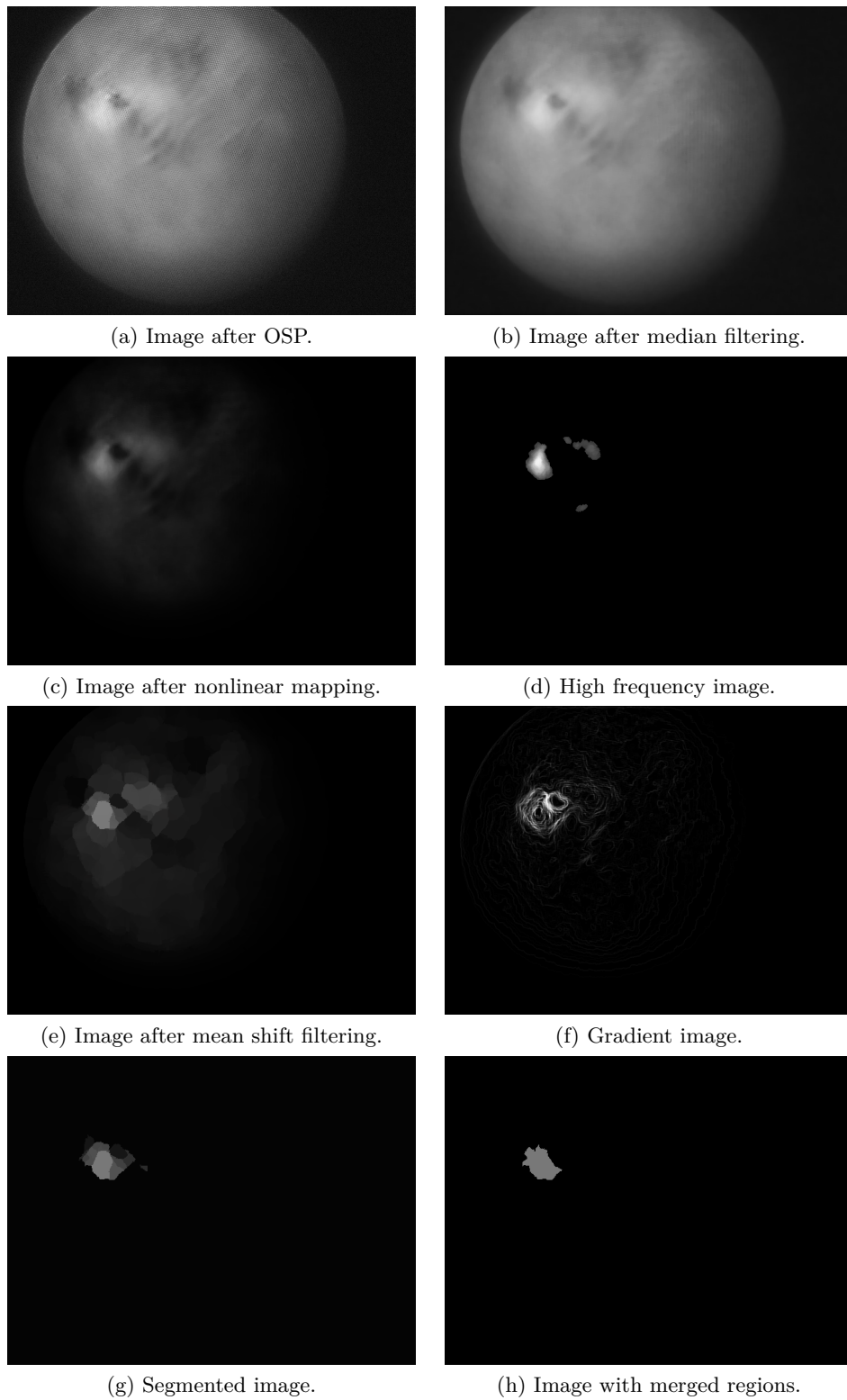
Figure 7.8: Cancer recognition for tissue sample signature - 13602/9 (cancer).

(a) Image after OSP.

(b) Image after median filtering.

(c) Image after nonlinear mapping.

(d) High frequency image.

(e) Image after mean shift filtering.

(f) Gradient image.

(g) Segmented image.

(h) Image with merged regions.
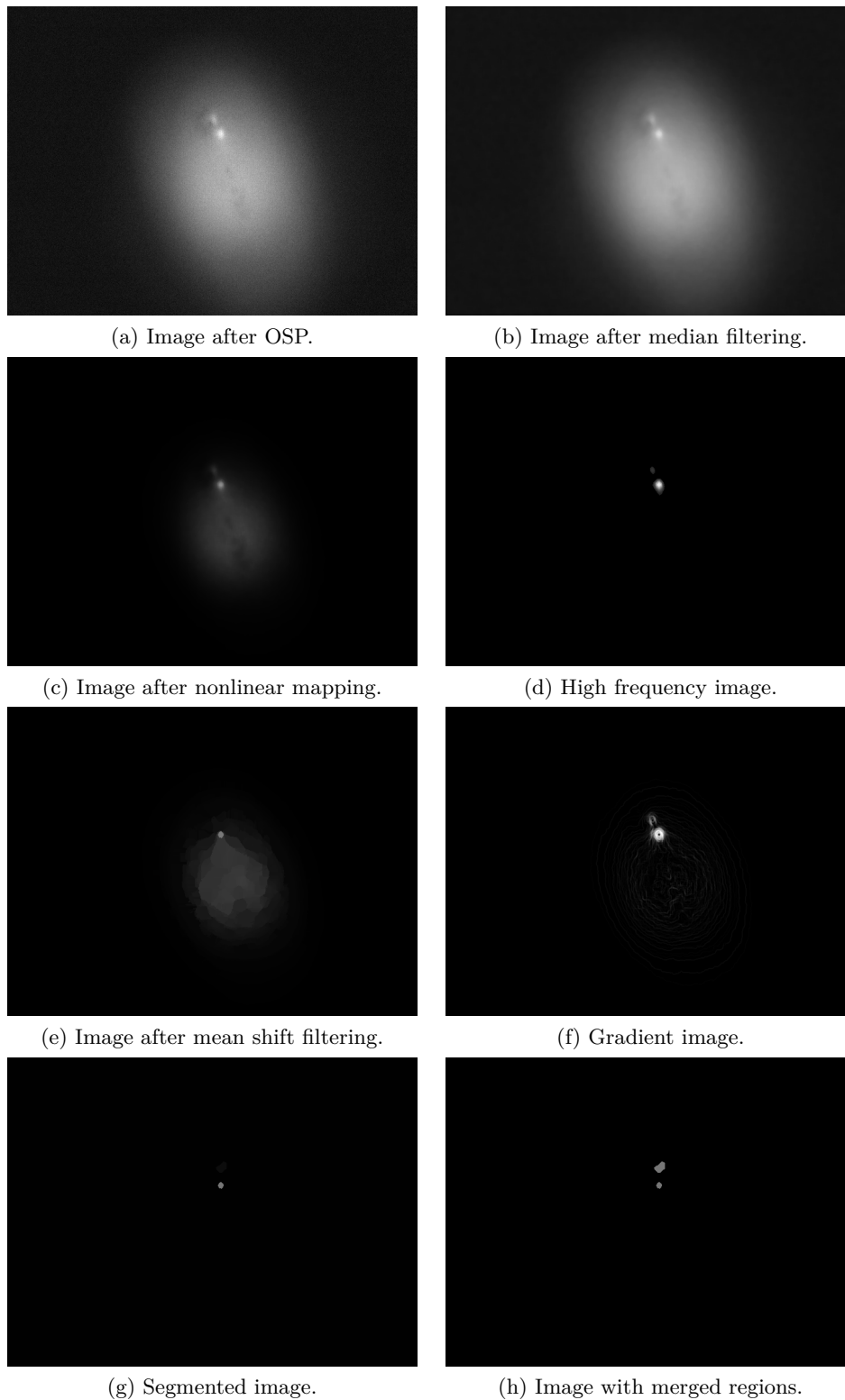
Figure 7.9: Cancer recognition for tissue sample signature - 13952/8 (cancer).

(a) Image after OSP.

(b) Image after median filtering.

(c) Image after nonlinear mapping.

(d) High frequency image.

(e) Image after mean shift filtering.

(f) Gradient image.

(g) Segmented image.

(h) Image with merged regions.
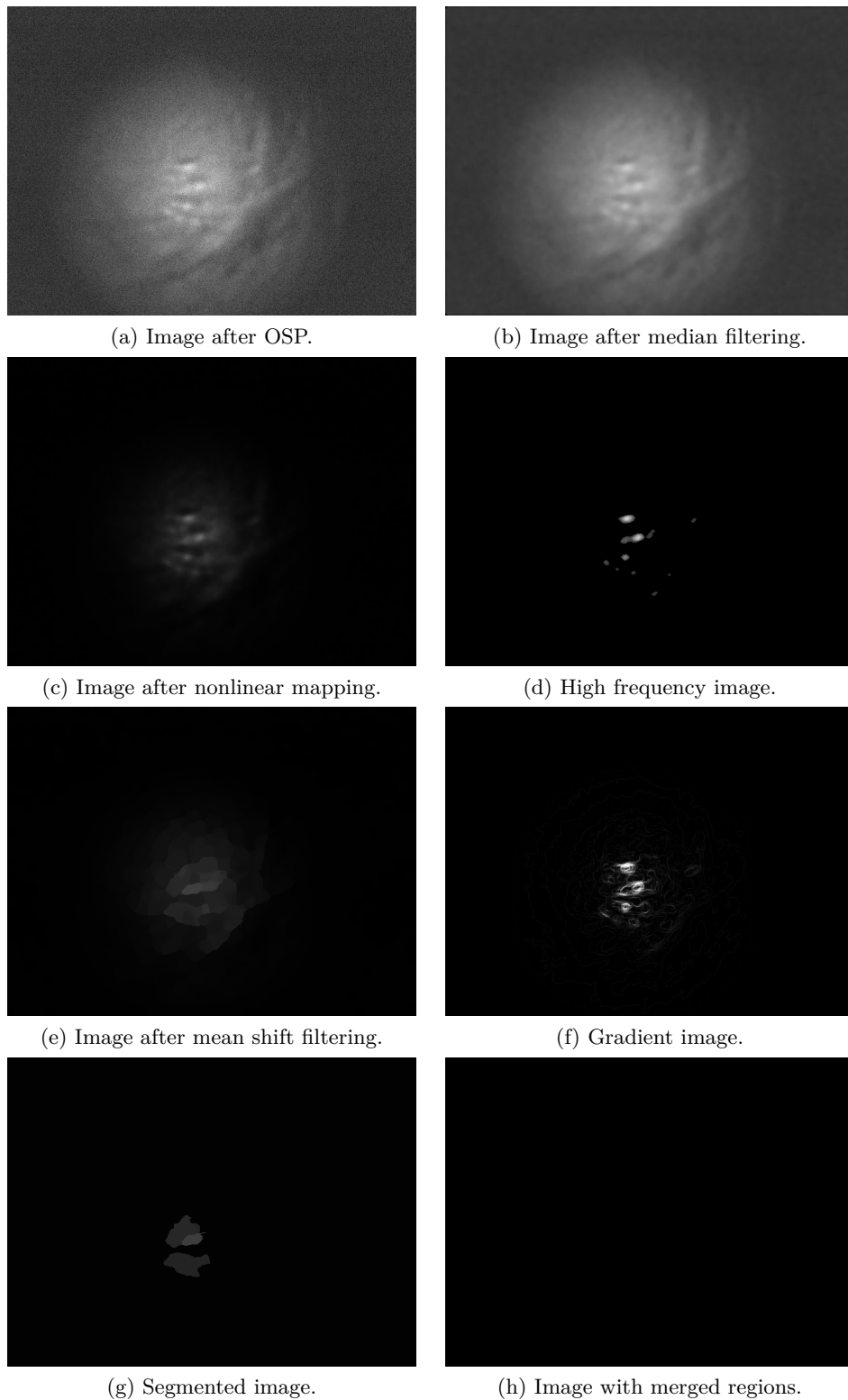
Figure 7.10: Cancer recognition for tissue sample signature - 13124/5 (cancer).

(a) Image after OSP.

(b) Image after median filtering.

(c) Image after nonlinear mapping.

(d) High frequency image.

(e) Image after mean shift filtering.

(f) Gradient image.

(g) Segmented image.

(h) Image with merged regions.
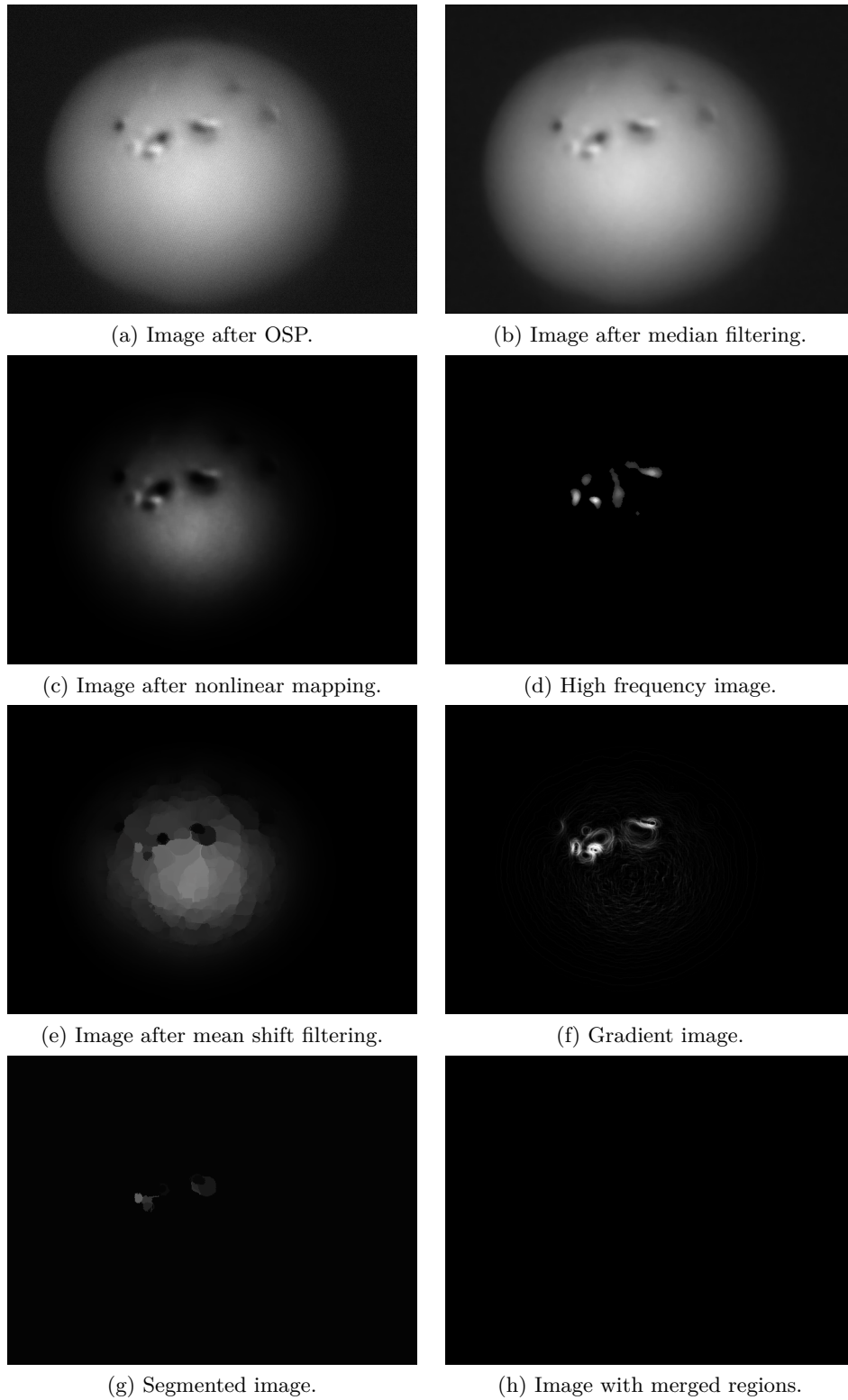
Figure 7.11: Cancer recognition for tissue sample signature - 13124/7 (cancer).

(a) Image after OSP.

(b) Image after median filtering.

(c) Image after nonlinear mapping.

(d) High frequency image.

(e) Image after mean shift filtering.

(f) Gradient image.

(g) Segmented image.

(h) Image with merged regions.
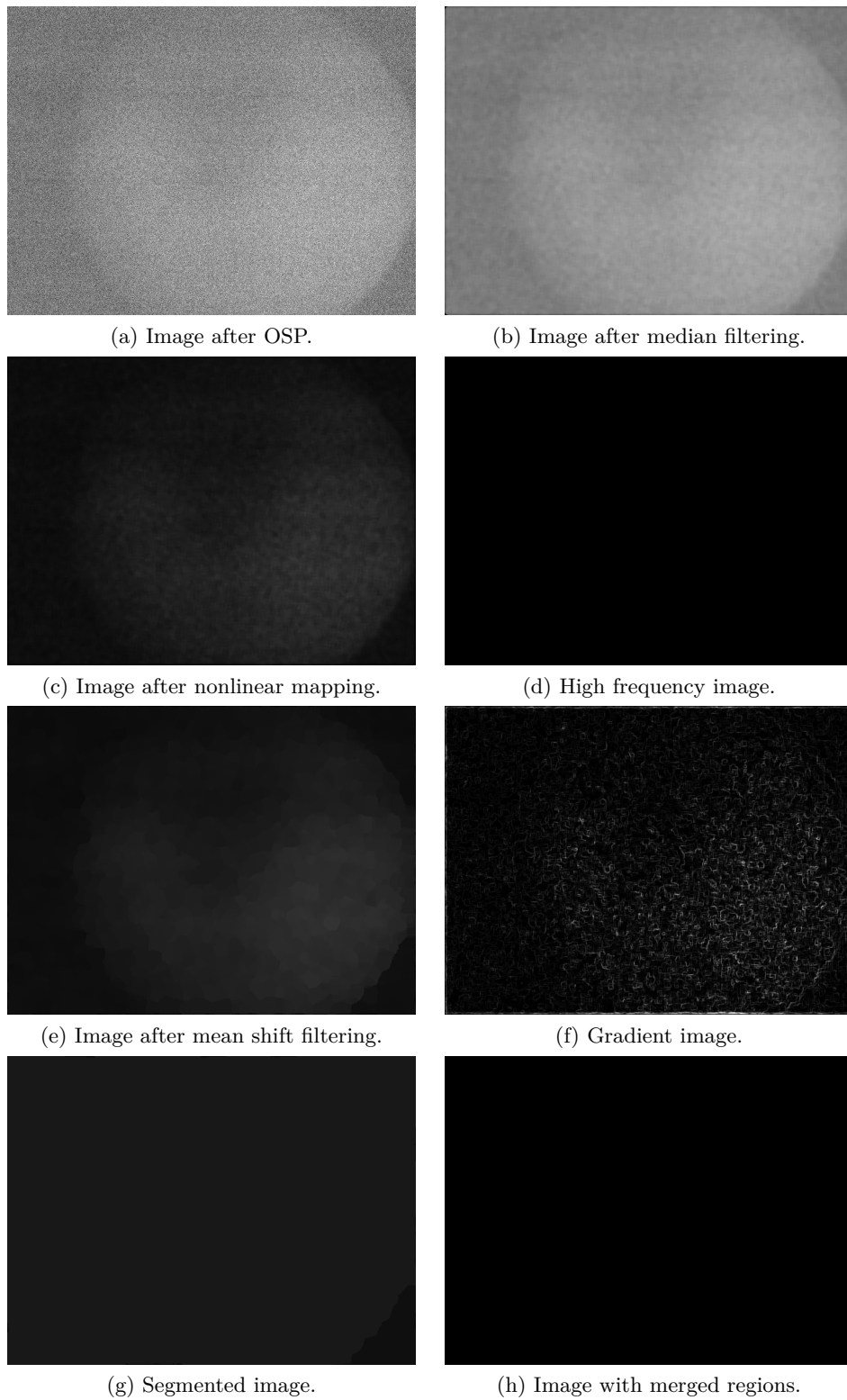
Figure 7.12: Cancer recognition for tissue sample signature - 13124/11 (healthy).

(a) Image after OSP.

(b) Image after median filtering.

(c) Image after nonlinear mapping.

(d) High frequency image.

(e) Image after mean shift filtering.

(f) Gradient image.

(g) Segmented image.

(h) Image with merged regions.
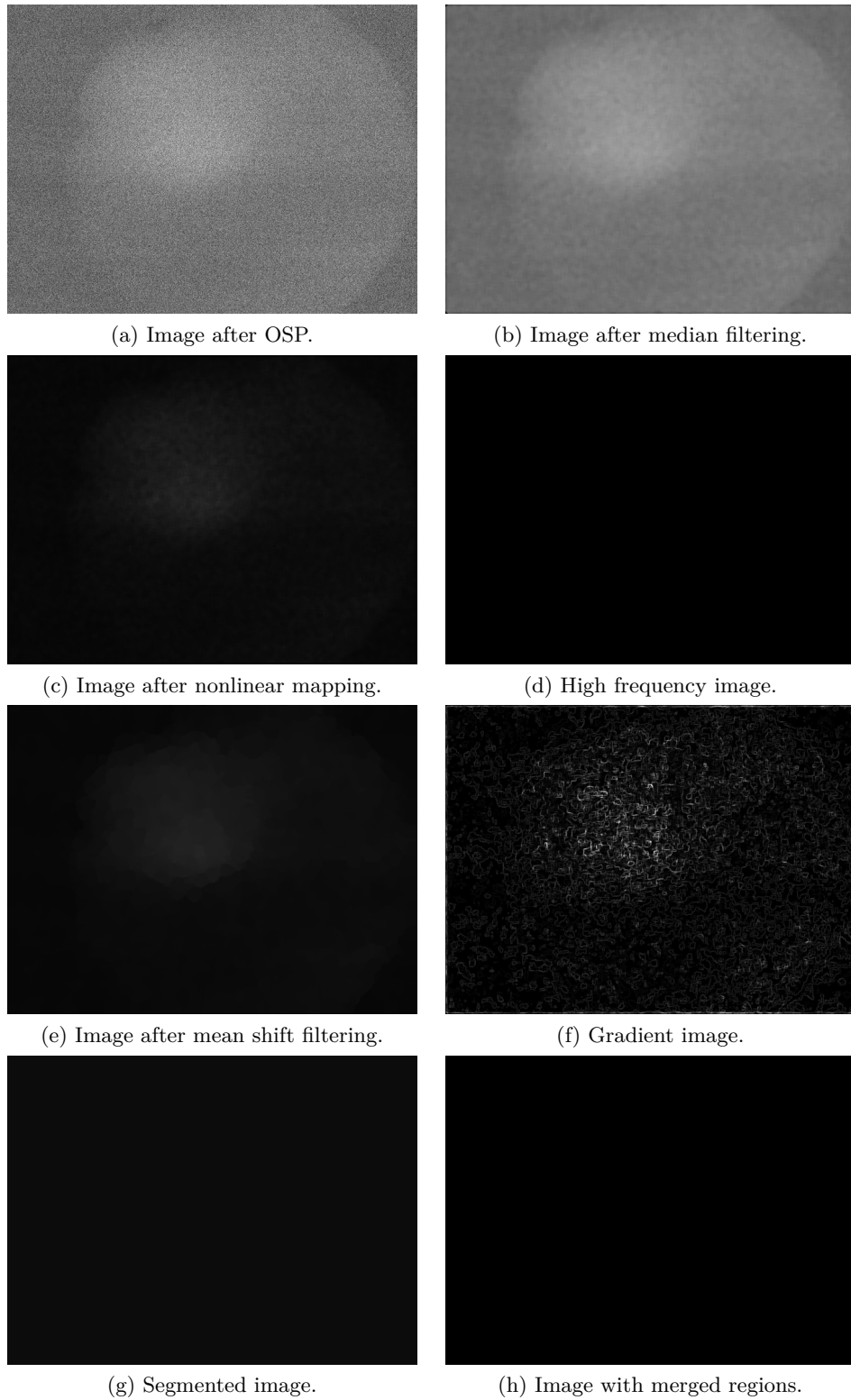
Figure 7.13: Cancer recognition for tissue sample signature - 13124/12 (cancer).

(a) Image after OSP.

(b) Image after median filtering.

(c) Image after nonlinear mapping.

(d) High frequency image.

(e) Image after mean shift filtering.

(f) Gradient image.

(g) Segmented image.

(h) Image with merged regions.
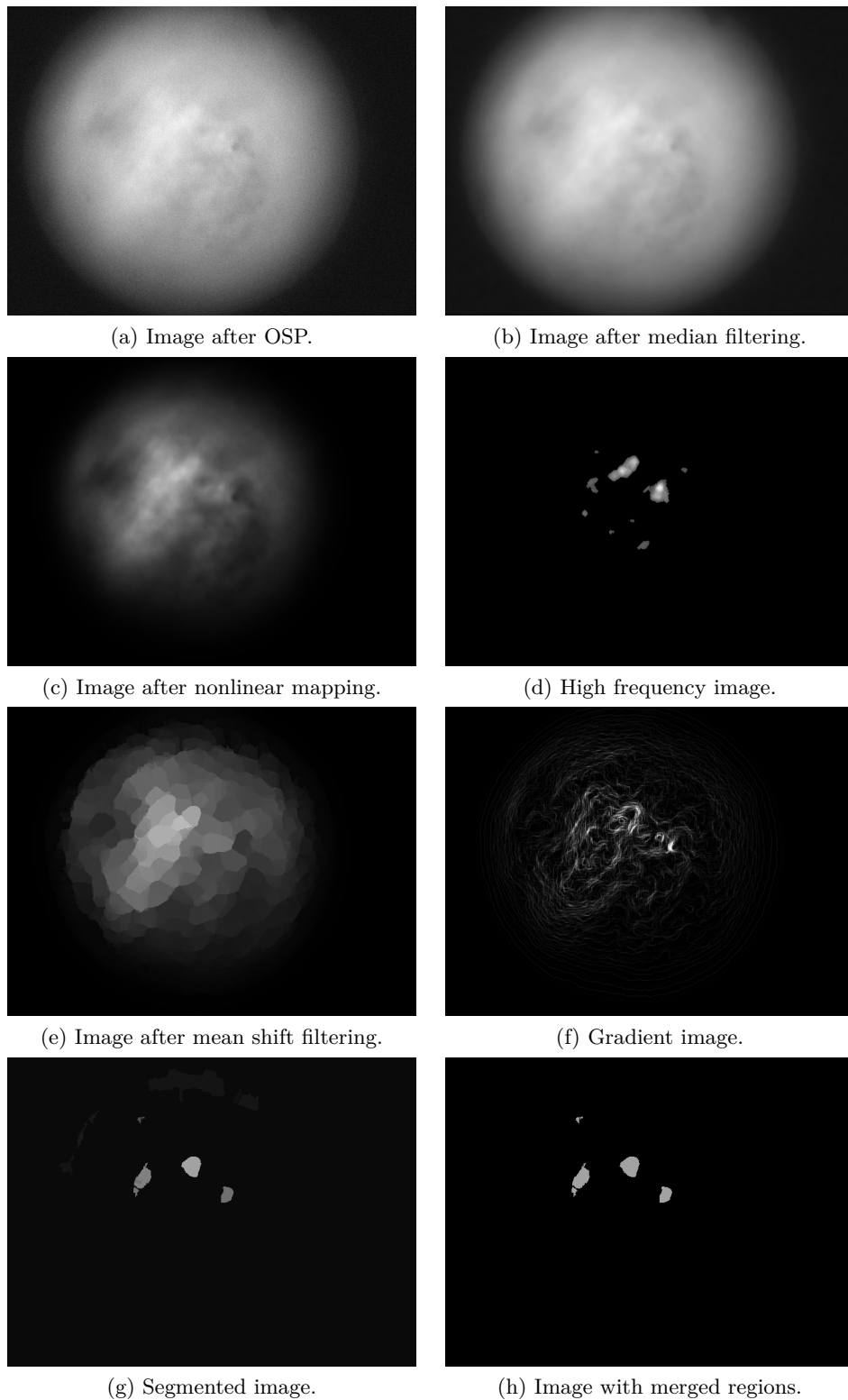
Figure 7.14: Cancer recognition for tissue sample signature - 13002/1 (cancer).

(a) Image after OSP.

(b) Image after median filtering.

(c) Image after nonlinear mapping.

(d) High frequency image.

(e) Image after mean shift filtering.

(f) Gradient image.

(g) Segmented image.

(h) Image with merged regions.
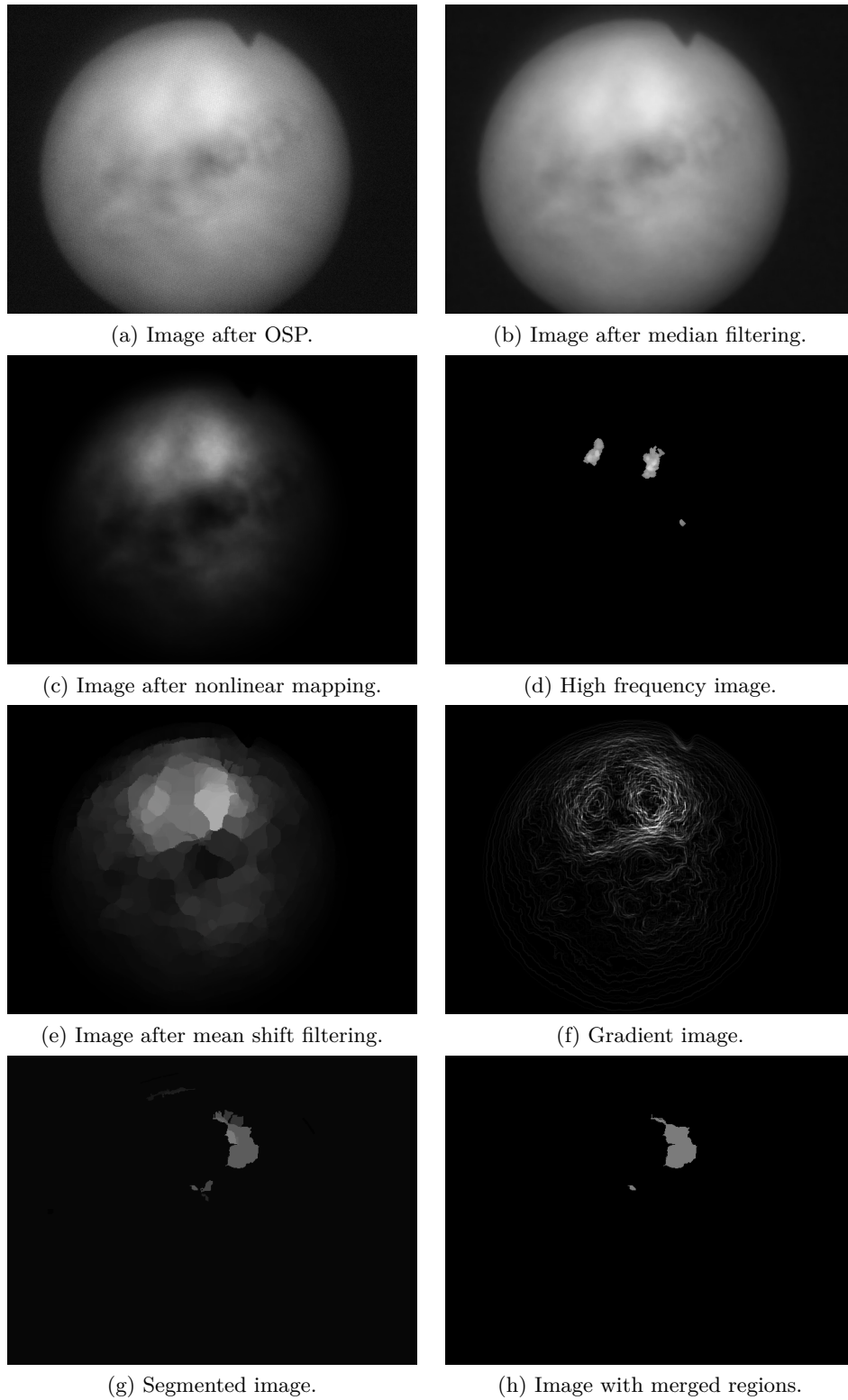
Figure 7.15: Cancer recognition for tissue sample signature - 13002/4 (cancer).

(a) Image after OSP.

(b) Image after median filtering.

(c) Image after nonlinear mapping.

(d) High frequency image.

(e) Image after mean shift filtering.

(f) Gradient image.

(g) Segmented image.

(h) Image with merged regions.
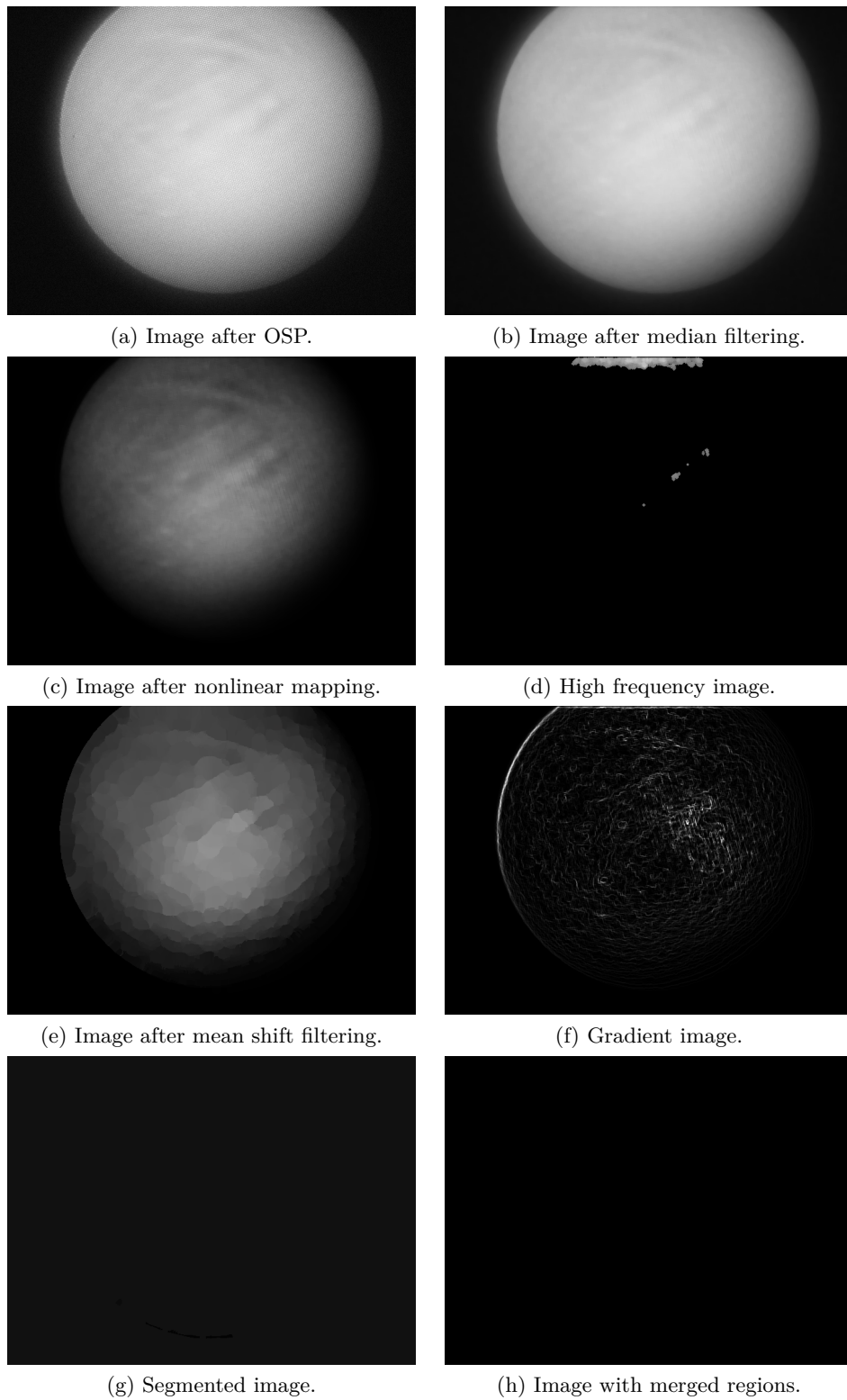
Figure 7.16: Cancer recognition for tissue sample signature - 0/4 (healthy).

(a) Image after OSP.

(b) Image after median filtering.

(c) Image after nonlinear mapping.

(d) High frequency image.

(e) Image after mean shift filtering.

(f) Gradient image.

(g) Segmented image.

(h) Image with merged regions.
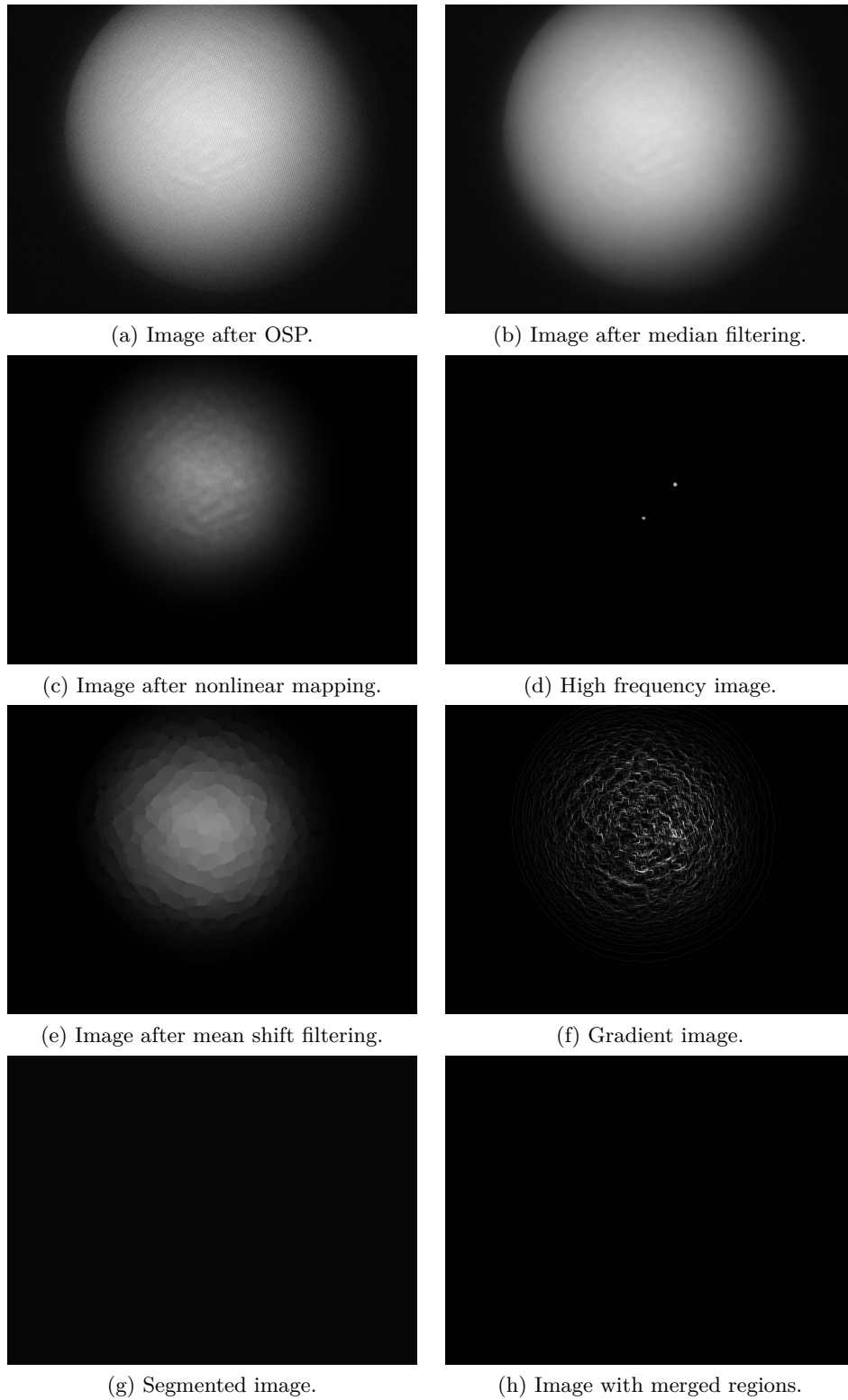
Figure 7.17: Cancer recognition for tissue sample signature - 0/5 (healthy).

(a) Image after OSP.

(b) Image after median filtering.

(c) Image after nonlinear mapping.

(d) High frequency image.

(e) Image after mean shift filtering.

(f) Gradient image.

(g) Segmented image.

(h) Image with merged regions.
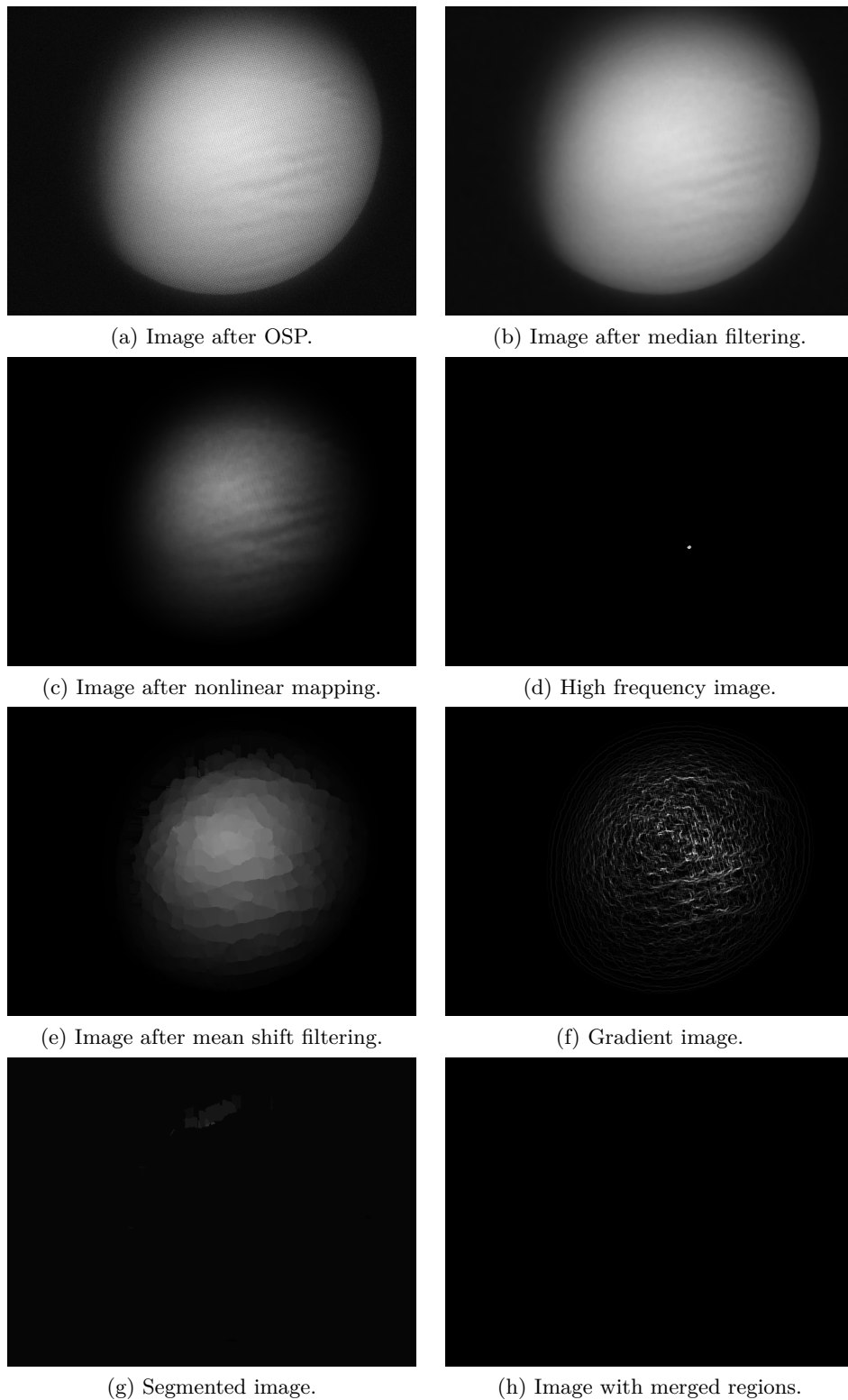
Figure 7.18: Cancer recognition for tissue sample signature - 0/7 (healthy).

Sample signature	Description
15674/1	Skin tissue classified by experts as cancer. Already at OSP image some discontinuities are visible. After removing low frequency disturbance a cancer is clearly visible. The tight concentration of bright edges on gradient image also enabled to find tissue anomalies by mean shift segmentation. However not everything was detected.
15674/5	Skin tissue classified by experts as healthy. No malformation in OSP image, also on high frequency image no cancer symptoms were observed. Gradient image contained only mild edges and finally mean shift segmentation after region merging didn't detect anything. That was the same patient as for tissue 15674/1.
15674/7	Skin tissue classified by experts as cancer. OSP image did not give any unambiguous information. Frequency filtered image gave some suspicion about the location of small regions with cancer. However, mean shift segmentation was more greedy and indicated the bigger area of fluorophore concentration.
15674/9	Skin tissue classified by experts as cancer. That was the same patient as for tissue 15674/7. OSP image looked smooth and safe. However, both filtered and segmented images denoted many cancerous deformations. Gradient image was not very helpful.
15674/11	Skin tissue classified by experts as healthy. Again the same patient as in 15674/7 and 15674/9. Image after OSP transformation looks very smooth. In this case both applied techniques gave the expected result i.e. no cancerous regions of skin were detected.
13602/5	A scar after removal of Basal Cell Carcinoma. Since no histopathology was performed, the condition of skin is unknown. OSP image showed however a place, where cancer was previously located. After filtering or segmenting the image there is no indication that a tissue still suffers from BCC disease.

13602/7	Skin tissue with suspicion of cancer, but histopathology was not available. Already OSP image indicates some areas with higher pixel intensities. After low frequency signal removal there was no doubts that in the left hand side of the image fluorescence phenomenon occurred. The same conclusion could be drawn after looking at segmented or gradient image.
13602/9	Again skin tissue with potential of cancer, but without histopathology investigation. Clear evidence of skin malformation in the left hand part of the image. All utilized algorithms gave very good results.
13952/8	Skin tissue on the nose classified by experts as cancer. Bright point on the OSP image indicated that there is a risk of disease. After frequency filtering or synergistic segmentation a white dot was not eliminated. It suggests that cancerous changes were detected.
13124/5	Suspicious wart on skin tissue. Generally region was classified as healthy. OSP image didn't give precise information about skin condition. However, high frequency and gradient image denoted exact parts where cancerogenesis occurred. For synergistic segmentation those regions were very weak and as a result merged to the background color.
13124/7	Leukoplakia located on the bottom lip. It isn't usually dangerous, but a small percentage of incidents show early signs of cancer. As in the previous case the best results were obtained for filtered and gradient image. Changes detected by mean shift segmentation were again too low and disappeared during merging.
13124/11	A part of tissue in the oesophagus. It was very difficult to take sharp and unblurred multi-spectral images. The result is presented on OSP image, which together with the rest of generated images, didn't give any useful information about cancer occurrence and location.
13124/12	A part of tissue in the oesophagus classified by experts as cancer. As before OPS image is very noisy, but despite of that it is possible to localize brighter regions, which can potentially signalise cancerous regions. Intensity changes were too low to be distinguished by image filtering or mean shift segmentation.

13002/1	Skin tissue on the human back classified by experts as Morbus Bowen cancer. OSP image with nonlinear mapping gave quite good indication where cancer is located. The rest of the job is done by removing low frequency signal from the image. Also synergistic segmentation denotes precisely the position of cancerous changes.
13002/4	Skin tissue on the human chest classified by experts as Basal Cell Carcinoma. Already OSP image denoted some discontinuities in the tissue reflectance spectrum. After removing low frequency perturbation a cancer is very well visible. Two circle areas depicted by gradient image weren't however found by mean shift segmentation. The left hand side region was to weak and wasn't detected by the algorithm.
0/4	Skin tissue on my wrist taken from distance of 1mm. OSP image looked quite smooth and coherently. Very small bright dots were observer for filtered image, however mean shift segmentation was not so sensitive and classified the tissue as unhealthy.
0/5	Skin tissue on my wrist taken from distance of 5mm. The position of camera didn't make any difference. As in the previous case, frequency filtering detected tiny dots of potential interests, but this time only in the number of two occurrences. With high probability they can be treated as an error. Synergistic segmentation gave correct results and this method seems to be less noise sensitive.
0/7	Skin tissue on my wrist taken from distance of 5mm and angle 45°. The direction of the camera also didn't influence the results. Both filtering and image segmentation gave good results and correct indication of no cancer in the tissue.

Table 7.5: The analysis of results for white light

The analysis from table 7.5 gave very optimistic results. All of the presented tissue examples were classified correctly by either image filtering or mean shift segmentation. It was proven that the algorithm is able to recognize healthy and cancerous skin for different and also for the same patient. It was also able to localize diseased tissue on the image very accurately. As the advantage, the process of recognition has several steps. Each of them can help to provide more accurate and reliable diagnosis. Sometimes even single OSP image is enough to get good understanding of tissue condition. In all 18 cases filtering always correctly recognized cancerous changes. Synergistic segmentation was however successful in 16 cases, which is still very good.

It is needed to note that it is difficult to take a multi-spectral photograph of a skin tissue illuminated with white light. Among 27 available samples only 18 could be used. The rest didn't contain any useful information or was very noisy. It means that only 66% of provided samples could be analyzed.

7.5.2 Blue light source

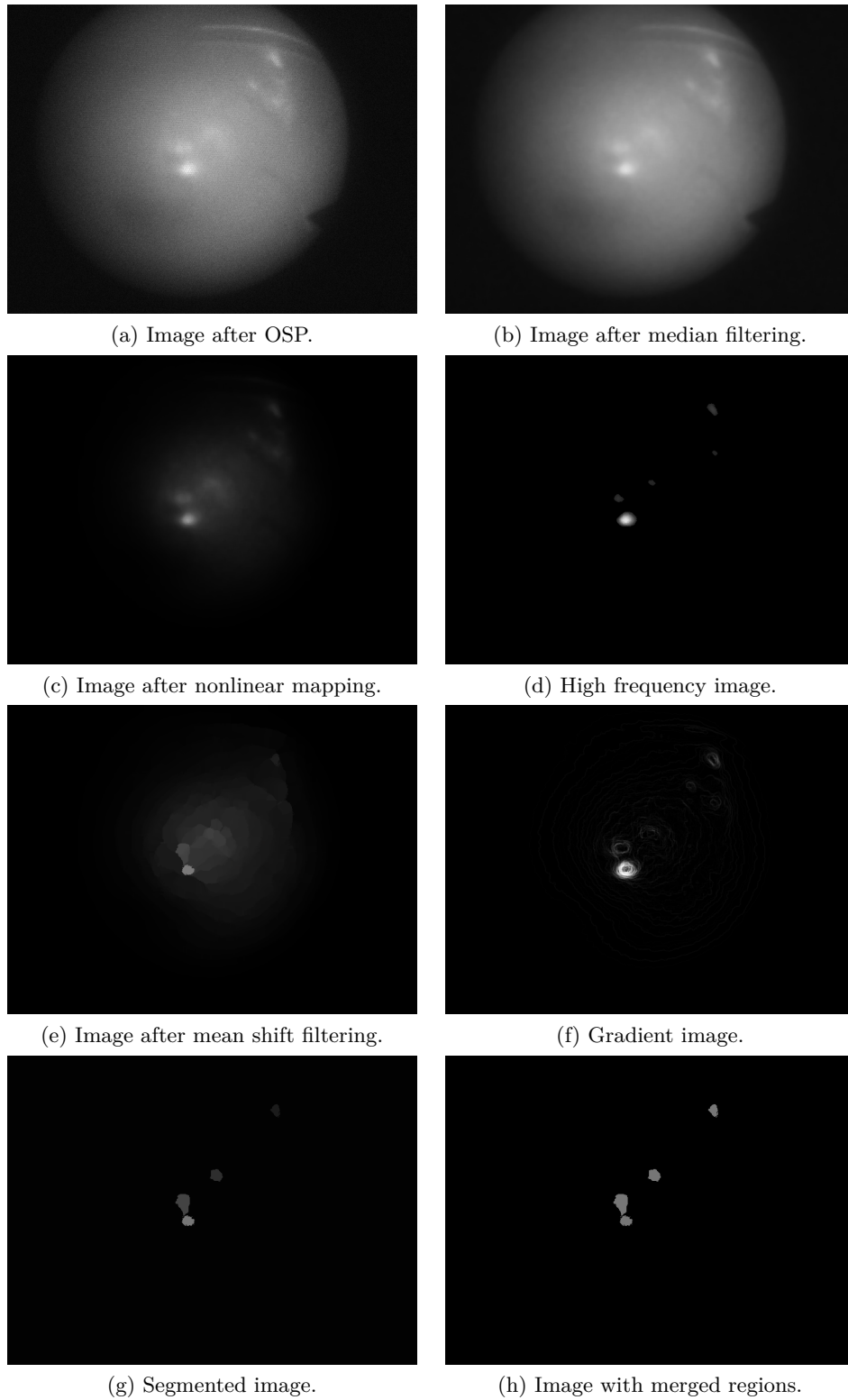When blue light source was applied the results of cancer recognition process looks in the following way.

(a) Image after OSP.

(b) Image after median filtering.

(c) Image after nonlinear mapping.

(d) High frequency image.

(e) Image after mean shift filtering.

(f) Gradient image.

(g) Segmented image.

(h) Image with merged regions.

Figure 7.19: Cancer recognition for tissue sample signature - 13602/6 (cancer).

(a) Image after OSP.

(b) Image after median filtering.

(c) Image after nonlinear mapping.

(d) High frequency image.

(e) Image after mean shift filtering.

(f) Gradient image.

(g) Segmented image.

(h) Image with merged regions.
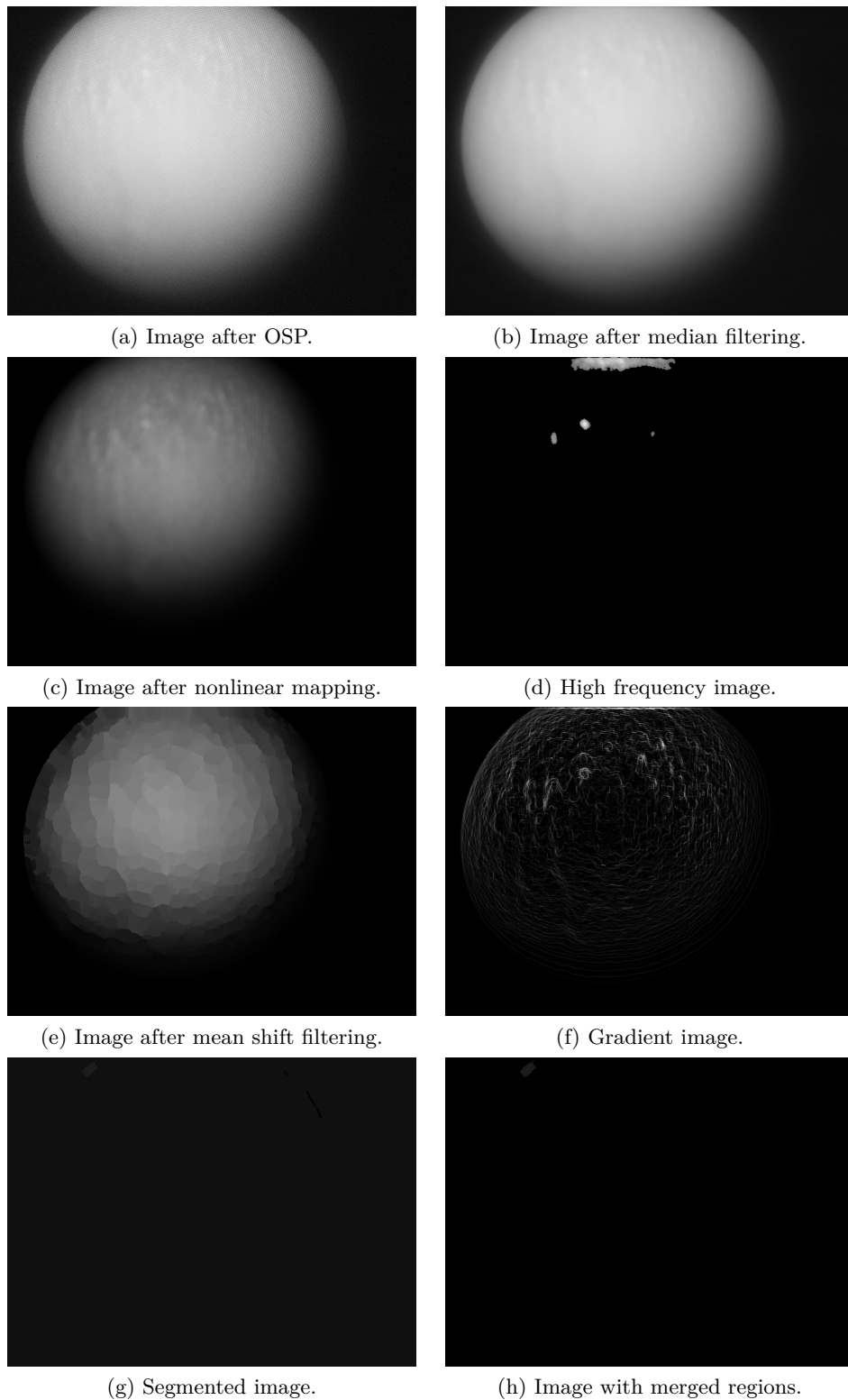
Figure 7.20: Cancer recognition for tissue sample signature - 13602/8 (cancer).

(a) Image after OSP.

(b) Image after median filtering.

(c) Image after nonlinear mapping.

(d) High frequency image.

(e) Image after mean shift filtering.

(f) Gradient image.

(g) Segmented image.

(h) Image with merged regions.
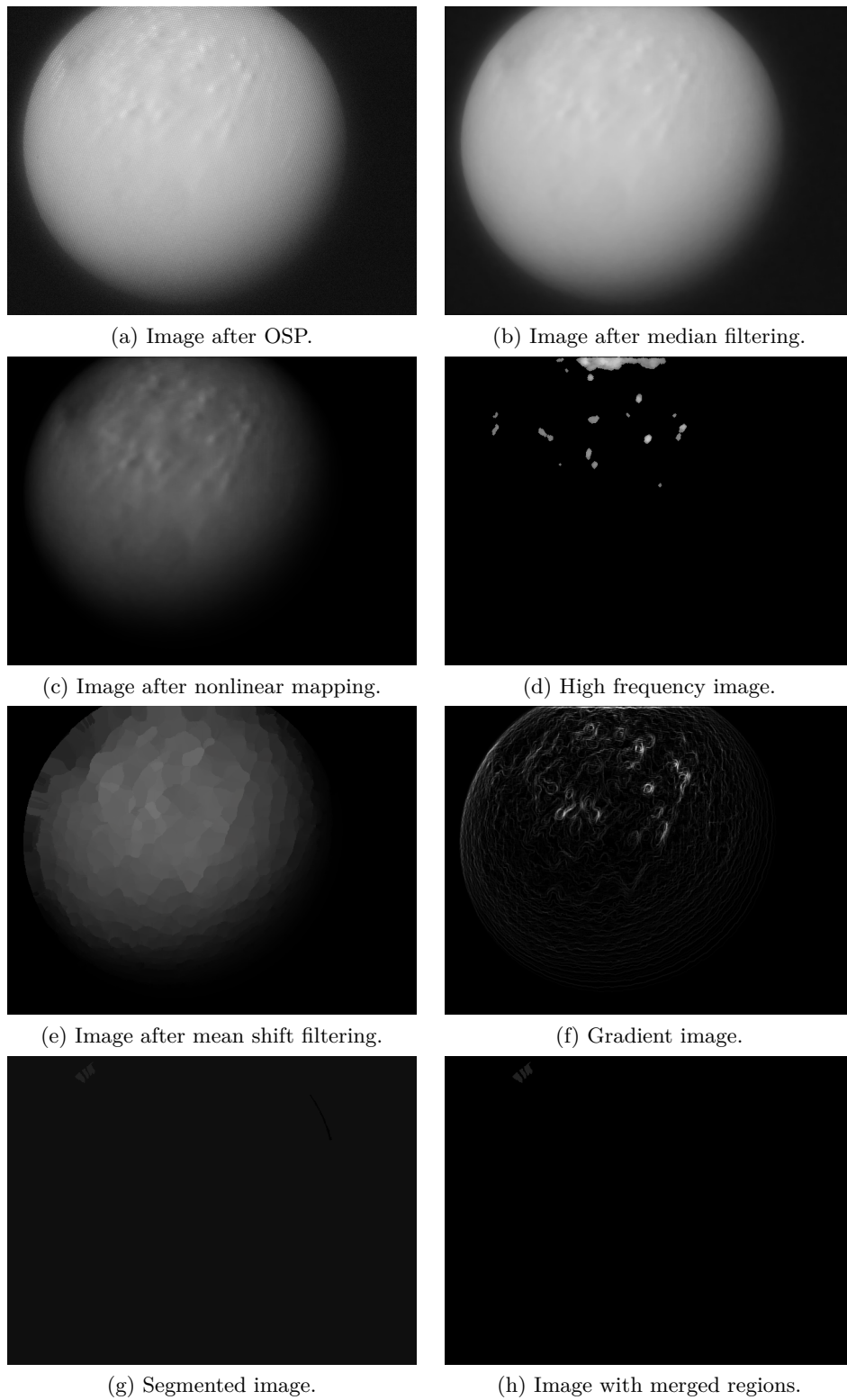
Figure 7.21: Cancer recognition for tissue sample signature - 13602/10 (cancer).

(a) Image after OSP.

(b) Image after median filtering.

(c) Image after nonlinear mapping.

(d) High frequency image.

(e) Image after mean shift filtering.

(f) Gradient image.

(g) Segmented image.

(h) Image with merged regions.
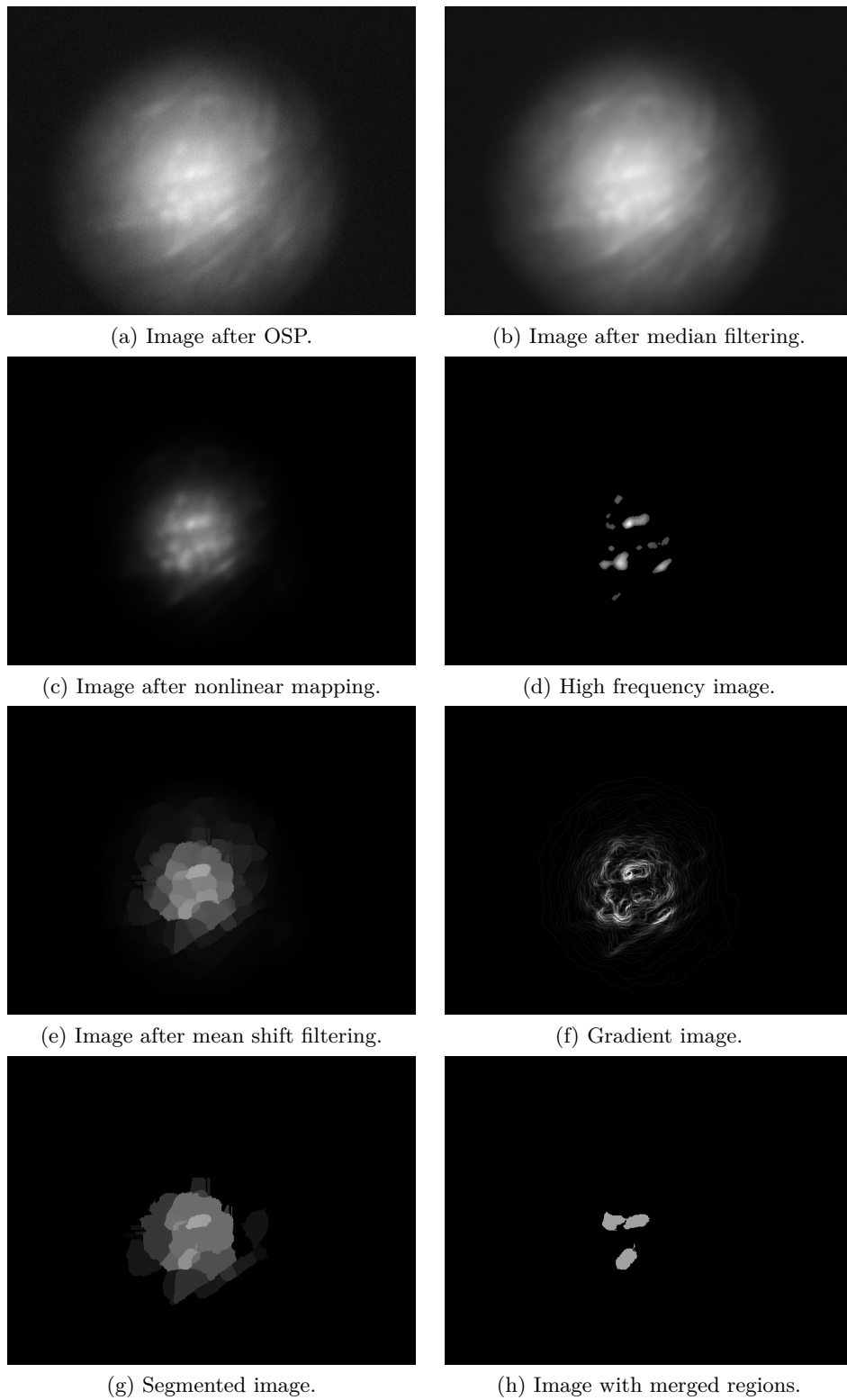
Figure 7.22: Cancer recognition for tissue sample signature - 13124/6 (cancer).

(a) Image after OSP.

(b) Image after median filtering.

(c) Image after nonlinear mapping.

(d) High frequency image.

(e) Image after mean shift filtering.

(f) Gradient image.

(g) Segmented image.

(h) Image with merged regions.
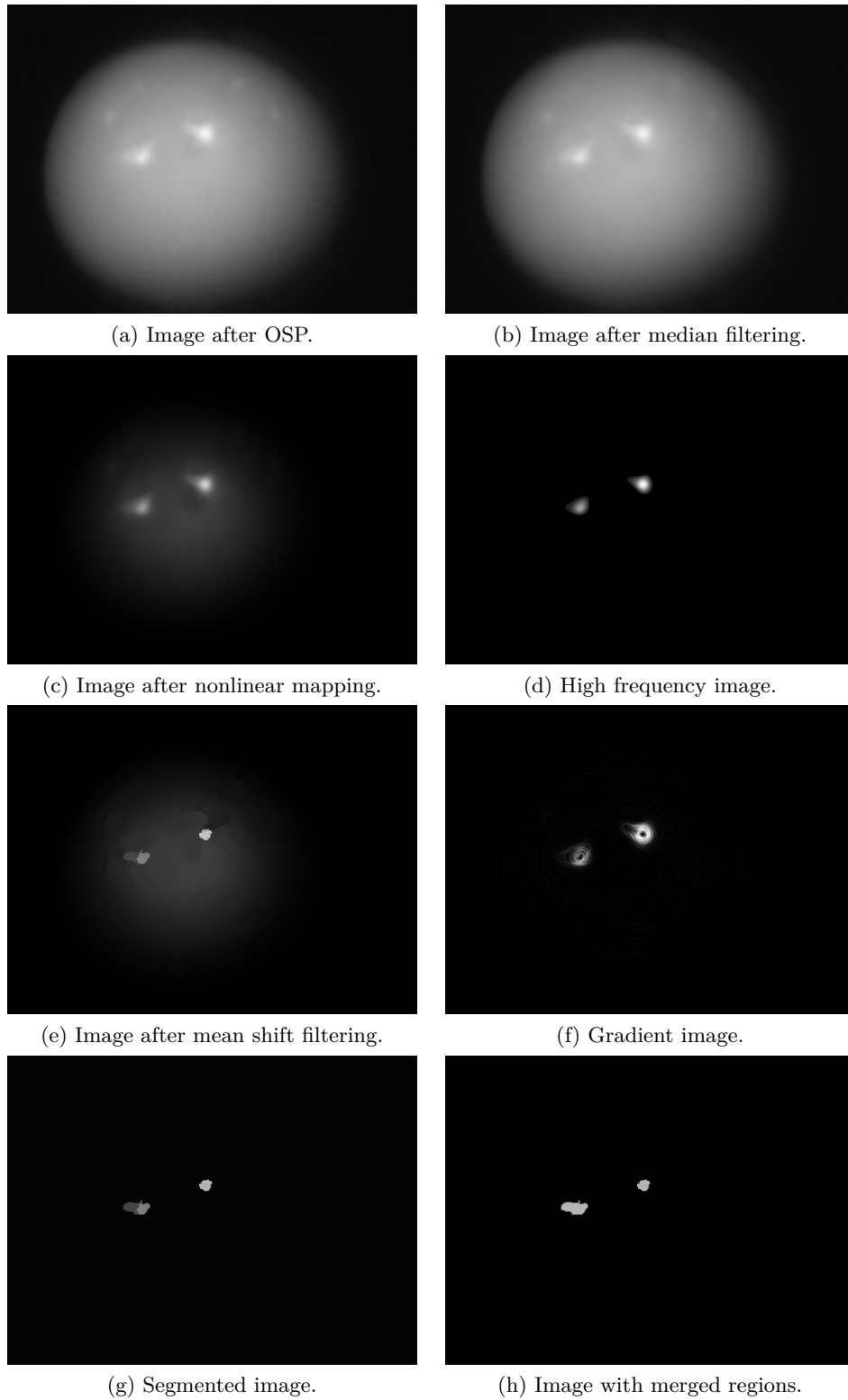
Figure 7.23: Cancer recognition for tissue sample signature - 13124/8 (cancer).

(a) Image after OSP.

(b) Image after median filtering.

(c) Image after nonlinear mapping.

(d) High frequency image.

(e) Image after mean shift filtering.

(f) Gradient image.

(g) Segmented image.

(h) Image with merged regions.
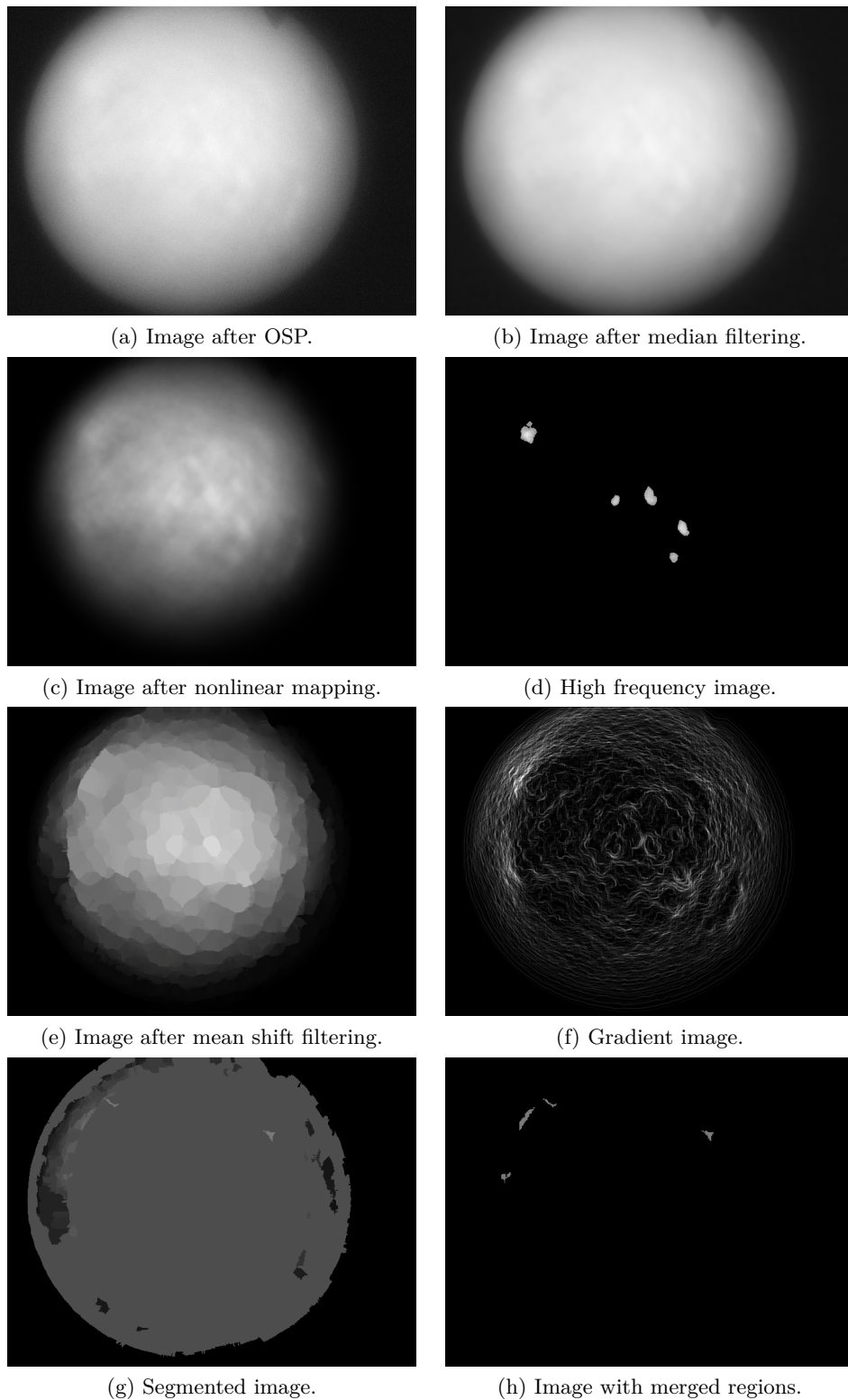
Figure 7.24: Cancer recognition for tissue sample signature - 13002/2 (cancer).

(a) Image after OSP.

(b) Image after median filtering.

(c) Image after nonlinear mapping.

(d) High frequency image.

(e) Image after mean shift filtering.

(f) Gradient image.

(g) Segmented image.

(h) Image with merged regions.
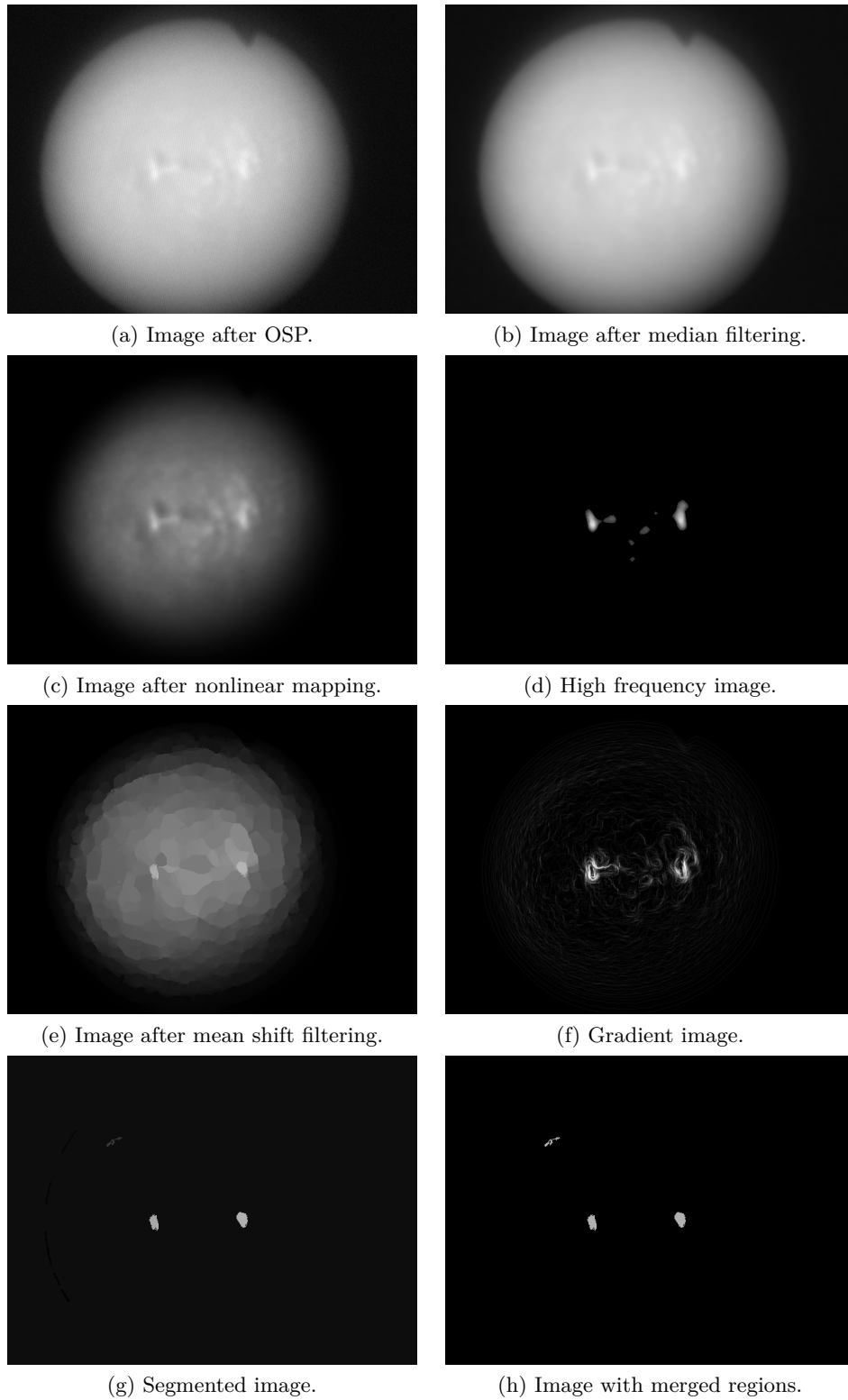
Figure 7.25: Cancer recognition for tissue sample signature - 13002/3 (cancer).

Sample signature	Description
13602/6	A scar after removal of Basal Cell Carcinoma. That was the same patient as for tissue 13602/5 and again there was no histopathology performed before. The camera was in slightly different position than for the white light and already OSP image showed some place of medical interest. Image filtering, gradient image and segmentation method indicated that even after cancer removal BCC was not completely eliminated.
13602/8	Skin tissue without histopathology, but with suspicion of cancer. That was the same patient as for tissue 13602/7. In OSP image some discontinuities are visible, however of very low intensity. Low frequency removal was able to extract those changes. The second technique is not so sensitive and didn't detected a cancer.
13602/10	Skin tissue classified by experts as cancer, but there was no data from histopathology. That was the same patient as for tissue 13602/9. As in the previous cases, only frequency filtering was able to emphasise cancerous changes. Synergistic segmentation was not powerful enough, even with good gradient image.
13124/6	Suspicious wart on skin tissue. The region around was classified as healthy. That was the same patient as for tissue 13124/5. Some indication about possible cancerogenesis. Two image processing methods that were applied, denoted very precisely a places of fluorophore concentration. Both techniques gave good results, but filtering was more accurate.
13124/8	Again Leukoplakia located on the bottom lip. That was the same patient as for tissue 13124/7. Already OSP image presented a couple of places with very bright pixels. Further analysis using filtering, gradient image and mean shift segmentation confirmed that there were two regions, which with high probability can be classified as cancer.

13002/2	Skin tissue classified by experts as Morbus Bowen cancer. That was the same patient as for tissue 13002/1. OSP image looked very smooth and couldn't say anything about tissue condition. However, high frequency image gave more accurate results and also positions of cancerous changes. Image segmentation was not that good any more and classified the tissue incorrectly as healthy.
13002/3	Skin tissue classified by experts as Basal Cell Carcinoma. That was the same patient as for tissue 13002/4. Cancer is very well visible after low frequency removal or performing image segmentation. Also gradient image gave very good indication about the localization of fluorophores.

Table 7.6: The analysis of results for blue light

First of all it turned out that it is extremely difficult to take a multi-spectral photograph of a skin tissue illuminated with blue light. Among 21 available samples only 7 could be used by image recognition algorithms. It is only 33% of all obtained samples. The rest of them was very noisy or there was no data at all. It means that it is easier to take the photo of tissue illuminated with white light. Probably for blue light it is more difficult to find proper camera configuration and obtain sharp images. Also important seems to be the distance to the skin.

The rest of the images were examined in table 7.6 and the outcome is also very satisfactory. Removal of low frequency disturbances always correctly classified skin samples and gave exact position of diseased parts of a tissue. However, mean shift segmentation wasn't that good as for the white light and only for 4 among 7 cases gave the expected results. It seems that for blue light illumination synergistic segmentation cannot correctly recognize intensity changes on the image. Most probably another parameters settings would be needed.

7.5.3 Cancer detection on simulated human skin tissue

As the final experiment a photon mapping algorithm was run, so that fluorescence of Protoporphyrin IX occurred in the middle of the simulated skin structure. The skin tissue was rendered using direct illumination model. Contrast tone mapping algorithm was used. Cancerous changes was modeled with 1000 subsurface photons, which entered the object and left it in different place after a contact with fluorophore. To find a pixel intensity value, 50 neighbor photons were gathered and their influence calculated. The rest of the skin was simulated as direct illumination in order to get consistent appearance. The tissue color spectrum was calculated as the average of all multi-spectral vectors for two tissue samples with different signatures. The skin was illuminated with white light. As the result of

experiment 21 multi-spectral images were created, which were eventually processed by image recognition procedures i.e. frequency filtering and mean shift segmentation.

Surprisingly, the generated color image does not contain cancerous changes. The influence of fluorophore is so low that the skin seems to be healthy. However after applying image processing procedures, already OSP image shows Protoporphyrin IX in the middle and eliminates the tissue color - figure 7.26. After removal of low frequency disturbances only subareas of higher intensities are displayed. More general location of cancer presents synergistic segmentation, which merged also most similar clusters.

This experiments proved again that Monte Carlo model of skin tissue is physically correct and gives expected results also for multi-spectral images. It also shows how difficult it is to find and diagnose the cancer with the unaided eye. In many cases fluorescence effect is simply invisible. In other situations the suspicious area can be a non-dangerous wart or a skin disease not related with cancer. The presented method was able to solve both problems.

As a comparison the same simulation was performed for another tissue color spectrum calculated from different skin signature - figure 7.27. Again cancerous changes are not visible, but the image recognition procedure is able to detect interesting parts of tissue. It also correctly classified images generated for other tissue signatures, but not presented here. It means that the algorithm is able to detect cancer and healthy skin correctly, no matter what color spectrum the background tissue has.

It is important to note that images obtained during image processing for both skin signatures are almost the same. It is because the shape of the surface is in both cases the same and photons have exactly the same localizations and intensities.

(a) Generated image.

(b) Image after OSP.

(c) Image after nonlinear mapping.

(d) High frequency image.

(e) Image after mean shift filtering.

(f) Gradient image.

(g) Segmented image.

(h) Image with merged regions.
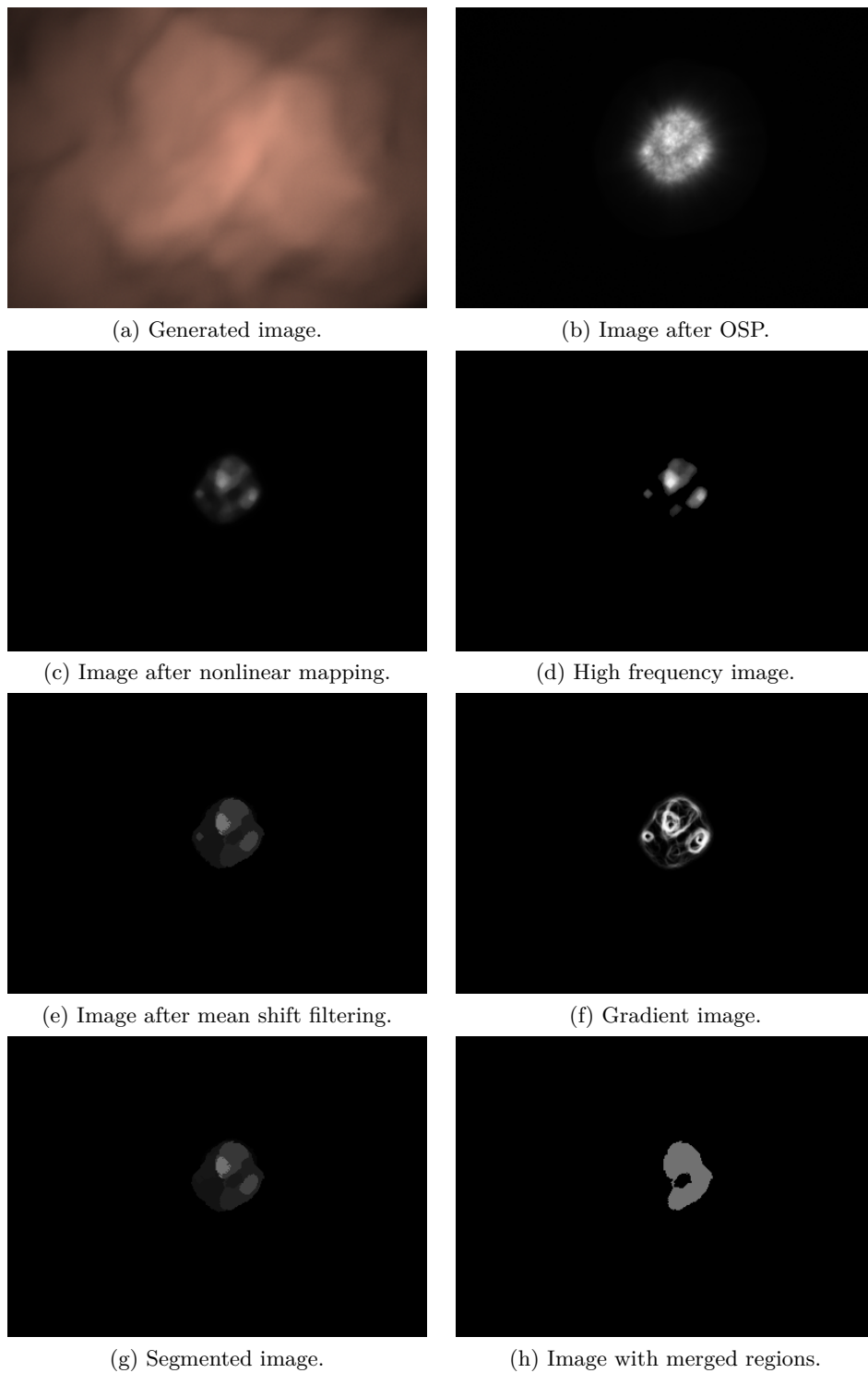
Figure 7.26: Cancer recognition for tissue sample generated using skin background of signature - 13124/7 (cancer detected).

(a) Generated image.

(b) Image after OSP.

(c) Image after nonlinear mapping.

(d) High frequency image.

(e) Image after mean shift filtering.

(f) Gradient image.

(g) Segmented image.

(h) Image with merged regions.
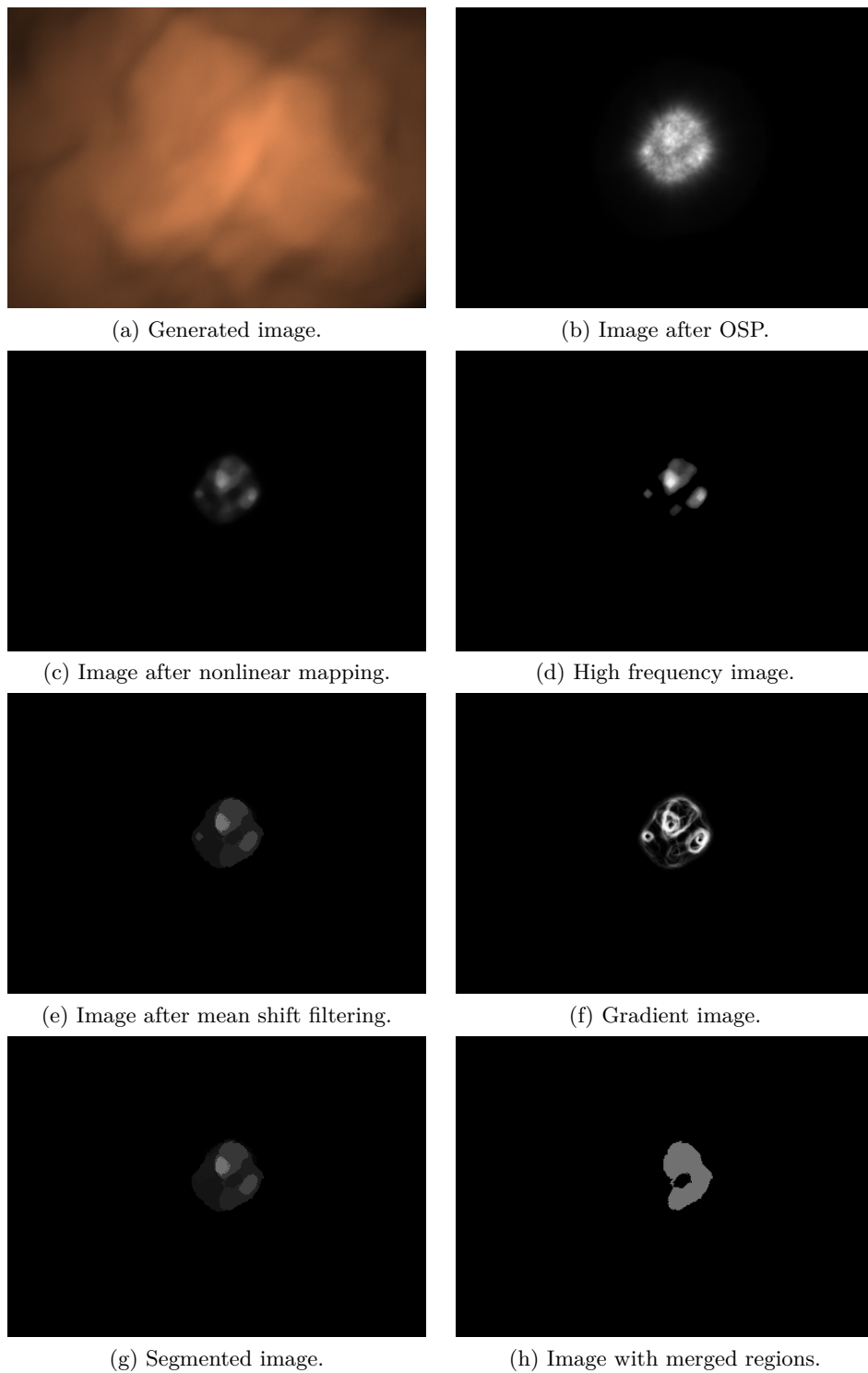
Figure 7.27: Cancer recognition for tissue sample generated using skin background of signature - 13602/9 (cancer detected).

8 Conclusions

The novel aspect of this dissertation is that simulation of light transport in human tissue together with multi-spectral imaging can be applied to find most optimal parameters of endoscope and detect photosensitizer accumulation in cancerous cells simpler and quicker. In order to provide satisfactory results, it was necessary to achieve the goals from chapter 2:

1. **Define parameters and optical model of human skin tissue** - in chapter 4.3 the simplified optical model of human skin tissue was presented. It is a one-layered structure that consists of absorbing, scattering and fluorescent elements. It was assumed that all of those parameters can be calculated as an average of real tissue coefficient. The provided model gave satisfactory results.

2. **Define types and concentration of natural fluorophores in human skin tissue** - in chapter 4.2 all fluorophores existing in human skin tissue were described, including their excitation-emission matrices. However, there is no valid documentation describing how much of given fluorophore a unit volume contains. This value was necessary to compute the probability of photon interaction with fluorescent molecule for the photon mapping algorithm. It was decided to guess those values and analyze obtained results. Since the frequency of occurrence of fluorescence phenomenon is not that important, but the reflectance spectra is the most critical, the proposed simplification was acceptable.

3. **Simulate the propagation of light rays in human skin tissue utilizing photon maps** - in chapter 5 the Monte Carlo algorithm of light transport in turbid media was presented. This technique could be easily converted to photon mapping simulation, including the fluorescence phenomenon. Two types of photon maps were introduced i.e. surface and volumetric. In order to obtain better looking results ray marching method was described. As the important parameter of rendering procedure various types of tone mapping techniques was used. Each of them was later applied in different situations. For the purpose of fluorescence simulation the excitation-emission matrix was defined, which expresses the changes in light spectrum after contact with fluorescent molecule. The whole idea was further used to perform simulation and analyze quantitatively and qualitatively obtained results.

4. **Propose the most efficient light source parameters during photodynamic diagnosis** - chapter 6.2 shows the simulated human skin tis-

sue when different light sources were applied. For blue laser light beam, the biggest contrast between collagen and protoporphyrin was obtained for wavelength equals 400nm. Ideal white light source or Xenon lamp also gave good results, but the level of discrimination is much lower - the influence of collagen is still noticeable. The worst outcome was obtained for Mercury lamp, where both fluorophores were red color. However, it needs to be stressed that collagen is not the only natural fluorophore influencing reflectance spectra, but dominates over the rest components.

5. **Propose the best angle of endoscopic device with respect to tissue surface during photodynamic diagnosis** - the dependence between the light source incident angle and the image quality was presented in chapter 6.2. Generated images suggest that the best position of endoscope is not the angle β equal to $0°$. The optimal direction is also not greater than $30°$. Only quantitative analysis described in chapter 6.4.2 provides better understanding of situation. From the point of view of total energy collected on the tissue surface the maximum value is located somewhere around $\beta = 30°$.

6. **Analyze quantitatively the process of light transport in human skin tissue using photon map algorithm** - the influence of light initial angle of incidence on simulation outcome was presented in quantitative way in chapter 6.4. The number of emitted photons, their total energy, excitant direction, quantum yield and penetration depth were analyzed. General conclusion that can be drawn is that when increasing the angle of incidence more photons get absorbed or reflected from the medium. In such a case more photons energy is stored on the tissue surface and they penetrate the medium less and less deeply. The excitant direction of the photons is opposite to the initial light direction, which is also the expected behavior. Obtained data prove that the mathematical model of human skin tissue and chosen algorithm are mathematically correct and give not biased results. The data investigation also suggest that the best angle of incidence is not $0°$, since for the angle the greatest number of photons get absorbed.

7. **Investigate autofluorescence phenomenon and fluorescence of cancerous human skin tissue with photosensitisers** - chapter 6.5.3 compare the multispectral images for healthy and tissue with Basal Cell Cancer. By simply looking at images a human observer is not able to directly recognize and fully diagnose a cancerous changes. It is better to find a suspicious area, plot its spectrum and compare it with the spectrum of the region that for sure is healthy. If the cancer spectrum contains a characteristic peak around 624nm, then it can suggests that some protporphyrin was there accumulated. Also simple spectrum difference can be done to detect tumor, when as the result almost clean photosensitizer spectrum is obtained. But

it is important to note, that it is not always clear, where healthy or cancerous changes are located. This is why this method is not good enough for photodynamic diagnosis. Additionally in chapter 6.5.6 the reflectance spectrum of healthy human skin from different endoscope configuration was presented. They show that human skin tissue parameters like absorption and scattering influence differently various wavelengths of reflected spectrum. This phenomenon was not taken into account in tissue model to keep the algorithm quick and simple.

8. **Generate images representing human skin tissue with similar appearance and properties like real tissue sample** - the result of photon mapping algorithm as a fully rendered human tissue skin sample was presented in 6.5.4. The aim of this dissertation was not to generate photo-realistic images, but some kind of the presentation that enables to decide whether obtained results are reasonable and can be used in further analysis or not. The most important feature is the spectrum of every rendered pixel. By comparing the reflectance spectra of simulated and real protoporphyrin IX, the similarity is quite good visible. It again proves that proposed model gave physically correct results.

9. **Analyze multi-spectral images and their properties** - the beginning of chapter 7 presents all problems and concerns about multi-spectral images. It is worth to also mention that every image is taken manually by human and slightly from different position, because of camera shaking. This effect is noticeable from image to image, but cannot be removed easily. In order to detect the accumulation of protoporphyrin IX in the human skin in chapter 7.1 Orthogonal Subspace Projection classifier was presented. For every pixel it calculate a measure describing the content photosensitizer in the pixel spectrum. This method is very promising and was used as a basis for further image processing and cancer detection. The choice of classification method was dictated by no information where the cancer is located and if at all it is somewhere. It is difficult to prepare training set, so supervised classification methods couldn't be applied.

10. **Propose the most optimal methods of using multi-spectral images in photodynamic diagnosis** - after pixel classification presented in chapter 7.1 it was necessary to separate regions with cancer from healthy parts of a tissue. For that purpose two unsupervised classifying techniques were presented. The first idea covered non-linear mapping with low frequency signal removal. The second conception utilized mean shift segmentation enhanced with edge detection for better region recognition. Both proposals gave successful results, as it can be seen in chapters 7.5.1 and 7.5.2.

11. **Compare multi-spectral images of human skin tissue with multispectral images generated during photon mapping simulation**

- finally in chapter 7.5.3 human tissue samples was simulated by photon mapping and as the result also multi-spectral images were produced. Those sequences of spectral images were the subject of cancer recognition methods described in previous chapters. In both cases the proposed techniques were able to correctly detect diseased regions. It again proves that Monte Carlo simulation of light transport in human skin tissue was implemented correctly and give accurate results.

By finishing all those tasks, it was possible to prove and show the correctness of all thesis formulated in chapter 2. The list of tasks that were fulfilled in the scope of given thesis is presented below. The successful realization of all of them can be considered as a proof of selected thesis.

1. **It is possible to create mathematical model of subsurface light transport of chosen human tissue, defined by absorption, scattering and fluorescence phenomenon.**

   - Define parameters and optical model of human skin tissue,
   - Define types and concentration of natural fluorophores in human skin tissue,

2. **It is possible create such a model, which basing on the Monte Carlo method is able to generate multi-spectral images qualitatively compliant with real multi-spectral images taken during photodynamic diagnosis.**

   - Simulate the propagation of light rays in human skin tissue utilizing photon maps,
   - Analyze quantitatively the process of light transport in human skin tissue using photon map algorithm,
   - Investigate autofluorescence phenomenon and fluorescence of cancerous human skin tissue with photosensitisers,
   - Generate images representing human skin tissue with similar appearance and properties like real tissue sample,
   - Analyze multi-spectral images and their properties
   - Compare multi-spectral images of human skin tissue with multispectral images generated during photon mapping simulation

3. **The created model enables to optimize the chosen parameters of image acquisition process like light incident angle, the light source spectrum or the distance to the investigated tissue surface and enables to unambiguously distinguish between cancerous and healthy tissue sample.**

   - Propose the most efficient light source parameters during photodynamic diagnosis,

- Propose the best angle of endoscopic device with respect to tissue surface during photodynamic diagnosis,
- Propose the most optimal methods of using multi-spectral images in photodynamic diagnosis

Summarizing it was possible to provide good human skin tissue model with properties similar to real skin signatures. The Monte Carlo algorithm extended by light optical properties, photon mapping and fluorescence phenomenon gave accurate details about processes that happen below the tissue surface. Observations about reflected spectrum could be utilized to apply Orthogonal Subspace Projection on real multi-spectral images. The algorithm was able to correctly detect tumor and healthy human skin tissue in almost 100% cases for white and blue light sources. The obtained results are very promising. As the future work it would be challenging to adjust this method to internal parts of the human body like oesophagus or stomach.

9 Streszczenie

Pojęcie diagnozy fotodynamicznej zostało wprowadzone już na początku lat 80'. Diagnoza fotodynamiczna wykorzystuje zjawisko fluorescencji w cząsteczkach endo- i egzogennych występujące w tkankach ludzkich. Specjalne substancje o właściwościach fluorescencyjnych są wprowadzane do krwiobiegu, a następnie gromadzone w komórkach rakowych cechujących się szybszą przemianą materii. Pod wpływem oświetlenia o odpowiedniej długości fali, tkanki rakowe mogą być rozpoznawane poprzez zwiększone natężenie koloru czerwonego w widmie odbitym. Substancja odpowiedzialna za to zjawisko to Protoporfiryna IX występująca w procesie syntezy hemoglobiny. Istnieją także naturalne substancje występujące w tkankach ludzkich, które pod wpływem światła laserowego wykazują właściwości fluorescencyjne. Kontrast między tkanką zdrową a rakową wynika z różnego rozproszenia endogennych cząsteczek fluorescencyjnych w tkance oraz innego widma emisji światła. Głównymi fluoroforami w warstwie nabłonkowej są tryptofan, dinukleotyd nikotynamidoadeninowy (NADH) oraz dinukleotyd flawinoadeninowy (FAD), natomiast w skórze właściwej są to włókna kolagenowe.

W celu dokładnego zbadania zjawiska fluorescencji w tkance ludzkiej zaproponowany został matematyczny model, który wiernie odzwierciedla proces transportu, załamania, rozproszenia i absorpcji światła. Zdefiniowano parametry tkanki skóry, substancje wchodzące w jej skład, ich właściwości, ilość oraz macierze EEM (*Excitation Emission Matrix*) pozwalające określić widmo emitowanego światła dla danego widma światła pobudzenia. Symulacja wykorzystuje metodę Monte Carlo polegającą na śledzeniu promieni wysłanych ze źródła światła, po których przemieszcza się cząsteczka nazywana umownie fotonem. W momencie, gdy dojdzie do kontaktu pomiędzy fotonem a powierzchnią rozpraszającą, jego położenie, kierunek oraz energia zapisywana jest w specjalnej strukturze zwanej mapą fotonową. Jeśli wymagana liczba promieni została wyemitowana oraz zgromadzona odpowiednia liczba fotonów , to otrzymane w ten sposób dane mogą zostać użyte w procesie renderingu i wyliczania koloru piksela w określonym miejscu na ekranie. Metoda ta jest szeroko używana przez grupę algorytmów wykorzystujących techniki śledzenia promieni, włączając w to mapowanie fotonów.

W celu zwiększenia dokładności algorytmu, poza mapami fotonowymi zawierającymi dane dotyczące oświetlenia na powierzchni tkanki, wprowadzono także mapy wolumetryczne. Posiadają one informacje o energii fotonów wewnątrz badanej struktury. Otrzymane w ten sposób dodatkowe informacje pozwalają na lepsze zrozumienie zjawiska fluorescencji w tkance ludzkiej oraz przeprowadzenie analizy jakościowej i ilościowej wygenerowanych obrazów.

Badania pokazały, że dla wiązki laserowej w kolorze niebieskim największy

kontrast pomiędzy kolagenem a cząsteczkami protoporfiryny zaobserwowano dla długości fali wynoszącej 400nm. Idealne światło białe oraz lampa xenonowa także dały zadowalające wyniki, jednakże gorsze od światła laserowego. Z uwagi na znaczne podobieństwa w widmie odbitym, lampa typu Merkury nie nadaje się do tego rodzaju badań.

Przeprowadzono także ilościowe badania wpływu kąta padania promieni światła na wyniki symulacji. Liczba emitowanych fotonów, energia całkowita, kąt opuszczenia tkanki, wydajność kwantowa oraz głębokość to parametry, których rozkład został przeanalizowany. Im większy kąt początkowy, tym większa energia fotonów i większa ich liczba odbija się od powierzchni tkanki, a ich kąty wyjścia są skierowane w kierunku odpowiadającym odbiciu lustrzanemu. Otrzymane wyniki nie są zaskakujące i sugerują, że najlepszy kierunek padania promieni światła to nie 0°, kiedy to największa liczba fotonów ulega absorpcji. Biorąc pod uwagę jakość wygenerowanych obrazów i dane ilościowe dotyczące energii całkowitej zgromadzonej na powierzchni skóry sugerowany kąt to około 30°.

Opisany model w połączeniu z obrazami wielospektralnymi znajduje zastosowanie w medycynie i pozwala na szybkie wykrycie oraz zdiagnozowanie zmian nowotworowych tkanki ludzkiej skóry. Specjalne filtry podatne tylko na wybraną długość fali są w stanie zarejestrować natężenie światła dla jednej tylko jej składowej. Powstające w ten sposób obrazy wielospektralne zawierają informacje niewidoczne w normalnych warunkach dla ludzkiego oka. Zdjęcia, które były dostępne w czasie badań posiadały tę właściwość, że każdemu pikselowi odpowiadało widmo światła odbitego zdefiniowane pomiędzy 400nm-720nm i częstotliwością próbkowania wynoszącą 16nm.

W ten sposób porównano widma tkanki skóry dla różnych konfiguracji źródła światła, czyli odległości od powierzchni i kąta padania. Przygotowano także zestawienie widma tkanki zdrowej z widmem tkanki dotkniętej zmianami nowotworowymi po zaaplikowaniu fotouczulacza. Charakterystyczna wartość szczytowa w okolicach 624nm jasno sugerowała lokalizację fragmentu tkanki ze zmianami nowotworowymi. Co więcej, porównano widmo protoporfiryny z obrazów wielospektralnych z widmem wygenerowanym metodą map fotonowych. Podobieństwo było bardzo widoczne. Sugeruje to ponownie, że proponowany model tkanki skóry z fizycznego punktu widzenia jest poprawny.

Jednakże nie zawsze da się w prosty sposób wskazać miejsca co do których istnieje podejrzenie nowotworu. W tym celu wykorzystano metodę *Orthogonal Subspace Projection*, która dla każdego piksela oblicza miarę określającą zawartość widma protoporfiryny w danym widmie sumarycznym. Otrzymany w ten sposób czarno-biały obraz poddano dalszej obróbce graficznej. Między innymi poprzez segmentację oraz usuwanie niektórych składowych obrazu udało się wyizolować zmiany nowotworowe w tkance. Metodę tę zastosowano z powodzeniem dla próbki około 25 rzeczywistych obrazów wielospektralnych. Opisany algorytm

także prawidłowo wykrywa obszary nowotworowe w obrazach wygenerowanych metodą Monte Carlo. Po raz kolejny pokazuje to słuszność i dokładność przedstawionego modelu ludzkiej skóry.

W wyniku wszystkich przeprowadzonych badań udało się wykazać, że możliwe jest stworzenie matematycznego modelu podpowierzchniowego transportu światła w wybranych fragmentach tkanki ludzkiej, obejmującego zjawiska absorpcji, rozpraszania, a także fluorescencji. Dzięki stworzeniu symulacji komputerowej opartej na metodzie Monte Carlo, udało się wygenerować obrazy wielospektralne, które są jakościowo zgodne z rzeczywistymi obrazami powstałymi w czasie diagnozy fotodynamicznej. Uzyskanie zgodności pomiędzy obrazami otrzymanymi w wyniku symulacji a realnymi obrazami wielospektralnymi, pozwoliło na dokładniejszą analizę procesu akwizycji zdjęć w celu jej uproszczenia oraz optymalizacji. Z tego powodu wpływ takich parametrów jak m.in. kąt padania promieni światła na tkankę, widmo optyczne źródła światła i jego odległość od badanej tkanki został poddany szczególnej analizie. W połączeniu z metodami przetwarzania obrazów wielospektralnych udało się w znaczący sposób przyspieszyć przygotowanie diagnozy oraz jednoznacznie rozróżnić tkankę zdrową od chorej. Ma to szczególne znaczenie, gdyż wszystkie badania zmierzające do ustalenia optymalnych parametrów obrazowania wymagają zebrania danych oraz akwizycję zdjęć od rzeczywistych pacjentów cierpiących z powodu rożnego rodzaju zmian nowotworowych. Na podobieństwo, bądź też unikalność otrzymanych zdjęć wpływają dodatkowo warunki przeprowadzonych badań, które nie zawsze mogą być jednakowe. Dodatkowo koszt odpowiedniej aparatury i jej dostępność znacząco ogranicza możliwości przeprowadzania eksperymentów oraz analizy otrzymanych wyników. Biorąc pod uwagę wszystkie wymienione czynniki, zaproponowany model tkanki i transportu światła pozwoli na lepsze zrozumienie procesów i zjawisk zachodzących zaraz pod powierzchnią tkanki i zoptymalizowanie diagnozy fotodynamicznej bez konieczności angażowania w tym celu lekarzy, pacjentów i kosztownej aparatury.

Bibliography

[1] Latos W., Kawczyk-Krupka A., Ledwon A., Kosciarz-Grzesiok A., Misiak A., Sieron-Stoltny K., and A. Sieron. The role of autofluorescence colonoscopy in diagnosis and management of solitary rectal ulcer syndrome. *Biomedical Optics. Imaging, Manipulation and analysis of Biomolecules, Cells and Tissues VI. Cell and tissue functional imaging.*, 2008.

[2] Zhu C., Liu Q., and Ramanujam N. Effect of fiber optic probe geometry on depth-resolved fluorescence measurements from epithelial tissues: a monte carlo simulation. *Journal of Biomedical Optics*, 8(2):237–247, 2003.

[3] Ledwon A., Bieda R., Kawczyk-Krupka A., Polanski A., Wojciechowski K., Sieron-Stoltny K., and Sieron A. The possibilities of improvement the sensitivity of cancer fluorescence diagnostics by computer image processing. *Biomedical Optics. Biomedical Optics.Imaging, Manipulation and analysis of Biomolecules, Cells and Tissues VI. Advances in Bioimaging: Computation and Image Analysis.*, 2008.

[4] Dacosta R.S., Andersson H., and Wilson B.C. Molecular fluorescence excitation-emission matrices relevant to tissue spectroscopy. *Photochem Photobiol.*, 78(4):384–392, 2003.

[5] Svanberg K., Liu DL., Wang I., Andersson-Engels S., Stenram U., and Svanberg S. Photodynamic therapy using intravenous d-aminolaevulinic acid-induced protoporphyrin ix sensitisation in experimental hepatic tumours in rats. *British Journal of Cancer*, 74:1526–1533, 1996.

[6] Sil S., Bose T., Roy D., and Chakraborti A. S. Protoporphyrin ix-induced structural and functional changes in human red blood cells, haemoglobin and myoglobin. *Journal of Biosciences*, 29(3):281–291, 2004.

[7] Ramanujam N. Fluorescence spectroscopy in vivo. *Encyclopedia of Analytical Chemistry.*, 1:20–56, 2000.

[8] Enejder A. *Light scattering and absorption in tissue - models and measurements.* PhD thesis, Lund University., 1997.

[9] Johansson A. *Spectroscopic Techniques for Photodynamic Therapy Dosimetry.* PhD thesis, Lund University., 2007.

[10] Russell J. A., Diamond K. R., Collins T. J., Tiedje H. F., Hayward J. E., Farrell T. J., Patterson M. S., and Fang Q. Characterization of fluorescence lifetime of photofrin and delta-aminolevulinic acid induced protoporphyrin ix in living cells using single- and two-photon excitation. *IEEE journal of selected topics in quantum electronics*, 14(1):158–166, 2008.

[11] Sokolov K., Follen M., and Richards-Kortum R. Optical spectroscopy for detection of neoplasia. *Current Opinion in Chemical Biology*, 6(5):651–658, 2002.

[12] Nielsen K. P., Zhao L., Stamnes J. J., Stamnes K., and Moan J. The optics of human skin: Aspects important for human health. *In proceedings from the symposium 'Solar Radiation and Human Health'*, 2008.

[13] Wilkie A., Tobler R. F., and Purgathofer W. Combined rendering of polarization and fluorescence effects. *Proceedings of the 12th Eurographics Workshop on Rendering Techniques*, pages 197–204, 2001.

[14] Prahl S. A. *Light transport in tissue.* PhD thesis, The University of Texas at Austin., 1988.

[15] Yavari N. *Optical spectroscopy for tissue diagnostics and treatment control.* PhD thesis, Department of Physics and Technology, University of Bergen, 2006.

[16] Zeng H. *Human skin optical properties and autofluorescence decay dynamics.* PhD thesis, The University of British Columbia., 1993.

[17] Marschner S. R., Westin S. H., Lafortune E. P. F., Torrance K. E., and Greenberg D. P. Image-based brdf measurement including human skin. *In Proceedings of 10th Eurographics Workshop on Rendering.*, pages 139–152, 1999.

[18] Jensen H. W. Global illumination using photon maps. *Proceedings of the eurographics workshop on Rendering techniques '96*, pages 21–30, 1996.

[19] B. Jalil. Multispectral image processing applied to dermatology. Master's thesis, Université de Bourgogne, 2008.

[20] K. Krishnamurthy. *Spectral Image Processing Theory and Methods: Reconstruction, Target Detection, and Fundamental Performance Bounds.* PhD thesis, Department of Electrical and Computer Engineering, Duke University, 2011.

[21] J. C. Harsanyi and C-I Chang. Hyperspectral image classification and dimensionality reduction: An orthogonal subspace projection approach. *IEEE Transactions on geoscience and remote sensing*, 32(4):779–785, 1994.

[22] Jensen H.W., Marschner S.R., Levoy M., and Hanrahan P. A practical model for subsurface light transport. *In Proceedings to Siggraph*, pages 511–518, 2001.

[23] Dorsey J., Edelman A., Jensen H. W., Legakis J., and Pedersen H. K. Modeling and rendering of weathered stone. *In Proceedings of Siggraph*, pages 225–234, 1999.

[24] Gutierrezy D., Munoz A., Anson O., and Seron F. J. Non-linear volume photon mapping. *Eurographics Symposium on Rendering*, 2005.

[25] Donner C. and H.W. Jensen. Rendering translucent materials using photon diffusion. *Eurographics Symposium on Rendering*, pages 234–251, 2007.

[26] Donner C. and Jensen H. W. Light diffusion in multi-layered translucent materials. *International Conference on Computer Graphics and Interactive Techniques.*, pages 1032–1039, 2005.

[27] Jacques S. L. Light distributions from point, line and plane sources for photo-chemical reactions and fluorescence in turbid biological tissues. *Photochemistry and Photobiology*, 67(1):23–32, 1998.

[28] Zeng H., MacAulay C., McLean D. I., and Palcic B. Reconstruction of in vivo skin autofluorescence spectrum from microscopic properties by monte carlo simulation. *Journal of Photochemistry and Photobiology B*, 38:234–240, 1997.

[29] Jakobsson A. and Nilsson G. E. Prediction of sampling depth and photon pathlength in laser doppler flowmetry. *Medical & biological engineering & computing.*, 31(3):301–307, 1993.

[30] Quan L., Nimunkar A., and Hagl D. M. Verification of monte carlo modeling of fluorescence in turbid medium. *Optical Society of America*, 2001.

[31] Song Z., Dong K., Hu X. H., and Lu J. Q. Monte carlo simulation of converging laser beams propagating in biological materials. *Applied Optics*, 38(13):2944–2949, 1999.

[32] Eker C. *Optical Characterization of tissue for medical diagnostics.* PhD thesis, Department of Physics. Lund Institute of Technology, 1999.

[33] N.M. Marin. *Autofluorescence and diffuse reflectance patterns in cervical spectroscopy.* PhD thesis, The University of Texas at Austin, 2005.

[34] Drakaki E., Makropoulu M., and Serafetinides A. A. In vitro fluorescence measurements and monte carlo simulation of laser irradiation propagation in porcine skin tissue. *Lasers in medical science*, 23(3):267–276, 2008.

[35] Barton J. K., Pfefer T. J., Welch A. J., Smithies D. J., Nelson J. S., and van Gemert M. J. C. Optical monte carlo modeling of a true port wine stain anatomy. *Optics Express*, 2(9):391–396, 1998.

[36] Wang CY., Lin JK., and Chiang H. K. Autofluorescence spectroscopy to identify normal and cancerous colorectal tissues. *Proceedings of the 20th Annual International Conference of the IEEE Engineering in Medicine and Biology Society*, 20(2):967–969, 1998.

[37] Huang Z., Chia TC., Krishnan S. M., and Seow C. Study of laser autofluorescence of human colon tissues. *Proceedings of the 20th Annual International Conference of the IEEE Engineering in Medicine and Biology Society.*, 20(6):2963–2966, 1998.

[38] Wei HJ., Xing D., Lu JJ., Gu HM., Wu GY., and Jin Y. Determination of optical properties of normal and adenomatous human colon tissues in vitro using integrating sphere techniques. *World Journal of Gastroenterology*, 11(16):2413–2419, 2005.

[39] Prince S. and Malarvizhi S. Estimation of optical properties of normal and diseased tissue based on diffuse reflectance spectral model. *Proceedings of the World Congress on Engineering*, 1:578–582, 2010.

[40] Li Y., Li M., and Xu T. Quantitative time-resolved fluorescence spectrum of the cortical sarcoma and the adjacent normal tissue. *Journal of fluorescence*, 17(6):643–648, 2007.

[41] Katikaa K. M., Pilona L., Dippleb K., Levinc S., Blackwell J., and Berberoglu H. In-vivo time-resolved autofluorescence measurements on human skin. *Proceedings of the SPIE*, 6078:83–93, 2006.

[42] Perelman L. T., Wu J., Itzkan I., and Feld M. S. Photon migration in turbid media using path integrals. *Physical Review Letters*, 72(9):1341–1344, 1994.

[43] Wilkie A., Weidlich A., Larboulette C., and Purgathofer W. A reflectance model for diffuse fluorescent surfaces. *In Proceedings of Graphite*, pages 321–328, 2006.

[44] Adiga U., Malladi R., Fernandez-Gonzalez R., and de Solorzano C. O. High-throughput analysis of multispectral images of breast cancer tissue. *IEEE transactions on image processing.*, 15(8):2259–2268, 2006.

[45] S. Derrode, G. Mercier, and W. Pieczynski. Unsupervised multicomponent image segmentation combining a vectorial hmc model and ica. *IEEE International Conference on image processing*, 2003.

[46] F. Woolfe, M. Maggioni, G. Davis, F. Warner, R. Coifman, and S. Zucker. Hyperspectral microscopic discrimination between normal and cancerous colon biopsies. *IEEE Transactions on medical imaging and remote sensing*, 99(99), 1999.

[47] Jensen H. W. and Buhler J. A rapid hierarchical rendering technique for translucent materials. *ACM Transactions on Graphics (Siggraph)*, 21(3):576–581, 2002.

[48] Mertens T., Kautz J., Bekaert P., Van Reeth F., and Seidel H.P. Efficient rendering of local subsurface scattering. *Computer Graphics Forum*, 24(1):41–49, 2005.

[49] Zeng H., MacAulayl C.and McLean D. I., Palcic B., and Lui H. The dynamics of laser-induced changes in human skin autofluorescence - experimental measurements and theoretical modeling. *Photochemistry and Photobiology*, 68(2):227–236, 1998.

[50] Wang L. and Jacques S.L. *Monte Carlo Modeling of Light Transport in Multi-layered Tissues in Standard C.* University of Texas M. D. Anderson Cancer Center, 1992.

[51] Tuchin V. V. Light scattering study of tissues. *Physics - Uspekhi*, 40(5):495–515, 1997.

[52] J. Rodes, J. P. Benhamou, A. Blei, J. Reichen, and M. Rizzetto. *The Textbook of Hepatology: From Basic Science to Clinical Practice.* Wiley-Blackwell, 3rd edition, 2007.

[53] Zonios G.I., Cothren R.M., Arendt J.T., Wu J., Van Dam J., Crawford J.M., Manoharan R., and M.S. Feld. Morphological model of human colon tissue fluorescence. *IEEE Transactions on Biomedical Engineering*, 43(9), 1993.

[54] Li BH. and Xie SS. Autofluorescence excitation-emission matrices for diagnosis of colonic cancer. *World J Gastroenterol*, 11(25):3931–3934, 2005.

[55] Aubin J. E. Autofluorescence of viable cultured mammalian cells. *The journal of histochemistry and cytochemistry*, 27(1):36–43, 1979.

[56] Diamond K. R., Farrell T. J., and Patterson M. S. Measurement of fluorophore concentrations and fluorescence quantum yield in tissue-simulating phantoms using three diffusion models of steady-state spatially resolved fluorescence. *Physics in medicine and biology.*, 48:4135–4149, 2003.

[57] Young A. R. Chromophores in human skin. *Phys. Med. Biol.*, 42:789–802, 1997.

[58] Meglinski I. V. and Matcher S. J. Computer simulation of the skin reflectance spectra. *Computer Methods and Programs in Biomedicine*, 70(2):179–186, 2003.

[59] Palmer G. M. and Ramanujam N. Monte-carlo-based model for the extraction of intrinsic fluorescence from turbid media. *Journal of Biomedical Optics*, 13(2), 2008.

[60] Stepp H., Beck T., Beyer W., Pfaller C., Schuppler M., Sroka R., and Baumgartner R. Measurement of fluorophore concentration in turbid media by a single optical fiber. *Medical Laser Application.*, 22:23–34, 2007.

[61] Drezek R., Sokolov K., Utzinger U., Boiko I., Malpica A., Follen M., and Richards-Kortum R. Understanding the contributions of nadh and collagen to cervical tissue fluorescence spectra: Modeling, measurements, and implications. *Journal of Biomedical Optics.*, 6(4):385–396, 2001.

[62] Long R. and McShane M. J. Modeling of selective photon capture for collection of fluorescence emitted from dermally-implanted microparticle sensors. *Engineering in Medicine and Biology Society. 29th Annual International Conference of the IEEE*, pages 2972–2975, 2007.

[63] Welch A.J., Gardner C., Richards-Kortum R., Chan E., Criswell G., Pfefer J., and Warren S. Propagation of fluorescent light. *Lasers in Surgery and Medicine.*, 21:166–178, 1997.

[64] Ma G., Delorme J. F., Gallant P., and Boas D. A. Comparison of simplified monte carlo simulation and diffusion approximation for the fluorescence signal from phantoms with typical mouse tissue optical properties. *Applied Optics*, 46(10):1686–1692, 2007.

[65] Cheong WF., Prahl S. A., and Welch A. J. A review of the optical properties of biological tissues. *IEEE Journal of quantum electronics*, 26(12):2166–2185, 1990.

[66] Prahl S. A., Keijzer M., Jacques S. L., and Welch A. J. A monte carlo model of light propagation in tissue. *SPIE Proceedings of Dosimetry of Laser Radiation in Medicine and Biology*, IS 5:102–111, 1989.

[67] Jacques S. L., Alter C. A., and Prahl S. A. Angular dependency of hene laser light scattering by human dermis. *Laser in the Life Sciences*, 1(4):309–334, 1987.

[68] Pharr M. and Humphereys G. *Physically based rendering. From theory to implementation.* Morgan Kaufmann, 2004.

[69] Yu TT., Lowther J., and Shene CK. Photon mapping made easy. *SIGCSE*, 2005.

[70] Christensen P. H., Jensen H. W., Kato T., and Suykens F. A practical guide to global illumination using photon mapping. *Siggraph*, 43, 2002.

[71] Christensen P. H. Faster photon map global illumination. *Journal of Graphics Tools*, 4(3):1–10, 1999.

[72] Veach E. *Robust Monte Carlo methods for light transport simulation.* PhD thesis, Stanford University., 1997.

[73] Zhou K., Ren Z., Lin S., Bao H., Guo B., and Shum HY. Real-time smoke rendering using compensated ray marching. *International Conference on Computer Graphics and Interactive Techniques, ACM Siggraph*, 2008.

[74] Moon J. T. and Marschner S. R. Simulating multiple scattering in hair using a photon mapping approach. *ACM Transactions on Graphics, Proceedings of Siggraph*, 25(3), 2006.

[75] Jarosz W., Zwicker M., and Jensen H. W. The beam radiance estimate for volumetric photon mapping. *Eurographics*, 27(2), 2008.

[76] Hey H. and Purgathofer W. Global illumination with photon map compensation. *TR-186-2-01-04*, 2001.

[77] Jensen H. W. and Christensen P. H. Efficient simulation of light transport in scenes with participating media using photon maps. *In Proceedings of Siggraph*, pages 311–320, 1999.

[78] Reinhard E., Stark M., Shirley P., and Ferwerda J. Photographic tone reproduction for digital images. *ACM Transactions on Graphics*, 21(3):267–276, 2002.

[79] Mantiuk R., Daly S., and Kerofsky L. Display adaptive tone mapping. *ACM Transactions on Graphics*, 27(3), 2008.

[80] Swenson E.A., Rosenberger A.E., and Howell P.J. Validation of endoscopy for determination of maturity in small salmonids and sex of mature individuals. *Transactions of the American Fisheries Society*, 136:994–998, 2007.

[81] Day D.C. Spectral sensitivities of the sinarback 54 camera. Technical report, Spectral Color Imaging Laboratory Group, 2003. www.art-si.org.

[82] Pate M. Color from projectors with mercury lamps. Technical report, Optical Short Course International, 2005. www.oscintl.com.

[83] Hanrahan P. and Krueger W. Reflection from layered surfaces due to subsurface scattering. *Computer Graphics (Proc. Siggraph)*, 1993.

[84] Skillman J. B. Quantum yield variation across the three pathways of photosynthesis: not yet out of the dark. *Journal of Experimental Botany*, 59(7):1647–1661, 2008.

[85] Flock S. T., Patterson M. S., Wilson B. C., and Wyman D. R. Monte carlo modeling of light propagation in highly scattering tissues-i: Model predictions and comparison with diffusion theory. *IEEE Transactions on Biomedical Engineering*, 36(12), 1989.

[86] Farina B., Saponaro S., Pignoli E., Tomatis S., and Marchesini R. Monte carlo simulation of light fluence in tissue in a cylindrical diffusing fibre geometry. *Physics in medicine and biology.*, 44:1–11, 1999.

[87] Bradford P. T. Skin cancer in skin of color. *Dermatology nursing*, 21(4):170–206, 2009.

[88] Ren H. and Chang C-I. A generalized orthogonal subspace projection approach to unsupervised multispectral image classification. *IEEE Transactions on geoscience and remote sensing*, 38(6):2515–2528, 2000.

[89] Ientilucci E. J. Hyperspectral image classification using orthogonal subspace projections: Image simulation and noise analysis. Technical report, Rochester Institute of Technology, College of Science, Center for Imaging Science, Digital Imaging and Remote Sensing Laboratory, Rochester, New York, United States, April 2001.

[90] Comaniciu D. and Meer P. Mean shift: A robust approach toward feature space analysis. *IEEE Transactions on pattern analysis and machine intelligence*, 24(5):603–619, 2002.

[91] Christoudias C. M., Georgescu B., and Meer P. Synergism in low level vision. *16th International Conference on Pattern Recognition, Quebec City, Canada*, IV:150–155, 2002.

[92] K. T. Moesta, B. Ebert, T. Handke, D. Nolte, C. Nowak, W. E. Haensch, R. K. Pandey, T. J. Dougherty, H. Rinneberg, and P. M. Schlag. Protoporphyrin ix occurs naturally in colorectal cancers and their metastases. *Cancer Research*, 61(3):991–999, 2001.

[93] Krogstad H. E. How to use the matlab fft2-routines. http://read.pudn.com/downloads122/doc/519928/HowToUseFFT2.pdf, 2004.

List of Figures

List of Tables

List of Listings